

Mathematical Problems in Engineering

Theory, Methods, and Applications

Editor-in-Chief: Jose Manoel Balthazar

Special Issue

Uncertainties in Nonlinear Structural Dynamics

Guest Editors: José Manoel Balthazar, Paulo Batista Gonçalves,
and Reyolando M. R. L. F. Brasil



Uncertainties in Nonlinear Structural Dynamics

Mathematical Problems in Engineering

Uncertainties in Nonlinear Structural Dynamics

**Guest Editors: José Manoel Balthazar, Paulo Batista
Gonçalves, and Reyolando M. R. L. F. Brasil**



Copyright © 2008 Hindawi Publishing Corporation. All rights reserved.

This is an issue published in volume 2008 of "Mathematical Problems in Engineering." All articles are open access articles distributed under the Creative Commons Attribution License, which permits unrestricted use, distribution, and reproduction in any medium, provided the original work is properly cited.

Editor-in-Chief

Jose Manoel Balthazar, State University of Sao Paulo, Brazil

Associate Editors

David Chelidze, USA
Horst Ecker, Austria
Oleg Gendelman, Israel
Oded Gottlieb, Israel
Katica R. Hedrih, Serbia
J. Horacek, Czech Republic
J. Jiang, China
Tamas Kalmar-Nagy, USA
Shijun Liao, China

Angelo Luongo, Italy
Mehrdad Massoudi, USA
Yuri V. Mikhlin, Ukraine
Ben T. Nohara, Japan
Ekaterina Pavlovskaja, UK
Francesco Pellicano, Italy
F. Lobo Pereira, Portugal
Sergio Preidikman, USA
Dane Quinn, USA

Saad A Ragab, USA
K. R. Rajagopal, USA
Giuseppe Rega, Italy
Alexander P. Seyranian, Russia
Alois Steindl, Austria
Irina Trendafilova, UK
Jerzy Warminski, Poland
Mohammad I. Younis, USA

Contents

Uncertainties in Nonlinear Structural Dynamics, José Manoel Balthazar,
Paulo Batista Gonçalves, and Reyolando M. R. L. F. Brasil
Volume 2008, Article ID 538725, 4 pages

Effect of Imperfections and Damping on the Type of Nonlinearity of Circular Plates and Shallow Spherical Shells, Cyril Touzé, Cédric Camier, Gaël Favraud,
and Olivier Thomas
Volume 2008, Article ID 678307, 19 pages

The Effect of Infinitesimal Damping on the Dynamic Instability Mechanism of Conservative Systems, Dimitris S. Sophianopoulos, George T. Michaltsos,
and Anthony N. Kounadis
Volume 2008, Article ID 471080, 25 pages

Nonlinear Modeling of Cables with Flexural Stiffness, Walter Lacarbonara and
Arnaud Pacitti
Volume 2008, Article ID 370767, 21 pages

Probabilistic and Fuzzy Arithmetic Approaches for the Treatment of Uncertainties in the Installation of Torpedo Piles, Denise Margareth Kazue Nishimura Kunitaki,
Beatriz Souza Leite Pires de Lima, Alexandre Gonçalves Evsukoff,
and Breno Pinheiro Jacob
Volume 2008, Article ID 512343, 26 pages

Effects of Variations in Nonlinear Damping Coefficients on the Parametric Vibration of a Cantilever Beam with a Lumped Mass, Demian G. Silva and Paulo S. Varoto
Volume 2008, Article ID 185351, 19 pages

Influence of Uncertainties on the Dynamic Buckling Loads of Structures Liable to Asymmetric Postbuckling Behavior, Paulo B. Gonçalves and Donald Mark Santee
Volume 2008, Article ID 490137, 24 pages

Model Validation Using Coordinate Distance with Performance Sensitivity,
Jiann-Shiun Lew
Volume 2008, Article ID 298146, 8 pages

Guaranteed Performance Robust Kalman Filter for Continuous-Time Markovian Jump Nonlinear System with Uncertain Noise, Jin Zhu, Junhong Park, Kwan-Soo Lee,
and Maksym Spiryagin
Volume 2008, Article ID 583947, 12 pages

GA-Based Fuzzy Sliding Mode Controller for Nonlinear Systems, P. C. Chen,
C. W. Chen, and W. L. Chiang
Volume 2008, Article ID 325859, 16 pages

Experimental Active Vibration Control in Truss Structures Considering Uncertainties in System Parameters, Douglas Domingues Bueno, Clayton Rodrigo Marqui,
Rodrigo Borges Santos, Camilo Mesquita Neto, and Vicente Lopes Jr.
Volume 2008, Article ID 754951, 14 pages



Sliding Mode Control of Uncertain Neutral Stochastic Systems with Multiple Delays,
Dilan Chen and Weidong Zhang
Volume 2008, Article ID 761342, 9 pages

Performance of Composite Implicit Time Integration Scheme for Nonlinear Dynamic Analysis, William Taylor Matias Silva and Luciano Mendes Bezerra
Volume 2008, Article ID 815029, 16 pages

Identification of Stochastic Loads Applied to a Nonlinear Dynamical System Using an Uncertain Computational Model, C. Soize and A. Batou
Volume 2008, Article ID 181548, 16 pages

Homotopy Perturbation Method for Solving Reaction-Diffusion Equations, Yu-Xi Wang, Hua-You Si, and Lu-Feng Mo
Volume 2008, Article ID 795838, 5 pages

Numerical Stability Test of Neutral Delay Differential Equations, Z. H. Wang
Volume 2008, Article ID 698043, 10 pages

Dynamical Models for Computer Viruses Propagation, José R. C. Piqueira and Felipe Barbosa Cesar
Volume 2008, Article ID 940526, 11 pages

Editorial

Uncertainties in Nonlinear Structural Dynamics

**José Manoel Balthazar,¹ Paulo Batista Gonçalves,²
and Reyolando M. R. L. F. Brasil³**

¹ *Department of Statistics, Applied Mathematics, and Computation,
State University of São Paulo (UNESP) at Rio Claro, 13500-230 Rio Claro, SP, Brazil*

² *Civil Engineering Department, Pontifical Catholic University of Rio de Janeiro (PUC-Rio),
22453-900 Rio de Janeiro, RJ, Brazil*

³ *Department of Structural and Geotechnical Engineering, University of São Paulo (PEF/EPUSP/USP),
05508-900 São Paulo, SP, Brazil*

Correspondence should be addressed to José Manoel Balthazar, jmbaltha@rc.unesp.br

Received 10 September 2008; Accepted 10 September 2008

Copyright © 2008 José Manoel Balthazar et al. This is an open access article distributed under the Creative Commons Attribution License, which permits unrestricted use, distribution, and reproduction in any medium, provided the original work is properly cited.

Nonlinear dynamical systems usually display high complexity. The last decades have seen a remarkable and fruitful development of nonlinear dynamics, and a large number of papers have been published in all branches of science. In modeling natural and man-made systems, it is assumed in general that the system is perfect and that all parameters of the system are known. However, real systems are usually imperfect, and uncertainties are present both in system parameters and in the modeling stage. This is associated with the lack of precise knowledge of the system parameters, random or noisy external loading, operating conditions, and variabilities in manufacturing processes, among other things. In many situations, these uncertainties are not important and may be overlooked in the mathematical modeling of the problem. However in several situations, the uncertainties can have significant influence on the dynamic response and the stability of the system. Uncertainties may also be found in system response, even in cases where all parameters are well established, such as systems exhibiting high sensitivity to initial conditions. This is particularly important in strongly nonlinear chaotic systems and those with fractal-basin boundaries. However, the influence of uncertainties in local and global bifurcations and basins of attractions and on important engineering concepts such as reliability, safety, and robustness is not well studied in literature. Even the definition of a random bifurcation is still an open problem in nonlinear dynamics. This is a rather broad topic in nonlinear dynamics.

So, the present special issue is dedicated to the influence of uncertainties in structural dynamics. In engineering structures, the main sources of uncertainties are: imperfections, uncertainties in system parameters (mass, damping, and stiffness), uncertainties in the external load, such as random loads (wind and earthquake), sensitivity to initial conditions,

and interaction between load and structure. These types of uncertainties coupled to system nonlinearities may have a marked influence on the structure's response, particularly in a dynamic environment. So, it is useful to study their influence on bifurcations, stability boundaries, and basins of attraction. It is also interesting to discuss their influence on safety factors, integrity measures, and confiability. These topics are essential for a safe design of structures and the development of mathematically based safe (but not too conservative) design codes and methodologies.

This issue comprises 16 contributions from 8 different countries, which give a picture of the current research on uncertainties in engineering problems. Several aspects are addressed, including the following: influence of uncertainties on buckling and vibration of structural elements: trusses, cables, piles, beams, plates, and shells, the consideration of uncertainties in vibration control, stochastic systems, and numerical algorithms for the analysis of systems with different types of uncertainties.

The effect of geometric imperfections, unavoidable in real systems, and viscous damping on the type of nonlinearity (i.e., the hardening or softening behavior) of circular plates and shallow spherical shells is investigated in the paper written by C. Touzé et al. The von Kármán large-deflection theory is used to derive the continuous models. Then, nonlinear normal modes (NNMs) are used for predicting the structures' nonlinear behavior.

D. S. Sophianopoulos et al. study the local instability of a 2 degree of freedom (DOF) weakly damped systems using the Liénard-Chipart stability criterion. The individual and coupling effects of mass and stiffness distribution on the dynamic asymptotic stability due to mainly infinitesimal damping are examined. The validity of the theoretical findings presented herein is verified via a nonlinear dynamic analysis.

The nonlinear modeling of cables with flexural stiffness is discussed by W. Lacarbonara and A. Pacitti. A geometrically exact formulation of cables suffering axis stretching and flexural curvature is presented. The dynamical formulation is based on nonlinearly viscoelastic constitutive laws for the tension and bending moment with the additional constitutive nonlinearity accounting for the no-compression condition.

The paper by D. M. K. N. Kunitaki et al. uses probabilistic and fuzzy arithmetic approaches for the treatment of uncertainties in the installation of torpedo piles used in the foundations of mooring lines and risers of floating production systems for offshore oil exploitation. Methodologies involving, respectively, the Monte Carlo method and concepts of fuzzy arithmetic are used to assess the sensitivity of the response to the variation of the uncertain parameters.

The effects of uncertainties in nonlinear damping coefficients on the parametric vibration of a cantilever beam with a lumped mass are investigated by D. G. Silva and P. S. Varoto. The effects of a turbulent frictional damping force on the dynamic behavior of the flexible structure are studied numerically and experimentally. The results indicate that variations on the damping coefficient significantly alter the dynamics of the structure under investigation.

The influence of uncertainties on the dynamic buckling loads of structures liable to asymmetric postbuckling behavior is studied by P. B. Gonçalves and D. M. Santee. A parametric analysis illustrates the influence of uncertainties in system parameters and random perturbations of the forcing on the dynamic buckling load. A lower bound for the buckling loads, obtained by the application of the Melnikov criterion, is proposed, which compare well with the scatter of buckling loads obtained numerically.

The paper by J. Lew presents an approach to model validation for structures with significant parameter variations. Model uncertainty of the structural dynamics is quantified

with the use of a singular value decomposition technique to extract the principal components of parameter change, and an interval model is generated to represent the system with parameter uncertainty. A beam structure with an attached subsystem, which has significant parameter uncertainty, is used to demonstrate the proposed approach.

J. Zhu et al. investigate a robust Kalman filtering design for continuous-time Markovian jump nonlinear systems with uncertain noise. The statistical characteristics of system noise and observation noise are time-varying or unmeasurable instead of stationary. By view of robust estimation, maximum admissible upper bound of the uncertainty to noise covariance matrix is given based on system state estimation performance. The robustness of the Kalman filter against noise uncertainty and stability of dynamic systems is studied by Game theory.

The “Ga-based fuzzy sliding mode controller for nonlinear systems” is studied by P. C. Chen et al. First, they approximate and describe an uncertain and nonlinear plant for the tracking of a reference trajectory via a fuzzy model incorporating fuzzy logic control rules. Next, the initial values of the consequent parameter vector are decided via a genetic algorithm. After this, an adaptive fuzzy sliding model controller, designed to simultaneously stabilize and control the system, is derived. The stability of the nonlinear system is ensured by the derivation of the stability criterion based upon Lyapunov’s direct method.

The robust active vibration control of flexible structures considering uncertainties in system parameters is addressed by D. D. Bueno et al. The paper proposes an experimental methodology for vibration control in a 3D truss structure using PZT wafer stacks and a robust control algorithm solved by linear matrix inequalities.

The paper written by D. Chen and W. Zhang is concerned with the sliding mode control for uncertain stochastic neutral systems with multiple delays. A switching surface is adopted first. Then, by means of linear matrix inequalities, a sufficient condition is derived to ensure the global stochastic stability of the stochastic system in the sliding mode for all admissible uncertainties. The synthesized sliding mode controller guarantees the existence of the sliding mode.

W. T. M. Lima and L. M. Bezerra’s paper presents an implicit time integration scheme for transient response solution of structures under large deformations and long-time durations. The influence of different substep sizes on the numerical dissipation of the method is studied throughout three practical examples. The method shows good performance and may be considered good for nonlinear transient response of structures.

C. Soize and A. Batou study the identification of stochastic loads applied to a nonlinear dynamical system for which a few experimental responses are available using an uncertain computational model. A nonparametric probabilistic approach of both parameter uncertainties and model uncertainties is implemented to take into account uncertainties, and the level of uncertainties is identified using the maximum likelihood method. The identified stochastic simplified computational model which is obtained is then used to perform the identification of the stochastic loads applied to the real nonlinear dynamical system.

A homotopy perturbation method for solving reaction-diffusion equations is proposed by L. Mo et al. In this method, the trial function (initial solution) is chosen with some unknown parameters, which are identified using the method of weighted residuals. Some examples are given, and the obtained results are compared with the exact solutions.

Z. H. Wang presents, on the basis of Lambert W function, an iterative algorithm for the calculation of the rightmost roots of the neutral delay differential equations so that the stability of the delay equations can be determined directly. The application of the method is illustrated with two examples.

Finally, dynamical models for computer viruses propagation are proposed by J. R. C. Piqueira and F. B. Cesar. Data from three different viruses are collected in the Internet, and two different identification techniques, autoregressive and Fourier analyses, are applied showing that it is possible to forecast the dynamics of a new virus propagation by using the data collected from other viruses that formerly infected the network.

José Manoel Balthazar
Paulo Batista Gonçalves
Reyolando M. R. L. F. Brasil

Research Article

Effect of Imperfections and Damping on the Type of Nonlinearity of Circular Plates and Shallow Spherical Shells

Cyril Touzé,¹ Cédric Camier,¹ Gaël Favraud,¹ and Olivier Thomas²

¹ ENSTA-UME, Unité de Mécanique, Chemin de la Hunière, 91761 Palaiseau Cedex, France

² CNAM-LMSSC, Laboratoire de Mécanique des Structures et Systèmes Couplés,
2 rue Conté, 75003 Paris, France

Correspondence should be addressed to Cyril Touzé, cyril.touze@ensta.fr

Received 28 November 2007; Accepted 20 February 2008

Recommended by Paulo Gonçalves

The effect of geometric imperfections and viscous damping on the type of nonlinearity (i.e., the hardening or softening behaviour) of circular plates and shallow spherical shells with free edge is here investigated. The Von Kármán large-deflection theory is used to derive the continuous models. Then, nonlinear normal modes (NNMs) are used for predicting with accuracy the coefficient, the sign of which determines the hardening or softening behaviour of the structure. The effect of geometric imperfections, unavoidable in real systems, is studied by adding a static initial component in the deflection of a circular plate. Axisymmetric as well as asymmetric imperfections are investigated, and their effect on the type of nonlinearity of the modes of an imperfect plate is documented. Transitions from hardening to softening behaviour are predicted quantitatively for imperfections having the shapes of eigenmodes of a perfect plate. The role of 2:1 internal resonance in this process is underlined. When damping is included in the calculation, it is found that the softening behaviour is generally favoured, but its effect remains limited.

Copyright © 2008 Cyril Touzé et al. This is an open access article distributed under the Creative Commons Attribution License, which permits unrestricted use, distribution, and reproduction in any medium, provided the original work is properly cited.

1. Introduction

When continuous structures such as plates and shells undergo large amplitude motions, the geometrical nonlinearity leads to a dependence of free oscillation frequencies on vibration amplitude. The type of nonlinearity describes this dependency, which can be of the hardening type (the frequency increases with amplitude), or of the softening type (the frequency decreases). A large amount of literature is devoted to predicting this type of nonlinearity for continuous structures, and especially for structures with an initial curvature such as arches or shells because the presence of the quadratic nonlinearity makes the problem more difficult to solve. On the other hand, the hardening behaviour of flat structures such as beams and plates

is a clearly established fact, on the theoretical as well as the experimental viewpoint, (see, e.g., [1–6]). The presence of the quadratic nonlinearity may change the behaviour from hardening to softening type, depending on the relative magnitude of quadratic and cubic nonlinear terms.

Among the available studies concerned with this subject, quite all of them that were published before 1992 could not be considered as definitive since they generally restrict to the case of a single-mode vibration through Galerkin method, see, for example, [7–9] for shallow spherical shells, or [10] for imperfect circular plates. Unfortunately, it has been shown by a number of more recent investigations that too severe truncations lead to erroneous results in the prediction of the type of nonlinearity, see, for example, [11, 12], or the abundant literature on circular cylindrical shells, where the investigators faced this problem for a long time [13–18]. As a consequence, a large number of modes must mandatory be kept in the truncation of the partial differential equations (PDEs) of motion, in order to accurately predict the type of nonlinearity. Recent papers are now available where a reliable prediction is realized, for the case of buckled beams [19], circular cylindrical shells [20], suspended cables [21], and shallow spherical shells [22].

However, these last studies are restricted to the case of perfect structures, and the damping is neglected in the computations; and both of them have an influence on the type of nonlinearity, so that a complete and thorough theoretical study that could be applied to real structures need to address the effect of imperfections and damping. The geometric imperfections have a first-order effect on the linear as well as the nonlinear characteristics of structures. A large amount of studies are available, where the effect of imperfections on the eigenfrequencies and on the buckling loads are generally addressed, see, for example, [23–28] for the case of circular cylindrical shells, [29] for shallow cylindrical panels, and [30] for the case of rectangular plates. Nonlinear frequency-responses curves are shown in [31, 32] for clamped circular plates, [33–35] for rectangular plates, [36] for circular cylindrical shells, and [37] for circular cylindrical panels. Even though the presence of geometric imperfection has been recognized as a major factor that could make the hardening behaviour of the flat plate turn to softening behaviour for an imperfection amplitude of a fraction of the plate thickness [10, 38], a quantitative study, which is not restricted to axisymmetric modes and that does not perform too crude truncations in the Galerkin expansion, is still missing.

To the authors' knowledge, the role of the damping in the prediction of the type of nonlinearity has been only recently detected as an important factor that could change the behaviour from hardening to softening type [39]. In particular, it is shown in [39] on a simple two degrees-of-freedom (dofs) system, that the damping generally favours the softening behaviour. The aim of the present study is thus to apply this theoretical result to the practical case of a damped shallow spherical shell, so as to quantitatively assess the effect of structural damping of the viscous type on the type of nonlinearity of a two-dimensional vibrating structure.

The article is organized as follows. In Section 2, local equations and boundary conditions for an imperfect circular plate with free edge are given. Then the method used for computing the type of nonlinearity is explained. Section 3 investigates how typical imperfections may turn the hardening behaviour of flat plates to softening behaviour. Quantitative results are given for selected imperfections having the shape of eigenmodes of the perfect structure. Section 4 is devoted to the effect of viscous damping. The particular case of a spherical imperfection is selected, and the results are shown for three different damping dependences on frequency.

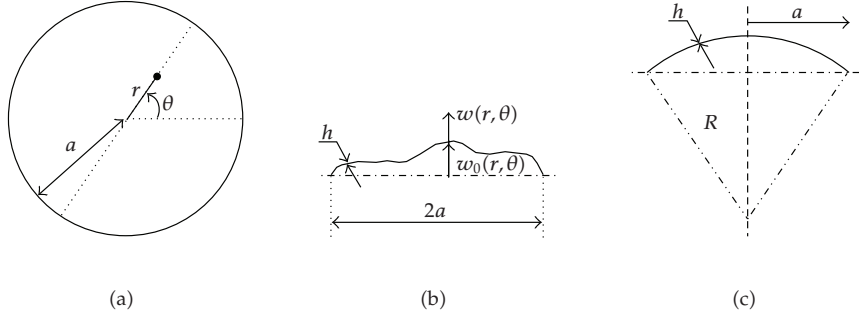


Figure 1: (a) Top view and (b) cross-section of an imperfect circular plate of radius a and thickness h . (c) The particular case of a spherical imperfection, with radius of curvature R .

2. Theoretical formulation

2.1. Local equations and boundary conditions

A thin plate of diameter $2a$ and uniform thickness h is considered, with $h \ll a$, and free-edge boundary condition. The local equations governing the large-amplitude displacement of a perfect plate, assuming the nonlinear Von Kármán strain-displacement relationship and neglecting in-plane inertia, are given, for example, in [5, 40]. An initial imperfection, denoted by $w_0(r, \theta)$ and associated with zero initial stresses is also considered, see Figure 1. The shape of this imperfection is arbitrary, and its amplitude is small compared to the diameter (shallow assumption): $w_0(r, \theta) \ll a$. The local equations for an imperfect plate deduce from the perfect case [18, 41, 42]. With $w(r, \theta, t)$ being the transverse displacement from the imperfect position at rest, the equations of motion write

$$D\Delta\Delta w + \rho h \ddot{w} = L(w, F) + L(w_0, F) - c\dot{w}, \quad (2.1a)$$

$$\Delta\Delta F = -\frac{Eh}{2} [L(w, w) + 2L(w, w_0)], \quad (2.1b)$$

where $D = Eh^3/12(1-\nu^2)$ is the flexural rigidity, Δ stands for the laplacian operator, c accounts for structural damping of the viscous type, F is the Airy stress function, and L is a bilinear operator, whose expression in polar coordinates reads

$$L(w, F) = w_{,rr} \left(\frac{F_{,r}}{r} + \frac{F_{,\theta\theta}}{r^2} \right) + F_{,rr} \left(\frac{w_{,r}}{r} + \frac{w_{,\theta\theta}}{r^2} \right) - 2 \left(\frac{w_{,r\theta}}{r} - \frac{w_{,\theta}}{r^2} \right) \left(\frac{F_{,r\theta}}{r} - \frac{F_{,\theta}}{r^2} \right). \quad (2.2)$$

The equations are then written with nondimensional variables, by introducing

$$\begin{aligned} r &= a\bar{r}, & t &= a^2\sqrt{\rho h/D}\bar{t}, & w &= h\bar{w}, & w_0 &= h\bar{w}_0, \\ F &= Eh^3\bar{F}, & c &= [Eh^3/a^2]\sqrt{\rho h/D}\bar{c}. \end{aligned} \quad (2.3)$$

As nondimensional equations will be used in the remainder of the study, overbars are now omitted in order to write the dimensionless form of the equations of motion

$$\Delta \Delta w + \ddot{w} = \varepsilon [L(w, F) + L(w_0, F) - c\dot{w}], \quad (2.4a)$$

$$\Delta \Delta F = -\frac{1}{2} [L(w, w) + 2L(w, w_0)], \quad (2.4b)$$

where $\varepsilon = 12(1 - \nu^2)$.

The boundary conditions for the case of a free edge write, in nondimensional form [5]

$$F_{,r} + F_{,\theta\theta} = 0, \quad F_{,r\theta} + F_{,\theta} = 0, \quad \text{at } r = 1, \quad (2.5a)$$

$$w_{,rr} + \nu w_{,r} + \nu w_{,\theta\theta} = 0, \quad \text{at } r = 1, \quad (2.5b)$$

$$w_{,rrr} + w_{,rr} - w_{,r} + (2 - \nu)w_{,r\theta\theta} - (3 - \nu)w_{,\theta\theta} = 0, \quad \text{at } r = 1. \quad (2.5c)$$

In order to discretize the PDEs, a Galerkin procedure is used. As the eigenmodes cannot be computed analytically because the shape of the imperfection is arbitrary, the eigenmodes of the perfect plate $\Psi_p(r, \theta)$ are selected as basis functions. Analytical expressions of $\Psi_p(r, \theta)$ involve Bessel functions and can be found in [5]. The unknown displacement is expanded with

$$w(r, \theta, t) = \sum_{p=1}^{+\infty} q_p(t) \Psi_p(r, \theta), \quad (2.6)$$

where the time functions q_p are now the unknowns. In this expression, the subscript p refers to a specific mode of the perfect plate, defined by a couple (k, n) , where k is the number of nodal diameters and n the number of nodal circles. If $k \neq 0$, a binary variable is added, indicating the preferential configuration considered (*sine* or *cosine* companion mode). Inserting the expansion (2.6) into (2.4a) and (2.4b) and using the orthogonality properties of the expansion functions, the dynamical equations are found to be, for all $p = 1 \cdots N$,

$$\ddot{q}_p + 2\xi_p \omega_p \dot{q}_p + \varepsilon \left[\sum_{i=1}^{+\infty} \alpha_i^p q_i + \sum_{i,j=1}^{+\infty} \beta_{ij}^p q_i q_j + \sum_{i,j,k=1}^{+\infty} \Gamma_{ijk}^p q_i q_j q_k \right] = 0. \quad (2.7)$$

Linear coupling terms between the oscillator equations are present, as the natural modes have not been used for discretizing the PDEs. Analytical expressions of the coupling coefficients $(\alpha_i^p, \beta_{ij}^p, \Gamma_{ijk}^p)$ are given in [42]. The generic viscous damping term c of (2.4a) has been specialized in the discretized equations so as to handle the more general case of a modal viscous damping term of the form $2\xi_p \omega_p \dot{q}_p$, where ξ_p is the damping factor and ω_p the eigenfrequency of mode p . On the other hand, external forces have been cancelled, as the remainder of the study will consider free vibrations only.

In order to work with diagonalized linear parts, the matrix of eigenvectors \mathbf{P} of the linear part $\mathbf{L} = [\alpha_i^p]_{p,i}$ is numerically computed. A linear change of coordinates is processed, $\mathbf{q} = \mathbf{P}\mathbf{X}$, where $\mathbf{X} = [X_1 \cdots X_N]^T$ is, by definition, the vector of modal coordinates, and N is the number of expansion function kept in practical application of the Galerkin's method. Application of

\mathbf{P} makes the linear part diagonal, so that the discretized equations of motion finally writes, $\forall p = 1 \dots N$,

$$\ddot{X}_p + 2\xi_p \omega_p \dot{X}_p + \omega_p^2 X_p + \varepsilon \left[\sum_{i,j=1}^N g_{ij}^p X_i X_j + \sum_{i,j,k=1}^N h_{ijk}^p X_i X_j X_k \right] = 0. \quad (2.8)$$

The temporal equations (2.8) describe the dynamics of an imperfect circular plate. The type of nonlinearity can be inferred from these equations. Unfortunately, too severe truncations in (2.8), for example, by keeping only one degree-of-freedom (dof) ($N = 1$) when studying the nonlinear behaviour of the p th mode, lead to incorrect predictions. Nonlinear normal modes (NNMs) offer a clean framework for deriving a single oscillator equation capturing the correct type of nonlinearity [12]. This is recalled in Section 3, where the analytical expression of the coefficient dictating the type of nonlinearity is given.

2.2. Type of nonlinearity

Non-linear oscillators differ from linear ones by the frequency dependence on vibration amplitude. The type of nonlinearity defines the behaviour, which can be of the hardening or the softening type.

As shown in [12], NNMs provide an efficient framework for properly truncating nonlinear oscillator equations like (2.8) and predict the type of nonlinearity (hardening or softening behaviour). The method has already been successfully applied to the case of undamped shallow spherical shells in [22]. The main idea is to derive a nonlinear change of coordinates, allowing one to pass from the *modal* X_p coordinates to new-defined *normal* coordinates R_p , describing the motions in an invariant-based span of the phase space. The nonlinear change of coordinates is computed from Poincaré and Poincaré-Dulac's theorems, by successive elimination of nonessential coupling terms in the nonlinear oscillator equations. Formally, it reads

$$X_p = R_p + \sum_{i=1}^N \sum_{j \geq i}^N (a_{ij}^p R_i R_j + b_{ij}^p S_i S_j) + \sum_{i=1}^N \sum_{j=1}^N c_{ij}^p R_i S_j \quad (2.9a)$$

$$+ \sum_{i=1}^N \sum_{j \geq i}^N \sum_{k \geq j}^N (r_{ijk}^p R_i R_j R_k + s_{ijk}^p S_i S_j S_k) + \sum_{i=1}^N \sum_{j=1}^N \sum_{k \geq j}^N (t_{ijk}^p S_i R_j R_k + u_{ijk}^p R_i S_j S_k),$$

$$Y_p = S_p + \sum_{i=1}^N \sum_{j \geq i}^N (\alpha_{ij}^p R_i R_j + \beta_{ij}^p S_i S_j) + \sum_{i=1}^N \sum_{j=1}^N \gamma_{ij}^p R_i S_j \quad (2.9b)$$

$$+ \sum_{i=1}^N \sum_{j \geq i}^N \sum_{k \geq j}^N (\lambda_{ijk}^p R_i R_j R_k + \mu_{ijk}^p S_i S_j S_k) + \sum_{i=1}^N \sum_{j=1}^N \sum_{k \geq j}^N (\nu_{ijk}^p S_i R_j R_k + \zeta_{ijk}^p R_i S_j S_k).$$

A third-order approximation of the complete change of coordinates is thus computed. The analytical expressions of the introduced coefficients $\{a_{ij}^p, b_{ij}^p, c_{ij}^p, r_{ijk}^p, s_{ijk}^p, t_{ijk}^p, u_{ijk}^p\}$ and $\{\alpha_{ij}^p, \beta_{ij}^p, \gamma_{ij}^p, \lambda_{ijk}^p, \mu_{ijk}^p, \nu_{ijk}^p, \zeta_{ijk}^p\}$ are not given here for the sake of brevity. The interested reader may find them in [12] for the undamped case, and in [39] for the damped case.

Once the nonlinear change of coordinates operated, proper truncations can be realized. In particular, keeping only the normal coordinates R_p allows prediction of the correct type of nonlinearity for the p th mode. The dynamics onto the p th NNM reads

$$\ddot{R}_p + \omega_p^2 R_p + 2\xi_p \omega_p \dot{R}_p + (\varepsilon h_{ppp}^p + A_{ppp}^p) R_p^3 + B_{ppp}^p R_p \dot{R}_p^2 + C_{ppp}^p R_p^2 \dot{R}_p = 0, \quad (2.10)$$

where A_{ppp}^p , B_{ppp}^p , and C_{ppp}^p are new coefficients coming from the change of coordinates. Their expressions involve the quadratic coefficients $\{g_{ij}^p\}$ only, together with some of the transformation coefficients, $\{a_{ij}^p, b_{ij}^p, c_{ij}^p\}$ from (2.9a) and (2.9b) [39]:

$$A_{ppp}^p = \varepsilon \left[\sum_{l \geq i}^N g_{pl}^p a_{pp}^l + \sum_{l \leq i}^N g_{lp}^p a_{pp}^l \right], \quad (2.11a)$$

$$B_{ppp}^p = \varepsilon \left[\sum_{l \geq i}^N g_{pl}^p b_{pp}^l + \sum_{l \leq i}^N g_{lp}^p b_{pp}^l \right], \quad (2.11b)$$

$$C_{ppp}^p = \varepsilon \left[\sum_{l \geq i}^N g_{pl}^p c_{pp}^l + \sum_{l \leq i}^N g_{lp}^p c_{pp}^l \right]. \quad (2.11c)$$

The asymptotic third-order approximation of the dynamics onto the p th NNM given by (2.10) allows one to accurately predict the type of nonlinearity of mode p . A first-order perturbative development from (2.10) gives the dependence of the nonlinear oscillation frequency ω_{NL} on the amplitude of vibration a by the relationship:

$$\omega_{NL} = \omega_p (1 + T_p a^2), \quad (2.12)$$

where ω_p is the natural angular frequency. In this expression, T_p is the coefficient governing the type of nonlinearity. If $T_p > 0$, then hardening behaviour occurs, whereas $T_p < 0$ implies softening behaviour. The analytical expression for T_p writes [12, 22]

$$T_p = \frac{1}{8\omega_p^2} [3(A_{ppp}^p + \varepsilon h_{ppp}^p) + \omega_p^2 B_{ppp}^p]. \quad (2.13)$$

Finally, the method used for deriving the type of nonlinearity can be summarized as follows. For a geometric imperfection of a given amplitude, the discretization leading to the nonlinear oscillator (2.8) is first computed. The numerical effort associated to this operation is the most important but remains acceptable on a standard computer. Then the nonlinear change of coordinates is computed, which allows derivation of the A_{ppp}^p and B_{ppp}^p terms occurring in (2.13), the sign of which determines the type of nonlinearity. Numerical results are given in Section 3 for specific imperfections.

3. Effect of imperfections

This section is devoted to numerical results about the effect of typical imperfections on the type of nonlinearity of imperfect plates. Two typical imperfections are selected. The first one is axisymmetric and has the shape of mode (0,1), the second one has the shape of the first asymmetric mode (2,0). Consequently, damping is not considered, so that in each equation we have: $\forall p = 1 \cdots N$, $\xi_p = 0$. The study of the effect of damping will be done separately and is postponed to Section 4.

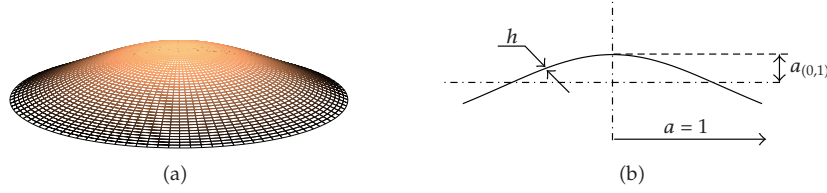


Figure 2: (a) Three-dimensional view and (b) cross-section of the circular plate with geometric imperfection having the shape of the first axisymmetric mode. As nondimensional quantities are used, $a = 1$ and the amplitude $a_{(0,1)}$ of the imperfection is made nondimensional with respect to the thickness h .

3.1. Axisymmetric imperfection

In this section, the particular case of an axisymmetric imperfection having the shape of mode (0,1) (i.e., with one nodal circle and no nodal diameter) is considered. The expression of the static deflection writes

$$w_0(r) = a_{(0,1)} \Psi_{(0,1)}(r), \quad (3.1)$$

where $\Psi_{(0,1)}(r)$ is the mode shape, depending only on the radial coordinate r as a consequence of axisymmetry, and $a_{(0,1)}$ the considered amplitude. The mode shape $\Psi_{(0,1)}(r)$ depends on Bessel function [5], and is shown in Figure 2. The eigenmode is normalized so that $\int_0^1 \Psi_{(0,1)}^2(r) dr = 1$.

Figure 3 shows the effect of the imperfection on the eigenfrequencies, for an imperfection amplitude from 0 (perfect plate) to $10h$. It is observed that the purely asymmetric modes $(k,0)$, having no nodal circle and k nodal diameters, are marginally affected by the axisymmetric imperfection. The computation has been done by keeping 51 basis functions: purely asymmetric modes from (2,0) to (10,0), purely axisymmetric modes from (0,1) to (0,13); and mixed modes from (1,1) to (6,1), (1,2), (2,2), (3,2) and (1,3). More details and comparisons with a numerical solution based on finite elements are provided in [42, 43]. The slight dependence of purely asymmetric eigenfrequencies on an axisymmetric imperfection has already been observed in [44] with the case of the shallow spherical shell.

First, the effect of the imperfection on the axisymmetric modes (0,1) and (0,2) is studied. In this case, the problem is fully axisymmetric so that all the truncations can be limited to axisymmetric modes only, which drastically reduces the numerical burden. The result for mode (0,1) is shown in Figure 4. It is observed that the huge variation of the eigenfrequency with respect to the amplitude of the imperfection results in a quick turn of the behaviour from the hardening to the softening type, occurring for an imperfection amplitude of $a_{(0,1)} = 0.38h$. This small value has direct implication for the case of real plates. As the behaviour changes for a fraction of the plate thickness, it should not be intriguing to measure a softening behaviour with real plates having small imperfections. This result can also be compared to an earlier result obtained by Hui [10]. Although Hui did not study free-edge boundary condition, he reported a numerical result for the case of simply supported boundary conditions, where the behaviour changes for an imperfection amplitude of $0.28h$. The second main observation inferred from Figure 4 is the occurrence of 2:1 internal resonance between eigenfrequencies, leading to discontinuities in the coefficient $T_{(0,1)}$ dictating the type of nonlinearity. This fact has already been observed and commented for the case of shallow spherical shells in [22].

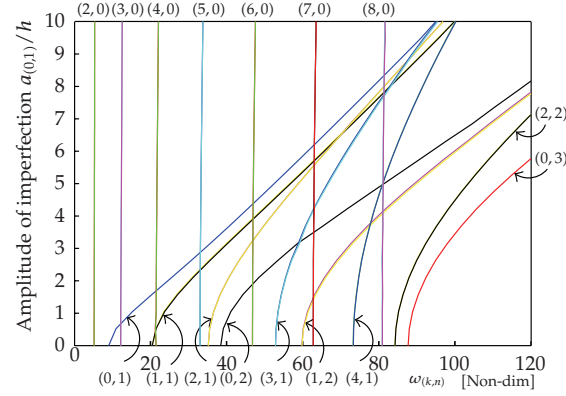


Figure 3: Nondimensional natural frequencies $\omega_{(k,n)}$ of the imperfect plate versus the amplitude of the imperfection having the shape of mode (0,1).

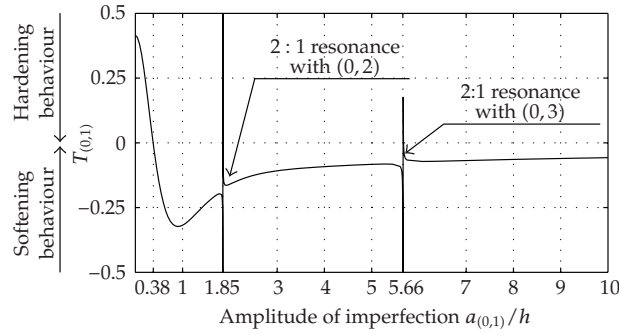


Figure 4: Type of nonlinearity for mode (0,1) with an axisymmetric imperfection having the shape of mode (0,1).

It has also been observed for buckled beams and suspended cables [19, 21]. This is a small denominator effect typical of internal resonance, that is, when the frequency of the studied mode (0,1) exactly fulfills the relationship $2\omega_{(0,1)} = \omega_{(0,n)}$ with another axisymmetric mode. 2:1 resonance arises here with mode (0,2) at $1.85h$ and with mode (0,3) at $5.66h$. On a practical point of view, one must bear in mind that when 2:1 internal resonance occurs, single-mode solution does not exist anymore, only coupled solutions are possible. Hence the concept of the type of nonlinearity, intimately associated with a single dof behaviour, loses its meaning in a narrow interval around the resonance.

The numerical result for mode (0,2) is shown in Figure 5. Once again, the geometric effect is important and leads to a change of behaviour occurring at $a_{(0,1)} = 0.75h$, that is, for a small level of imperfection. 2:1 internal resonance also occurs, thus creating narrow region where hardening behaviour could be observed. This result extends Hui's analysis since only mode (0,1) was studied. Moreover, as a single-mode truncation was used in [10], 2:1 resonances were missed.

Finally, the effect of the imperfection on asymmetric modes is shown in Figure 6 for modes (2,0) and (4,0). The very slight variation of the eigenfrequencies of these modes versus

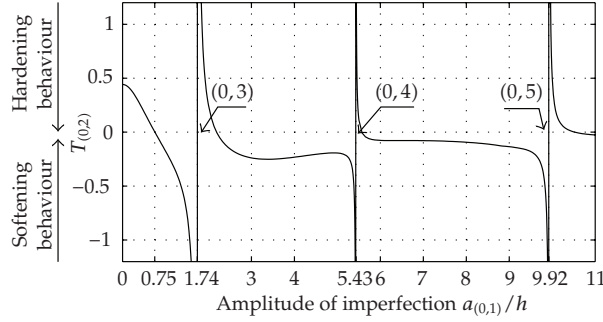


Figure 5: Type of nonlinearity for mode (0,2) with an axisymmetric imperfection having the shape of mode (0,1). 2:1 internal resonances with modes (0,3), (0,4), and (0,5) occurs, respectively, for $a_{(0,1)}/h = 1.74, 5.43$, and 9.92 .

the axisymmetric imperfection results in a very slight effect of the geometry. It is observed that before the first 2:1 internal resonance, the type of nonlinearity shows small variations. Hence it is the behaviour of the other eigenfrequencies and the occurrence of 2:1 internal resonance that makes, in these cases, the behaviour turn from hardening to softening behaviour. For mode (2,0), this occurs for an imperfection amplitude of $a_{(0,1)} = 0.44h$, where 2:1 resonance with mode (0,1) is observed. For mode (4,0), the first 2:1 resonance occurs with mode (0,2) at $a_{(0,1)} = 1.39h$, but do not change the behaviour. It is the resonance with mode (0,1) at $a_{(0,1)} = 4h$ which makes the behaviour turn from hardening to softening.

These results corroborate those obtained on shallow spherical shells [22]. The fundamental importance of axisymmetric modes in the study of asymmetric ones is confirmed, showing once again that reduction to single mode has no chance to deliver correct results. The behaviour of purely asymmetric modes is found to be of the hardening type until the 2:1 internal resonance with mode (0,1) occurs. However, a specificity of mode (2,0) with regard to all the other purely asymmetric modes is that after this resonance, hardening behaviour (though with a very small value of $T_{(2,0)}$) is observed. This was also the case for shallow spherical shells [22]. Finally, for very large values of the imperfection, the behaviour tends to be neutral.

3.2. Asymmetric imperfection

In this section, the effect of an imperfection having the shape of mode (2,0) is studied. Due to the loss of symmetry, degenerated modes are awaited to cease to exist : the equal eigenfrequencies of the *sine* and *cosine* configuration of degenerated modes split. In the following, distinction is made systematically between the sine or cosine configuration of companion modes, for example, mode (2,0,C) (resp., (2,0,S)) refers to the cosine (resp., sine) configuration. More precisely, the imperfection has the shape of (2,0,C) and is shown in Figure 7.

The behaviour of the eigenfrequencies with the imperfection is shown in Figure 8. As expected, the variation of the eigenfrequency corresponding to (2,0,C) is huge, whereas (2,0,S) keep quite a constant value. The symmetry is not completely broken. One can show that only eigenmodes of the type $(2k, n)$ split. On the other hand, as shown in Figure 8, modes (3,0), (5,0), and (1,1) are still degenerated.

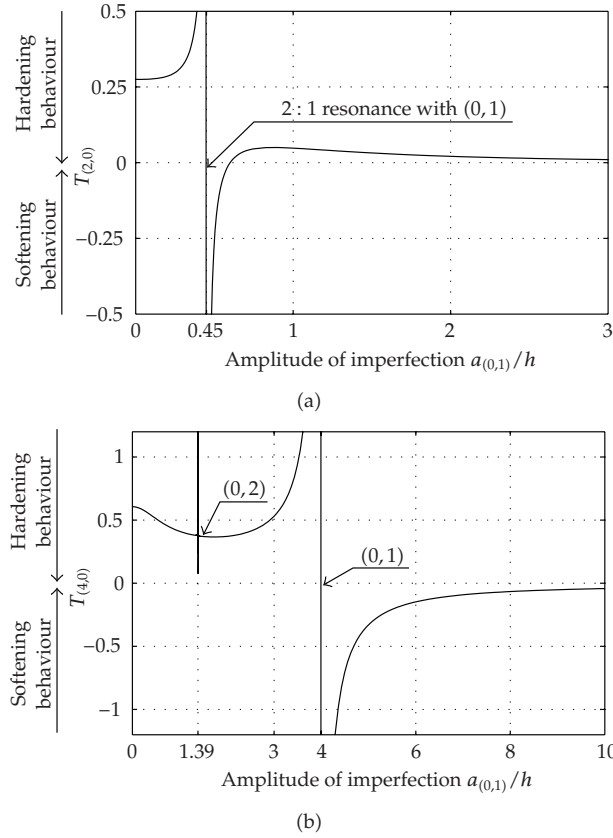


Figure 6: Type of nonlinearity for (a): mode (2,0), and (b): mode (4,0) with an axisymmetric imperfection having the shape of mode (0,1).

The numerical results for type of nonlinearity relative to the two configurations (2,0,C) and (2,0,S) are shown in Figure 9. The natural frequency of mode (2,0,C) undergoes a huge variation, which results in a quick change of behaviour, occurring at $0.54h$. Then, a 2:1 internal resonance with (0,2) is noted, but without a noticeable change in the type of nonlinearity, as the interval where the discontinuity present is very narrow. In this case, the behaviour of $T_{(2,0,C)}$ looks like the one observed in the precedent case, that is, the variation of $T_{(0,1)}$ versus an imperfection having the same shape. On the other hand, the eigenfrequency of mode (2,0,S) remains quite unchanged, so that the behaviour of $T_{(2,0,S)}$ is not much affected by the imperfection until the 2:1 internal resonance is encountered. In that case, the resonance occurs with the other configuration, that is, mode (2,0,C).

Finally, the results for the first two axisymmetric modes (0,1) and (0,2) are shown in Figure 10. Mode (0,1) shows a very slight variation of its eigenfrequency with respect to the asymmetric imperfection (2,0,C). Consequently, the type of nonlinearity is not much affected, until the eigenfrequency of (2,0,C) comes to two times $\omega_{(0,1)}$: 2:1 internal resonance occurs, and the behaviour becomes softening. On the other hand, the eigenfrequency of (0,2) is more affected by the imperfection. This result in an important decrease of $T_{(0,2)}$ while still remaining positive. A 2:1 internal resonance with (0,3) is encountered for $3.51h$, and two others 2:1

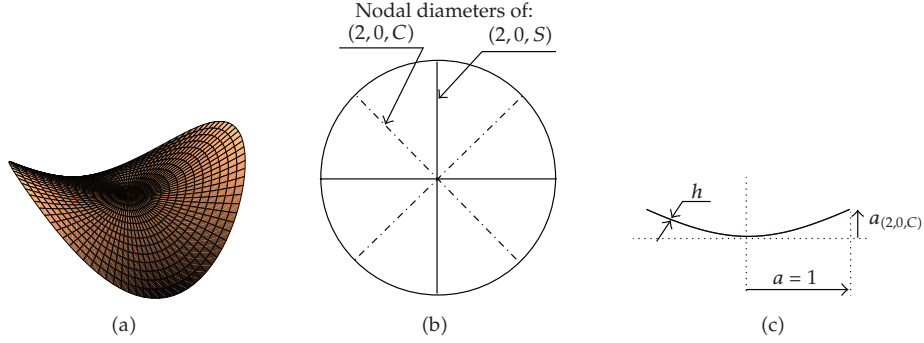


Figure 7: (a) 3D view, (b) top view, and (c) cross-section along $\theta = 0$ for the plate with imperfection having the shape of mode $(2,0,C)$.

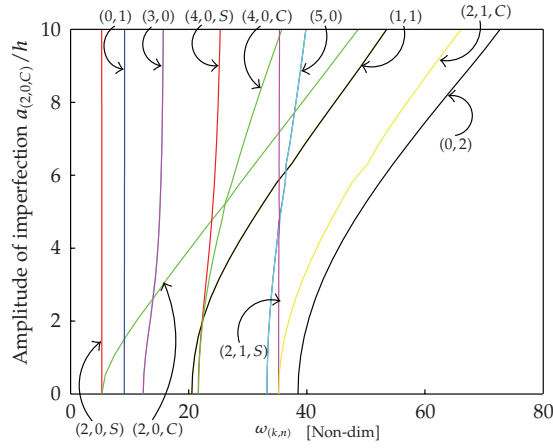


Figure 8: Nondimensional natural frequencies $\omega_{(k,n)}$ of the imperfect plate versus the amplitude of the imperfection having the shape of mode $(2,0,C)$.

resonance, with $(0,4)$ and $(0,5)$, occur around $8h$. However, the interval on which the type of nonlinearity changes its sign is so narrow that it can be neglected. The behaviour is thus mainly of the hardening type for $(0,2)$.

4. Effect of damping

In this section, the effect of viscous damping on the type of nonlinearity is addressed. The particular case of the shallow spherical shell is selected to establish the results. The equations of motion are first briefly recalled. Then specific cases of damping are considered, hence complementing the results of [22], that were limited to the undamped shell.

4.1. The shallow spherical shell equations

The local equations of motions for the shallow spherical shell can be obtained directly, see [44] for a thorough presentation. They can also be obtained from (2.4a) and (2.4b), by selecting an

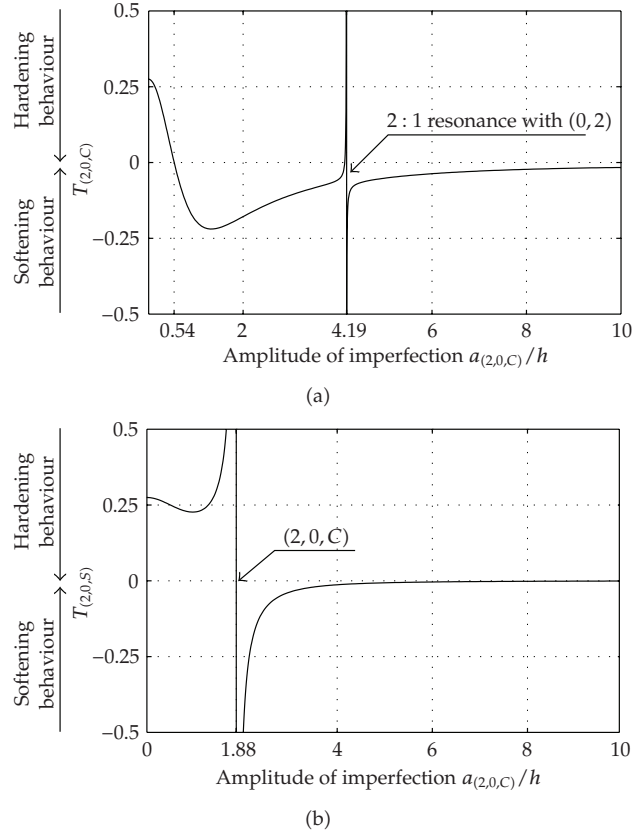


Figure 9: Type of nonlinearity for (a): mode (2,0,C) and (b): (2,0,S); for an imperfection having the shape of mode (2,0,C).

imperfection having a spherical shape, as shown in Figure 1(c), see [42]. With R , the radius of curvature of the spherical shell ($R \gg a$ to fulfill the shallow assumption), the local equations write [44]

$$\Delta \Delta w + \varepsilon_q \Delta F + \ddot{w} = \varepsilon [L(w, F) - c\dot{w} + p(r, \theta, t)], \quad (4.1a)$$

$$\Delta \Delta F - \sqrt{\kappa} \Delta w = -\frac{1}{2} L(w, w), \quad (4.1b)$$

where the aspect ratio κ of the shell has been introduced:

$$\kappa = \frac{a^4}{R^2 h^2}, \quad (4.2)$$

and $\varepsilon_q = 12(1 - \nu^2)\sqrt{\kappa}$. The boundary conditions for the case of the spherical shell with free edge write exactly as in the case of the imperfect circular plates so that (2.5a), (2.5b) and (2.5c) are still fulfilled [42, 44]. A peculiarity of the spherical shell is that all the involved quantities, linear (eigenfrequencies and mode shapes), and nonlinear (coupling coefficients and type of nonlinearity) only depends on κ , which is the only free-geometric parameter. Hence all the results will be presented as functions of κ .

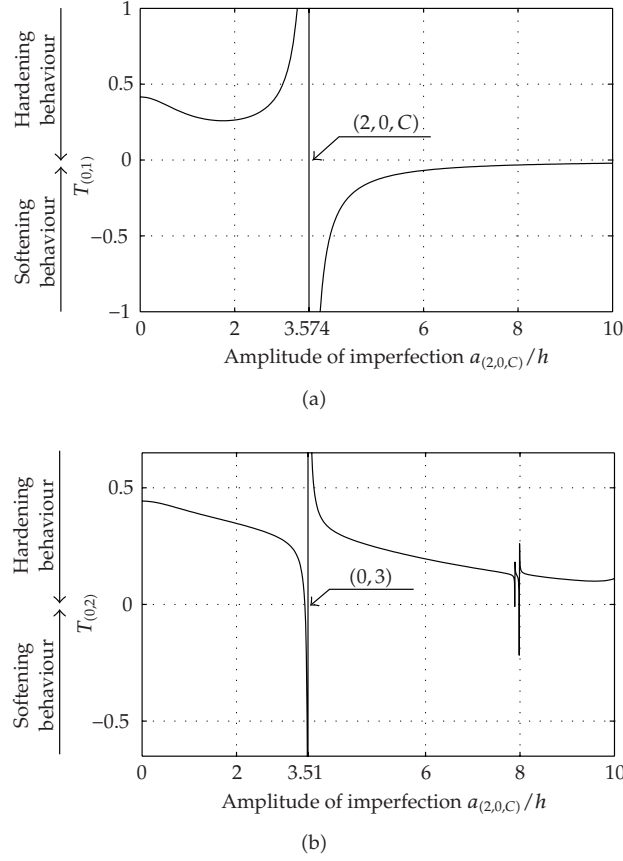


Figure 10: Type of nonlinearity for (a): mode (0,1) and (b): (0,2); for an imperfection having the shape of mode (2,0,C).

A Galerkin expansion is used for discretizing the PDEs of motion. As the eigenmodes $\Phi_p(r, \theta)$ are known analytically [44], they are used for expanding the unknown transverse displacement:

$$w(r, \theta, t) = \sum_{p=1}^{+\infty} X_p(t) \Phi_p(r, \theta). \quad (4.3)$$

The modal displacements X_p are the unknowns, and their dynamics are governed by, $\forall p \geq 1$

$$\ddot{X}_p + 2\xi_p \omega_p \dot{X}_p + \omega_p^2 X_p + \varepsilon_q \sum_{i,j=1}^{+\infty} \tilde{g}_{ij}^p X_i X_j + \varepsilon \sum_{i,j,k=1}^{+\infty} \tilde{h}_{ijk}^p X_i X_j X_k = 0. \quad (4.4)$$

The analytical expressions for the quadratic and cubic coupling coefficients $(\tilde{g}_{ij}^p, \tilde{h}_{ijk}^p)$ involve integrals of products of eigenmodes on the surface, they can be found in [22, 44]. As in Section 3, a modal viscous damping term of the form $2\xi_p \omega_p \dot{X}_p$ is considered, whereas external forces have been cancelled as only free responses are studied.

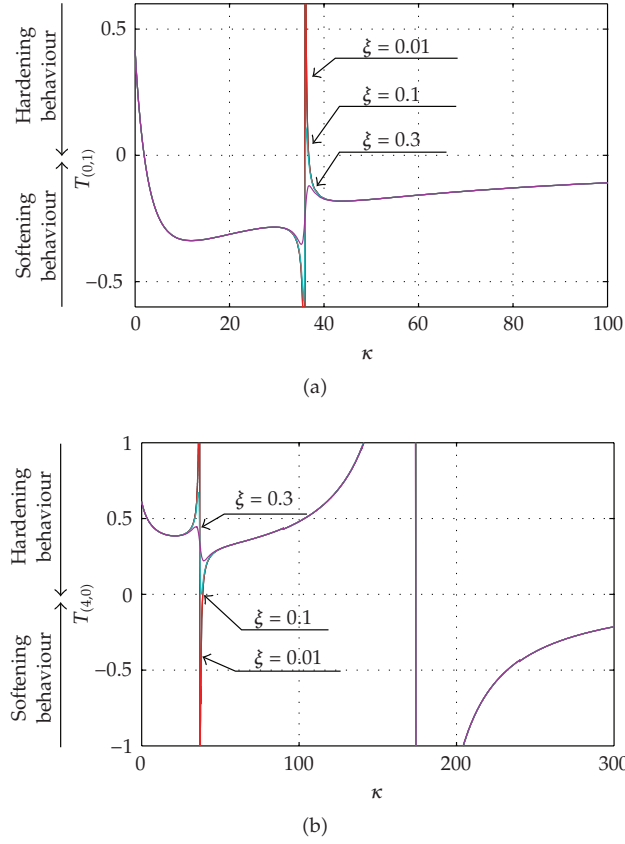


Figure 11: Type of nonlinearity for (a): mode (0,1) and (b): (4,0) versus the aspect ratio κ of a shallow spherical shell. Increasing values of damping for Case 1 ($\forall p = 1 \cdots N$, $\xi_p = \xi/\omega_p$) are shown, with $\xi = 0$ and 0.01 (red), 0.1 (cyan) and 0.3 (violet).

The type of nonlinearity can be inferred from (4.4) by using the NNM method. The results for an undamped shell have already been computed and are presented in [22]. However, an extension of the NNM-method, taking into account the damping term, has been proposed in [39]. Amongst other things, it has been shown on a simple two dofs system of coupled oscillators, that the type of nonlinearity depends on the damping. The aim of this section is thus to complement the results presented in [22] for documenting the dependence of a shell on viscous damping and for assessing its effect.

4.2. Numerical results

Three cases are selected in order to derive results for a variety of damping behaviours:

Case 1. For all $p = 1 \cdots N$, $\xi_p = \xi/\omega_p$;

Case 2. For all $p = 1 \cdots N$, $\xi_p = \xi$;

Case 3. For all $p = 1 \cdots N$, $\xi_p = \xi\omega_p$;

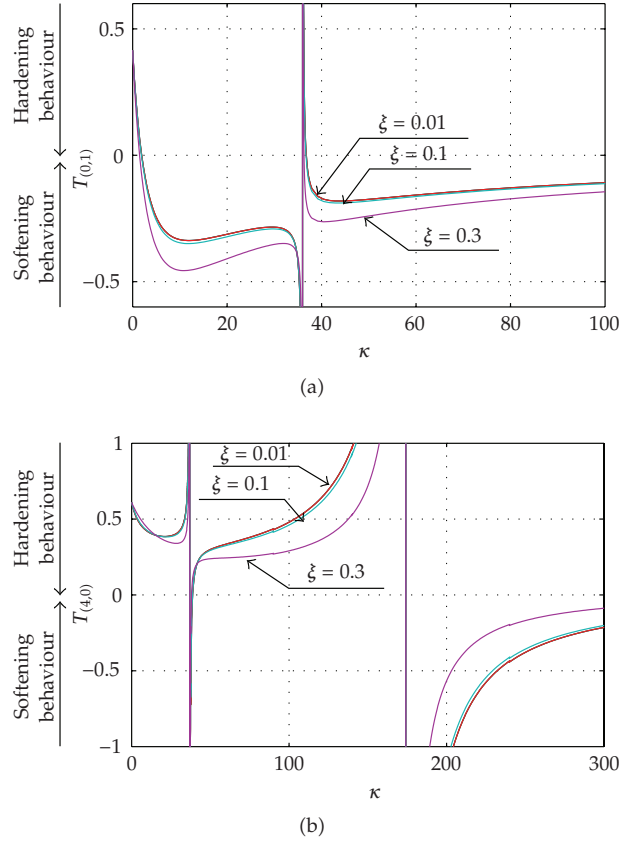


Figure 12: Type of nonlinearity for (a): mode (0,1) and (b): (4,0) versus the aspect ratio κ . Increasing values of damping for Case 2 ($\forall p = 1 \dots N$, $\xi_p = \xi$) are shown, with $\xi = 0$ and 0.01 (red), 0.1 (cyan), and 0.3 (violet).

In the above cases, ξ is a constant value, ranging from 0 to 0.3. Case 1 corresponds to a decay factor ($2\xi_p\omega_p = 2\xi$) that is independent from the frequency, that is, with a constant 2ξ value for any mode. With a small value of ξ , it may model the low-frequency (i.e., below the critical frequency) behaviour of thin metallic structures such as aluminium plates [45, 46]. Case 2 describes a decay factor that is linear with the frequency, and may model, for instance, damped structures as glass plates in the low-frequency range [45]. Finally, Case 3 accounts for a strongly damped structure, with a center manifold limited to a few modes.

The effect of increasing damping is shown for modes (0,1) and (4,0), for Case 1 in Figure 11, Case 2 in Figure 12, and Case 3 in Figure 13. Mode (0,1) undergoes a rapid change of behaviour: the transition from hardening to softening type nonlinearity occurs at $\kappa = 1.93$. Then 2:1 internal resonance with mode (0,2) occurs at $\kappa = 36$, but the behaviour remains of the softening type. Mode (4,0) displays a hardening behaviour until the 2:1 resonance with mode (0,1) at $\kappa = 174.1$. The first resonance with (0,2) at $\kappa = 36.9$ does not change the behaviour on a large interval. Adding the damping of Case 1 shows that the discontinuity occurring at 2:1 internal resonance is smoothened. However, it happens for a quite large amount of damping in the structure. Damping values of 0, 1e-4, 1e-3, and 1e-2 have been tested and

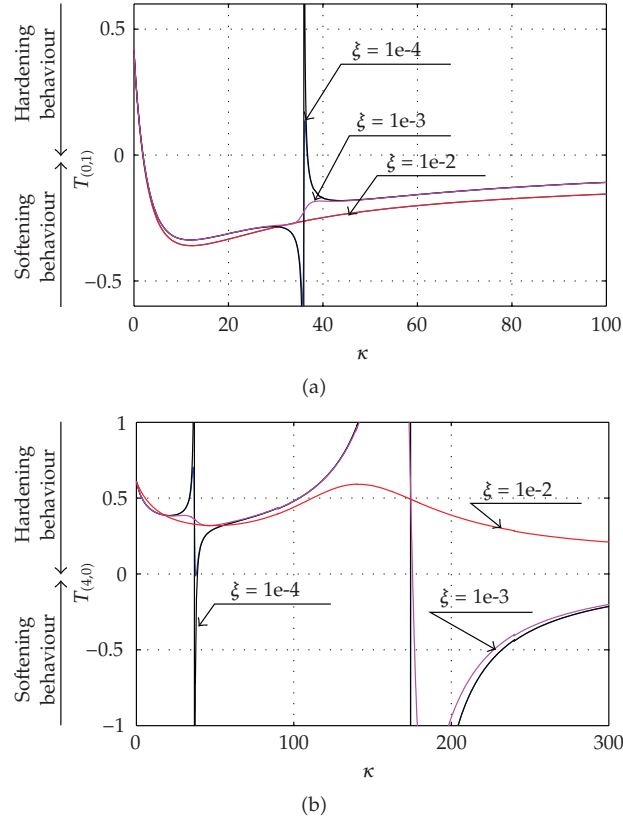


Figure 13: Type of nonlinearity for (a): mode (0,1) and (b): (4,0) versus the aspect ratio κ . Increasing values of damping for Case 3 ($\forall p = 1 \cdots N$, $\xi_p = \xi \omega_p$) are shown, with $\xi = 0$ and $1e-4$ (black), $1e-3$ (magenta), and $1e-2$ (red).

give exactly the same behaviour so that only one curve is visible in Figure 11. Large values of the damping term ξ , namely, 0.1 and 0.3 (which correspond to strongly damped structures) must be selected to see the discontinuity smoothened. Moreover, outside the narrow intervals where 2:1 resonance occurs, the effect of damping is not visible. As a conclusion for Case 1, it appears that this kind of damping has a really marginal effect on the type of nonlinearity, so that undamped results can be estimated as reliable for lightly damped structures with modal damping factor below 0.1.

Case 2 corresponds to a more damped structure than Case 1. However, it is observed in Figure 12 that the discontinuity is not smoothened at the 2:1 internal resonance. Inspecting back the analytical results shows that this is a natural consequence of the expression of the coefficients of the nonlinear change of coordinates for asymptotic NNMs. When the specific Case of constant damping factors is selected, small denominators remain present. On the other hand, outside the regions of 2:1 resonance, the effect of damping is pronounced and enhances the softening behaviour. But once again, very large values of damping factors such as 0.3 must be reached to see a prominent influence.

Finally, Case 3 depicts the case of a rapidly increasing decay factor with respect to the frequency. As the overall damping in the structure is thus larger, smaller values of ξ have been

selected, namely, $1e-4$, $1e-3$, and $1e-2$. $\xi = 1e-4$ gives quite coincident results with $\xi = 0$. But from $\xi = 1e-3$, the effect of the damping is very important: the discontinuities are smoothened, except the larger one occurring for mode (4,0) with mode (0,1). For $\xi = 1e-2$, 2:1 resonance are not visible anymore. A particular result with this value is for mode (4,0): the smoothening effect is so important that the nonlinearity remains of the hardening type. Finally, the fact that the damping generally favours the softening behaviour cannot be declared as a general rule, as one counterexample has been exhibited here. From these results, it can be inferred that the damping has little incidence on the type of nonlinearity for thin structures, until very large values are attained. It is observed that the damping generally favours the softening behaviour, but this rule is not true in general. In particular when the transition from hardening to softening type nonlinearity is due to a 2:1 internal resonance and is not the direct effect of the change of geometry, a large value of damping may favours hardening behaviour, as observed here for mode (4,0) in Case 3.

5. Conclusion

The effect of geometric imperfections on the hardening/softening behaviour of circular plates with a free edge has been studied. Thanks to the NNMs, quantitative results for the transition from hardening to softening behaviour has been documented, for a number of modes and for two typical imperfections. Two general rules have been observed from the numerical results: for modes which eigenfrequency strongly depends on the imperfection, the type of nonlinearity changes rapidly, and softening behaviour occurs for a very small imperfection with an amplitude being a fraction of the plate thickness. On the other hand, some eigenfrequencies show a slight dependence with the considered imperfection. For these, 2:1 internal resonances are the main factor for changing the type of nonlinearity. In a second part of the paper, the effect of viscous damping on the type of nonlinearity of shallow spherical shells has been studied. It has been shown quantitatively that this effect is slight for usual damping values encountered in thin structures.

References

- [1] S. A. Tobias, "Free undamped nonlinear vibrations of imperfect circular disks," *Proceedings of the Institution of Mechanical Engineers*, vol. 171, pp. 691–715, 1957.
- [2] N. Yamaki, "Influence of large amplitudes on flexural vibrations of elastic plates," *Zeitschrift für Angewandte Mathematik und Mechanik*, vol. 41, no. 12, pp. 501–510, 1961.
- [3] K. A. V. Pandalai and M. Sathymoorthy, "On the modal equations of large amplitude flexural vibration of beams, plates, rings and shells," *International Journal of Non-Linear Mechanics*, vol. 8, no. 3, pp. 213–218, 1973.
- [4] S. Sridhar, D. T. Mook, and A. H. Nayfeh, "Nonlinear resonances in the forced responses of plates—I: symmetric responses of circular plates," *Journal of Sound and Vibration*, vol. 41, no. 3, pp. 359–373, 1975.
- [5] C. Touzé, O. Thomas, and A. Chaigne, "Asymmetric nonlinear forced vibrations of free-edge circular plates—I: theory," *Journal of Sound and Vibration*, vol. 258, no. 4, pp. 649–676, 2002.
- [6] O. Thomas, C. Touzé, and A. Chaigne, "Asymmetric nonlinear forced vibrations of free-edge circular plates—II: experiments," *Journal of Sound and Vibration*, vol. 265, no. 5, pp. 1075–1101, 2003.
- [7] P. L. Grossman, B. Koplik, and Y.-Y. Yu, "Nonlinear vibrations of shallow spherical shells," *Journal of Applied Mechanics*, vol. 36, no. 3, pp. 451–458, 1969.
- [8] D. Hui, "Large-amplitude vibrations of geometrically imperfect shallow spherical shells with structural damping," *AIAA Journal*, vol. 21, no. 12, pp. 1736–1741, 1983.
- [9] K. Yasuda and G. Kushida, "Nonlinear forced oscillations of a shallow spherical shell," *Bulletin of the Japan Society of Mechanical Engineers*, vol. 27, no. 232, pp. 2233–2240, 1984.

- [10] D. Hui, "Large-amplitude axisymmetric vibrations of geometrically imperfect circular plates," *Journal of Sound and Vibration*, vol. 91, no. 2, pp. 239–246, 1983.
- [11] A. H. Nayfeh, J. F. Nayfeh, and D. T. Mook, "On methods for continuous systems with quadratic and cubic nonlinearities," *Nonlinear Dynamics*, vol. 3, no. 2, pp. 145–162, 1992.
- [12] C. Touzé, O. Thomas, and A. Chaigne, "Hardening/softening behaviour in nonlinear oscillations of structural systems using nonlinear normal modes," *Journal of Sound and Vibration*, vol. 273, no. 1–2, pp. 77–101, 2004.
- [13] M. Amabili, F. Pellicano, and M. P. Païdoussis, "Nonlinear vibrations of simply supported, circular cylindrical shells, coupled to quiescent fluid," *Journal of Fluids and Structures*, vol. 12, no. 7, pp. 883–918, 1998.
- [14] E. H. Dowell, "Comments on the nonlinear vibrations of cylindrical shells," *Journal of Fluids and Structures*, vol. 12, no. 8, pp. 1087–1089, 1998.
- [15] M. Amabili, F. Pellicano, and M. P. Païdoussi, "Further comments on nonlinear vibrations of shells," *Journal of Fluids and Structures*, vol. 13, no. 1, pp. 159–160, 1999.
- [16] D. A. Evensen, "Nonlinear vibrations of cylindrical shells—logical rationale," *Journal of Fluids and Structures*, vol. 13, no. 1, pp. 161–164, 1999.
- [17] M. Amabili and M. P. Païdoussis, "Review of studies on geometrically nonlinear vibrations and dynamics of circular cylindrical shells and panels, with and without fluid-structure interaction," *Applied Mechanics Reviews*, vol. 56, no. 4, pp. 349–356, 2003.
- [18] M. Amabili, *Nonlinear Vibrations and Stability of Shells and Plates*, Cambridge University Press, New York, NY, USA, 2008.
- [19] G. Rega, W. Lacarbonara, and A. H. Nayfeh, "Reduction methods for nonlinear vibrations of spatially continuous systems with initial curvature," in *IUTAM Symposium on Recent Developments in Nonlinear Oscillations of Mechanical Systems (Hanoi, 1999)*, vol. 77 of *Solid Mech. Appl.*, pp. 235–246, Kluwer Academic Publishers, Dordrecht, The Netherlands, 2000.
- [20] F. Pellicano, M. Amabili, and M. P. Païdoussis, "Effect of the geometry on the nonlinear vibration of circular cylindrical shells," *International Journal of Non-Linear Mechanics*, vol. 37, no. 7, pp. 1181–1198, 2002.
- [21] H. N. Arafat and A. H. Nayfeh, "Nonlinear responses of suspended cables to primary resonance excitations," *Journal of Sound and Vibration*, vol. 266, no. 2, pp. 325–354, 2003.
- [22] C. Touzé and O. Thomas, "Nonlinear behaviour of free-edge shallow spherical shells: effect of the geometry," *International Journal of Non-Linear Mechanics*, vol. 41, no. 5, pp. 678–692, 2006.
- [23] A. Rosen and J. Singer, "Effect of axisymmetric imperfections on the vibrations of cylindrical shells under axial compression," *AIAA Journal*, vol. 12, no. 7, pp. 995–997, 1974.
- [24] D. Hui and A. W. Leissa, "Effects of uni-directional geometric imperfections on vibrations of pressurized shallow spherical shells," *International Journal of Non-Linear Mechanics*, vol. 18, no. 4, pp. 279–285, 1983.
- [25] P. B. Goncalves, "Axisymmetric vibrations of imperfect shallow spherical caps under pressure loading," *Journal of Sound and Vibration*, vol. 174, no. 2, pp. 249–260, 1994.
- [26] M. Amabili, "A comparison of shell theories for large-amplitude vibrations of circular cylindrical shells: Lagrangian approach," *Journal of Sound and Vibration*, vol. 264, no. 5, pp. 1091–1125, 2003.
- [27] V. D. Kubenko and P. S. Koval'chuk, "Influence of initial geometric imperfections on the vibrations and dynamic stability of elastic shells," *International Applied Mechanics*, vol. 40, no. 8, pp. 847–877, 2004.
- [28] E. L. Jansen, "The effect of geometric imperfections on the vibrations of anisotropic cylindrical shells," *Thin-Walled Structures*, vol. 45, no. 3, pp. 274–282, 2007.
- [29] C.-Y. Chia, "Nonlinear free vibration and postbuckling of symmetrically laminated orthotropic imperfect shallow cylindrical panels with two adjacent edges simply supported and the other edges clamped," *International Journal of Solids and Structures*, vol. 23, no. 8, pp. 1123–1132, 1987.
- [30] D. Hui and A. W. Leissa, "Effects of geometric imperfections on vibrations of biaxially compressed rectangular flat plates," *Journal of Applied Mechanics*, vol. 50, no. 4, pp. 750–756, 1983.
- [31] N. Yamaki, K. Otomo, and M. Chiba, "Nonlinear vibrations of a clamped circular plate with initial deflection and initial edge displacement—I: theory," *Journal of Sound and Vibration*, vol. 79, no. 1, pp. 23–42, 1981.

- [32] N. Yamaki, K. Otomo, and M. Chiba, "Nonlinear vibrations of a clamped circular plate with initial deflection and initial edge displacement—II: experiment," *Journal of Sound and Vibration*, vol. 79, no. 1, pp. 43–59, 1981.
- [33] N. Yamaki and M. Chiba, "Nonlinear vibrations of a clamped rectangular plate with initial deflection and initial edge displacement—I: theory," *Thin-Walled Structures*, vol. 1, no. 1, pp. 3–29, 1983.
- [34] N. Yamaki, K. Otomo, and M. Chiba, "Nonlinear vibrations of a clamped rectangular plate with initial deflection and initial edge displacement—I: experiment," *Thin-Walled Structures*, vol. 1, no. 1, pp. 101–119, 1983.
- [35] M. Amabili, "Theory and experiments for large-amplitude vibrations of rectangular plates with geometric imperfections," *Journal of Sound and Vibration*, vol. 291, no. 3–5, pp. 539–565, 2006.
- [36] M. Amabili, "Theory and experiments for large-amplitude vibrations of empty and fluid-filled circular cylindrical shells with imperfections," *Journal of Sound and Vibration*, vol. 262, no. 4, pp. 921–975, 2003.
- [37] M. Amabili, "Theory and experiments for large-amplitude vibrations of circular cylindrical panels with geometric imperfections," *Journal of Sound and Vibration*, vol. 298, no. 1–2, pp. 43–72, 2006.
- [38] C. C. Lin and L. W. Chen, "Large-amplitude vibration of an initially imperfect moderately thick plate," *Journal of Sound and Vibration*, vol. 135, no. 2, pp. 213–224, 1989.
- [39] C. Touzé and M. Amabili, "Nonlinear normal modes for damped geometrically nonlinear systems: application to reduced-order modelling of harmonically forced structures," *Journal of Sound and Vibration*, vol. 298, no. 4–5, pp. 958–981, 2006.
- [40] G. J. Efstathiades, "A new approach to the large-deflection vibrations of imperfect circular disks using Galerkin's procedure," *Journal of Sound and Vibration*, vol. 16, no. 2, pp. 231–253, 1971.
- [41] G. L. Ostiguy and S. Sassi, "Effects of initial geometric imperfections on dynamic behaviour of rectangular plates," *Nonlinear Dynamics*, vol. 3, no. 3, pp. 165–181, 1992.
- [42] C. Camier, C. Touzé, and O. Thomas, "Nonlinear vibrations of imperfect free-edge circular plates," submitted to *European Journal of Mechanics: A/Solids*.
- [43] C. Camier, C. Touzé, and O. Thomas, "Effet des imperfections géométriques sur les vibrations nonlinéaires de plaques circulaires minces," in *Proceedings of 18^{ème} Congrès Français de Mécanique*, Grenoble, France, August 2007.
- [44] O. Thomas, C. Touzé, and A. Chaigne, "Nonlinear vibrations of free-edge thin spherical shells: modal interaction rules and 1:1:2 internal resonance," *International Journal of Solids and Structures*, vol. 42, no. 11–12, pp. 3339–3373, 2005.
- [45] A. Chaigne and C. Lambourg, "Time-domain simulation of damped impacted plates—I: theory and experiments," *Journal of the Acoustical Society of America*, vol. 109, no. 4, pp. 1422–1432, 2001.
- [46] M. Amabili, "Nonlinear vibrations of rectangular plates with different boundary conditions: theory and experiments," *Computers and Structures*, vol. 82, no. 31–32, pp. 2587–2605, 2004.

Research Article

The Effect of Infinitesimal Damping on the Dynamic Instability Mechanism of Conservative Systems

Dimitris S. Sophianopoulos,¹ George T. Michaltsos,² and Anthony N. Kounadis³

¹ Department of Civil Engineering, University of Thessaly, Pedion Areos, 38 334 Volos, Greece

² Laboratory of Metal Structures, Department of Civil Engineering,
National Technical University of Athens, Zografou Campus, 157 80 Athens, Greece

³ Research Center Pure and Applied Mathematics, Academy of Athens, Soranou Efessiou 4,
115 27 Athens, Greece

Correspondence should be addressed to Anthony N. Kounadis, kounadis@bioacademy.gr

Received 17 December 2007; Accepted 19 February 2008

Recommended by Jose Balthazar

The local instability of 2 degrees of freedom (DOF) weakly damped systems is thoroughly discussed using the Liénard-Chipart stability criterion. The individual and coupling effect of mass and stiffness distribution on the dynamic asymptotic stability due to mainly infinitesimal damping is examined. These systems may be as follows: (a) unloaded (free motion) and (b) subjected to a suddenly applied load of constant magnitude and direction with infinite duration (forced motion). The aforementioned parameters combined with the algebraic structure of the damping matrix (being either positive semidefinite or indefinite) may have under certain conditions a tremendous effect on the Jacobian eigenvalues and then on the local stability of these autonomous systems. It was found that such systems when unloaded may exhibit periodic motions or a divergent motion, while when subjected to the above step load may experience either a degenerate Hopf bifurcation or periodic attractors due to a generic Hopf bifurcation. Conditions for the existence of purely imaginary eigenvalues leading to global asymptotic stability are fully assessed. The validity of the theoretical findings presented herein is verified via a nonlinear dynamic analysis.

Copyright © 2008 Dimitris S. Sophianopoulos et al. This is an open access article distributed under the Creative Commons Attribution License, which permits unrestricted use, distribution, and reproduction in any medium, provided the original work is properly cited.

1. Introduction

In previous studies of the 3rd author, based on 2-DOF and 3-DOF cantilevered models [1] under partial follower loading (nonconservative systems), it was shown that in a small region of *divergence instability*, flutter (dynamic instability) may occur before divergence (static instability), if very small damping is included [2, 3]. Bolotin et al. [4] using an aeroelastic model presented a similar result. Paidoussis et al. [5] and Paidoussis [6] have shown that flutter may

occur in an inherently conservative system but for large damping. However, the effect of damping, being of paramount importance in nonconservative autonomous systems, was in general ignored when these systems are subjected to a step conservative (potential) loading. This is so because it was widely accepted that dynamic stability in nondissipative conservative systems, which are *stable*, does not change by the inclusion of damping [7].

The local dynamic stability of discrete systems under step conservative loading when small dissipative forces are included is governed by the matrix-vector differential equation [8–11]:

$$\mathbf{M}\ddot{\mathbf{q}} + \mathbf{C}\dot{\mathbf{q}} + \mathbf{V}\mathbf{q} = 0, \quad (1.1)$$

where the dot denotes a derivative with respect to time t ; $\mathbf{q}(t)$ is an n -dimensional *state* vector with coordinates $q_i(t)$ ($i = 1, \dots, n$); \mathbf{M} , \mathbf{C} and \mathbf{V} are $n \times n$ real symmetric matrices. More specifically, matrix \mathbf{M} associated with the total kinetic energy of the system is a function of the concentrated masses m_i ($i = 1, \dots, n$), being always *positive definite*; matrix \mathbf{C} the elements of which are the damping coefficients c_{ij} ($i, j = 1, \dots, n$) may be *positive definite*, positive *semidefinite* as in the case of pervasive damping [12, 13], or *indefinite* [14–16]; \mathbf{V} is a generalized *stiffness* matrix with coefficients k_{ij} ($i, j = 1, \dots, n$) whose elements V_{ij} are also linear functions of a *suddenly* applied external load λ with constant direction and infinite duration [17], that is, $V_{ij} = V_{ij}(\lambda; k_{ij})$. Apparently, due to this type of loading, the system under discussion is *autonomous*. When the external loading λ is applied *statically*, one can obtain the static (divergence) instability or buckling loads λ_j^c ($j = 1, \dots, n$) by vanishing of the determinant of the stiffness matrix $\mathbf{V}(\lambda; k_{ij})$, that is,

$$|\mathbf{V}(\lambda; k_{ij})| = 0. \quad (1.2)$$

Clearly, (1.2) yields an n th degree algebraic equation in λ . Assuming *distinct* critical states, the matrix $\mathbf{V}(\lambda; k_{ij})$ is *positive definite* for $\lambda < \lambda_1^c$, *positive semidefinite* for $\lambda = \lambda_1^c$, and *indefinite* for $\lambda > \lambda_1^c$.

Kounadis in two very recent publications [10, 11] has established the conditions under which the above autonomous dissipative systems under step (conservative) loading may exhibit dynamic bifurcational modes of instability *before* divergence (static) instability, that is, for $\lambda < \lambda_1^c$, when *infinitesimal* damping is included. These bifurcational modes may occur through either a *degenerate* Hopf bifurcation (leading to periodic motion around centers) or a *generic* Hopf bifurcation (leading to periodic attractors or to flutter). These unexpected findings (implying failure of Ziegler's kinetic criterion and other singularity phenomena) may occur for a certain combination of values of the mass (primarily) and stiffness distribution of the system in connection with a *positive semidefinite* or an *indefinite* damping matrix.

The question which now arises is whether there are combinations of values of the above-mentioned parameters (mass and stiffness distribution) which in connection with the algebraic structure of damping matrices may lead to dynamic bifurcational modes of instability when the system under discussion is *unloaded*. Such local (due to unforced motion) dynamic instability will be sought through the set of asymptotic stability criteria of Liénard-Chipart [8, 18] which are elegant and more readily employed than the well-known Routh-Hurwitz stability criteria.

As another main objective of this work, some new dynamic bifurcations related to the algebraic structure of the damping matrix when the systems are loaded by the above type of step conservative load will be also discussed, using the Liénard-Chipart criterion by analyzing

2-DOF models for which a lot of numerical results are available. Finally, the conditions of a double purely imaginary root leading to a new dynamic bifurcation, whose response is similar to that of a generic Hopf bifurcation, are properly established.

2. Basic equations

Solution of (1.1) can be sought in the form

$$\mathbf{q} = \mathbf{r}e^{\rho t}, \quad (2.1)$$

where ρ is in general a complex number and \mathbf{r} is a complex vector independent of time t .

Introducing \mathbf{q} from (2.1) into (1.1), we get

$$(\rho^2 \mathbf{M} + \rho \mathbf{C} + \mathbf{V}) \mathbf{r} = 0. \quad (2.2)$$

For given stiffness coefficients $k_{ij}(i, j = 1, \dots, n)$, the generalized stiffness matrix \mathbf{V} is a linear function of λ . Thus, if matrices \mathbf{M} , \mathbf{C} , \mathbf{V} are given, solutions of (2.2) are intimately related to the algebraic properties of the matrix-valued function $\mathbf{L}(\rho) = \rho^2 \mathbf{M} + \rho \mathbf{C} + \mathbf{V}$, and more specifically to the Jacobian eigenvalues $[\rho = \rho(\lambda)]$ obtained through the vanishing of the determinant:

$$|\rho^2 \mathbf{M} + \rho \mathbf{C} + \mathbf{V}| = 0, \quad (2.3)$$

whose expansion gives the characteristic (secular) equation for an N-DOF system:

$$\rho^{2n} + \alpha_1 \rho^{2n-1} + \dots + \alpha_{2n-1} \rho + \alpha_{2n} = 0, \quad (2.4)$$

where the real coefficients $\alpha_i(i = 1, \dots, 2n)$ are determined by means of Bôcher formula [19]. The eigenvalues (roots) of (2.4) $\rho_j(j = 1, \dots, 2n)$ are, in general, *complex conjugate* pairs $\rho_j = \nu_j \pm \mu_j i$ (where ν_j and μ_j are real numbers and $i = \sqrt{-1}$) with corresponding *complex conjugate* eigenvectors \mathbf{r}_j and $\bar{\mathbf{r}}_j(j = 1, \dots, n)$. Since $\rho_j = \rho_j(\lambda)$, clearly $\nu_j = \nu_j(\lambda)$, $\mu_j = \mu_j(\lambda)$, $\mathbf{r}_j = \mathbf{r}_j(\lambda)$, and $\bar{\mathbf{r}}_j = \bar{\mathbf{r}}_j(\lambda)$. Thus, the solutions of (1.1) are of the form

$$Ae^{\nu_j t} \cos \mu_j t, \quad Be^{\nu_j t} \sin \mu_j t, \quad (2.5)$$

where A and B are *constants* which are determined from the *initial* conditions. Solutions in (2.5) are *bounded*, tending to zero as $t \rightarrow \infty$, if all eigenvalues of (2.4) have *negative* real parts, that is, when $\nu_j < 0$ for all j . In this case, the algebraic polynomial (2.4) is called a *Hurwitz polynomial* (since all its roots have negative real parts) and the *origin* ($\mathbf{q} = \dot{\mathbf{q}} = 0$) of the system is *asymptotically stable*.

2.1. Criteria for asymptotic stability

The *necessary and sufficient* conditions which assure that all roots of (2.4) have negative real parts (i.e., $\nu_j < 0$ for all j) which means that the corresponding polynomial $|L(\rho)|$ is a Hurwitz polynomial are of great practical importance.

Consider the more general case of a polynomial in z with real coefficients $\alpha_i (i = 1, \dots, n)$:

$$f(z) = \alpha_0 z^n + \alpha_1 z^{n-1} + \dots + \alpha_{n-1} z + \alpha_n = 0 \quad (\alpha_0 > 0) \quad (2.6)$$

for which we will seek the *necessary and sufficient* conditions so that all its roots have *negative* real parts.

Denoting by $z_\kappa (\kappa = 1, \dots, m)$ the real roots and by $r_j \pm is_j (j = 1, \dots, (n-m)/2; i = \sqrt{-1})$ the complex roots of (2.6), we may assure that all these roots in the complex plane lie to the *left* of the imaginary axis, that is,

$$z_\kappa < 0, \quad r_j < 0 \quad \left(\kappa = 1, \dots, m; j = 1, \dots, \frac{n-m}{2} \right). \quad (2.7)$$

Then one can write

$$f(z) = \alpha_0 \prod_{\kappa=1}^m (z - z_\kappa) \prod_{j=1}^{n-m} (z^2 - 2r_j z + r_j^2 + s_j^2). \quad (2.8)$$

Since due to inequality (2.7), each term in the last part of (2.8) has *positive* coefficients, it is deduced that *all* coefficients of (2.6) are also *positive*. However, this (i.e., $\alpha_i > 0$ for all i with $\alpha_0 > 0$) is a *necessary* but by no means *sufficient* condition for all roots of (2.6) to lie in the left half-plane (i.e., $\text{Re}(z) < 0$).

According to *Routh-Hurwitz* criterion [18] of asymptotic stability for all roots of (2.6) to have *negative* real parts, the *necessary and sufficient* conditions are

$$\Delta_1 > 0, \Delta_2 > 0, \dots, \Delta_n > 0 \quad (2.9)$$

where

$$\Delta_1 = \alpha_1, \Delta_2 = \begin{vmatrix} \alpha_1 & \alpha_3 \\ \alpha_0 & \alpha_2 \end{vmatrix}, \Delta_3 = \begin{vmatrix} \alpha_1 & \alpha_3 & 0 \\ \alpha_0 & \alpha_2 & \alpha_4 \\ 0 & \alpha_1 & \alpha_3 \end{vmatrix}, \dots, \Delta_n = \begin{vmatrix} \alpha_1 & \alpha_3 & \alpha_5 & \dots & \dots & \dots & \dots \\ \alpha_0 & \alpha_2 & \alpha_4 & \dots & \dots & \dots & \dots \\ 0 & \alpha_1 & \alpha_3 & \dots & \dots & \dots & \dots \\ 0 & \alpha_0 & \alpha_2 & \alpha_4 & \dots & \dots & \dots \\ \dots & \dots & \dots & \dots & \dots & \dots & \dots \\ \dots & \dots & \dots & \dots & \dots & \dots & \dots \\ \dots & \dots & \dots & \dots & \dots & \dots & \alpha_i \end{vmatrix} \quad (2.10)$$

(with $\alpha_\kappa = 0$ for $\kappa > n$). Note the last equality $\Delta_n = \alpha_n \Delta_{n-1}$.

It should be noted that when the above necessary conditions $\alpha_i > 0$ (for all i) hold, inequalities (2.9) are *not* independent. For instance, for $n = 4$, the Routh-Hurwitz conditions reduce to the single inequality $\Delta_3 > 0$; for $n = 5$, they reduce to $\Delta_2 > 0$ and $\Delta_4 > 0$; while for $n = 6$, they reduce also to two inequalities, $\Delta_3 > 0$, $\Delta_5 > 0$. This case was discussed by Liénard and Chipart who established the following elegant criterion for asymptotic stability [8].

The Liénard-Chipart stability criterion

For a polynomial with real coefficients $f(z) = \alpha_0 z^n + \alpha_1 z^{n-1} + \dots + \alpha_{n-1} z + \alpha_n = 0$ ($\alpha_0 > 0$) to have all roots with *negative* real parts, it is *necessary and sufficient* that

(1) all coefficients of $f(z)$ be positive, that is,

$$\alpha_i > 0 \quad (i = 1, \dots, n); \quad (2.11a)$$

(2) the determinant inequalities be also positive, that is,

$$\Delta_{n-1} > 0, \Delta_{n-3} > 0, \dots, \quad (2.11b)$$

where Δ_κ denotes as before the Hurwitz determinant of κ th order.

It can be shown that if the Hurwitz determinants of *odd* order are *positive*, then those of *even* order are also *positive*, and vice versa. This holds even when *only part* of the coefficients α_i of $f(z)$ (with $\alpha_0 > 0$) are positive. According to this, the Liénard-Chipart criterion is defined as follows.

Necessary and sufficient conditions for all roots of the real polynomial $f(z) = \alpha_0 z^n + \alpha_1 z^{n-1} + \dots + \alpha_{n-1} z + \alpha_n = 0$, ($\alpha_0 > 0$) to have *negative real parts* can be given in any one of the following forms [18]:

(1)

$$\alpha_n > 0, \alpha_{n-2} > 0, \dots; \text{ with } \begin{cases} \text{either } \Delta_1 > 0, & \Delta_3 > 0, \dots, \\ \text{or } \Delta_2 > 0, & \Delta_4 > 0, \dots, \end{cases} \quad (2.12a)$$

(2)

$$\alpha_n > 0, \alpha_{n-1} > 0, \alpha_{n-3} > 0, \dots; \text{ with } \begin{cases} \text{either } \Delta_1 > 0, & \Delta_3 > 0, \dots, \\ \text{or } \Delta_2 > 0, & \Delta_4 > 0, \dots, \end{cases} \quad (2.12b)$$

This stability criterion was rediscovered by Fuller [20].

For instance, for a 2-DOF cantilevered model, the characteristic (secular) (2.4) is

$$\rho^4 + \alpha_1 \rho^3 + \alpha_2 \rho^2 + \alpha_3 \rho + \alpha_4 = 0 \quad (\alpha_0 = 1). \quad (2.13)$$

According to the last criterion, all roots of (2.13) have negative real parts provided that $\alpha_4 > 0$, $\alpha_2 > 0$, $\Delta_1 = \alpha_1 > 0$ and $\Delta_3 = \alpha_3(\alpha_1 \alpha_2 - \alpha_3) - \alpha_1^2 \alpha_4 > 0$. Clearly, from the last inequality, it follows that $\alpha_3 > 0$. Hence, the positivity of α_1 and α_3 was assured via the above conditions (i.e., $\alpha_4 > 0$, $\alpha_2 > 0$, $\Delta_1 > 0$, $\Delta_3 > 0$).

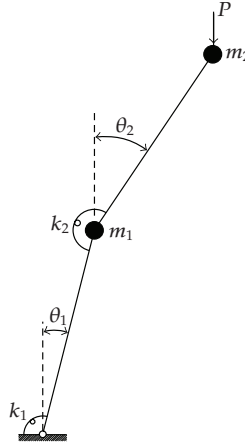


Figure 1: 2-DOF autonomous system under conservative loading.

3. Mathematical analysis

Subsequently, using the spring cantilevered dynamical model of 2-DOF shown in Figure 1, we will examine in detail the *effect of violation* of one or more of the conditions of Liénard-Chipart criterion on its asymptotic stability. The response of this dynamic model carrying two concentrated masses is studied when it is either *unloaded* or *loaded* by a suddenly applied load of constant magnitude and direction with infinite duration. Such autonomous dissipative systems with infinitesimal damping (including the case of zero loading) are properly discussed. If at least one root of the secular equation (2.13) has a positive real part, the corresponding solution (2.5) will contain an exponentially increasing function and the system will become unstable.

The seeking of an *imaginary root* of the secular equation (2.13) which represents a border line between dynamic stability and instability is a first but important step in our discussion. Clearly, an imaginary root gives rise to an oscillatory motion of the form $e^{i\mu t}$, ($i = \sqrt{-1}$, μ real number) around the trivial state. However, the existence of at least one *multiple imaginary root* of the κ th order of multiplicity leads to a solution containing functions of the form $e^{i\mu t}, te^{i\mu t}, \dots, t^{\kappa-1}e^{i\mu t}$ which increases with time. Hence, the *multiple imaginary root* on the imaginary axis of the complex plane denotes *local dynamic instability*. The discussion of such a situation is also another objective of this study.

The nonlinear equations of motion for the 2-DOF model of Figure 1 with rigid links of equal length ℓ are given by [11]

$$\begin{aligned} (1 + m)\ddot{\theta}_1 + \ddot{\theta}_2 \cos(\theta_1 - \theta_2) + \dot{\theta}_2^2 \sin(\theta_1 - \theta_2) + c_{11}\dot{\theta}_1 + c_{12}\dot{\theta}_2 + k\theta_1 - \theta_2 + \theta_1 - \lambda \sin \theta_1 &= 0, \\ \ddot{\theta}_2 + \ddot{\theta}_1 \cos(\theta_1 - \theta_2) - \dot{\theta}_1^2 \sin(\theta_1 - \theta_2) + c_{22}\dot{\theta}_2 + c_{12}\dot{\theta}_1 - \theta_1 + \theta_2 - \lambda \sin \theta_2 &= 0, \end{aligned} \quad (3.1)$$

where $m = m_1/m_2$, $k = k_1/k_2$, $\lambda = P\ell/k_2$.

Linearization of (3.1) after setting

$$\Theta = \begin{bmatrix} \theta_1 \\ \theta_2 \end{bmatrix} = e^{\rho t} \begin{bmatrix} \varphi_1 \\ \varphi_2 \end{bmatrix} = e^{\rho t} \boldsymbol{\varphi} \quad (3.2)$$

gives

$$(\rho^2 \mathbf{M} + \rho \mathbf{C} + \mathbf{V}) \boldsymbol{\varphi} = 0, \quad (3.3)$$

where

$$\mathbf{M} = \begin{bmatrix} m_{11} & m_{12} \\ m_{12} & m_{22} \end{bmatrix} = \begin{bmatrix} 1+m & 1 \\ 1 & 1 \end{bmatrix}, \quad \mathbf{C} = \begin{bmatrix} c_{11} & c_{12} \\ c_{12} & c_{22} \end{bmatrix}, \quad \mathbf{V} = \begin{bmatrix} V_{11} & V_{12} \\ V_{12} & V_{22} \end{bmatrix} = \begin{bmatrix} k+1-\lambda & -1 \\ -1 & 1-\lambda \end{bmatrix}. \quad (3.4)$$

Note that in case of a Rayleigh's dissipative function the damping coefficients are, $c_{11} = c_1 + c_2$, $c_{12} = -c_2$, $c_{21} = -c_2$, and $c_{22} = c_2$, where $c_i (i = 1, 2)$ is dimensionless coefficient for the i th rigid link. This case (for which $\det \mathbf{C} = |c| = c_1 c_2$) is a specific situation of the damping matrix \mathbf{C} which is not discussed herein.

The *static* buckling (divergence) equation is given by

$$\lambda^2 - (2+k)\lambda + k = 0, \quad (3.5)$$

whose lowest root is the *first* buckling load λ_1^c equal to

$$\lambda_1^c = 0.5(k + 2 - \sqrt{k^2 + 4}). \quad (3.6)$$

Clearly, for the entire interval of values of $k > 0$, (3.6) yields $0 \leq \lambda_1^c < 1$.

The characteristic (secular) equation is

$$\rho^4 + \alpha_1 \rho^3 + \alpha_2 \rho^2 + \alpha_3 \rho + \alpha_4 = 0, \quad (3.7)$$

where

$$\begin{aligned} \alpha_1 &= \frac{1}{m} (m_{11} c_{22} + m_{22} c_{11} - 2m_{12} c_{12}), \\ \alpha_2 &= \frac{1}{m} (m_{11} V_{22} + m_{22} V_{11} - 2V_{12} m_{12} + |c|), \\ \alpha_3 &= \frac{1}{m} (c_{11} V_{22} + c_{22} V_{11} - 2V_{12} c_{12}), \\ \alpha_4 &= \frac{1}{m} (V_{11} V_{22} - V_{12}^2). \end{aligned} \quad (3.8)$$

Let us first examine the effect of violation of Liénard-Chipart criterion on the system stability in the case of *zero loading* (i.e., $\lambda = 0$). Then expressions in (3.8) due to relations (3.4) are written as follows:

$$\begin{aligned} \alpha_1 &= \frac{1}{m} [(1+m)c_{22} + c_{11} - 2c_{12}], \\ \alpha_2 &= \frac{1}{m} [k + m + 4 + c_{11} c_{22} - c_{12}^2], \\ \alpha_3 &= \frac{1}{m} [c_{11} + c_{22}(k+1) + 2c_{12}], \\ \alpha_4 &= \frac{k}{m}. \end{aligned} \quad (3.9)$$

According to Liénard-Chipart criterion, inequalities (2.12a) imply

$$\alpha_4 > 0, \quad \alpha_2 > 0, \quad \Delta_1, \Delta_3 > 0, \quad (3.10)$$

where $\Delta_1 = \alpha_1 > 0$ and $\Delta_3 = \alpha_3(\alpha_1\alpha_2 - \alpha_3) - \alpha_1^2\alpha_4 > 0$. Clearly, from the last inequality, it follows that $\alpha_3 > 0$.

For $c_{ii} > 0$ ($i = 1, 2$), $k > 0$, and $m > 0$ (implying $\alpha_4 > 0$), it is deduced that this criterion is *violated* if either one of α_1 or α_2 is zero or Δ_3 is zero. These three cases will be discussed separately in connection with the algebraic structure of the damping matrix $\mathbf{C} = [c_{ij}]$.

Case 1 ($\alpha_1 = 0$ with $\alpha_2 > 0$). If $\alpha_1 = 0$ (yielding $\Delta_3 = -\alpha_3^2 < 0$), then

$$(1 + m)c_{22} + c_{11} - 2c_{12} = 0. \quad (3.11)$$

Equation (3.11), being independent of λ and k , is satisfied only when the damping matrix \mathbf{C} is *indefinite*, that is,

$$c_{11}c_{22} - c_{12}^2 < 0 \quad (c_{ii} > 0 \text{ for } i, j = 1, 2). \quad (3.12)$$

Indeed, the last inequality due to relation (3.11) implies

$$(1 + m)^2 c_{22}^2 + 2(m - 1)c_{11}c_{22} + c_{11}^2 > 0 \quad (3.13)$$

which is always satisfied, regardless of the value of c_{22}/c_{11} , since for $m > 0$, the discriminant of (3.13) (equal to $-16c_{11}^2 m$) is *always negative*.

Thus, we have explored the *unexpected finding* that an *unloaded* (stable) system becomes *dynamically unstable* at any small disturbance in case of an *indefinite* damping matrix even when *infinitesimal* damping is included.

Since all coefficients of (3.7) are positive from the *theory of algebraic equations* it follows that this equation *cannot* have positive root. Also the case of existence of a pair of pure imaginary roots associated with $\Delta_3 = 0$ is ruled out, since $\Delta_3 < 0$ (due to $\alpha_1 = 0$). Hence, (3.7) has either two *negative* roots combined with a pair of complex conjugate roots with *positive* real part or two pairs of *complex conjugate* roots with *opposite* real parts. Both cases imply local dynamic instability.

Case 2 ($\alpha_2 = 0$ with $\alpha_1 > 0$). If $\alpha_2 = 0$ (implying also $\Delta_3 < 0$), then

$$|c| = -k - m - 4 < 0 \quad (k, m > 0). \quad (3.14)$$

Namely, the damping matrix $[c_{ij}]$ is *indefinite* but with large negative determinant (rather unrealistic case). Since the Liénard-Chipart criterion is violated, the model is again locally dynamically unstable.

Since all coefficients of (3.7) are *positive*, from the *theory of algebraic equations*, it is deduced that this equation cannot have *positive* root. Also the case of existence of a pair of pure imaginary roots associated with $\Delta_3 = 0$ is ruled out, since $\Delta_3 < 0$ (due to $\alpha_2 = 0$). Hence, (3.7) has either *two negative* roots combined with a pair of complex conjugate roots with *positive* real part or two pairs of *complex conjugate* roots with *opposite* real parts. Both cases imply local dynamic instability.

Case 3 ($\Delta_3 = 0$). In this case, stability conditions in (3.10) are satisfied except for the last one, since $\Delta_3 = 0$ which yields [11]

$$\Delta_3 = \alpha_3(\alpha_1\alpha_2 - \alpha_3) - \alpha_1^2\alpha_4 = 0. \quad (3.15)$$

Note that $\lambda < \lambda_1^c$ implies $\alpha_4 > 0$ (i.e., $\det \mathbf{V} > 0$).

This is a necessary condition for the secular (3.7) to have one pair of *pure imaginary* roots $\pm\mu i$, ($i = \sqrt{-1}$). Indeed, this can be readily established by inserting $\rho = \pm\mu i$ into (3.7) and then equating to zero real and imaginary parts.

Consider now the more general case of *nonzero loading* (i.e., $\lambda \neq 0$). Using relations in (3.8), (3.15) can be written as follows:

$$A\lambda^2 + B\lambda + \Gamma = 0, \quad (3.16)$$

where

$$A = (c_{11} + c_{22})(m + 2)\bar{\alpha}_1 - m(c_{11} + c_{22})^2 - [(1 + m)c_{22} + c_{11} - 2c_{12}]^2, \quad (3.17a)$$

$$B = -\bar{\alpha}_1 \{ (m + 2)[c_{11} + (k + 1)c_{22} + 2c_{12}] + (c_{11} + c_{22})[k + m + 4 + |c|] \} \\ + 2m[c_{11} + (k + 1)c_{22} + 2c_{12}](c_{11} + c_{22}) + (k + 2)[(1 + m)c_{22} + c_{11} - 2c_{12}]^2, \quad (3.17b)$$

$$\Gamma = (k + m + 4 + |c|)[c_{11} + (k + 1)c_{22} + 2c_{12}]\bar{\alpha}_1 - m[c_{11} + (k + 1)c_{22} + 2c_{12}]^2 \\ - k[(1 + m)c_{22} + c_{11} - 2c_{12}]^2, \quad (3.17c)$$

where

$$c_{11} = \frac{c_{12}^2 + |c|}{c_{22}}, \quad \bar{\alpha}_1 = m\alpha_1. \quad (3.17d)$$

For real λ , the discriminant \mathbf{D} of (3.16) must be greater than or equal to zero, that is,

$$\mathbf{D} = B^2 - 4A\Gamma \geq 0. \quad (3.18)$$

Subsequently, attention is focused on the following: (a) matrix \mathbf{C} is *positive semidefinite* (i.e., $|c| = 0$ with $c_{ii} > 0$, $i = 1, 2$) and (b) matrix \mathbf{C} is *indefinite* ($|c| < 0$ with $c_{ii} > 0$, $i = 1, 2$).

Using the symbolic manipulation of *Mathematica* [21], one can find that

$$\mathbf{D} = |c|f(|c|), \quad (3.19)$$

where $f(|c|)$ is an algebraic polynomial of 5th degree in $|c|$.

Case 4 ($|c| = 0$, $f \neq 0$). For $|c| = 0$, (3.16) implying $\mathbf{D} = 0$ admits a *double root*, which due to (3.17a), (3.17b), (3.17d) is given by

$$\lambda_1^H = \frac{2c_{12}^2 + c_{12}c_{22}(k - m) - c_{22}^2(k + m + 2)}{c_{12}^2 - c_{22}^2 - c_{12}c_{22}m}. \quad (3.20)$$

Using the *Reduce* command embedded in *Mathematica*, one can find the conditions under which $0 < \lambda_1^H < \lambda_1^c$, given in the appendix, relation (A.1).

Case 5 ($f = 0, |c| \neq 0$). Moreover, it was found symbolically that the 5th degree polynomial $f(|c|)$ possesses *three real* roots (one double and one single), and two *pure imaginary* ones. Discussing their nature, one can find that the double root of $f(|c|)$, being equal to $|c| = -(c_{12} - c_{22})^2 - c_{22}^2 m < 0$, yields

$$c_{12} = \frac{1}{2} [c_{11} + (m+1)c_{22}]. \quad (3.21)$$

Then, the double root of (3.16) becomes

$$\lambda_2^H = \frac{2c_{11} + c_{22}(k+m+2)}{c_{11} + c_{22}} \quad (3.22)$$

which is always greater than λ_1^c and hence of minor importance for the present analysis.

The third real root of $f(|c|)$, if substituted in (3.16), yields again a double root in λ , always less than zero, which is rejected. Thus, only the case of a *positive semidefinite* damping matrix may lead to an acceptable value of the corresponding load (i.e., $0 < \lambda_H < \lambda_1^c$) associated with a *degenerate* Hopf bifurcation, as theoretically was shown by Kounadis [10, 11].

Case 6 ($\lambda = 0$). If $\lambda = 0$, (3.16) implies $\Gamma = 0$, which after symbolic manipulation of (3.17c) can be written in the following form:

$$\Gamma = \frac{1}{c_{22}^2} (|c|^3 + A_2|c|^2 + A_1|c| + A_0) = 0, \quad (3.23)$$

where A_i ($i = 0, 1, 2$) are given in the appendix, relations (A.2). It is evident that $A_2 > 0$ and $A_0 \geq 0$, a fact implying that (3.23) can be satisfied only for $|c| \leq 0$ if also $A_1 \geq 0$; otherwise (i.e., if $A_1 < 0$) the system may be locally stable or unstable. For $|c| = 0$, one can find the corresponding values of c_{ii} ($i = 1, 2$), given in (A.3) and (A.4) in the appendix, which are always positive. This special case, for which the trivial (unloaded) state is associated with a pair of *pure imaginary* eigenvalues (necessary condition for a Hopf bifurcation), implies a local dynamic instability.

Conditions for a double imaginary root

For a *double imaginary* root, the first derivative of the secular equation (3.7) must be also zero, which yields

$$4\rho^3 + 3\alpha_1\rho^2 + 2\alpha_2\rho + \alpha_3 = 0. \quad (3.24)$$

Inserting into (3.24) $\rho = \mu i$, we obtain $\mu^2 = 0.5\alpha_2 = \alpha_3/3\alpha_1$ and thus $\alpha_3 = 3\alpha_1\alpha_2/2$. Introducing this expression of α_3 into (3.15), it follows that $\alpha_1 = 0$, which also implies that $\alpha_3 = 0$ and hence (3.24) becomes $\rho^2 = -0.5\alpha_2$. If $\rho^2 = -0.5\alpha_2$ is inserted into the secular equation $\rho^4 + \alpha_2\rho^2 + \alpha_4 = 0$, for a *double imaginary* root, it follows that $\alpha_2^2 - 4\alpha_4 = 0$ which due to relations (3.8) yields

$$\begin{aligned} & (m^2 + 4)\lambda^2 - 2\lambda(m^2 + (2-k)m + 2k + 8 + (m+2)|c|) \\ & + |c|^2 + 2(k+m+4)|c| + (k+m+4)^2 - 4mk = 0. \end{aligned} \quad (3.25)$$

For real λ , the discriminant \mathbf{D} of (3.25) must satisfy the inequality

$$\mathbf{D} = |c|^2 + (4 - mk)|c| - (m + k)^2 \geq 0 \quad (3.26)$$

which yields

$$\begin{aligned} \text{either } |c| &< 0.5 \left(mk - 4 - \sqrt{m^2(k^2 + 4) + 4k^2 + 16} \right), \\ \text{or } |c| &> 0.5 \left(mk - 4 + \sqrt{m^2(k^2 + 4) + 4k^2 + 16} \right). \end{aligned} \quad (3.27)$$

Using the conditions found above

$$\alpha_1 = \alpha_3 = 0, \quad (3.28)$$

relations (3.9) yield

$$\begin{aligned} (1 + m)c_{22} + c_{11} - 2c_{12} &= 0, \\ c_{11}(1 - \lambda) + c_{22}(k + 1 - \lambda) + 2c_{12} &= 0. \end{aligned} \quad (3.29)$$

Adding the last two equations, we obtain

$$(2 - \lambda)c_{11} + (k + m + 2 - \lambda)c_{22} = 0. \quad (3.30)$$

Since $k, m > 0$, and $\lambda < \lambda_1^c < 1$, it follows that both coefficients of c_{11} and c_{22} in (3.30) are positive. Hence, c_{11} and c_{22} are of *opposite* sign (i.e., $c_{11}/c_{22} < 0$) and consequently $|c| = c_{11}c_{22} - c_{12}^2 < 0$; thus the 2nd of inequalities (3.27) is excluded.

Solving simultaneously the system of equations $\alpha_2^2 - 4\alpha_4 = 0$, $\alpha_1 = \alpha_3 = 0$ in k, m, λ , two ternaries of values for k, m , and λ are obtained, given in the appendix, expressions (A.5). For all these values to be greater than zero, the *Reduce* command embedded in Mathematica [21] yields two sets of conditions, given also in the appendix, relations (A.6). Further symbolic computations are needed for establishing the conditions for a *double pure imaginary* root for loading values less than λ_1^c . Nevertheless, suitable combinations of values of c_{ij} , k , and m may be found. This will be demonstrated in Section 4. The corresponding dynamic response, since the system is associated with a codimension-2 local bifurcation, is anticipated to be related to isolated periodic orbits which will be established via a straightforward complete nonlinear dynamic analysis.

4. Numerical results

In this section, numerical results corresponding to all the above cases of violation of the Liénard-Chipart stability criterion are given below in tabular and graphical forms.

Case 1 ($\alpha_1 = 0$). (a) $\lambda = 0$. For an unloaded system with $k = m = 1$, choosing $c_{11} = 0.015$ and $c_{22} = 0.002$, (3.11) yields $c_{12} = 0.0095$ and as expected the damping matrix is *indefinite* with determinant $|c| = -0.0006025$. The two pairs of corresponding eigenvalues are $\rho_{1,2} = -0.00332577 \pm 0.41421i$ and $\rho_{3,4} = 0.00335877 \pm 0.41421i$ ($i = \sqrt{-1}$), implying *local* dynamic instability. Solving numerically the system of nonlinear equations (3.1), we find that the

dynamic response of the system is associated with a divergent motion, as depicted in Figure 2, with the aid of the time series

$[\tau, \theta_1(\tau)]$, time velocities $[\tau, \dot{\theta}_1(\tau)]$ and phase-plane portraits $[\theta_1(\tau), \dot{\theta}_1(\tau)]$.

(b) $\lambda \neq 0$. For a system with $k = 5$, $m = 4$, and $\lambda = 0.5 < \lambda_1^c = 0.807418$ and for $c_{11} = 0.01$, $c_{22} = 0.002$, (2.13) yields $c_{12} = -0.0175$ implying $|c| = -2.5625 \times 10^{-4}$. The trivial state is locally dynamically unstable, since $\rho_{1,2} = -0.00397748 \pm 0.4351i$ and $\rho_{3,4} = 0.00397748 \pm 0.4351i$. The corresponding dynamic response is again related to a *divergent* (unbounded) motion, as shown in the phase-plane portraits of Figures 3(a) and 3(b).

Case 2 ($\alpha_2 = 0$). (a) $\lambda = 0$: If $k = m = 1$ relation (3.14) is satisfied, for example, for the damping coefficients $c_{11} = 0.50$, $c_{22} = 2.00$, yielding $c_{12} = \sqrt{7}$ and $|c| = -6$. For this, rather unrealistic, subcase, the corresponding eigenvalues are equal to $\rho_1 = -1.86617$, $\rho_2 = -0.102227$, and $\rho_{3,4} = 1.37995 \pm 1.8269i$ (local instability). Hence, the response of the system is also related to a *divergent* (unbounded) motion, presented graphically in the phase-plane curves of Figures 4(a) and 4(b).

(b) $\lambda \neq 0$. Similarly, for a system with $k = 0.10$, $m = 0.20$ (for which $\lambda_1^c = 0.0487508$) in order that $\alpha_2 = 0$, we must choose an indefinite damping matrix with $|c| = -4.25$. Setting, for example, $c_{11} = 2.375$, $c_{12} = 3.00$, $c_{22} = 2.00$, and $\lambda = 0.227273 < \lambda_1^c$, the trivial state is locally dynamically unstable with $\rho_1 = -2.46657$, $\rho_2 = -0.00503929$, and $\rho_{3,4} = 4.2983 \pm 1.6612i$. The system exhibits a *divergent* (unbounded) motion, as shown in Figures 5(a) and 5(b).

Case 3 ($\Delta_3 = 0$ with $\alpha_1 \alpha_2 \neq 0$). (a) *Positive semidefinite damping matrix* ($|c| = 0$). Choosing $c_{11} = 0.01$, $c_{22} = 0.0004$ (and thus $c_{12} = 0.002$), the 1st requirement of the 2nd set of conditions given in the appendix, relation (A.1), is satisfied (i.e., $c_{12} > c_{22}$). The 2nd requirement, that is, $m > 2(c_{12} - c_{22})/c_{22}$, yields $m > 8$, and hence one can choose $m = 10$. The 3rd requirement in (A.1) implies that $0.8333 < k < 3$ and thus one can take $k = 1$. Solving numerically (3.15) with respect to λ , we obtain the value of $\lambda_H = 0.307692256 < \lambda_1^c = 0.381966$, associated with a pair of pure imaginary eigenvalues, while the other pair has negative real parts. The evolution of both pairs of eigenvalues in the complex plane as λ varies is presented in Figure 6 for $\lambda < \lambda_1^c$. For $\lambda = \lambda_H$, a *degenerate Hopf bifurcation* occurs and the system exhibits a periodic motion, whose amplitude depends on the initial conditions. Relevant results in graphical form can be found in recent publications of the 3rd author [10, 11].

(b) *Indefinite damping matrix* ($|c| < 0$). It has been proven by Kounadis [10, 11] that in this subcase (for $\lambda < \lambda_1^c$) all the necessary and sufficient conditions for a *generic Hopf bifurcation* are fulfilled and hence the system experiences a periodic attractor response (stable limit cycles) with constant final amplitudes regardless of the initial conditions. Numerical results are given in the aforementioned papers by Kounadis.

(c) $\Delta_3 = 0$ and $\lambda = 0$. If at the same time $|c| = 0$, one can find the values of c_{ii} ($i = 1, 2$) through (A.3) and (A.4) in the appendix, which are always positive. A further investigation of this case as well as of the case $|c| < 0$ for the global stability of the system can be performed through a nonlinear dynamic analysis.

(d) *Double pure imaginary eigenvalues*. For this special case, three combinations of damping matrix coefficients c_{ij} are examined. These, along with the corresponding critical values of k , λ and m , satisfying relations (A.5) of the appendix, are given in Table 1. Note that Cases 3(d)1 and 3(d)2 are the outcome of the 1st set from relations (A.5), while Case 3(d)3 is the outcome from the 2nd set. Clearly, in all cases, $\lambda < \lambda_1^c$.

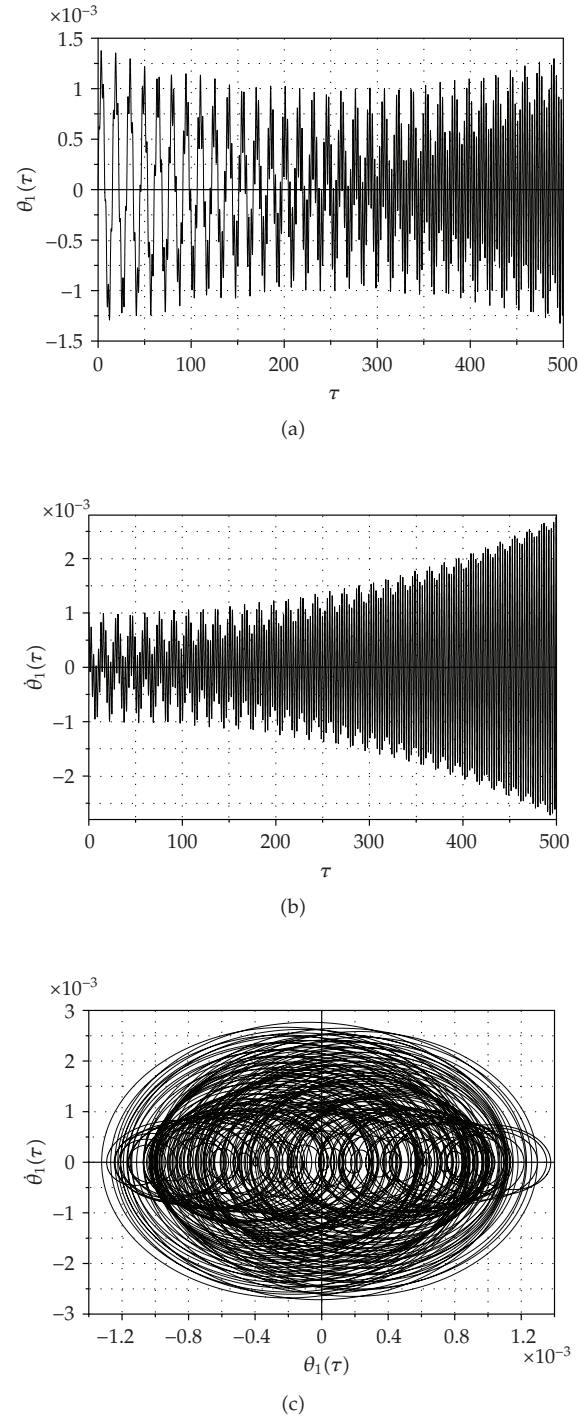


Figure 2: (a) Time series $[\tau, \theta_1(\tau)]$, (b) time velocities $[\tau, \dot{\theta}_1(\tau)]$, and (c) phase-plane portraits $[\theta_1(\tau), \dot{\theta}_1(\tau)]$, for the system of Case 1(a), exhibiting a divergent motion.

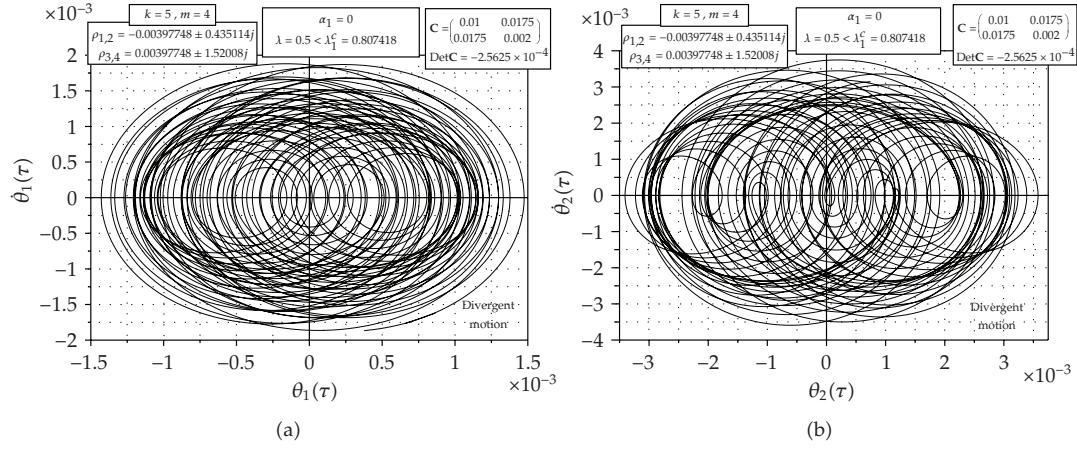


Figure 3: Phase-plane portraits $[\theta_i(\tau), \dot{\theta}_i(\tau)]$ ($i = 1, 2$) for the system of Case 1(b), associated with a divergent motion.

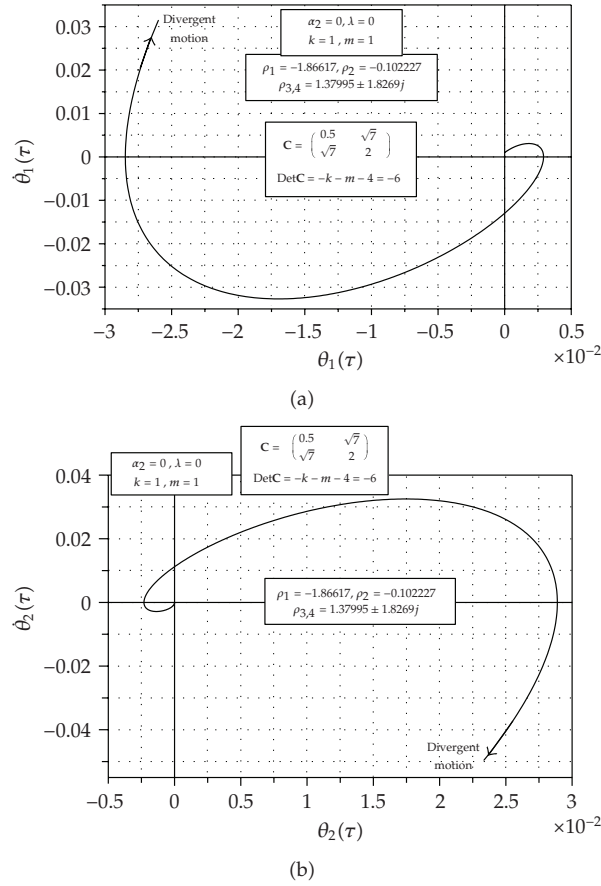


Figure 4: Phase-plane portraits $[\theta_i(\tau), \dot{\theta}_i(\tau)]$ ($i = 1, 2$) for the system of Case 2(a), associated with a divergent motion.

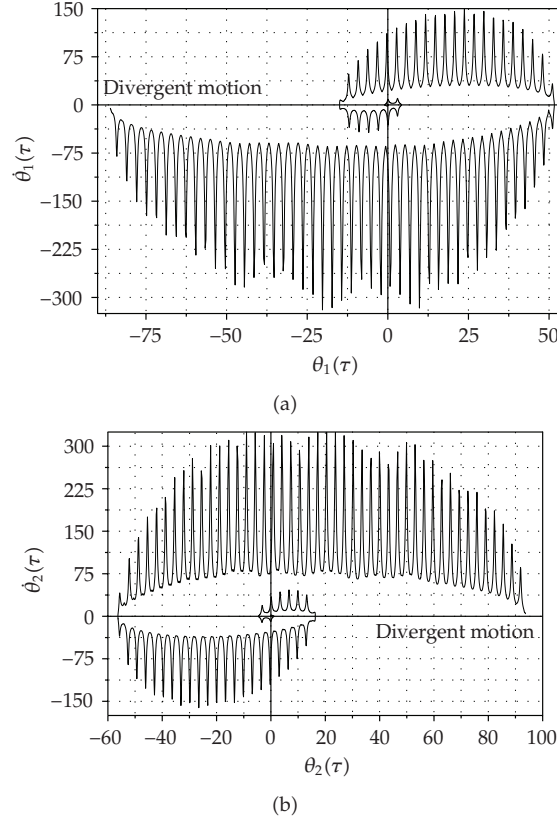
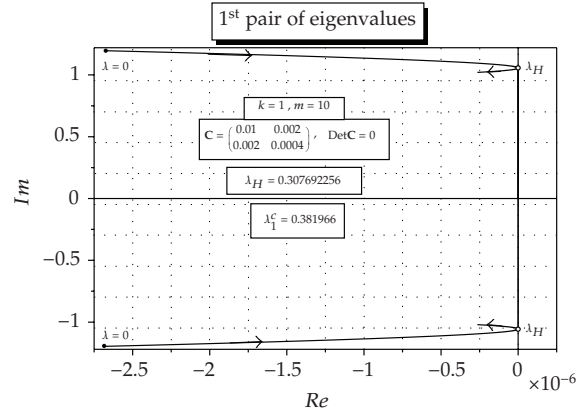


Figure 5: Phase-plane portraits $[\theta_i(\tau), \dot{\theta}_i(\tau)]$ ($i = 1, 2$) for the system of Case 2(b), associated with a divergent motion.

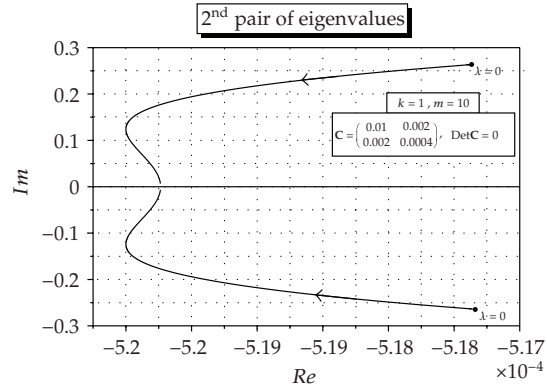
Table 1: Values of damping coefficients (c_{ij}) and critical system parameters (k, λ_{cr}, m) for three subcases with double pure imaginary eigenvalues.

Case no.	c_{11}	c_{12} $ c $	c_{22}	k	λ_{cr}	m	λ_1^c
3(d)1	3.45	1.00 -5.83	-1.40	2.65201108	0.164480292	0.035714286	0.665195
3(d)2	3.60	1.00 -5.32	-1.20	3.178585026	0.244040821	0.333333333	0.711568
3(d)3	3.40	1.00 -5.08	-1.20	2.346316274	0.629282032	0.166666666	0.631633

In the three above subcases, the evolution of both pairs of λ -dependent eigenvalues in the complex plane is depicted in Figures 7, 8, 9(a), and 9(b), from which it is evident that for all $\lambda < \lambda_1^c$, except for $\lambda < \lambda_{cr}$ (where a codimension-2 bifurcation occurs), the pairs of eigenvalues remain always in *opposite* planes of the Im axis, but symmetric with respect to the Re axis. This symmetry is always present for the pair with negative real parts, while for the other pair (with



(a)



(b)

Figure 6: Evolution of both pairs of eigenvalues in the complex plane for the system of Case 3(a), associated with a degenerate Hopf bifurcation.

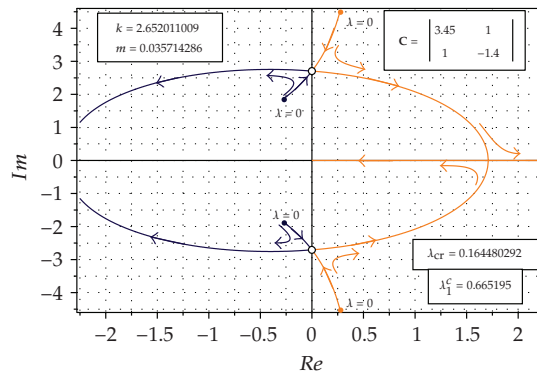


Figure 7: Evolution of both pairs of eigenvalues in the complex plane for the system of Case 3(d)1.

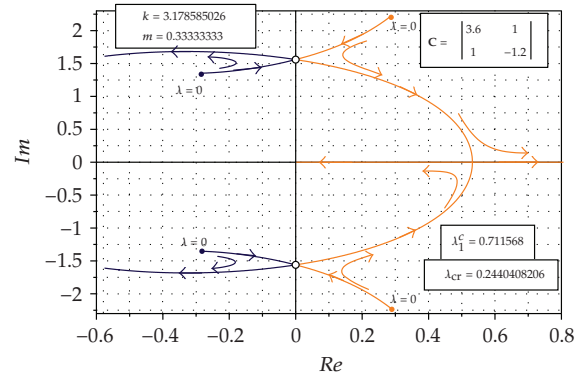
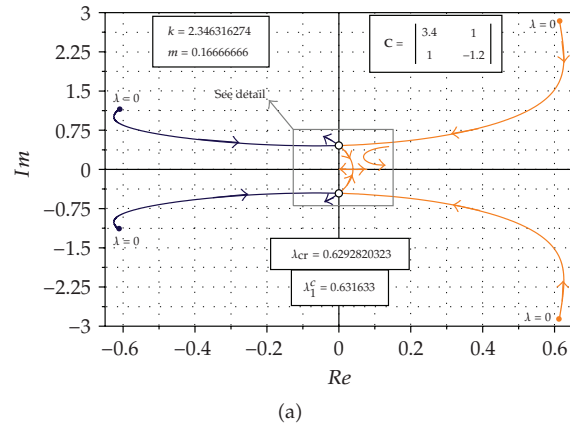
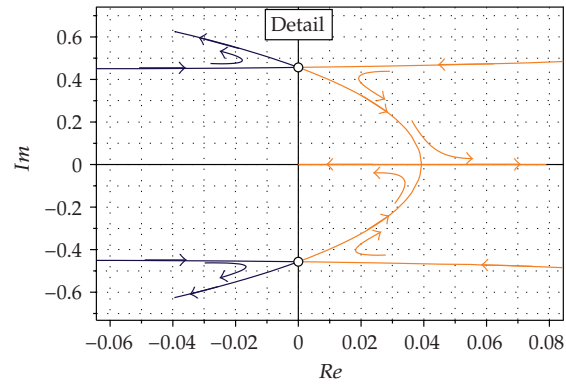


Figure 8: Evolution of both pairs of eigenvalues in the complex plane for the system of Case 3(d)2.



(a)



(b)

Figure 9: Evolution of both pairs of eigenvalues in the complex plane (a), and corresponding detail (b), for the system of Case 3(d)3.

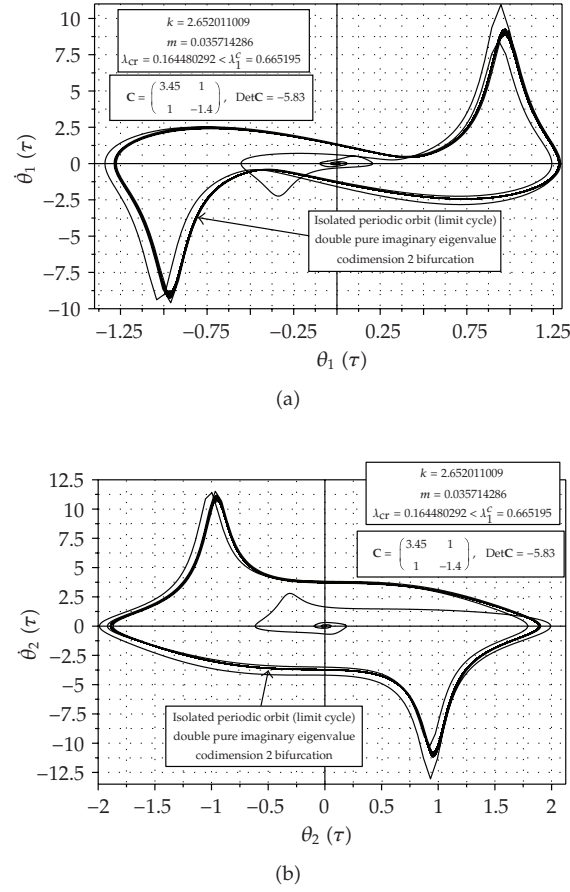


Figure 10: Phase-plane portraits $[\theta_i(\tau), \dot{\theta}_i(\tau)]$ ($i = 1, 2$) for the system of Case 3(d)1, associated with an isolated periodic orbit.

positive real parts), this feature remains until their imaginary part vanishes simultaneously at a certain value of the loading λ less than λ_1^c .

The dynamic response of the system for all these subcases is associated with isolated periodic orbits (whose final amplitude is constant and independent of the initial conditions), as shown in the phase-plane trajectories of Figures 10, 11, and 12.

The corresponding dynamic bifurcations related to the above *double pure imaginary* eigenvalues behave like a *generic* Hopf bifurcation, whose basic feature is the intersection of the λ -dependent path of one eigenvalue with the imaginary axis. On the other hand, in all the above subcases, the branches of two consecutive λ -dependent eigenvalues meet the imaginary axis at the same point with $\lambda = \lambda_{cr}$. Namely, the *transversality* condition is satisfied through two intersected lines at the same point of the imaginary axis, but whose branches in the left (negative) and right (positive) half planes belong to the 1st and 2nd pairs of eigenvalues, respectively.

Finally, Figure 13 verifies the unexpected phenomenon (Kounadis [11]) of *discontinuity* in the dynamic loading λ_H associated with either a *degenerate* or a *generic* Hopf bifurcation.

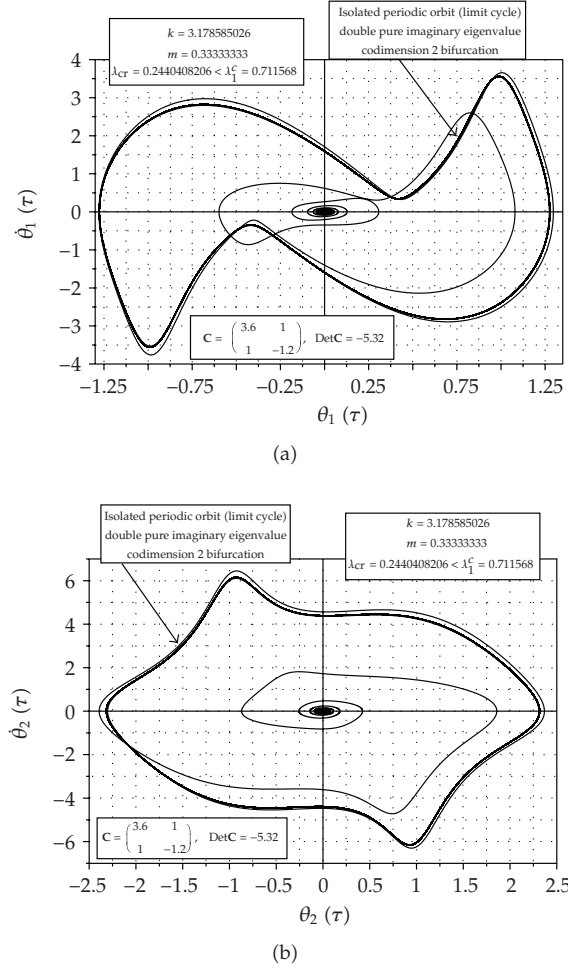


Figure 11: Phase-plane portraits $[\theta_i(\tau), \dot{\theta}_i(\tau)]$ ($i = 1, 2$) for the system of Case 4c2, associated with an isolated periodic orbit.

5. Concluding remarks

This study discusses in detail the coupling effect of (infinitesimal mainly) damping with the mass and stiffness distribution in a 2-DOF cantilevered model under step potential loading. Such an autonomous system may be associated either with a positive semidefinite or indefinite damping matrix (with positive or negative diagonal elements). Attention is focused on the violation of the Liénard-Chipart stability criterion when this system is either *unloaded* or *loaded* by a suddenly applied load of constant magnitude and direction with infinite duration (step potential loading). The most important findings of this study are the following.

(1) Usage of Liénard-Chipart, simple and readily employed, stability criterion compared to that of Routh-Hurwitz brought into light a variety of new types of dynamic bifurcations reported below.

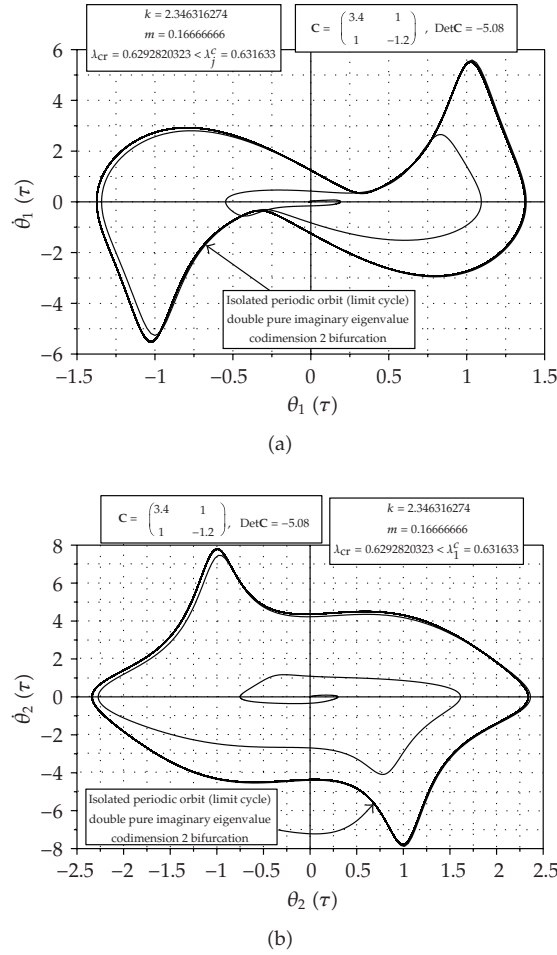


Figure 12: Phase-plane portraits $[\theta_i(\tau), \dot{\theta}_i(\tau)]$ ($i = 1, 2$) for the system of Case 3(a), associated with an isolated periodic orbit.

(2) The mass and stiffness distribution combined either with a positive semidefinite or an indefinite damping matrix may have a considerable effect on the *asymptotic stability*, prior to divergence instability, even in case of *infinitesimal* damping.

(3) The cantilevered model when *unloaded* (being statically stable), strangely enough, under certain conditions becomes dynamically unstable to any small disturbance leading to a *divergent* (unbounded) motion.

(4) The above model when *loaded* under analogous of the previous conditions exhibits also a *divergent* motion at a certain value of the external load.

It is worth noting that both the above cases of divergent motion may occur for *negligibly small* negative determinant of the damping (indefinite) matrix when $\alpha_1 = 0$, while for $\alpha_2 = 0$ (regardless of whether

$\lambda = 0$ or $\lambda \neq 0$), the determinant of the damping matrix is negative but *finite*.

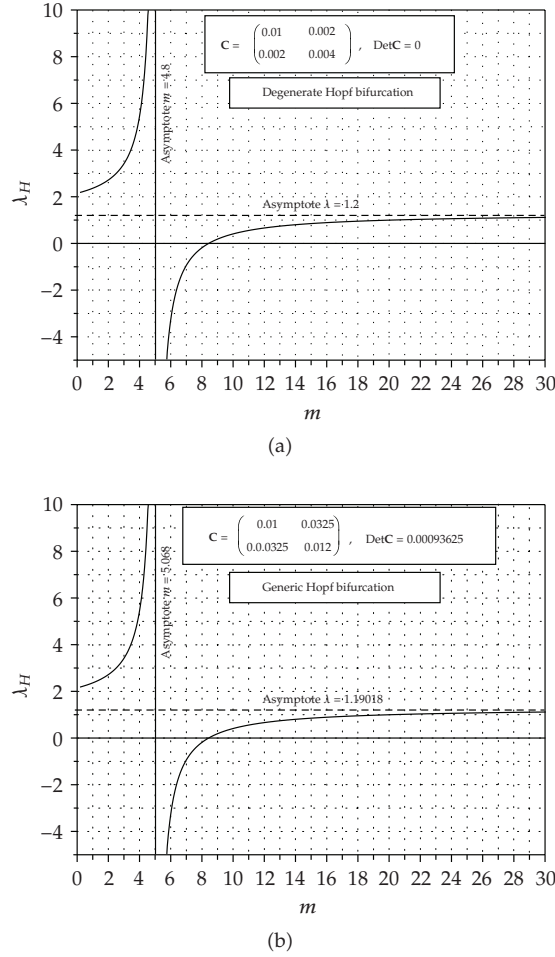


Figure 13: Plots m versus λ_H for a system with $k = 1$ exhibiting a discontinuity for the case of (a) degenerate and (b) generic Hopf bifurcation.

(5) When $\Delta_3 = 0$ and $\alpha_1\alpha_2 \neq 0$, four distinct responses may occur as follows.

- (a) If $|c| = 0$ (positive semidefinite damping matrix), the system exhibits a periodic motion associated with a *degenerate* Hopf bifurcation. Then, the final amplitude of motion depends on the initial conditions.
- (b) When the damping matrix is *indefinite* (even with infinitesimal but negative determinant, $|c| < 0$), the system may exhibit a periodic attractor response associated with a *generic* Hopf bifurcation. It is of paramount practical importance the case where such an unexpected dynamic instability occurs at a load λ_H less than the 1st buckling load.

In both the above cases, it was confirmed the recently reported unexpected finding [11] of discontinuity of the dynamic loading λ_H (associated with either a degenerate or a generic Hopf bifurcation) occurring at a certain value of the *mass* distribution.

- (c) When at the same time $\lambda = 0$, we have a *local* dynamic instability for $|c| \leq 0$, whose global stability can be established through a nonlinear dynamic analysis.
- (d) The case of a *double pure imaginary eigenvalue* may occur for an *indefinite* damping matrix with *finite* determinant and *negative ratio* of the corresponding diagonal elements. In this special case, there are *two pairs* of eigenvalues in the complex plane which touch the imaginary axis at the same point for a certain value $\lambda = \lambda_{cr}$. This situation yields local instability leading to a motion with final constant amplitude regardless of the initial conditions. Namely, such a dynamic bifurcation behaves in a way similar to that of a *generic* Hopf bifurcation. This new type of dynamic bifurcation was also verified via a nonlinear dynamic analysis.

Appendix

Results of symbolic computations

- (i) Conditions for $0 < \lambda_1^H < \lambda_1^c$ from (3.20), with $c_{ii} > 0$ ($i = 1, 2$), $k > 0$, $m > 0$ are

$$\left\{ \begin{array}{c} \left[(c_{12} < -c_{22}) \wedge \left(\frac{c_{22}^2 - c_{12}^2}{c_{12}c_{22}} < k < \frac{-2c_{12}^2 + c_{22}c_{12}m + (m+2)c_{22}^2}{c_{22}(c_{12} - c_{22})} \right) \right] \\ \vee \\ \left[(c_{12} > c_{22}) \wedge \left(m > \frac{2(c_{12} - c_{22})}{c_{22}} \right) \wedge \right. \\ \left. \left(\frac{-m^2c_{22}^2 - 2mc_{22}^2 + 2c_{12}c_{22}m}{c_{12}^2 - (m+2)c_{12}c_{22} + (m+1)c_{22}^2} < k < \frac{-2c_{12}^2 + c_{22}c_{12}m + (m+2)c_{22}^2}{c_{22}(c_{12} - c_{22})} \right) \right] \end{array} \right\}. \quad (A.1)$$

- (ii) Expressions of coefficients A_i ($i = 0, 1, 2$) of (3.23) are

$$\begin{aligned} A_2 &= (k + m + 2)c_{22}^2 + 2c_{12}^2 + 4 > 0, \\ A_1 &= \left\{ \begin{array}{l} c_{12}^4 - 2c_{12}c_{22}(c_{22}^2 - 2)(k - m) + c_{12}^2[c_{22}^2(k + m - 2) + 8] \\ + c_{22}^2[(k - m)^2 + c_{22}^2(k + 1)(m + 1) + 4(k + m + 2)] \end{array} \right\}, \\ A_0 &= [-2c_{12}^2 + c_{12}c_{22}(m - k) + c_{22}^2(k + m + 2)]^2 \geq 0, \end{aligned} \quad (A.2)$$

and corresponding values of c_{11} , c_{22} for $|c| = 0$ ($\Leftrightarrow A_0 = 0$) are

$$c_{22} = \frac{c_{12}}{k + m + 2} \left[k - m + \sqrt{k^2 - 2k(m - 4) + (m + 4)^2} \right] > 0 \quad \forall c_{12} \neq 0, k > 0, m > 0, \quad (A.3)$$

$$c_{11} = \frac{2c_{12}^2}{c_{22}} > 0 \quad \forall c_{12} \neq 0, k > 0, m > 0. \quad (A.4)$$

(iii) Values of λ , k , and m for which the secular equation (3.7) has a double pure imaginary pair of roots (eigenvalues) are

$$\begin{aligned} k_{1,2} &= \frac{1}{2c_{22}} \left(c_{22}c_{11}^2 + \left(c_{22}^2 - c_{12}c_{22} \mp \sqrt{c_{22}(c_{11} - 2c_{12} + c_{22})(c_{11}c_{22} + 4)} + 2 \right) c_{11} \right), \\ \lambda_{1,2} &= \frac{1}{2} \left(c_{22}(c_{11} - c_{12}) \mp \sqrt{c_{22}(c_{11} - 2c_{12} + c_{22})(c_{11}c_{22} + 4)} + 4 \right), \\ m &= -\frac{c_{11} - 2c_{12} + c_{22}}{c_{22}} \end{aligned} \quad (\text{A.5})$$

and the corresponding conditions for the above two sets of values to be positive are as follows.

For the 1st set (k_1, λ_1, m) ,

$$\begin{aligned} (-2 < c_{22} < 0) \wedge & \left\{ \begin{aligned} & \left(-\sqrt{\frac{c_{11}c_{22}^3 + 4c_{22}^2 - 4c_{11}c_{22} - 16}{c_{22}^2}} < c_{12} < \frac{c_{11} + c_{22}}{2} \right) \\ & \vee \\ & \left(-\frac{4}{c_{22}} < c_{11} < \frac{c_{22}^2}{8} \right) \wedge \left(\sqrt{\frac{c_{11}c_{22}^3 + 4c_{22}^2 - 4c_{11}c_{22} - 16}{c_{22}^2}} < c_{12} < \frac{c_{11} + c_{22}}{2} \right) \end{aligned} \right\} \\ (0 < c_{22} < 2) \wedge & \left(\frac{c_{22}^2 - 8}{c_{22}} < c_{11} \leq -\frac{4}{c_{22}} \right) \wedge \left(\frac{c_{11} + c_{22}}{2} < c_{12} < -\sqrt{\frac{c_{11}c_{22}^3 + 4c_{22}^2 - 4c_{11}c_{22} - 16}{c_{22}^2}} \right). \end{aligned} \quad (\text{A.6})$$

For the 2nd set (k_2, λ_2, m) ,

$$\begin{aligned} (-2 < c_{22} < 0) \wedge & \left[\begin{aligned} & \left(-\frac{4}{c_{22}} \leq c_{11} \leq \frac{c_{22}^2 - 8}{c_{22}} \right) \wedge \mathbf{Q} \\ & \vee \\ & \left(c_{11} > \frac{c_{22}^2 - 8}{c_{22}} \right) \wedge \mathbf{X} \end{aligned} \right] \\ (0 < c_{22} < 2) \wedge & \left[\begin{aligned} & \left(c_{11} < \frac{c_{22}^2 - 8}{c_{22}} \right) \wedge \mathbf{Y} \\ & \vee \\ & \left(\frac{c_{22}^2 - 8}{c_{22}} \leq c_{11} < -\frac{4}{c_{22}} \right) \wedge \mathbf{W} \\ & \vee \\ & \left(c_{11} = -\frac{4}{c_{22}} \right) \wedge \mathbf{Z} \end{aligned} \right]. \end{aligned} \quad (\text{A.7})$$

where

$$\begin{aligned}
 Q &= \left(-\sqrt{\frac{c_{11}c_{22}^3 + 4c_{22}^2 - 4c_{11}c_{22} - 16}{c_{22}^2}} < c_{12} < \frac{c_{11} + c_{22}}{2} \right), \\
 X &= \left(-\sqrt{\frac{c_{11}c_{22}^3 + 4c_{22}^2 - 4c_{11}c_{22} - 16}{c_{22}^2}} < c_{12} < \sqrt{\frac{c_{11}c_{22}^3 + 4c_{22}^2 - 4c_{11}c_{22} - 16}{c_{22}^2}} \right), \\
 Y &= \left(-\sqrt{\frac{c_{11}c_{22}^3 + 4c_{22}^2 - 4c_{11}c_{22} - 16}{c_{22}^2}} < c_{12} < \sqrt{\frac{c_{11}c_{22}^3 + 4c_{22}^2 - 4c_{11}c_{22} - 16}{c_{22}^2}} \right), \quad (A.8) \\
 W &= \left(\frac{c_{11} + c_{22}}{2} < c_{12} < \sqrt{\frac{c_{11}c_{22}^3 + 4c_{22}^2 - 4c_{11}c_{22} - 16}{c_{22}^2}} \right), \\
 Z &= \left(\frac{c_{11} + c_{22}}{2} < c_{12} < -\sqrt{\frac{c_{11}c_{22}^3 + 4c_{22}^2 - 4c_{11}c_{22} - 16}{c_{22}^2}} \right).
 \end{aligned}$$

References

- [1] H. Ziegler, "Die Stabilitätskriterien der Elastomechanik," *Ingenieur Archiv*, vol. 20, no. 1, pp. 49–56, 1952.
- [2] A. N. Kounadis, "On the failure of static stability analyses of nonconservative systems in regions of divergence instability," *International Journal of Solids and Structures*, vol. 31, no. 15, pp. 2099–2120, 1994.
- [3] A. N. Kounadis, "Non-potential dissipative systems exhibiting periodic attractors in regions of divergence," *Chaos, Solitons & Fractals*, vol. 8, no. 4, pp. 583–612, 1997.
- [4] V. V. Bolotin, A. A. Grishko, and A. V. Petrovsky, "Secondary bifurcations and global instability of an aeroelastic non-linear system in the divergence domain," *Journal of Sound and Vibration*, vol. 191, no. 3, pp. 431–451, 1996.
- [5] M. P. Paidoussis, D. Mateescu, and W.-G. Sim, "Dynamics and stability of a flexible cylinder in a narrow coaxial cylindrical duct subjected to annular flow," *Journal of Applied Mechanics*, vol. 57, no. 1, pp. 232–240, 1990.
- [6] M. P. Paidoussis, *Fluid-Structure Interactions: Slender Structures and Axial Flow*, vol. 2, Elsevier Academic Press, London, UK, 2003.
- [7] K. Huseyin, *Multiple Parameter Stability Theory and Its Applications*, vol. 18 of *Oxford Engineering Science Series*, Clarendon Press, Oxford, UK, 1986.
- [8] F. R. Gantmacher, *Lectures in Analytical Mechanics*, Mir, Moscow, Russia, 1970.
- [9] K. Huseyin, *Vibrations and Stability of Damped Mechanical Systems*, Sijthoff & Noordhoff, Alphen aan den Rijn, The Netherlands, 1978.
- [10] A. N. Kounadis, "Hamiltonian weakly damped autonomous systems exhibiting periodic attractors," *Zeitschrift für Angewandte Mathematik und Physik*, vol. 57, no. 2, pp. 324–350, 2006.
- [11] A. N. Kounadis, "Flutter instability and other singularity phenomena in symmetric systems via combination of mass distribution and weak damping," *International Journal of Non-Linear Mechanics*, vol. 42, no. 1, pp. 24–35, 2007.
- [12] E. E. Zajac, "The Kelvin-Tait-Chetaev theorem and extensions," *Journal of the Astronautical Sciences*, vol. 11, no. 2, pp. 46–49, 1964.
- [13] E. E. Zajac, "Comments on 'stability of damped mechanical systems and a further extension'," *AIAA Journal*, vol. 3, no. 9, pp. 1749–1750, 1965.
- [14] R. Sygulski, "Dynamic stability of pneumatic structures in wind: theory and experiment," *Journal of Fluids and Structures*, vol. 10, no. 8, pp. 945–963, 1996.

- [15] A. Laneville and A. Mazouzi, "Wind-induced ovaling oscillations of cylindrical shells: critical onset velocity and mode prediction," *Journal of Fluids and Structures*, vol. 10, no. 7, pp. 691–704, 1996.
- [16] A. K. Misra, S. S. T. Wong, and M. P. Paidoussis, "Dynamics and stability of pinned-clamped and clamped-pinned cylindrical shells conveying fluid," *Journal of Fluids and Structures*, vol. 15, no. 8, pp. 1153–1166, 2001.
- [17] A. N. Kounadis, "A geometric approach for establishing dynamic buckling loads of autonomous potential two-degree-of-freedom systems," *Journal of Applied Mechanics*, vol. 66, no. 1, pp. 55–61, 1999.
- [18] F. R. Gantmacher, *The Theory of Matrices*, Chelsea, New York, NY, USA, 1959.
- [19] L. A. Pipes and L. R. Harvill, *Applied Mathematics for Engineers and Physicists*, International Student Edition, McGraw-Hill, Kogakusha, Tokyo, Japan, 3rd edition, 1970.
- [20] A. T. Fuller, "Conditions for a matrix to have only characteristic roots with negative real parts," *Journal of Mathematical Analysis and Applications*, vol. 23, no. 1, pp. 71–98, 1968.
- [21] T. B. Bahder, *Mathematica for Scientists and Engineers*, Addison-Wesley, Reading, Mass, USA, 1995.

Research Article

Nonlinear Modeling of Cables with Flexural Stiffness

Walter Lacarbonara¹ and Arnaud Pacitti²

¹ *Dipartimento di Ingegneria Strutturale e Geotecnica, Università degli studi di Roma la Sapienza, Via Eudossiana, 00184 Rome, Italy*

² *Ecole Nationale des Travaux Publics de L'Etat, Laboratoire des Séomatériaux, 69120 Vaulx-En-Velin, France*

Correspondence should be addressed to Walter Lacarbonara, walter.lacarbonara@uniroma1.it

Received 14 November 2007; Accepted 28 March 2008

Recommended by Paulo Gonçalves

A geometrically exact formulation of cables suffering axis stretching and flexural curvature is presented. The dynamical formulation is based on nonlinearly viscoelastic constitutive laws for the tension and bending moment with the additional constitutive nonlinearity accounting for the no-compression condition. A continuation method, combined with a mixed finite-difference spatial discretization, is then employed to path-follow the static responses of cables subject to forces or support displacements. These computations, conducted in the quasistatic regime, are based on cables with linearly elastic material behaviors, whereas the nonlinearity is in the geometric stiffness terms and the no-compression behavior. The finite-difference results have been confirmed employing a weak formulation based on quadratic Lagrangian finite elements. The influence of the flexural stiffness on the nonlinear static responses is assessed comparing the results with those obtained for purely extensible cables. The properties of the frequencies of the linear normal modes of cables with flexural stiffness are also investigated and compared with those of purely extensible cables.

Copyright © 2008 W. Lacarbonara and A. Pacitti. This is an open access article distributed under the Creative Commons Attribution License, which permits unrestricted use, distribution, and reproduction in any medium, provided the original work is properly cited.

1. Introduction

Cables are used in a variety of engineering applications such as in suspension or cable-stayed bridges, power transmission lines, moorings in ocean engineering, or in aerospace deployable structures. Cables are effectively employed in long-span structures because they can be easily engineered and are light-weight structural elements with an outstanding stiffness in the axial direction and a significantly high strength. However, they do possess limitations due to the lack of out-of-plane stiffness and very light damping that make them often prone to large-amplitude

vibrations. Another serious limitation is that they cannot resist compression, therefore, they are always prestressed to resist actions that may produce compression although under severe dynamic excitations, the low-tension regime is barely unavoidable.

Although a number of works have addressed the problem of modeling the flexural stiffness in cables, only a few works deal with nonlinear vibrations of general cables in low-tension regimes. Most of them consider nonlinear vibrations of shallow/taut cables, including also multiple resonances [1–4]. In [5, 6], a geometrically exact nonlinear model of linearly elastic nonshallow cables was proposed, and the nonlinear modal characteristics of the free planar motions were investigated neglecting flexural stiffness as it is commonly done in the literature. In fact, flexural stiffness appears in modeling cables only when the loosening effect is considered. When the excitation levels are high, the loss of tension can be such that the cable suffers local loosening in those segments where the overall tension vanishes and, as a result, the cable cannot locally sustain loads unless its flexural load-carrying capability is considered. Most of the times, the flexural rigidity and damping are considered in a cable model to overcome numerical divergence problems when loosening appears. For instance, when dealing with the dynamics of submerged cables, some works focus on a general mechanical formulation for the cable equations (e.g., [7–9]); such equations of motion are then solved by direct integration schemes. Other works focus on the derivation or modification of finite-element solution models (e.g., [10]), or even in simplified solution models such as the lumped mass approach of Chai et al. [11]. Similarly, Wu et al. [12–15] used a model of cables that includes the linear flexural stiffness contribution, and an approximate strain-displacement relationship for the elongation, to describe nonlinear vibrations of cables suffering loosening. Moreover, with the proposed model, the effects of loosening on the nonlinear parametric responses of taut cables subject to periodic horizontal displacements of the supports were investigated.

However, the effects of flexural rigidity and viscoelasticity on the nonlinear dynamics of cables have not been thoroughly investigated, especially when loosening appears. Furthermore, the flexural stiffness has a critical role in stock-bridge dampers used to dissipate energy. There is a need to have a reliable and accurate mechanical model of cables to assess the global load-carrying capability under these conditions. There are only a few studies addressing this challenging modeling problem and they are often based on ad hoc approximations that limit the physically meaningful dynamic regimes.

In this paper, a nonlinear geometrically exact formulation of cables undergoing axis stretching and flexural curvature, incorporating a nonlinearly viscoelastic constitutive law and the no-compression condition, is first presented. The derivation of the mechanical model is extensively inspired by the seminal work of Antman [16]. Thereafter, the linearization and the ensuing eigenvalue problem are addressed. Then, the finite-difference computational scheme is illustrated. Meaningful static responses of cables subject to various loading paths—support displacements or forces—are investigated in both cable models, here considered, the model with flexural stiffness and that without flexural resistance.

2. Mechanical formulation for cables with flexural stiffness

In this section, we illustrate the geometrically exact formulation of the equations of motion of cables suffering axis stretching and bending curvature [16]. Shear deformations are not considered. Moreover, a planar kinematic model is discussed neglecting out-of-plane bending

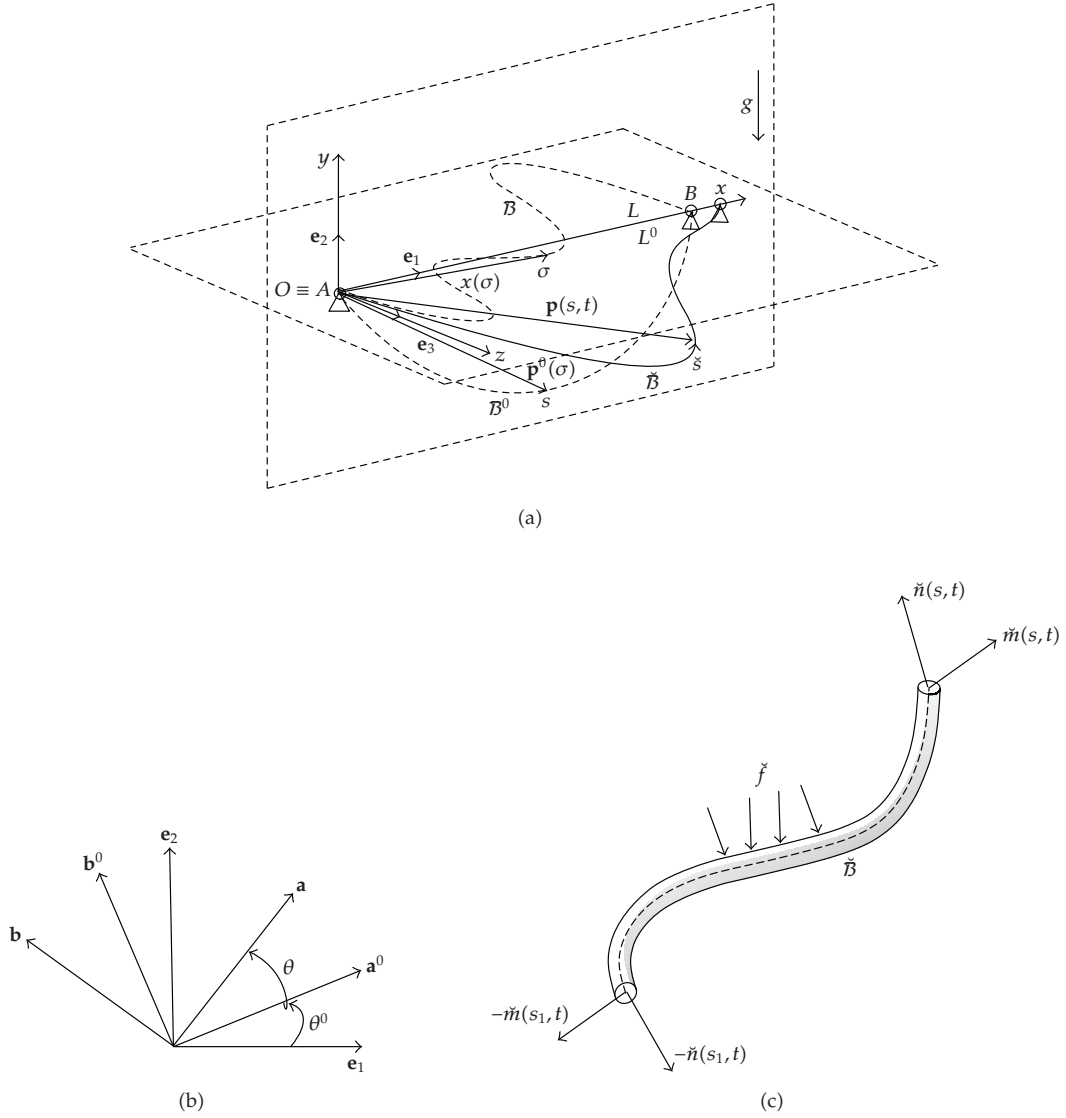


Figure 1: Stress-free configuration \mathcal{B} , prestressed configuration \mathcal{B}^0 , and actual configuration $\tilde{\mathcal{B}}$ (top). Unit vectors and rotations of the plane kinematics (bottom left) and internal/external forces in the cable (bottom right).

and torsion. The prestressed equilibrium is first discussed, then the dynamics around it are described in the kinematic, dynamic, and constitutive aspects.

2.1. The prestressed cable

The cable is stress-free in the configuration \mathcal{B} (Figure 1(a)). This configuration can be any arbitrary configuration assumed by the cable, for example, on a frictionless horizontal plane

when it is not subject to forces besides the gravity force. In this state, the internal stresses are expected to be practically vanishing. In particular, in Figure 1(a), \mathcal{B} represents any reference line along the cable in the stress-free configuration (e.g., the centroidal line) and L is its undeformed length. Further, we let the arc length, denoted σ , be the coordinate identifying the material sections of the cable. We consider the fixed Cartesian reference frame $(O, \mathbf{e}_1, \mathbf{e}_3, \mathbf{e}_2)$ shown in Figure 1(a). When the cable ends are fixed to two points, A and B , and the cable is let free to hang under the action of gravity, it occupies an equilibrium configuration, here denoted \mathcal{B}^0 , and considered as the reference configuration for the subsequent dynamic problem. The arc length in the configuration \mathcal{B}^0 is denoted s . Let the position vector of the material point P^0 of the cable in the reference configuration \mathcal{B}^0 be \mathbf{p}^0 . Among the different parameterizations for \mathbf{p}^0 , we employ σ , and let the Cartesian representation of \mathbf{p}^0 be $\mathbf{p}^0(\sigma) := x(\sigma)\mathbf{e}_1 + y(\sigma)\mathbf{e}_2$.

The cable stretch is then simply defined as

$$\mathbf{p}_\sigma^0(\sigma) = v^0(\sigma)\mathbf{a}^0(\sigma), \quad (2.1)$$

where \mathbf{a}^0 is the unit vector in the tangential direction to \mathcal{B}^0 ; the subscript here and henceforth will denote partial differentiation with respect to the indicated variable. Consequently, the stretch is

$$v^0(\sigma) = |\mathbf{p}_\sigma^0(\sigma)| = \frac{ds}{d\sigma}. \quad (2.2)$$

We suppose that the cable flexural rigidity is negligible in the equilibrium \mathcal{B}^0 under its own weight, hence the stress vector representing the contact force that the cable segment $\sigma > \sigma_1$ exerts on the cable segment $\sigma < \sigma_1$ through the material section at σ_1 has a resultant (integrated on the domain representing the deformed cable material section) referred to as contact force and denoted \mathbf{n}^0 . On the other hand, the resultant moment is vanishing. This assumption holds true because under its own weight (uniformly distributed), the cable will assume a funicular configuration having the tension carrying the weight.

By denoting \mathbf{f}^0 , the force per unit reference length σ , the local form of the balance of linear and angular momentum can be written as

$$\mathbf{n}_\sigma^0(\sigma) + \mathbf{f}^0(\sigma) = \mathbf{o}, \quad \mathbf{p}_\sigma^0(\sigma) \times \mathbf{n}^0(\sigma) = \mathbf{o}. \quad (2.3)$$

The second part of equation (2.3) implies that \mathbf{n}^0 is in the same direction as $\mathbf{p}_\sigma^0 = v^0\mathbf{a}^0$, that is, in the direction of the tangent to the deformed configuration \mathcal{B}^0 ; hence, $\mathbf{n}^0(\sigma) = N^0(\sigma)\mathbf{a}^0(\sigma)$, where N^0 denotes the magnitude of the contact force, commonly referred to as the tension. Moreover, the unit vector \mathbf{a}^0 can be expressed as

$$\mathbf{a}^0 = \frac{\mathbf{p}_\sigma^0}{|\mathbf{p}_\sigma^0|} = \frac{\mathbf{p}_\sigma^0}{v^0}. \quad (2.4)$$

The final balance equation is then rewritten as

$$[N^0(\sigma)\mathbf{a}^0(\sigma)]_\sigma + \mathbf{f}^0 = \mathbf{o}. \quad (2.5)$$

The constitutive law relating the tension N^0 to the stretch v^0 is introduced in the form

$$N^0(\sigma) = \widehat{N}^0(v^0, \sigma). \quad (2.6)$$

A few restrictions are imposed on \widehat{N}^0 as $\widehat{N}^0(\nu^0 = 1, \sigma) = 0$, $\widehat{N}_\nu > 0$. Moreover, for materials strong in resisting tension, we may require $\widehat{N}^0 \rightarrow \infty$ as $\nu^0 \rightarrow \infty$.

The governing equilibrium equation is obtained substituting (2.6) into (2.5). The equilibrium equation can be projected into the local basis $\{\mathbf{a}^0, \mathbf{b}^0, \mathbf{c}^0\}$ (with $\mathbf{c}^0 \equiv \mathbf{e}_3$) or the fixed basis $(\mathbf{e}_1, \mathbf{e}_2, \mathbf{e}_3)$. Using the local basis, accounting for $(\mathbf{a}^0)_\sigma = \nu^0 \mu^0 \mathbf{b}^0$, with $\mu^0 = \theta_s^0$ (the geometric curvature of \mathcal{B}^0), and letting $\mathbf{f}^0 = f_1^0 \mathbf{a}^0 + f_2^0 \mathbf{b}^0$ yield

$$\widehat{N}_\sigma^0 + f_1^0 = 0, \quad \nu^0 \mu^0 \widehat{N}^0 + f_2^0 = 0. \quad (2.7)$$

On the other hand, projecting (2.5) into the fixed basis $(\mathbf{e}_1, \mathbf{e}_2, \mathbf{e}_3)$ and accounting for $\mathbf{a}^0 = \cos \theta^0 \mathbf{e}_1 + \sin \theta^0 \mathbf{e}_2$ and $\mathbf{b}^0 = -\sin \theta^0 \mathbf{e}_1 + \cos \theta^0 \mathbf{e}_2$ yield

$$[\widehat{N}^0 \cos \theta^0]_\sigma + b_1^0 = 0, \quad [\widehat{N}^0 \sin \theta^0]_\sigma + b_2^0 = 0, \quad (2.8)$$

where $\mathbf{f}^0 = b_1^0 \mathbf{e}_1 + b_2^0 \mathbf{e}_2$.

The relationships between $(\cos \theta^0, \sin \theta^0)$ and $(x_\sigma, y_\sigma, \nu^0)$ can be obtained considering $\mathbf{p}_\sigma^0 = x_\sigma \mathbf{e}_1 + y_\sigma \mathbf{e}_2$ and $\mathbf{a}^0 = \cos \theta^0 \mathbf{e}_1 + \sin \theta^0 \mathbf{e}_2$, that is,

$$\cos \theta^0 = \frac{x_\sigma}{\nu^0}, \quad \sin \theta^0 = \frac{y_\sigma}{\nu^0}. \quad (2.9)$$

From the fundamental trigonometric identity ($\sin^2 \theta^0 + \cos^2 \theta^0 = 1$), the stretch becomes $\nu^0 = \sqrt{x_\sigma^2 + y_\sigma^2}$. The solution for the static configuration \mathcal{B}^0 under the dead loads and, more specifically, under the action of gravity, is described in the Appendix. We will discuss cables suspended from two points at the same level (horizontal cables) or at different levels (inclined cables).

2.2. The dynamic incremental problem

The transformation from the static configuration \mathcal{B}^0 to the current configuration $\check{\mathcal{B}}$ is illustrated next. We let $\mathbf{p}(s, t) = \mathbf{p}^0(s) + \mathbf{u}(s, t)$ be the position vector of the point of the cable in $\check{\mathcal{B}}$ and let the arc length in $\check{\mathcal{B}}$ be denoted \check{s} . We will treat, to start with, the planar problem (see Figure 1(b)). Hence, let $\mathbf{b}(s, t)$ be the unit vector giving the orientation of the cable cross-section in $\check{\mathcal{B}}$ so that the cable-fixed basis in $\check{\mathcal{B}}$ is $(\mathbf{a}(s, t), \mathbf{b}(s, t))$ and θ denotes the rotation angle from $(\mathbf{a}^0, \mathbf{b}^0)$ to (\mathbf{a}, \mathbf{b}) . Therefore, the angle that \mathbf{a} makes with \mathbf{e}_1 is $\check{\theta} = \theta^0 + \theta$.

The cable total stretch is obtained, by enforcing the shear strain to vanish, as $\mathbf{p}_\sigma = \check{\nu} \mathbf{a}$, where $\check{\nu} = d\check{s}/d\sigma = \nu \nu^0$, that is, the product of the initial stretch and the incremental stretch ν . To calculate the cable incremental stretch ν that arises in the motion from \mathcal{B}^0 to $\check{\mathcal{B}}$, we consider $\mathbf{p}_s = \nu \mathbf{a}$. Then, by letting $\mathbf{u}(s, t) = u(s, t) \mathbf{a}^0(s, t) + v(s, t) \mathbf{b}^0$ represent the displacement vector from \mathcal{B}^0 to $\check{\mathcal{B}}$, the position vector is $\mathbf{p} = \mathbf{p}^0 + \mathbf{u}$ and its gradient becomes $\mathbf{p}_s = \mathbf{p}_s^0 + \mathbf{u}_s = (1 + u_s - \mu^0 v) \mathbf{a}^0 + (v_s + \mu^0 u) \mathbf{b}^0$. Consequently,

$$\nu = \sqrt{(1 + u_s - \mu^0 v)^2 + (v_s + \mu^0 u)^2}, \quad (2.10)$$

$$\mathbf{a} = \frac{(1 + u_s - \mu^0 v) \mathbf{a}^0 + (v_s + \mu^0 u) \mathbf{b}^0}{\nu}. \quad (2.11)$$

Moreover,

$$\sin \theta = \frac{\mathbf{p}_s \cdot \mathbf{b}^0}{v} = \frac{v_s + \mu^0 u}{v}, \quad \cos \theta = \frac{\mathbf{p}_s \cdot \mathbf{a}^0}{v} = \frac{1 + u_s - \mu^0 v}{v}. \quad (2.12)$$

Dividing the left- and right-hand sides of the two preceding equations and considering the inverse tangent function yield the incremental angle θ as

$$\theta = \tan^{-1} \left(\frac{v_s + \mu^0 u}{1 + u_s - \mu^0 v} \right). \quad (2.13)$$

Therefore, the flexural curvature μ is

$$\mu = \frac{d\theta}{ds} = \frac{1}{v^2} [(v_{ss} + (\mu^0 u)_s)(1 + u_s - \mu^0 v) - (u_{ss} - (\mu^0 v)_s)(v_s + \mu^0 u)]. \quad (2.14)$$

The presentation of the kinematic model is complete once the boundary conditions are prescribed. For generality, we consider the cable supports lying in the $(\mathbf{e}_1, \mathbf{e}_2)$ -plane and being placed at different levels and immovable under the dead loads, $\mathbf{x}(0) = \mathbf{p}^0(0) = \mathbf{o}$, $\mathbf{x}(L) = \mathbf{p}^0(L) = \ell \mathbf{e}_1 + h \mathbf{e}_2$. On the contrary, the supports prescribe some smooth motions during the dynamic change of configuration from \mathcal{B}^0 to \mathcal{B} . Hence, the time-dependent boundary conditions become

$$\mathbf{p}(0, t) = \mathbf{u}_A(t) = u_A(t) \mathbf{e}_2, \quad \mathbf{p}(L, t) = \mathbf{p}^0(L) + \mathbf{u}_B(t) = (l + u_B(t)) \mathbf{e}_1 + h \mathbf{e}_2. \quad (2.15)$$

Next, the dynamical aspects of the problem are discussed. We let $\check{\mathbf{n}} = \check{N} \mathbf{a} + \check{H} \mathbf{b}$ be the contact force in the cable at \check{s} , let $\check{\mathbf{f}}$ be the incremental external forces such that $\check{\mathbf{f}}(s, t) = \mathbf{f}^0(s) + \mathbf{f}(s, t)$ indicates the total external force density acting on the cable (per unit reference length s), and let $\check{\mathbf{m}}$ be the total flexural moment of the cable at \check{s} . Please note that here $\mathbf{f}^0(s)$ denotes the force acting in \mathcal{B}^0 , however, referred, for convenience, to the unit reference length s instead of σ . In the current configuration \mathcal{B} , the local form of the balance of linear and angular momentum requires

$$\begin{aligned} \check{\mathbf{n}}_s(s, t) + \check{\mathbf{f}}(s, t) &= \rho A^0 \mathbf{p}_{tt}(s, t), \\ \check{\mathbf{m}}_s(s, t) + \mathbf{p}_s(s, t) \times \check{\mathbf{n}}(s, t) &= \mathbf{o}. \end{aligned} \quad (2.16)$$

By accounting for $\mathbf{p}_s(s, t) = v \mathbf{a}$, the balance of angular momentum yields

$$\check{\mathbf{m}}_s + v \check{H} \mathbf{e}_3 = \mathbf{o}. \quad (2.17)$$

Further, let N and H be the incremental axial and shear forces such that $\check{N} = N^0 + N$ and $\check{H} \equiv H$, since the reactive shear force H^0 in \mathcal{B}^0 is zero. Hence, the total contact force is $\check{\mathbf{n}} = (N^0 + N) \mathbf{a} + H \mathbf{b}$. Similarly, \mathbf{m} is the incremental flexural moment coinciding with the total flexural moment since the cable flexural stiffness is neglected in the initial static configuration, therefore, $\check{\mathbf{m}} = \mathbf{m}$. Since $\mathbf{m} = M \mathbf{e}_3$, (2.17), solved for H , yields the shear force as $H = -M_s/v$. We can rewrite the equation of motion (2.16) as

$$\left(\check{N} \mathbf{a} - \frac{M_s}{v} \mathbf{b} \right)_s + \mathbf{f}^0 + \mathbf{f} = \rho A^0 \mathbf{p}_{tt}. \quad (2.18)$$

By considering the equilibrium in \mathcal{B}^0 , $(N^0 \mathbf{a}^0)_s + \mathbf{f}^0 = \mathbf{0}$, and by letting $\tilde{N} \mathbf{a} = N^0 \mathbf{a}^0 + N^0 (\mathbf{a} - \mathbf{a}^0) + N \mathbf{a}$, the equation of motion (2.18) becomes

$$(N \mathbf{a})_s + [N^0 (\mathbf{a} - \mathbf{a}^0)]_s - \left(\frac{M_s}{\nu} \mathbf{b} \right)_s + \mathbf{f} = \rho A^0 \mathbf{p}_{tt}. \quad (2.19)$$

The componential form of (2.19) in the cable-fixed basis $(\mathbf{a}^0, \mathbf{b}^0)$ becomes

$$\left[(N^0 + N)_s + \frac{M_s}{\nu} (\mu^0 + \mu) \right] \cos \theta - \left[(N^0 + N) (\mu^0 + \mu) - \left(\frac{M_s}{\nu} \right)_s \right] \sin \theta - N_s^0 + f_1 = \rho A^0 u_{tt}, \quad (2.20)$$

$$\left[(N^0 + N)_s + \frac{M_s}{\nu} (\mu^0 + \mu) \right] \sin \theta + \left[(N^0 + N) (\mu^0 + \mu) - \left(\frac{M_s}{\nu} \right)_s \right] \cos \theta - \mu^0 N^0 + f_2 = \rho A^0 v_{tt}, \quad (2.21)$$

where $\mathbf{f} = f_1 \mathbf{a}^0 + f_2 \mathbf{b}^0$, $\rho A^0 \mathbf{p}_{tt} = \rho A^0 u_{tt} \mathbf{a}^0 + \rho A^0 v_{tt} \mathbf{b}^0$.

Suitable nonlinearly viscoelastic constitutive laws for the tension N and the bending moment M are given in the form

$$\begin{aligned} N(s, t) &= \widehat{N}(\nu, \nu_t, s), \quad \text{iff } \check{\nu} = \nu^0 \nu > 1, \\ M(s, t) &= \widehat{M}(\mu, \mu_t, s). \end{aligned} \quad (2.22)$$

For materials whose constitutive behavior is linearly viscoelastic also at large strains and strain rates, the linearized version of the nonlinear constitutive laws can be expressed in the form

$$\begin{aligned} \widehat{N} &= EA(\nu - 1) + (\widehat{N}_{\check{\nu}}) \nu_t, \quad \text{iff } \check{\nu} = \nu^0 \nu > 1, \\ \widehat{M} &= EJ\mu + (\widehat{M}_{\mu}) \mu_t. \end{aligned} \quad (2.23)$$

The constitutive law for \tilde{N} is nonlinear in the sense that, because the cable cannot resist compression, in those segments of the cable where $\check{\nu} \leq 1$, the total tension vanishes, that is, $\tilde{N} = N^0 + \widehat{N} = 0$. When a total loss of tension occurs, the cable does not undergo any local length changes, hence letting $\check{\nu} = \nu^0 \nu = 1$ yields the incremental stretching in terms of the prestretching, that is, $\nu = 1/\nu^0$. In the corresponding cable subdomains, the balance equations are accordingly modified putting $\tilde{N} = 0$ and $\check{\nu} = 1$. Hence,

$$-[N^0 \mathbf{a}^0]_s - \left(\frac{M_s}{\nu} \mathbf{b} \right)_s + \mathbf{f} = \rho A^0 \mathbf{p}_{tt}. \quad (2.24)$$

The strain-displacement relationships (2.10) and (2.14) are substituted into the constitutive equations (2.22) and these, in turn, are substituted, along with (2.12), into the equations of (2.20) and (2.21) delivering the final governing equations of motion in the unknown displacements u and v .

We finally nondimensionalize the equations of motion introducing the following nondimensional quantities:

$$\begin{aligned} s^* &= \frac{s}{\ell'}, & u^* &= \frac{u}{\ell'}, & v^* &= \frac{v}{\ell'}, & t^* &= \sqrt{\frac{H^0}{\rho A^0 \ell'^2}} t, \\ \mu^{0*} &= \ell \mu^0, & \mu^* &= l \mu, & f^* &= \frac{\ell f}{H^0}, & k &= \frac{EA^0}{H^0}, \\ N^{0*} &= \frac{N^0}{H^0}, & N^* &= \frac{N}{H^0}, & M^* &= \frac{M}{\ell H^0}, & \Lambda &= \frac{EJ^0}{\ell^2 H^0}. \end{aligned} \quad (2.25)$$

By dropping the star for notational simplicity and by neglecting the dissipative parts of the incremental dynamic tension and moment, the nondimensional equations of motion, for linearly elastic cables, become

$$\begin{aligned} N_s^0 \left[\frac{1 + u_s - \mu^0 v}{v} - 1 \right] - N^0 (\mu^0 + \mu) \left(\frac{v_s + \mu^0 u}{v} \right) \\ + k \left[v_s \frac{1 + u_s - \mu^0 v}{v} - (v - 1) (\mu^0 + \mu) \left(\frac{v_s + \mu^0 u}{v} \right) \right] \\ + \Lambda \left[(\mu^0 + \mu) \left(\frac{\mu_s}{v} \right) \left(\frac{1 + u_s - \mu^0 v}{v} \right) + \left(\frac{\mu_{ss}}{v} - \frac{v_s \mu_s}{v^2} \right) \left(\frac{v_s + \mu^0 u}{v} \right) \right] + f_1 = u_{tt}, \end{aligned} \quad (2.26)$$

$$\begin{aligned} N_s^0 \left[\frac{v_s + \mu^0 u}{v} \right] + N^0 \left[(\mu^0 + \mu) \frac{1 + u_s - \mu^0 v}{v^2} - \mu^0 \right] \\ + k \left[(v - 1) (\mu^0 + \mu) \left(\frac{1 + u_s - \mu^0 v}{v} + v_s \frac{v_s + \mu^0 u}{v} \right) \right] \\ + \Lambda \left[(\mu^0 + \mu) \left(\frac{\mu_s}{v} \right) \left(\frac{v_s + \mu^0 u}{v} \right) + \left(\frac{\mu_s v_s}{v^2} - \frac{\mu_{ss}}{v} \right) \left(\frac{1 + u_s - \mu^0 v}{v} \right) \right] + f_2 = v_{tt}, \end{aligned} \quad (2.27)$$

where the stretch v and the curvature μ are expressed by (2.10) and (2.14). On the other hand, the equations of motion in the case of a total decompression, with a linearly elastic material, become

$$\begin{aligned} v^{02} (\mu^0 + \mu) (1 + u_s - \mu^0 v) (\Lambda \mu)_s + v^0 (v_s + \mu^0 u) [v^0 (\Lambda \mu)_s]_s - N_s^0 + f_1 = u_{tt}, \\ v^{02} (\mu^0 + \mu) (v_s + \mu^0 u) (\Lambda \mu)_s - v^0 (1 + u_s - \mu^0 v) [v^0 (\Lambda \mu)_s]_s - \mu^0 N^0 + f_2 = v_{tt}. \end{aligned} \quad (2.28)$$

3. The linearization and vibration eigenvalue problem

The linearization of (2.19) can be systematically obtained once we introduce a small parameter, denoted ϵ , which suitably quantifies the deviations from the prestressed configuration \mathcal{B}^0 . We

neglect the dissipative parts of the tension and bending moment and the forcing. We assume $v = v(\epsilon)$, $\mu = \mu(\epsilon)$, $\widehat{N} = \widehat{N}(v(\epsilon))$, $\widehat{M} = \widehat{M}(\mu(\epsilon))$, $\mathbf{u}_s = \mathbf{u}_s(\epsilon)$, $\mathbf{a} = \mathbf{a}(\epsilon)$ as continuously differentiable functions of ϵ . Further,

$$\begin{aligned} v(0) &= 1, & \mu(0) &= 0, & \widehat{N}(v(0)) &= 0, & \widehat{M}(\mu(0)) &= 0, \\ \mathbf{a}(0) &= \mathbf{a}^0, & \mathbf{b}(0) &= \mathbf{b}^0, & \mathbf{u}_s(0) &= \mathbf{o}. \end{aligned} \quad (3.1)$$

Therefore, the elastic parts of the tension and flexural moment can be expanded in series of ϵ as

$$\widehat{N}(v(\epsilon))\mathbf{a}(\epsilon) = \epsilon EA^0 v_1 \mathbf{a}^0 + O(\epsilon^2), \quad \frac{\widehat{M}(\mu(\epsilon))}{v(\epsilon)} \mathbf{b}(\epsilon) = \epsilon (EJ^0 \mu_1)_s \mathbf{b}^0 + O(\epsilon^2), \quad (3.2)$$

where $v_1 = v_\epsilon(0)$ and $\mu_1 = \mu_\epsilon(0)$ denote the first-order part of the stretch and the curvature (i.e., containing only linear terms in \mathbf{u}_s). On the other hand, the geometric part of the internal force, expanded in series of ϵ , yields $N^0(\mathbf{a}(\epsilon) - \mathbf{a}^0) = N^0 \mathbf{a}_1 + O(\epsilon^2)$, where $\mathbf{a}_1 = \mathbf{a}_\epsilon(0)$ is the first-order deviation of \mathbf{a} from \mathbf{a}^0 . By retaining only first-order terms in the expansion of the equations of motion, we obtain the linearized equations of motion

$$(EA^0 v_1 \mathbf{a}^0)_s + (N^0 \mathbf{a}_1)_s - ((EJ^0 \mu_1)_s \mathbf{b}^0)_s = \rho A^0 \mathbf{u}_{tt}. \quad (3.3)$$

To calculate v_1 , μ_1 , and \mathbf{a}_1 , we consider (2.10), (2.14), and (2.11), and by differentiating them with respect to ϵ and by setting $\epsilon = 0$, we obtain

$$v_1 = u_s - \mu^0 v, \quad \mu_1 = v_{ss} + \mu_s^0 u + \mu^0 u_s, \quad \mathbf{a}_1 = (v_s + \mu^0 u) \mathbf{b}^0. \quad (3.4)$$

The first-order variation of \mathbf{a} can be alternatively obtained from $\mathbf{a} = \cos \theta(\epsilon) \mathbf{a}^0 + \sin \theta(\epsilon) \mathbf{b}^0 = \mathbf{a}^0 + \epsilon \theta_1 \mathbf{b}^0 + O(\epsilon^2)$, where the first-order variation of θ , given by (2.13), is $\theta_1 = v_s + \mu^0 u$. Therefore,

$$\begin{aligned} [EA^0(u_s - \mu^0 v)]_s + \mu^0 [EJ^0(v_{ss} + \mu_s^0 u + \mu^0 u_s)]_s - \mu^0 N^0(v_s + \mu^0 u) &= \rho A^0 u_{tt}, \\ \mu^0 [EA^0(u_s - \mu^0 v)] - [EJ^0(v_{ss} + \mu_s^0 u + \mu^0 u_s)]_{ss} + N_s^0(v_s + \mu^0 u) + N^0(v_s + \mu^0 u)_s &= \rho A^0 v_{tt}. \end{aligned} \quad (3.5)$$

In nondimensional form,

$$\begin{aligned} [k(u_s - \mu^0 v)]_s + \mu^0 [\Lambda(v_{ss} + \mu_s^0 u + \mu^0 u_s)]_s - \mu^0 N^0(v_s + \mu^0 u) &= u_{tt}, \\ \mu^0 k(u_s - \mu^0 v) - [\Lambda(v_{ss} + \mu_s^0 u + \mu^0 u_s)]_{ss} + N_s^0(v_s + \mu^0 u) + N^0(v_{ss} + \mu_s^0 u + \mu^0 u_s) &= v_{tt}. \end{aligned} \quad (3.6)$$

3.1. The cable elastogeometric parameters

The linear as well as nonlinear free motions of linearly elastic nonshallow cables without flexural stiffness depend on two parameters [5] related to their geometric and elastic stiffnesses, namely, γ and k , contrary to shallow cables [1] whose linear motions depend solely

on Irvine's elastogeometric parameter λ . Irvine's parameter combines the two characteristic parameters of nonshallow cables according to $\lambda^2 := \gamma^2 k / \eta^e$ with $\eta^e = \int_0^{\eta^0} \sec^2 \theta^0 ds$, $\eta^0 = L/\ell$. For cables suffering stretching and bending in the plane and made of a linearly elastic material, the independent governing parameters are three, namely, (γ, k, Λ) or, equivalently, $(\gamma, \lambda, \Lambda)$.

We discuss in more detail the cable parameters pointing out their mechanical significance and pertinent ranges of variation. The region of admissible elastic stiffness k in the (γ, λ) -plane was discussed in [5] considering the isostiffness curves according to the definition of Irvine's parameter. The boundaries of the admissible region correspond to $k_1 = 5 \cdot 10^2$ and $k_3 = 5 \cdot 10^4$, respectively. These values were determined considering that $k = E/S^0$ and $S^0 = H^0/A^0$ denotes the engineering tensile stress at the mid-span section. Hence, the minimum k_1 is attained when S^0 is maximum, here taken as the yielding tensile strength S^y . Because typical working tensile stresses are around 5–10% of S^y , a reasonable value of k is of the order of 10^3 . However, by considering lower tensile stresses in the static configuration, values of k of the order of 10^4 can be reasonably reached.

By assuming a typical circular cross-section, $J^0 = (A^0)^2/(4\pi)$, hence the nondimensional flexural stiffness becomes $\Lambda = kA^0/(4\pi\ell^2)$. Further, it is $\gamma = \rho g \ell / S^0$ and $k = E/S^0$. Hence, by considering the following as design data: (i) the sag ℓ , (ii) the material properties (ρ, E) , and (iii) the working tensile stress S^0 , the parameters γ and k (or λ) are accordingly determined and are independent of A^0 whereas Λ depends on k , ℓ , and A^0 . Therefore, considering iso- k curves, the nondimensional flexural stiffness parameter Λ remains constant only if the cable cross-sectional areas do not vary.

4. Computational scheme: finite-difference versus finite elements

We employ a finite-difference discretization method to path-follow the nonlinear static solutions of (2.26) and (2.27) with f_1 and f_2 being time-independent and being applied through a loading device with a sufficiently slow rate, that is, in a quasistatic fashion. The boundary conditions at A and B prescribe the displacements and the bending moments. In particular, the six boundary conditions are as follows:

$$u(0) = u_A, \quad v(0) = v_A, \quad u(\eta^0) = u_B, \quad v(\eta^0) = v_B, \quad M(0) = M(\eta^0) = 0. \quad (4.1)$$

By considering a grid with n points including the boundary points A and B , the interior points are $n - 2$. At the interior points, we enforce the two balance equations, with an ensuing number of $2(n - 2)$ field equations. Overall, the number of equations is $2(n + 1)$. If the problem is fully formulated in the displacement components (u, v) , then the unknowns would be $2n$ leading to an overconstrained system of nonlinear equations. The problem is circumvented by employing a standard mixed approach (in the sense that it is neither the displacement nor the force method) consisting in taking as unknowns the displacement (u, v) and the bending moment M resulting into $3n$ unknowns. The bending moment, treated as unknown in the balance equations, has to satisfy the constitutive equation which is added explicitly as an independent equation. Therefore, the overall number of equations comprises the $3(n - 2)$ field equations to which the six boundary conditions are to be added, resulting into a system of $3n$ equations in $3n$ unknowns.

Therefore, the field equations read

$$\begin{aligned}
& \left[N_s^0 + (k(v-1))_s + \frac{M_s}{v}(\mu^0 + \mu) \right] \cos \theta \\
& - \left[(N^0 + k(v-1))(\mu^0 + \mu) - \left(\frac{M_s}{v} \right)_s \right] \sin \theta - N_s^0 + f_1 = 0, \\
& \left[N_s^0 + (k(v-1))_s + \frac{M_s}{v}(\mu^0 + \mu) \right] \sin \theta \\
& + \left[(N^0 + k(v-1))(\mu^0 + \mu) - \left(\frac{M_s}{v} \right)_s \right] \cos \theta - \mu^0 N^0 + f_2 = 0, \\
& M - \Lambda \frac{1}{v^2} \left[(v_{ss} + (\mu^0 u)_s)(1 + u_s - \mu^0 v) - (u_{ss} - (\mu^0 v)_s)(v_s + \mu^0 u) \right] = 0.
\end{aligned} \tag{4.2}$$

To enhance the accuracy of the finite-difference scheme, we employed a five-point scheme [17] based on an equidistant point grid which can be written, considering the first-order space derivative, as follows:

$$\frac{1}{12 \times \Delta} \begin{bmatrix} -25 & 48 & -36 & 16 & -3 \\ -3 & -10 & 18 & -6 & 1 \\ 1 & -8 & 0 & 8 & -1 \\ -1 & 6 & -18 & 10 & 3 \\ 3 & -16 & 36 & -48 & 25 \end{bmatrix}, \tag{4.3}$$

where $\Delta = s_i - s_{i-1}$ denotes the distance between two adjacent points of the grid.

For the chosen n -point grid, we have $3n$ equations, each expressed as a function of

$$[(u_{i-2}, u_{i-1}, u_i, u_{i+1}, u_{i+2}), (v_{i-2}, v_{i-1}, v_i, v_{i+1}, v_{i+2}), (M_{i-2}, M_{i-1}, M_i, M_{i+1}, M_{i+2})] \tag{4.4}$$

and the external force term f_i , where i is the index associated to the grid point. Out of the six boundary conditions, four equations are kinematic, namely, $u_0 = u_A$, $u_n = u_B$, $v_0 = v_A$, $v_n = v_B$, two of them are mechanical, $M_0 = M_n = 0$. Further, mention must be made of the fact that the discretization at the two points adjacent to the boundary points is not clearly centered.

The problem is solved step-by-step employing a zeroth-order path-following scheme where the Newton-Raphson iterative scheme is exploited at each load step to find the new solution point. The procedure was implemented in MATHEMATICA [18]. At each load step, the external force is increased by Δf_i and the solution point of the preceding step is used as the initial guess in the updated load step; in this sense, the continuation procedure is based on a zeroth-order predictor. At the end of each load step, the determined solution is expected to satisfy the balance equations ensuring that the pointwise remainders are below a prescribed numerical tolerance.

The same analyses have been conducted employing COMSOL [19]. COMSOL Multiphysics allows to approximate partial-differential equations of various kinds via a finite element procedure. The number of quadratic Lagrangian finite elements was set to 7680 in all calculations, for a total number of 76 805 degrees of freedom, and the tolerance was fixed to 10^{-6} . The high number of finite elements was not strictly needed, it was chosen in all calculations for accuracy reasons. A close agreement between the finite difference-based (with number of grid points greater than or equal to 30) and finite element-based results has been found and it is such that only the outcomes of COMSOL are reported next.

5. Illustrative examples of nonlinear static responses

It is of interest to investigate into the differences exhibited by the nonlinear structural responses of cables possessing flexural stiffness and those of cables whose flexural stiffness is neglected. The objective is to assess the extent of the bending stiffness contribution within the context of static loading processes. It is clear, however, that the most significant effects are expected to be exhibited in dynamic regimes, especially near resonances and instabilities.

In this section, we present some illustrative examples of nonlinear responses to three different loading scenarios. All loading cases are selected so as to induce a gradual loss of tension that enhances the bending moment contribution. The first case features a horizontal cable, lying under its own weight between two points at the same level. A constant uniformly distributed vertical upward load is applied over a central region of the cable. In the other two cases, the loading path is a prescribed incremental displacement of the right support to the left so as to loosen the cable. We consider both a horizontal and an inclined cable.

Two different cables are considered in the numerical computations and they have the following nondimensional governing parameters: $\eta^0 = 1.09615$, $\gamma = 1.5$, $k = 1.10 \cdot 10^4$, $\Lambda = 4.43 \cdot 10^{-4}$, for the horizontal cable, and $\gamma = 0.47$, $k = 3.70 \cdot 10^3$, $\Lambda = 1.40 \cdot 10^{-4}$, for the inclined cable. These parameters correspond to a steel cable whose initial length is $L = 142.5$ m for the first configuration whose span is $l = 130$ m, Young's effective modulus is $E = 100$ GPa; its cross-sectional area and moment of inertia are $A^0 = 8 \cdot 10^{-3}$ m² and $J^0 = 5.1 \cdot 10^{-6}$ m⁴, respectively. The height of the inclined cable is $h = 30$ m and its initial length is $L = 136.4$ m.

In all loading scenarios, we determine the cable response curves, depicting variations of the vertical displacement of a control point (point C whose arc length coordinate is $s = 1/3 L$) with the magnitude of the force or support displacement. In particular, the loading path is discretized into N_L steps so that, by indicating with f_{N_L} the load magnitude at the end of the loading path and with f_j the magnitude at the j th step, we let $\alpha_j = f_j / f_{N_L}$ be the load multiplier. We monitored the configurations and state of stress at three given load steps, namely, $\alpha = 1/3, 2/3, 1$. For each of those three states, the tension, shear force, and flexural moment distributions along the cable are analyzed so as to point out the influence of the flexural rigidity throughout a comparison of the results with those obtained using the standard model that neglects the flexural stiffness.

5.1. Horizontal cable subject to an upward vertical load

The first case is that of a horizontal cable, shown in Figure 2, subject to an upward vertical load, distributed over a small region centered about the midspan whose length is $\Delta s = 0.1873 \eta^0$. The nondimensional load amplitude is varied in the range $[0.03, 12]$. Because the force per unit reference length has been nondimensionalized with respect to mg/γ , and $\gamma = 1.5$; the maximum load is $f_{N_L} = 8 mg$ and the resultant load becomes $F = 8 mg(\Delta s \ell)$, which is about $3/2 W$, where $W = mgL^0$ is the total weight of the cable. The loading process is discretized into $N_L = 400$ load steps with a resulting load step $\Delta f = 0.02993$.

The response curve in Figure 2 shows a softening behavior of the cable control point in both models. We further note that the curve representing the model with flexural stiffness is globally above the curve obtained with the standard cable model as it is to be expected since the cable with flexural stiffness is clearly stiffer than the purely extensible cable. This difference in behaviors is exhibited neither at the beginning nor at the end of the loading path whereas

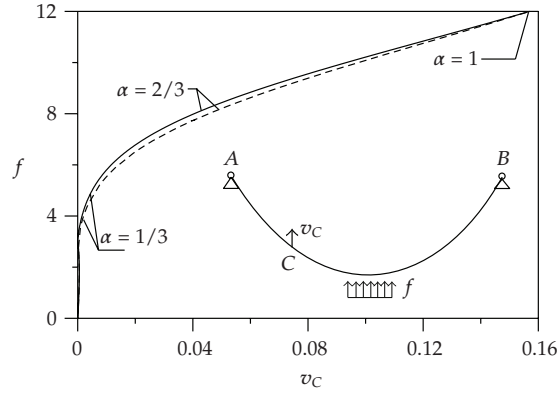


Figure 2: Response curves of the horizontal cable: variation of the vertical displacement of the control point C with the load magnitude obtained with the flexural stiffness (solid line) and without (dashed line).

the most prominent difference is appreciated when $\alpha = 2/3$, that is, when the upward load is nearly equal the weight of the cable.

Figure 3 shows the cable configurations at various load magnitudes, the initial static configuration \mathcal{B}^0 (catenary configuration), two intermediate configurations \mathcal{B} when $\alpha = 1/3$ ($F \simeq 1/2W$) and $\alpha = 2/3$ ($F \simeq W$) and the final configuration at the maximum load ($F \simeq 3/2W$). A region of negative curvatures is localized around the subdomain where the load is applied upward. In particular, when the load is between W and $3/2W$, the cable crosses the horizontal line passing through the supports and the extent of the central segment of the cable lifted above the horizontal line gradually increases up to the end of the loading path when it is nearly one third of the cable. At two thirds of the maximum load, the difference introduced by the flexural stiffness is quite remarkable especially if we consider the displacement of the midspan point around which we note appreciably different curvatures, sharper in the purely extensible cable. In Figure 4 (top), we show the tension along the cable whose evolution has two distinct phases. First, the application of the load tends to decrease uniformly the total tension in the cable until the load reaches a sufficient value to overcome the weight of the cable in the central region. At this stage, the curvature is reversed at the midspan and the tension gradually starts to exhibit sharp decreasing variations thus introducing a lack of uniformity of distribution. While at the midspan section the curvature (and the bending moment) increases, the tension tends to vanish; on the other hand, around the midspan, the tension has to balance part of the total weight of the cable. Concurrently, the shear load exhibits a boundary layer within the central loaded region, and the magnitude of the jump increases with the load amplitude. At the peak of the loading path, the bending moment is clearly localized within the central boundary layer with the peak moment being one order of magnitude higher than elsewhere in the cable.

5.2. Horizontal and inclined cables subject to support displacements

The right end boundary of the horizontal cable is moved horizontally to the left up to a nondimensional value of $u_B = 0.808$ (i.e., a dimensional displacement of the considered cable

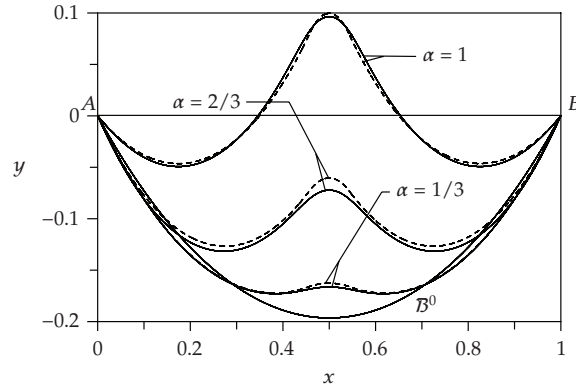
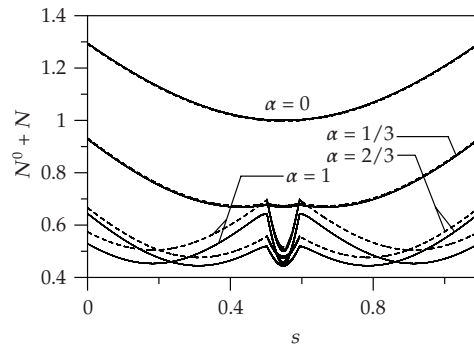
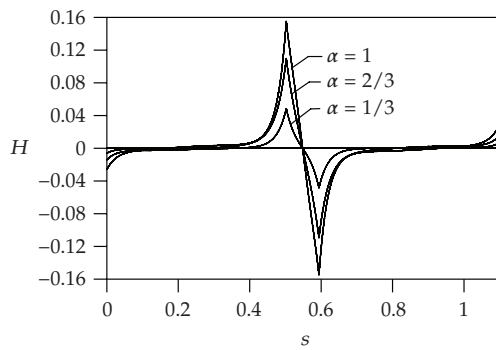


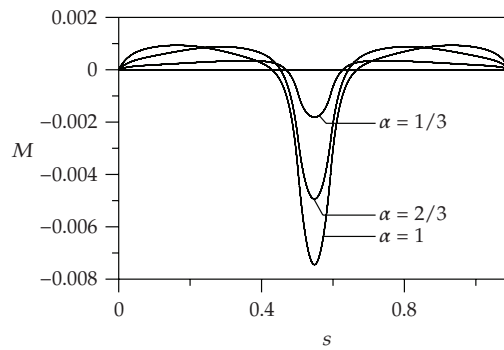
Figure 3: Cable configurations under an upward vertical load obtained with the flexural stiffness (solid lines) and without (dashed lines).



(a)



(b)



(c)

Figure 4: Tension (top), shear force (middle), and bending moments (bottom) of the cable under an upward vertical load obtained with the flexural stiffness (solid lines) and without (dashed lines).

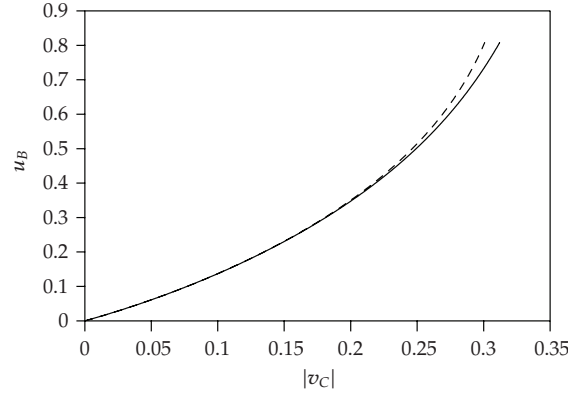


Figure 5: Response curves of the horizontal cable: variation of the vertical displacement of the control point C with the support displacement obtained with the flexural stiffness (solid line) and without (dashed line).

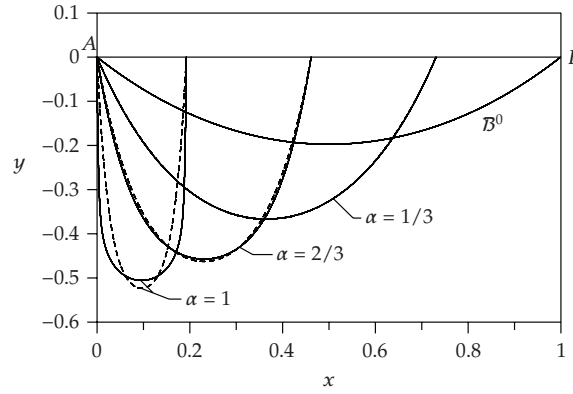


Figure 6: Cable configurations under a prescribed displacement of the support.

of 105 m) in $N_L = 1050$ steps. Figure 5 shows the response curve with the prescribed displacement u_B on the vertical axis and the displacement of the control point C on the abscissa axis. Besides, Figure 6 presents the configurations of both cables, with and without flexural stiffness, at the three load steps ($\alpha = 1/3, 2/3, 1$) and Figure 7 reports the associated tension, shear force, and bending moment.

During the whole loading path, a decrease of tension and an increase of shear force and bending moment are observed in the central region as the two boundaries are brought closer; further, as in the first loading scenario, the decrease becomes even more remarkable when the curvature is increasing. At the end of the loading path, the central region presents a tension that is almost close to zero bringing the cable close to a total loss of tension. Further, the shear force at the boundaries is appreciable. We also note that, as it has already been pointed out in previous studies, the standard model of purely extensible cables generates numerical instabilities when the tension levels are too low while the consideration of flexural

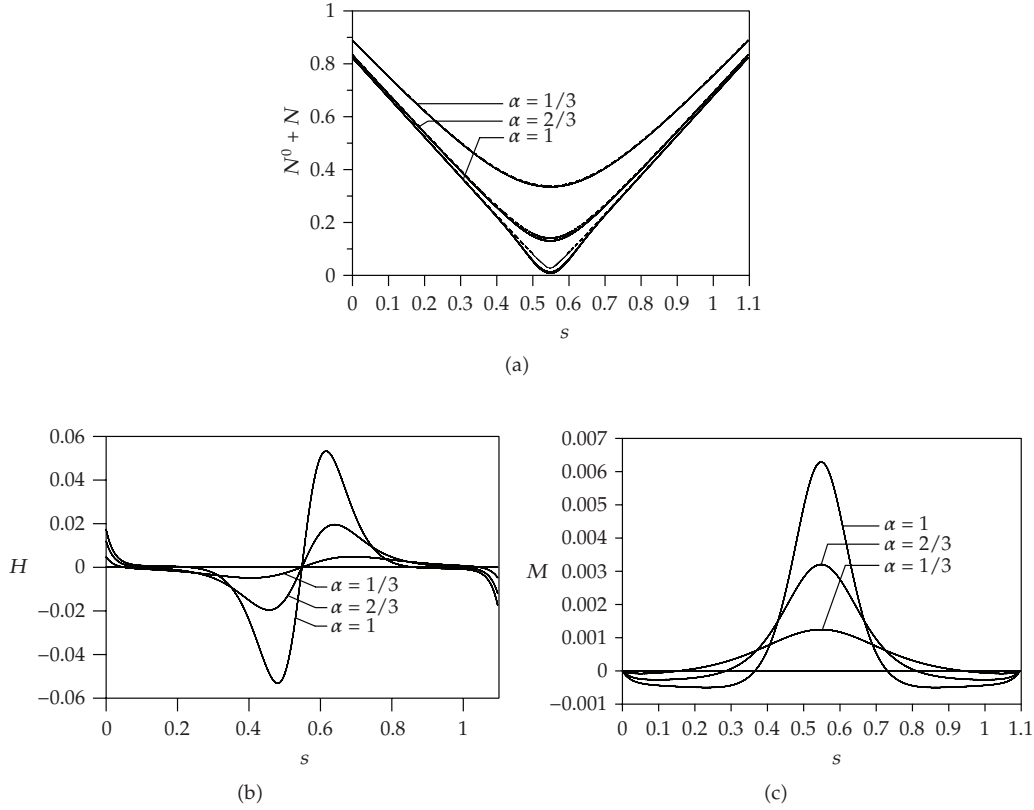


Figure 7: Tension (top), shear force (middle), and bending moments (bottom) of the cable subject to displacements of the support obtained with the flexural stiffness (solid lines) and without (dashed lines).

stiffness overcomes this problem. Moreover, the close observation of the differences in the configurations exhibited by the two cables reveals that the flexural stiffness has an appreciable influence on the equilibrium configuration even in the static regime, and points out the fact that it cannot be neglected in those segments of the cable where the tension is very low.

To quantify the differences in the state of stress, let us now consider the midspan section when $\alpha = 1$, and let $S = N/A^0$ denote the maximum tensile stress for the cable without flexural stiffness, and let $\bar{S} = \bar{N}/A^0 + \bar{M}/W_f^0$ be the tensile stress of the cable with flexural stiffness (where $W_f^0 = J^0/\sqrt{A/\pi}$ is the cable bending modulus). Calculating the relative percent difference between \bar{S} and S yields a value about 53% which indicates that we would be led to underestimate the maximum tensile stress by the same amount with the standard cable model.

In the last loading scenario, the right support of the inclined cable is moved horizontally to the left up to a nondimensional value of $u_B = 0.769$ (i.e., a dimensional displacement of the considered cable of 100 m) in $N_L = 1000$ steps. Figure 8 shows the response curves whereas Figure 9 presents the configurations of both cables, with and without flexural stiffness, at the three load steps ($\alpha = 1/3, 2/3, 1$), and Figure 10 reports the associated tension, shear force, and

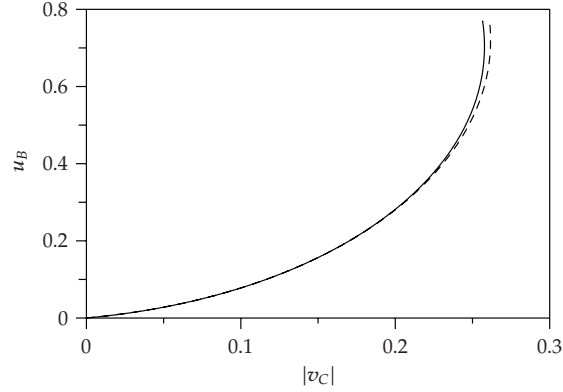


Figure 8: Response curves of the inclined cable: variation of the vertical displacement of the control point C with the support displacement obtained with the flexural stiffness (solid line) and without (dashed line).

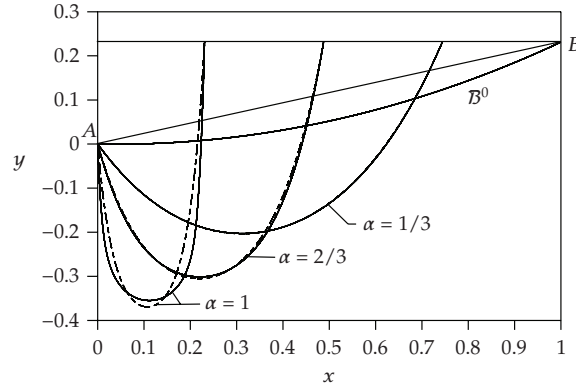


Figure 9: Cable configurations under a prescribed displacement of the support.

bending moment. This case is very similar to that of the horizontal cable although this cable is shallow and quite taut. The final maximum curvature is smaller than in the other case while the final lowest tension is bigger. It has to be noticed that, in this case, the most stressed region, on consideration of the shear force and flexural moment, is more shifted to the left due to the evident asymmetry of the problem.

6. Natural frequencies of cables with flexural stiffness

This section discusses concisely the vibration behavior of cables without flexural stiffness, in shallow and nonshallow regimes, with respect to the behavior of cables with flexural stiffness. To this end, variations of the lowest natural frequencies with Irvine's parameter λ are here reported. In Irvine's theory of shallow cables and in the generalized theory described in [5], the free motions of cables only depend on the two parameters (γ, λ) which completely

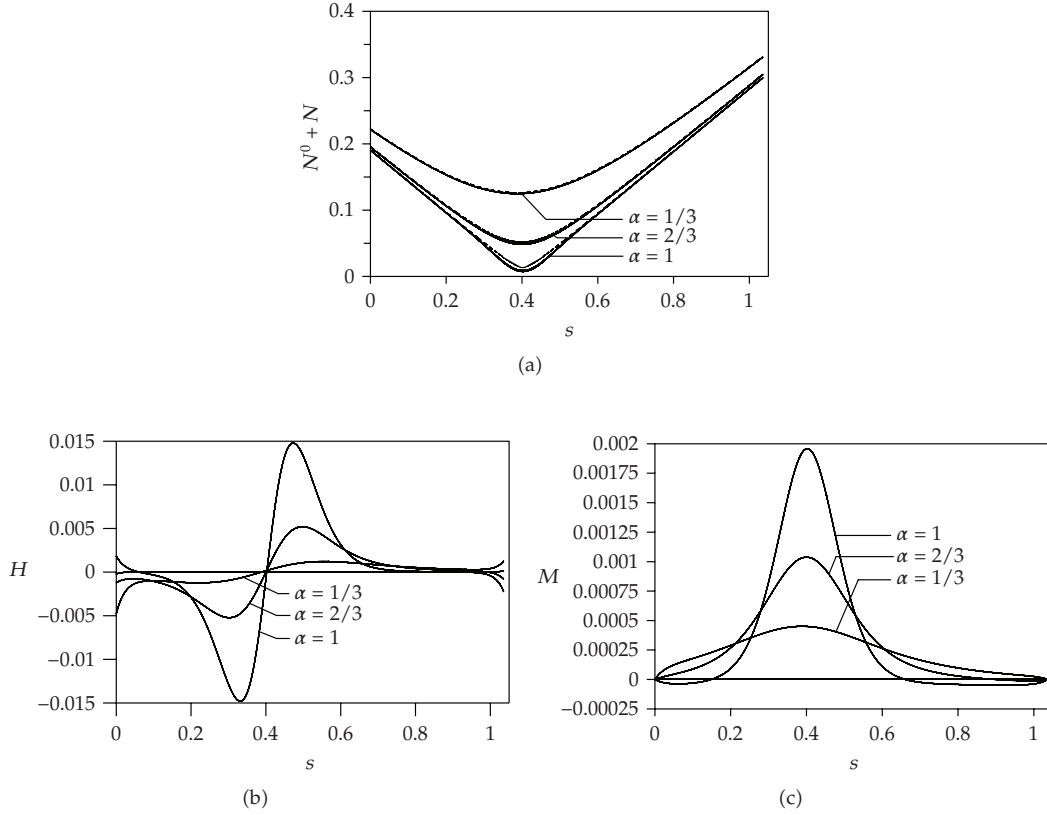


Figure 10: Tension (top), shear force (middle), and bending moments (bottom) of the cable subject to displacements of the support obtained with the flexural stiffness (solid lines) and without (dashed lines).

characterize the geometric and elastic properties of linearly elastic cables. Taking into account the flexural stiffness introduces a new elastogeometric parameter, Λ . In Figure 11, variations of the lowest natural frequencies with λ/π are shown as obtained with the two relevant models, with incorporation of the flexural stiffness (solid lines) and without flexural stiffness (dashed lines). We consider three different regimes: shallow cables with $\gamma = 0.1$, transition cables with $\gamma = 0.75$, and nonshallow cables with $\gamma = 1.5$. In Figure 11 (top), in the case of shallow cables ($\gamma = 0.1$), differences between the two models are not easily detectable except mild differences for $\lambda > 0.7\pi$. On the other hand, for nonshallow cables ($\gamma = 1.5$), we clearly observe a deviation of the loci of the eigenfrequencies to higher values with increasing λ . As a matter of fact, flexural stiffness effects are expected to be more significant for cables with larger cross-section areas, that is, in our case, those corresponding to larger values of λ . Here, the assumed data are γ (that defines the geometric stiffness) and E , Young's modulus. At the same time, higher modes present a number of curvature variations, hence a number of nodes, greater than the lower modes so that the flexural rigidity is expected to impact the frequencies of the higher modes as it can be seen in Figure 11. Furthermore, the increase of the natural frequencies due to the flexural stiffness effects do not seem to generate new crossovers.

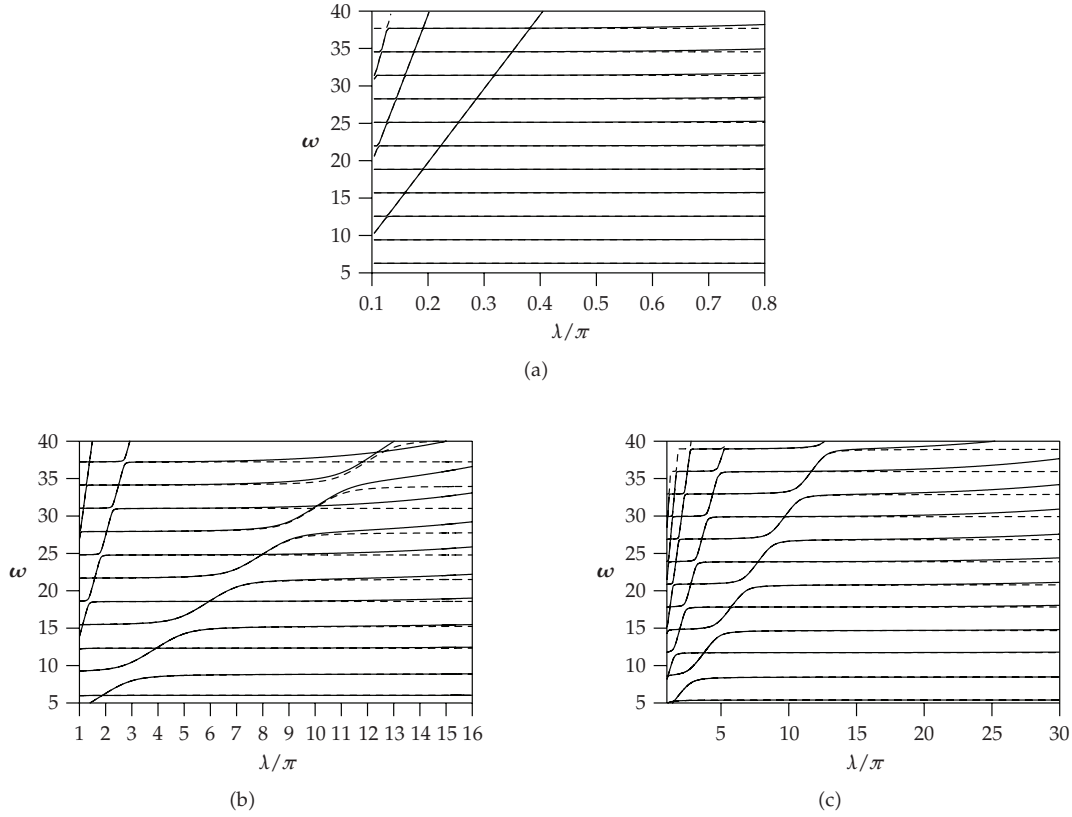


Figure 11: Variation of the lowest natural frequencies with λ/π obtained with the flexural stiffness (solid lines) and without (dashed lines) when $\gamma = 0.1, 0.75, 1.5$, respectively.

7. Concluding remarks

A geometrically exact formulation of cables undergoing axis stretching and flexural curvature has been proposed. The model, in its general form, is suitable to treat more general cable regimes, such as the loosening regime whereby a local loss of tension occurs.

The equations of motion have been formulated for cables with nonlinearly viscoelastic constitutive laws and general loading conditions. The particular case of cables with a linearly elastic constitutive law has been then considered in the numerical calculations conducted on horizontal and inclined cables by employing a path-following scheme with two different discretizations: a finite-difference approach and a finite element formulation. In particular, low-tension regimes have been investigated, and the flexural stiffness influence on shallow and nonshallow cable behaviors has been studied outlining its importance in the structural response in the mentioned low-tension regime.

The most remarkable loading case, presented in this paper, is relative to a displacement of the right support moved toward the left support. It has been shown that an underestimation of the maximum tensile stress of about 50% would be reached were we to employ the crude model of purely extensible cables. Although the probability of such a phenomenon is

low in civil engineering applications since the displacements are expected to be small, the extreme scenarios here reproduced can certainly concern mooring cables or cables in tethered space applications. In addition, consideration of the flexural stiffness is important to correctly evaluate the fatigue life of cables.

Modeling linearly elastic cables with flexural stiffness has led to a new independent parameter, denoted Λ , which represents the ratio between the flexural and the geometric stiffnesses. The presence of flexural stiffness modifies the loci of the higher frequencies at higher stiffnesses, especially in nonshallow cables.

More in-depth investigations are needed to correctly unfold the cables behavior near instabilities or in the fully developed post-critical scenarios (galloping, parametric resonance, ..., etc.) whereby loosening phenomena and nonlinear viscoelasticity within the boundary layers are expected to play a critical role on the response.

Appendix

The static configuration \mathcal{B}^0

The static configuration under the cable own weight is obtained integrating (2.8) with the inextensibility constraint $\nu^0 = 1$ which yields $\sigma = s$. By introducing the following nondimensional variables and parameters:

$$\gamma = \frac{mg\ell}{H^0}, \quad \beta = \frac{mg\ell}{V^0}, \quad (\text{A.1})$$

and integrating the equilibrium equations yields

$$\begin{aligned} x(s) &= \frac{1}{\gamma} \left[\sinh^{-1} \left(\frac{\gamma}{\beta} + \gamma s \right) - \sinh^{-1} \left(\frac{\gamma}{\beta} \right) \right], \\ y(s) &= \frac{1}{\gamma} \left[\sqrt{1 + \left(\frac{\gamma}{\beta} + \gamma s \right)^2} - \sqrt{1 + \left(\frac{\gamma}{\beta} \right)^2} \right], \end{aligned} \quad (\text{A.2})$$

where H^0 is the horizontal projection of the tension at the left support, the star was dropped, and \sinh^{-1} denotes the inverse function of \sinh . The boundary conditions give two transcendental equations in the unknowns γ and β . For instance, for horizontal cables, the compatibility condition becomes

$$\eta^0 \frac{\gamma}{2} = \sinh \left(\frac{\gamma}{2} \right). \quad (\text{A.3})$$

Typically, η^0 is known (the initial cable length as well as the span), hence the compatibility equation is solved for γ . On the other hand, in the case of inclined cables, imposing the boundary conditions yields the following transcendental equations:

$$\begin{aligned} \sqrt{1 + \left(\frac{\gamma}{\beta} + \gamma \eta^0 \right)^2} - \sqrt{1 + \left(\frac{\gamma}{\beta} \right)^2} &= \frac{\gamma h}{\ell}, \\ \frac{1}{\gamma} \left[\sinh^{-1} \left(\frac{\gamma}{\beta} + \gamma \eta^0 \right) - \sinh^{-1} \left(\frac{\gamma}{\beta} \right) \right] &= 1. \end{aligned} \quad (\text{A.4})$$

Acknowledgment

This work was partially supported by an FY 2005-2006 PRIN Grant from the Italian Ministry of Education, University and Scientific Research.

References

- [1] H. M. Irvine, *Cables Structures*, Dover, New York, NY, USA, 1984.
- [2] A. Luongo, G. Rega, and F. Vestroni, Planar nonlinear free vibrations of an elastic cable, *International Journal of Non-Linear Mechanics*, vol. 19, no. 1, pp. 3952, 1984.
- [3] G. Rega, W. Lacarbonara, A. H. Nayfeh, and C. M. Chin, Multiple resonances in suspended cables: direct versus reduced-order models, *International Journal of Non-Linear Mechanics*, vol. 34, no. 5, pp. 901924, 1999.
- [4] G. Rega, Nonlinear vibrations of suspended cables—part II: deterministic phenomena, *Applied Mechanics Reviews*, vol. 57, no. 6, pp. 479514, 2004.
- [5] W. Lacarbonara, A. Paolone, and F. Vestroni, Elastodynamics of nonshallow suspended cables: linear modal properties, *Journal of Vibration and Acoustics*, vol. 129, no. 4, pp. 425433, 2007.
- [6] W. Lacarbonara, A. Paolone, and F. Vestroni, Nonlinear modal properties of non-shallow cables, *International Journal of Non-Linear Mechanics*, vol. 42, no. 3, pp. 542554, 2007.
- [7] J. J. Burgess, Bending stiffness in a simulation of undersea cable deployment, *International Journal of Offshore and Polar Engineering*, vol. 3, no. 3, pp. 197204, 1993.
- [8] M. S. Triantafyllou and C. T. Howell, Dynamic response of cables under negative tension: an ill-posed problem, *Journal of Sound and Vibration*, vol. 173, no. 4, pp. 433447, 1994.
- [9] Y. Sun and J. W. Leonard, Dynamics of ocean cables with local low-tension regions, *Ocean Engineering*, vol. 25, no. 6, pp. 443463, 1998.
- [10] Y. Q. Ni, J. M. Ko, and G. Zheng, Dynamic analysis of large-diameter sagged cables taking into account flexural rigidity, *Journal of Sound and Vibration*, vol. 257, no. 2, pp. 301319, 2002.
- [11] Y. T. Chai, K. S. Varyani, and N. D. P. Barltrop, Three-dimensional Lump-Mass formulation of a catenary riser with bending, torsion and irregular seabed interaction effect, *Ocean Engineering*, vol. 29, no. 12, pp. 15031525, 2002.
- [12] Q. Wu, K. Takahashi, and S. Nakamura, The effect of cable loosening on seismic response of a prestressed concrete cable-stayed bridge, *Journal of Sound and Vibration*, vol. 268, no. 1, pp. 7184, 2003.
- [13] Q. Wu, K. Takahashi, and S. Nakamura, Nonlinear vibrations of cables considering loosening, *Journal of Sound and Vibration*, vol. 261, no. 3, pp. 385402, 2003.
- [14] Q. Wu, K. Takahashi, and S. Nakamura, Nonlinear response of cables subject to periodic support excitation considering cable loosening, *Journal of Sound and Vibration*, vol. 271, no. 1-2, pp. 453463, 2004.
- [15] Q. Wu, K. Takahashi, and B. Chen, Influence of cable loosening on nonlinear parametric vibrations of inclined cables, *Structural Engineering & Mechanics*, vol. 25, no. 2, pp. 219237, 2007.
- [16] S. S. Antman, *Nonlinear Problems of Elasticity*, vol. 107 of *Applied Mathematical Sciences*, Springer, New York, NY, USA, 2nd edition, 2005.
- [17] L. Fox, *The Numerical Solution of Two-Point Boundary Problems in Ordinary Differential Equations*, Oxford University Press, New York, NY, USA, 1957.
- [18] MATHEMATICA, 2007, Wolfram Research Inc., Urbana Champaign, Ill, USA.
- [19] COMSOL, 2005, Comsol Multiphysics Inc., Stokholm, Sweden.

Research Article

Probabilistic and Fuzzy Arithmetic Approaches for the Treatment of Uncertainties in the Installation of Torpedo Piles

Denise Margareth Kazue Nishimura Kunitaki,^{1,2} Beatriz Souza Leite Pires de Lima,² Alexandre Gonçalves Evsukoff,² and Breno Pinheiro Jacob^{1,2}

¹Laboratory of Computer Methods and Offshore Systems (LAMCSO), Civil Engineering Department, COPPE/UFRJ-Postgraduate Institute of the Federal University of Rio de Janeiro, 21945-970 Rio de Janeiro, RJ, Brazil

²COPPE/UFRJ, Civil Engineering Department, Centro de Tecnologia Bloco B sala B-101, Cidade Universitária, Ilha do Fundão, Caixa Postal 68.506, 21945-970 Rio de Janeiro, RJ, Brazil

Correspondence should be addressed to Breno Pinheiro Jacob, breno@coc.ufrj.br

Received 2 December 2007; Accepted 27 March 2008

Recommended by Paulo Gonçalves

The “torpedo” pile is a foundation system that has been recently considered to anchor mooring lines and risers of floating production systems for offshore oil exploitation. The pile is installed in a free fall operation from a vessel. However, the soil parameters involved in the penetration model of the torpedo pile contain uncertainties that can affect the precision of analysis methods to evaluate its final penetration depth. Therefore, this paper deals with methodologies for the assessment of the sensitivity of the response to the variation of the uncertain parameters and mainly to incorporate into the analysis method techniques for the formal treatment of the uncertainties. Probabilistic and “possibilistic” approaches are considered, involving, respectively, the Monte Carlo method (MC) and concepts of fuzzy arithmetic (FA). The results and performance of both approaches are compared, stressing the ability of the latter approach to efficiently deal with the uncertainties of the model, with outstanding computational efficiency, and therefore, to comprise an effective design tool.

Copyright © 2008 Denise Margareth Kazue Nishimura Kunitaki et al. This is an open access article distributed under the Creative Commons Attribution License, which permits unrestricted use, distribution, and reproduction in any medium, provided the original work is properly cited.

1. Introduction

1.1. Context: offshore platforms, mooring systems, and anchors

Petroleum companies around the world have been faced with the challenge of developing offshore oil production activities in deep and ultradeep waters. In shallow water, the traditional solution consists in employing platforms supported by fixed framed structures, such as the

jackets where the foundation system consists of driven piles [1]. Presently, as oil fields have been identified in deeper water such as in the Campos Basin (southeastern Brazil), offshore platforms have included several types of floating units, such as the *semisubmersible* platforms, the *tension-leg platforms* (TLPs), and *floating production, storage, and offloading* (FPSOs) units based on ships.

Floating platforms can be maintained in position by different types of mooring systems, which in turn may employ anchors based on different types of foundation elements. Semisubmersible platforms and FPSO units, for instance, may be kept in position by mooring lines in *catenary* or *taut-leg* configurations. Mooring lines in a free-hanging catenary configuration transmit essentially horizontal loads to the foundation system. This fact introduces a greater flexibility in the selection of the appropriate anchor type. However, the mooring radius (the horizontal distance, measured at the sea bottom, from the center of the platform) is relatively large; typically, about two to three times the water depth. Therefore, the application of catenary configurations may not be feasible in deep or ultradeep waters, due to the increased weight of the mooring lines, and also due to installation problems that may arise in congested scenarios with several platforms close together (as is the case of some oil fields in the Campos Basin).

The taut-leg configuration has been proposed to tackle these constraints. This configuration, where the lines are not slack, allows the use of smaller line lengths. When associated with the use of new materials (such as polyester fiber ropes) [2], this leads to considerable reduction in the weight of the mooring system. Moreover, since at the anchor point the lines are not in contact with the seabed, and may reach inclinations around 45° , the mooring radius is typically equal to the water depth, therefore, considerably shorter than in catenary configurations.

However, taut-leg mooring systems transmit vertical loads to the foundation system. This is also the case with the tension leg platforms, which are moored by vertical tendons. Therefore, care should be taken in the selection of anchor types that can withstand vertical loads.

Amongst the foundation elements that have been applied in deep water systems, two types of anchors can be mentioned: the *suction anchor* and the *vertically loaded anchor* (VLA) [3]. However, some installation difficulties have been reported for suction anchors, due to added mass effects and the resonant period for the lifting system at the installation depth that may approach the dominant wave period at the site [4]. Vertically loaded anchors are easier to install, but require drag procedures that may hinder their correct positioning, mainly in congested areas with many others nearby platforms.

1.2. The torpedo pile

The *torpedo pile* (illustrated in Figure 1) was proposed [5] as a solution to withstand vertical loads while circumventing the problems associated with other types of anchors. It consists simply in a metallic pipe, with closed tip, filled with scrap chain, and concrete [6].

The installation does not require drag procedures such as employed in VLAs; the procedure is quite simple, and is illustrated in Figure 2. First, the installation vessel hangs the pile (connected to the mooring line) at a specified drop height, above the target point on the seabed. The design embedment is then reached by simply releasing the pile, letting it accelerate, fall freely, and then penetrate into the soil.



Figure 1: Torpedo pile.

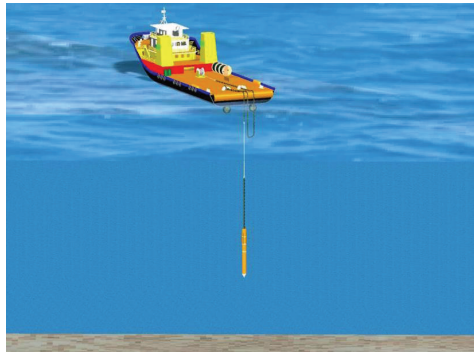


Figure 2: Installation of torpedo pile [5].

More than one hanging configuration has been conceived, for instance, one of the alternatives (considered for the installation of torpedo piles to anchor flexible risers or *mobile drilling units* (MODUs)) has a chain loop at the top of the installation line, as shown in Figure 3. As the pile falls, this loop is pulled and unfolded. Therefore, the torpedo pile presents not only low cost of manufacture, but also low cost of installation, since the same vessel can transport and install the pile.

There is another configuration, for permanent mooring of production units, which does not present the chain loop, but requires two vessels to hang, respectively, the installation line and the mooring line (to which the torpedo pile is connected). In this configuration, the bottom end of the installation line is connected to an intermediate point of the mooring line, therefore, maintaining the pile suspended at the desired drop height. Above this connection point, there is a trigger that allows the mooring line and the pile to be released, causing the pile to fall (dragging with it the mooring line), and penetrate the soil.

Another advantage of the torpedo pile concept is that, since it can withstand horizontal and vertical loads, it can be used with mooring lines in a taut-leg configuration that, as mentioned before, is the preferred alternative for semisubmersible platforms and FPSO units in deeper waters and congested scenarios.

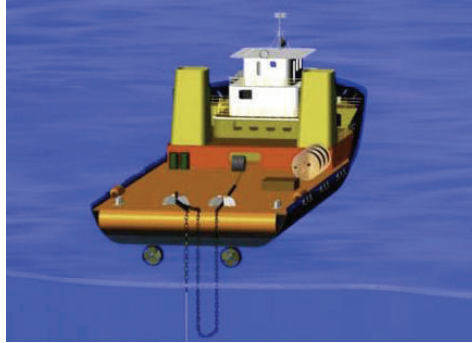


Figure 3: Chain loop [6].

1.3. Objective of the paper

The design of a torpedo pile should employ theoretical models to predict pile penetration depth, such as the dynamic penetration model proposed by True [7]. This model relies on soil parameters whose values are assumed as known, fixed, and deterministic.

However, it is well known that the soil properties present a significant degree of variability that, associated to imprecisions in the determination of their design values, can affect the accuracy of the response given by the simulation method. The objective of this paper, therefore, is to study techniques to deal with the uncertainty of the soil parameters, and to associate these techniques to an analytical/numerical penetration model for the torpedo pile.

Two different approaches are considered for the treatment of uncertainties of the penetration model. The first is a probabilistic approach, based on the classical Monte Carlo method. The second is a “possibilistic” approach, derived using concepts from *fuzzy arithmetic* and fuzzy sets.

The following sections of the paper begin by describing the theoretical model and solution procedure considered for the simulation of the pile penetration. Firstly, the analytical formulation originally presented by True [7] is described; then a numerical solution procedure in the time domain is described, followed by an application where a pile dropped from a height of 200 m above the seabed is analyzed for deterministic, fixed values of the soil parameters.

The paper then proceeds by describing the soil parameters that are considered uncertain. Methodologies to assess the sensitivity of the response to the variation of these uncertain parameters are then presented, based on the Monte Carlo method (MC) and fuzzy arithmetic (FA). More important, such methodologies allow the designer to incorporate, into the analysis method, techniques for the formal treatment of these uncertainties.

Finally, results of applications of these concepts for the treatment of uncertainties are presented for an actual case study, beginning with results of deterministic parametric studies in order to assess the sensitivity of the response to the variation of the uncertain parameters. Results for the “probabilistic” MC approach are then presented, followed by the novel implementation and application of the approach based on FA. The results and performance of both approaches are compared, stressing the ability of the latter approach to efficiently deal with the uncertainties of the model, with outstanding computational efficiency, and therefore, to comprise an effective design tool.

2. The Penetration Model

2.1. Original formulation: penetration of projectiles

Studies on the behavior of penetration of projectiles were initially intended for military applications [8] and were followed by studies on the prediction of final embedment depth of projectiles into soils [9, 10], and estimation of undrained shear strength [11, 12].

The development of a dynamic penetration model by the US navy was required to represent the penetration of propellant-embedded plate anchors into seafloor soils [13]. This kind of anchor is directly positioned on the mud line and an explosion, caused by the propeller system, pushes the anchor fluke down. In order to fulfill this objective, True [7] took into account recommendations given by authors of empirical models (such as Young [9]) and modified traditional bearing capacity formulations (for deep foundations in cohesive soils) to consider variations in penetration resistance with velocity and penetrator shape.

The analytical model developed in [7] to simulate the dynamic penetration of plate anchors is based on Newton's second law. Considering that the penetrator velocity v can be expressed as $v = dz/dt$ (where z stands for the soil depth), and therefore, its acceleration dv/dt can be expressed as $(dv/dz)(dz/dt)$, the governing equation can be written as follows:

$$M' \frac{dv}{dz} v = W_s - F_D - F_T - F_S + F_E, \quad (2.1)$$

where M' is the effective mass of the penetrator, given by

$$M' = M + 2\rho \cdot V. \quad (2.2)$$

In this latter equation, M and V are, respectively, the structural mass and the volume of the penetrator, and ρ is the mass density of the soil. It can be seen that the term $2\rho V$ is similar to the "added mass" term of the Morison equation [14], which has been traditionally employed to calculate hydrodynamic drag and inertia loads on cylinders immersed in fluid. In the present case, when multiplied by the acceleration at the left-hand side of (2.1), the term $2\rho V$ introduces an additional inertia force that corresponds to the contribution of the soil in which the penetrator is immersed.

The forces in the right-hand side of (2.1) are W_s (the submerged weight of the penetrator); F_D , F_T , and F_S (which are, resp., the drag force, the tip resistance, and the side resistance); and F_E (the external driving force applied by the propeller system).

The submerged weight W_s is defined in terms of the weight in air W , volume V , and the unit weight of soil γ by the following expression:

$$W_s = W - V \cdot \gamma. \quad (2.3)$$

The drag force F_D is similar to the longitudinal drag component given by Morison's equation [14], which is expressed as:

$$F_D = \frac{1}{2} \cdot v \cdot |v| \cdot A_f \cdot C_D \cdot \rho, \quad (2.4)$$

where A_f is the frontal or cross-sectional area of the penetrator and C_D is the empirical drag coefficient, that can have the value of 0.7 as proposed by True according to [13].

The classic formulation for *static* bearing capacity of deep pile foundation states that, for undrained conditions, the tip resistance Q_T and side resistance Q_S [15] are defined by

$$\begin{aligned} Q_T &= Su \cdot N_c \cdot A_f, \\ Q_S &= Su \cdot \alpha \cdot A_s, \end{aligned} \quad (2.5)$$

where Su is the undrained soil shear strength; N_c is the bearing capacity factor (assumed equals to 9 for homogeneous clay); α is the dimensionless side adhesion factor; and A_f and A_s are, respectively, the frontal and lateral areas of the pile.

The dynamic tip and side resistance F_T and F_S are now considered by the inclusion, in this classic static formulation, of a *side adhesion reduction factor* δ , a *soil strain rate factor* $S_{\dot{\epsilon}}$, and the *soil sensitivity value* Sti . The latter represents the loss of shear strength that clays suffer when remolded, and is defined as the ratio of undisturbed and remolded strengths [16]. Thus, the tip resistance F_T and side resistance F_S are defined by the following expressions:

$$\begin{aligned} F_T &= Su \cdot N_c \cdot A_f \cdot S_{\dot{\epsilon}}, \\ F_S &= \frac{Su \cdot A_s \cdot \delta}{Sti} \cdot S_{\dot{\epsilon}}. \end{aligned} \quad (2.6)$$

Values for the side adhesion reduction factor δ were determined in [17] based on results of model tests. An expression for the strain rate factor $S_{\dot{\epsilon}}$ was also defined in [17], as a function of the velocity v and the diameter (or thickness) of the penetrator d , the undrained soil shear strength Su , and other empirical parameters. This expression can be written as

$$S_{\dot{\epsilon}} = \left(\frac{S_e}{1 + \left(1/\sqrt{(C_e \cdot v/Su \cdot d) + C_0} \right)} \right). \quad (2.7)$$

Values for the empirical parameters S_e (maximum soil strain rate at high velocity values), C_e (strain rate velocity factor), and C_0 (strain rate constant) were also determined in [17] based on results of model tests.

In the penetration model considered for offshore applications in the Campos Basin [5], the undrained shear strength Su of the soil is assumed to vary linearly with depth z , according to the following expression:

$$Su(z) = Su_0 + Su_k \cdot z, \quad (2.8)$$

where Su_0 is the undrained shear strength at the mudline; and Su_k is the rate of increase with depth.

Original solution procedure

To solve (2.1), True [7] developed an incremental finite-difference algorithm and considered that the penetrator is a point object at the i th depth increment, thus some simplifications could be made:

$$M' \cdot v_i \cdot \frac{v_{i+1} - v_{i-1}}{2\Delta z} = W_s - F_D - F_T - F_S. \quad (2.9)$$

Substituting the expressions for M' , F_D , F_T , F_S , and W_s in (2.9), ignoring the external driving force F_E , and assuming $C_0 = 0.06$ (according to [7]), the following expression is obtained, which can be applied repeatedly to obtain the velocities of the penetrator at each depth increment Δz :

$$v_{i+1} = v_{i-1} + \frac{2\Delta z}{v_i(M + 2\rho_i V)} \cdot \left((W - V\gamma_i) - \left(\frac{1}{2}v_i^2 A_f C_D \rho_i \right) - \text{Su}_i \left(A_f N_c + \frac{A_s \delta}{\text{Sti}} \right) \right) \cdot \left(\frac{S_e}{1 + \left(1/\sqrt{(C_e v_i / \text{Su}_i d) + 0.06} \right)} \right). \quad (2.10)$$

The final penetration depth can then be seen as the product of the depth increment Δz by the number of the increment for which the penetrator velocity drops to zero. It should be recalled that, as in any numerical solution procedure, the accuracy of the results also depends on the careful selection of the depth increment. This will depend on the particular example that is analyzed, and may also involve the use of different increment values to assess the convergence to an accurate solution.

2.2. Formulation for free-falling pile

A free-falling cylindrical penetrometer, dropped from a given height above the mudline, is studied in [12] for the prediction of penetration depth and undrained shear strength. Equation (2.1), with some modifications, is also applied to describe the movement of this penetrometer. Firstly, since it is free falling and there is no external driving force, the term F_E is omitted. Also, the added mass in (2.2) is considered negligible for slender penetrometers moving along their long axis, thus, the effective mass is equal to the structural mass ($M' = M$). Therefore, also replacing the velocity v by dz/dt and considering that the acceleration a is equal to $(dv/dz)(dz/dt)$, (2.1) becomes

$$Ma = W_s - F_D - F_T - F_S. \quad (2.11)$$

Obviously, torpedo piles behave similarly to the free-falling penetrometers, therefore, their motions can also be described by the True formulation [7], with the same considerations as employed in [12], resulting in (2.11). Moreover, the traditional Morison hydrodynamic formulation can also be applied to describe the forces acting in the pile while it is still in the water, before reaching the seabed, and the same submerged weight can be assumed for both media.

It should be emphasized that such semiempirical formulations incorporate some assumptions, which in turn leads to uncertainties in the model. However, as mentioned in the introduction, this work is focused on the influence of the uncertainties in selected soil parameters. Studies regarding uncertainties associated with the penetration model itself will be dealt with in future works.

Solution procedure in the time domain

It can be observed that the procedure originally proposed by True [7], as described in (2.9) and (2.10), involved the spatial integration of (2.1) to obtain velocities as functions of depth z . This indeed would be the more natural solution procedure if one is concerned only with the representation of the isolated pile and the natural random variability of the soil parameters with depth. However, as will be commented later, there are other sources of uncertainty to be concerned as well.

Moreover, as will be commented in the final section of this paper, the final goal of the developments presented here is to incorporate the penetration model (including the techniques that will be described later, based on fuzzy arithmetic, for the formal treatment of uncertainties) in a finite element (FE) spatial discretization scheme, associated to a time domain nonlinear dynamic solver. The idea is to model not only the isolated pile, but also all the other components of the system being installed (i.e., the mooring line itself and the other lines and chains involved in the installation procedure), in a complete 3D model submitted to other loadings such as marine current.

With this scenario in mind, it is more convenient to integrate (2.11) in the time domain. At the current stage, where the focus is in modeling an isolated pile and evaluating the uncertainties in the soil parameters, the added mass can still be disregarded as assumed in [12] and in (2.11). In a posterior implementation of the penetration model in a time domain solver associated to the full FE model, the dynamic equations will also incorporate the added mass effects of the complete configuration of the pile with the installation and mooring lines.

The solution in the time domain, in terms of the acceleration a_{n+1} , velocity v_{n+1} , and displacement d_{n+1} , at a given time t_{n+1} , can be accomplished by applying a time-integration algorithm such as the Chung and Lee explicit method [18] that can be stated as:

$$\begin{aligned} M \cdot a_{n+1} &= f_n; & f_n &= W_s - F_D - F_T - F_S, \\ d_{n+1} &= d_n + \Delta t v_n + \Delta t^2 \left((1/2 - \beta) a_n + \beta a_{n+1} \right), \\ v_{n+1} &= v_n + \Delta t \left((1 - \gamma) a_n + \gamma a_{n+1} \right), \end{aligned} \quad (2.12)$$

where β and γ are algorithmic parameters defined as $1 \leq \beta \leq 28/27$, $\gamma = 3/2$; and Δt is the time step, which should not exceed a critical time step (Δt_c) in order to maintain the stability of the numerical solution [18]. The full time domain solution procedure is shown in Algorithm 1. It should also be recalled that the displacements, velocities, and accelerations are positive in the downward direction.

Application

The application of the penetration model described above is now illustrated for a problem also studied in [19], corresponding to a pile dropped from a height of 200 m above the seabed. The pile and soil data are presented in Tables 1 and 2. It should be emphasized that the soil parameters and the sensitivity value of 3 are related to a specific deposit and may not necessarily be representative of general applications.

This application is not intended to represent an actual installation procedure for a torpedo pile (such as the depicted in Figure 2), since, as mentioned before, the current implementation of the penetration model represents only the pile. Therefore, in order to take

(a) Initial calculations	
1. Calculate the torpedo mass M .	
2. Initialize d_0 , v_0 , f_0 , and a_0 , where $a_0 = f_0/M$.	
3. Select the appropriate algorithmic parameter β and time step Δt , $\Delta t \leq \Delta t_c$ and calculate the integration constants, $\beta_1 = \Delta t^2 \left(\frac{1}{2} - \beta \right)$, $\beta_2 = \Delta t^2 \beta$, $\gamma_1 = -\frac{1}{2} \Delta t$, $\gamma_2 = \frac{3}{2} \Delta t$.	
(b) For each time step ($n = 0, 1, \dots, N - 1$).	
1. Calculate the forces, $f_n = W_s - F_D - F_T - F_S$.	
2. Calculate the acceleration at time $t_{n+1} = t_n + \Delta t$, $a_{n+1} = f_n/M$.	
3. Calculate the displacement at time $t_{n+1} = t_n + \Delta t$, $d_{n+1} = d_n + \Delta t v_n + \beta_1 a_n + \beta_2 a_{n+1}$.	
4. Calculate the velocity at time $t_{n+1} = t_n + \Delta t$, $v_{n+1} = v_n + \gamma_1 a_n + \gamma_2 a_{n+1}$.	
5. $n \leftarrow n + 1$, go to (1) of step (b).	

Algorithm 1: Solution procedure in the time domain.**Table 1:** Problem definition: pile data.

W : weight in air	396 kN
W_b : submerged weight	340 kN
d : diameter	0.762 m

Table 2: Problem definition: soil data.

Su_0 : undrained shear strength at the soil surface	5.0 kPa
Su_k : rate of increase with depth	2.0 kPa/m
St_i : sensitivity	3.0
N_c : bearing capacity factor	9.0
δ : side adhesion reduction factor	0.9
S_e : empirical maximum strain rate factor	5.0
C_e : empirical strain rate velocity factor	0.02 kN · s/m ²

into account the increase on drag effects due to the mooring line and chain loop that are not explicitly represented, the model employs a value for the drag coefficient C_D equal to 2.7, larger than the value of 0.7 as proposed by True according to [13]. In future works, which will consider the implementation of a coupled finite element-based, time domain simulation program, there will be no need to perform this “fudging” of the drag coefficient C_D , since the coupled 3D model will explicitly include the complete installation configuration (e.g., the mooring line and chain loop for the application in MODUs described earlier).

The time domain solution considered a total time of 15 seconds (enough, as will be seen, for the pile to fully penetrate the soil). The analysis is performed with a time increment of 0.002 seconds. The value considered for the algorithmic parameter β of the time-integration algorithm is $\beta = 28/27$.

The results are presented in Figure 4, in terms of a graph relating the vertical position of the pile to its velocity, and in Figure 5 in terms of time histories of depth and velocity. The origin

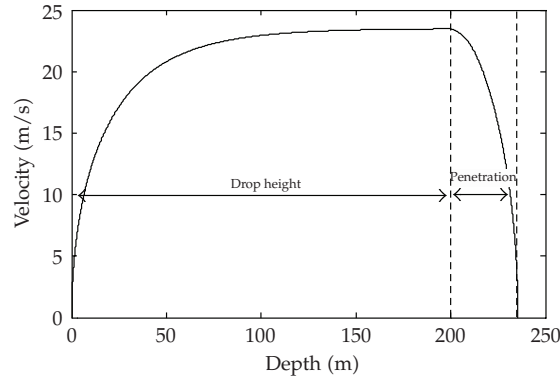


Figure 4: Deterministic pile penetration analysis: depth \times velocity.

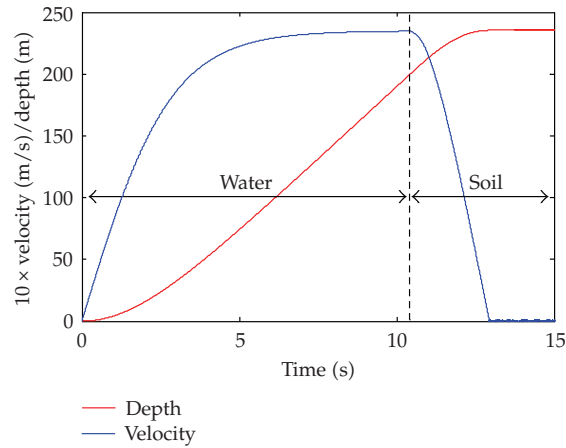


Figure 5: Deterministic pile penetration analysis: time histories.

of the graph of Figure 4 corresponds to the pile in its initial position, before being dropped (therefore, with velocity and displacement equal to zero). It is seen that, as the pile drops in the water, its velocity increases until it nearly reaches the so-called “terminal velocity” due to the water drag (of course, this requires the pile to be released from an appropriate height). As the pile reaches the seabed and begins to penetrate in the soil, the velocity is reduced; when it returns to zero the penetration is completed and the final depth of the pile tip is reached.

3. Uncertainties of The Soil Parameters

Selected parameters

As stated before in (2.8), for cohesive soils in offshore applications in Campos Basin [5], the undrained soil shear strength S_u is assumed to vary linearly with depth z , in terms of S_{u0} (undrained shear strength at the mudline) and of $S_{u\kappa}$ (the rate of increase with depth). For the normally consolidated clay encountered offshore in the Campos Basin [5], typical values that

may be considered for Su_0 and Su_k are, respectively, $Su_0 = 5 \text{ kPa}$ and $Su_k = 2 \text{ kPa/m}$. Therefore, (2.8) could be written as

$$Su(z) = 5 + 2 \cdot z \text{ (kPa)} \quad (3.1)$$

Actual values for these parameters that affect the undrained soil shear strength Su for offshore sites may be obtained from in situ tests (such as CPT—cone penetration tests [20], or vane tests based on a torsion procedure), or from laboratory tests with undisturbed samples, such as triaxial and minivane tests. It should also be recalled that the soil sensitivity Sti represents the loss of shear strength that clays suffer when remolded, and is defined as the ratio of undisturbed and remolded strengths [16]. Remolded strength values can be obtained from vane, triaxial, or minivane tests of disturbed soils.

Thus, it can be seen that values for Su (undrained shear strength) and Sti (sensitivity) are obtained from testing. Traditionally, a deterministic procedure is employed to obtain design values for these parameters, by calculating the average of values obtained from several tests. However, it is known that the results of both in-situ or laboratory tests may be influenced by several factors. The latter tests can be affected by factors such as mechanical disturbance in the soil samples, in the process of extraction and remolding; by changes in the samples during storage, and so forth. In-situ tests can also be affected by mechanical interferences, inadequate execution, and so on.

Therefore, it can be intuitively understood that there is a high degree of local soil variability, and imprecisions in the determination of the design values of these soil parameters. Large variations in the response of the torpedo pile, mainly in terms of the final penetration depth reached by the pile, may be expected due to these uncertainties. The main objective of this paper, then, is to present a methodology to take into account uncertainties and imprecision in the values of input parameters that define the physical and numerical models involved in the design and analysis of torpedo piles.

This work focuses on Su (specifically, the rate of increase with depth Su_k) and Sti . Of course, other parameters (not necessarily related only to the soil) could be considered; however, those can be dealt with in future works.

Sources of uncertainty

Before proceeding further, it is important to recall some basic concepts regarding sources of uncertainty. In soil profile modeling, they may be grouped in two types [21–23]: (1) noncognitive, random natural variability, usually referred as *aleatory* uncertainty; and (2) cognitive or *epistemic* uncertainties, that involve abstraction or subjectivity.

The first group comprises the inherent uncertainty type, due to natural heterogeneity or in-situ variability of the soil, such as varying depths of strata during soil formation, variation in mineral composition, and stress history [24]. This corresponds for instance to the natural variability of the soil strength from point to point vertically at the position where the pile is to be installed.

The second group includes epistemic uncertainties due to lack of knowledge; in this case, information about subsurface conditions is few, because soil profile characteristics must be inferred from field or laboratory investigation of a limited number of samples. It includes also uncertainties generated from sample disturbance, test imperfections, human factors, and also, when engineering properties are obtained through correlation with index properties, as

in the case of CPT tests where empirical models are used to calculate the undrained shear resistance by applying correlation factors to the cone tip resistance [24].

According to this classification, two major approaches, respectively, probabilistic or “possibilistic” can be employed to deal with uncertainties [25, 26]. Therefore, the remainder of this paper will deal with methodologies based on these approaches, to assess the sensitivity of the response to the variation of the selected parameters and mainly to incorporate, into the analysis method, techniques for the formal treatment of uncertainties. Section 4 will describe a probabilistic approach based on the Monte Carlo method and an approach based on fuzzy arithmetic (FA).

Before proceeding, some additional comments should be presented regarding these sources of uncertainty. Inherent or natural variability are random by nature and cannot be reduced by increasing the number of tests [27]. The cognitive, epistemic uncertainties are reducible; however, for offshore sites, they will usually be present since the cost of performing in-situ tests at offshore sites is very expensive. Such tests may not be performed for every installation site and sometimes the values of the parameters are even estimated or extrapolated from previous tests made at other locations. Moreover, disturbances in these few samples are very common.

As strange as it may seem to experienced geotechnical engineers, not involved in deepwater offshore activities, this is precisely what has happened in soil investigations in the Campos Basin. Those are the reasons why *epistemic uncertainties are always added to the natural variability*: the use of limited data, of data arising from disturbed soil samples, and data from locations other than the one at which the torpedo pile is to be installed. In summary, the fact that there may be no knowledge of the exact site local soil variability is the very reason why (as presented in the next section) probabilistic approaches may fail, and is the motivation of the use of the approach based on FA.

4. Approaches for Treatment of Uncertainties

4.1. Probabilistic approach: the Monte Carlo method

As mentioned before, noncognitive sources of uncertainty involve parameters that can be treated as random variables, and to which a probabilistic distribution can be associated, based on statistical data. In such cases, the probabilistic approach is traditionally recommended.

Probabilistic approaches for treatment of uncertainties can be divided in two main categories. The first one comprises statistical methods that involve simulation, such as the classical Monte Carlo simulation method and its variants. The second category comprises nonstatistical methods such as those based on perturbation techniques. For instance, the stochastic finite element method [26] falls in this latter category; it is based on expanding the random parameters around their mean values via Taylor series, in order to formulate linear relationships between some random characteristics of the response and the random input parameters.

In the implementation of the classical Monte Carlo simulation, N samples of the uncertain parameters are randomly generated using a given joint probability density function. The deterministic analysis procedure is employed for each sample of the simulation process [28], obtaining then N responses that are statistically treated to get the first two statistical moments of the response (mean and standard deviation values).

The MC method is completely general, for linear or nonlinear analyses. However, in general, the accuracy of the statistical response is only adequate when the number of sample data N is sufficiently large; therefore, it is usually considered too expensive in terms of computing time. This fact has motivated studies on variants of the classical method, involving for instance variance reduction techniques and the Neumann expansion [29].

Due to its robustness and ability to effectively treat the noncognitive, random uncertainties, the classical MC simulation method has been used to calibrate and validate all other probabilistic techniques. The studies presented in this paper will also employ this method as a benchmark to compare the performance of the approach based on fuzzy arithmetic, which will be described in Section 4.2, in the representation of the random uncertainties.

4.2. Fuzzy arithmetic (FA) approach

It is important to recall that the cognitive sources of uncertainty are related not to chance, but rather to imprecise or vague information, involving subjectivity and/or dependent on expert judgment. Moreover, the axioms of probability and statistics are not adequate to deal with such types of uncertainties, which can be more effectively treated by “possibilistic” approaches employing for instance the theory of *fuzzy sets*.

The theory of fuzzy sets was introduced by Zadeh in [30] to define classes of objects with continuous membership graduations or associations in the interval $[0, 1]$. A fuzzy set has vague limits, allowing graded changes from one class to another, instead of exact limits characteristic of ordinary or *crisp* sets. In classical Boolean algebra, the notion of false and true values is limited to 1 or zero. In fuzzy logic, values that are “more or less” true or false can be treated, defined by real numbers that vary continuously from 0 to 1.

The treatment of uncertainties that derive from imprecise information is then possible, avoiding the use of random information. Therefore, complex systems, that would be hard to model with the theory of conventional sets, can be easily modeled by fuzzy sets. The fuzzy set theory allows the representation of imprecise and uncertain measures as fuzzy numbers, defined as:

$$A = \{(x, A(x)), x \in R, A(x) \in [0, 1]\}, \quad (4.1)$$

where $x \in R$ is the numeric support of the fuzzy number A , and $A(x) \in [0, 1]$ is the membership function (MF).

Fuzzy numbers are completely characterized by their MFs, that are built based on knowledge of an expert, who can assign “low,” “probable,” or “high” values for the desired parameters. Based on this subjective information, MFs can be constructed presenting either linear or nonlinear shapes. The more usually employed shapes for engineering problems are triangular, trapezoidal, and sinusoidal; the choice will depend on the type of application, and will also follow the assessment of the expert. In this work, triangular fuzzy MFs are used, defined by estimating three values [31]:

- (i) a more reliable value, m , to which is attributed a membership degree equals to 1;
- (ii) an inferior value, a , that most certainly will be exceeded by another value, and to which is attributed a membership degree equals to 0;
- (iii) a superior value, b , that most certainly will not be exceeded by another value, and to which is also attributed a membership degree equals to 0.

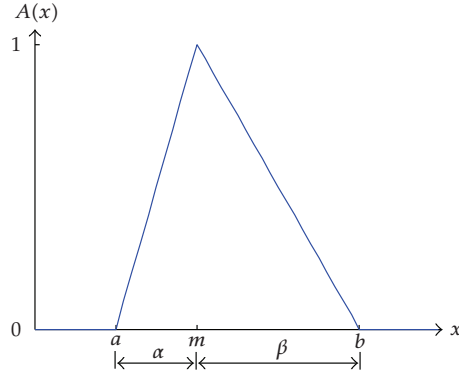


Figure 6: Triangular fuzzy number.

The membership function can then be defined as zero outside the interval $[a, b]$ of possible values; taken as linear into this range, increasing from a to m , and decreasing from m to b . This function is triangular, not necessarily symmetric, and can be defined as parameterized piecewise linear functions as:

$$A(x; a, m, b) = \begin{cases} \frac{x-a}{m-a}, & \text{if } x \in [a, m] \\ \frac{b-x}{b-m}, & \text{if } x \in [m, b] \\ 0, & \text{otherwise,} \end{cases} \quad (4.2)$$

where a and b are, respectively, the lower and upper bounds, and m is the dominant value, as illustrated in Figure 6.

Fuzzy numbers can also be defined by L (left) and R (right) MFs, resulting into the so-called L - R fuzzy numbers. In this context, a two-parameter modification of an L -type MF applies to all $x \leq m$, whereas the R -MF defines A for $x > m$, thus yielding

$$A(x) = \begin{cases} L\left(\frac{m-x}{\alpha}\right), & \text{if } x \leq m, \alpha > 0 \\ R\left(\frac{x-m}{\beta}\right), & \text{if } x > m, \beta > 0. \end{cases} \quad (4.3)$$

Therefore, the fuzzy number can also be identified by the notation $A = (m, \alpha, \beta)$, where α and β are the spreads of the number, which represents its uncertainty [32].

Fuzzy arithmetic (FA) operations, involving fuzzy numbers, can be used to propagate fuzziness from inputs to outputs. General operations can be deduced from the extension principle, which is used to transform fuzzy sets via functions [32], and plays a fundamental role in translating set-based concepts into their fuzzy set counterparts. However, simplified formulae can be obtained considering the L - R formulation of fuzzy numbers $A = (m, \alpha, \beta)_{LR}$ and $B = (n, \gamma, \delta)_{LR}$. The standard arithmetic operations are computed as follows.

The addition of triangular fuzzy numbers results in another triangular fuzzy number. Both addition and subtraction conserves the linearity of the numbers. These operations are expressed as, respectively,

$$\begin{aligned} A + B &= (m + n, \alpha + \gamma, \beta + \delta)_{LR}, \\ A - B &= (m - n, \alpha + \delta, \beta + \gamma)_{LR}. \end{aligned} \quad (4.4)$$

The multiplication of two fuzzy numbers produces a quadratic number. However, a linear approximation can be assumed when the spreads α and β are small in comparison to the modal or dominant values m . Therefore, this operation can be approximated to

$$\begin{aligned} A \cdot B &= (mn, m\gamma + n\alpha, m\delta + n\beta)_{LR} \quad (\text{if } A > 0, B > 0), \\ A \cdot B &= (mn, m\alpha - n\delta, m\beta - n\gamma)_{RL} \quad (\text{if } A > 0, B < 0), \\ A \cdot B &= (mn, n\alpha - m\delta, n\beta - m\gamma)_{RL} \quad (\text{if } A < 0, B > 0), \\ A \cdot B &= (mn, -n\beta - m\delta, -n\alpha - m\gamma)_{RL} \quad (\text{if } A < 0, B < 0). \end{aligned} \quad (4.5)$$

The multiplication of a fuzzy number by a scalar a is defined as:

$$\begin{aligned} aA &= (am, a\alpha, a\beta)_{LR}, \quad (\text{if } a \text{ is positive}), \\ aA &= (am, -a\beta, -a\alpha)_{RL}, \quad (\text{if } a \text{ is negative}). \end{aligned} \quad (4.6)$$

The division between two fuzzy numbers is computed as

$$\frac{A}{B} = \left(\frac{m}{n}, \frac{\delta m + \alpha n}{n^2}, \frac{\gamma m + \beta n}{n^2} \right)_{LR}. \quad (4.7)$$

To apply the FA in a given engineering problem, the uncertainty on each variable is modeled as a triangular fuzzy number; moreover, all the operations related to them have their expressions replaced by the corresponding FA expressions, as shown above on operations (4.4) to (4.7).

5. Implementation and Case Studies

Before proceeding with the study of the approaches described above, this section will begin with deterministic studies to assess the sensitivity of the response of the penetration model to the variation of the selected soil parameters. Later, in order to reach the goal of incorporating the formal treatment of uncertainties in the analysis of the penetration of torpedo piles, this section will proceed by presenting the application of the probabilistic approach based on the Monte Carlo method, followed by the implementation and application of the approach based on FA.

Recalling that uncertainties related to the penetration model involve a combination of both noncognitive (random, natural variability of soil parameters) and cognitive (epistemic, due to incomplete or imprecise information), it will be seen that, while the MC method can effectively deal only with the random uncertainties, the implementation of the fuzzy approach presented here can represent all sources of uncertainty.

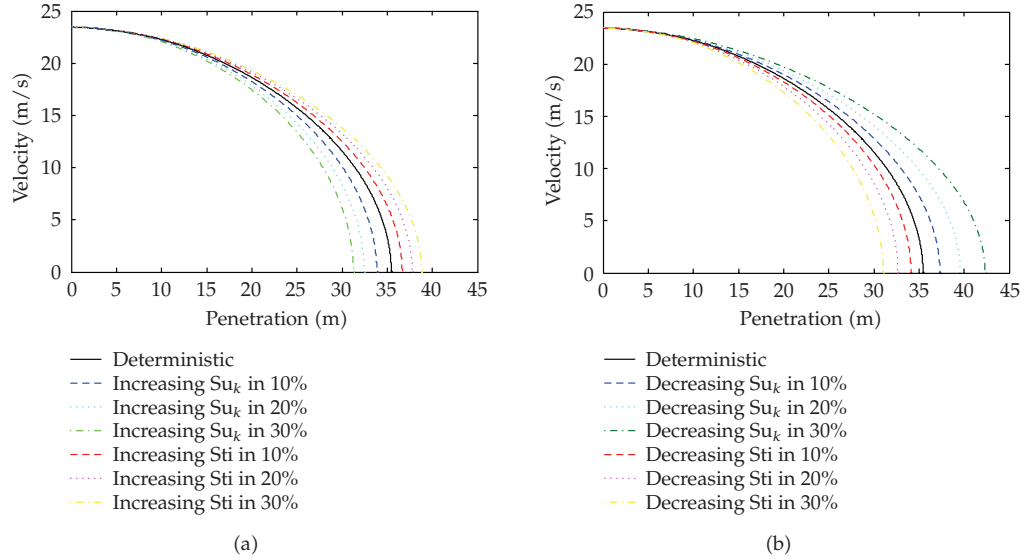


Figure 7: Deterministic sensitivity studies.

Table 3: Deterministic sensitivity studies: summary of results.

Varied parameter	Penetration (m)						
	-30%	-20%	-10%	0%	10%	20%	30%
Su_k	42.5	39.7	37.5	35.6	34.0	32.6	31.4
St_i	31.2	32.8	34.2	35.6	36.8	37.9	38.9

5.1. Deterministic sensitivity studies

In order to perform an assessment of the sensitivity of the torpedo pile penetration to the uncertainty of the selected soil parameters, a parametric study is performed by considering the same problem described in Tables 1 and 2. The penetration model is applied to deterministic and arbitrary variations on both uncertain parameters: the rate of increase with depth of the undrained shear strength (Su_k) and the soil sensitivity (St_i).

Recalling that according to Table 2, the fixed, “deterministic” values are $Su_k = 2.0$ kPa/m and $St_i = 3$. Initially, Su_k and St_i are individually increased by 10, 20, and 30%. Then, their values are reduced, also by 10, 20 and 30%. The results of the analyses for the different values of the parameters are presented in the graphs of Figure 7, corresponding to analyses where they are increased and reduced, respectively.

It should be noted that, since the drop height and the characteristics of the pile have not been changed, the behavior of the pile from the drop point until it reaches the seabed is the same as observed in Figure 4. Therefore, the graphs of Figure 7 represent only the behavior of the pile as it penetrates the soil, beginning from the depth of 200 m (that corresponds to the seabed) until it completes the penetration.

A summary of the results of Figure 7 is presented in Table 3 and Figure 8, in terms of penetration values (displacement minus the drop height) for each variation of the parameters Su_k and St_i . It can be verified that, as expected, reducing the undrained shear strength (and

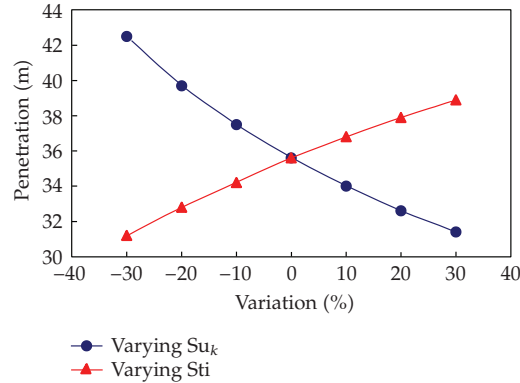


Figure 8: Deterministic sensitivity studies: summary of results.

Table 4: Statistical values from available soil data.

Parameter	Mean	Standard deviation
Su_k (kPa/m)	1.9	0.9
St_i (dimensionless)	3.2	1.0

therefore, the soil resistance) leads to the increase on the final depth values. On the other hand, decreasing the sensitivity values increases the soil resistance and, consequently, reduces the penetration of the pile.

5.2. Probabilistic analysis using the Monte Carlo method

Statistical treatment of the soil input parameters

In the probabilistic analysis using the MC method, both uncertain parameters (the undrained shear strength increase rate Su_k and soil sensitivity St_i) are varied simultaneously. Their values are randomly simulated, following a statistical distribution and its associated values of mean and standard deviation, derived from a given set of soil data from laboratory and/or in situ tests (in this case, the data were acquired from many tests performed at different sites in a certain cluster of Campos Basin). This is accomplished by performing a statistical treatment on the available data, representative of offshore fields in Campos Basin. As a result, for each uncertain parameter, the mean (which in this case is the sample average) and standard deviation values were estimated. These values are presented in Table 4.

In order to determine an appropriate probability distribution function for the data, a normality verification is performed for each parameter. Figure 9 present the results, respectively, for Su_k and St_i . It can be observed that, despite St_i data fits better than Su_k , the normal pdf is not the ideal approximation for them. Hence, other functions are fitted and verified, as presented in Figure 10. Observing this figure, it can be verified that the lognormal pdf provides a better fit for both sets of available data. Another advantage of this distribution is that it does not generate negative values for the soil parameters, which does not have physical meaning and can generate erroneous results.

The number of simulations in an MC strategy is dictated by the convergence of the mean value of the considered parameter to the deterministic design value. In the present case, 1000

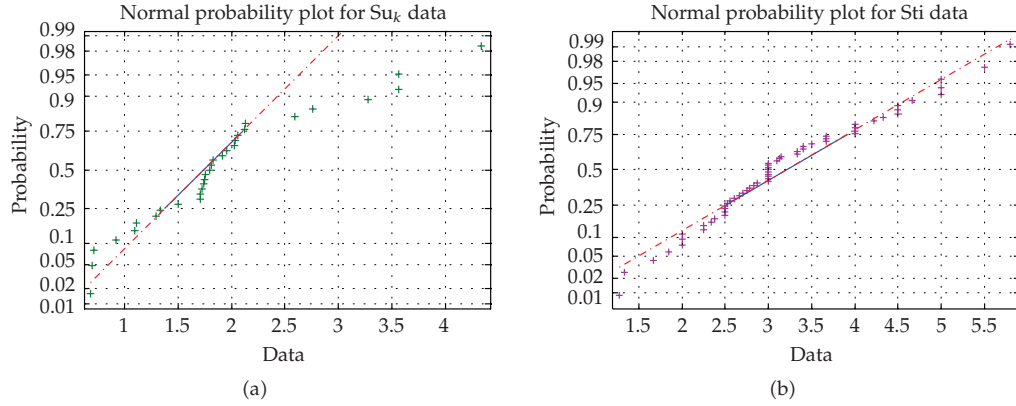


Figure 9: Normal probability verification of Su_k and Sti data.

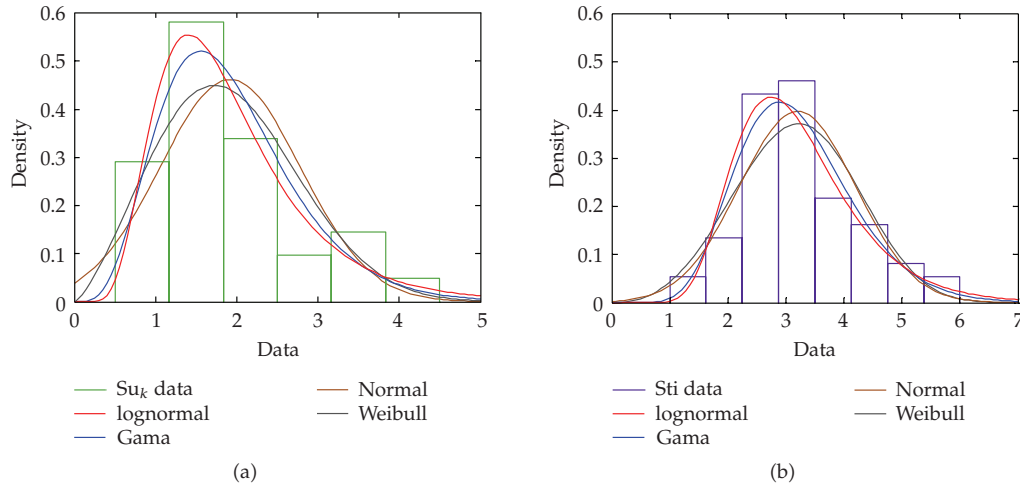


Figure 10: Probability function fitness for Su_k and Sti data.

generations were needed to obtain satisfactory convergence. Figure 11 depicts the distribution of the 1000 randomly generated values of Su_k and Sti , following the lognormal distribution.

Results

The probabilistic study then comprises a total number of 1000 analyses with the penetration model, each taking a randomly generated pair of values for the soil parameters Su_k and Sti , following the lognormal probability distribution with expected values and standard deviations given in Table 4.

The results of the 1000 analyses are then gathered to proceed to a statistical treatment, which will represent the penetration value in terms of mean and standard deviation. These results are presented in Table 5.

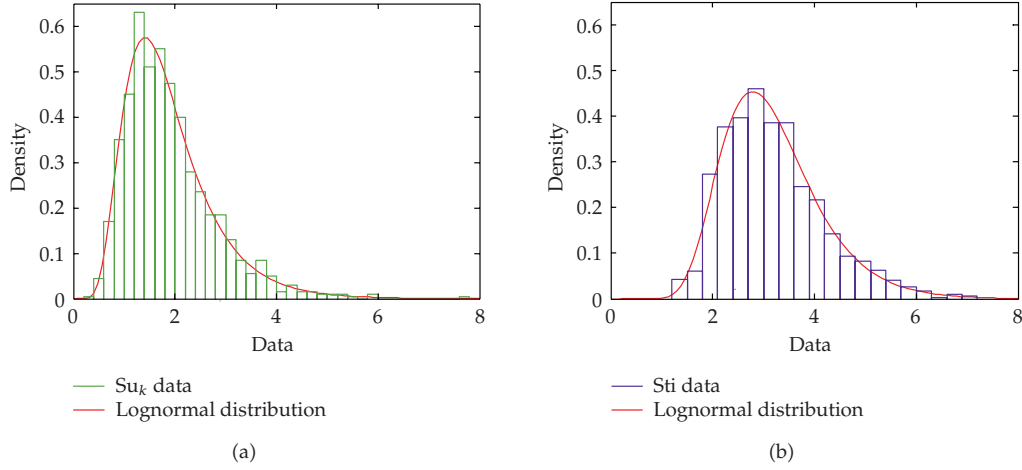
Figure 11: Lognormal distribution of Su_k and Sti .

Table 5: Probabilistic MC approach: statistical values of the results.

	Median	Mean	Standard deviation
Penetration (m)	38.5	39.8	10.1

These values will be compared with the results obtained with the approach using FA, which will be presented in Section 5.3. We recall that the mean value of 39.8 m for the penetration cannot be directly compared to the “deterministic” value of 35.6 m obtained in the previous section, since the fixed, “deterministic” values for the soil parameters were $Su_k = 2.0$ kPa/m and $Sti = 3.0$, and the mean probabilistic values gathered from the set of soil data considered are $Su_k = 1.9$ kPa/m and $Sti = 3.2$. Anyway, the results are consistent since, as could be observed in the results of the deterministic sensitivity studies summarized in Figure 8, lower values of Su_k and higher values of Sti lead to higher penetration values.

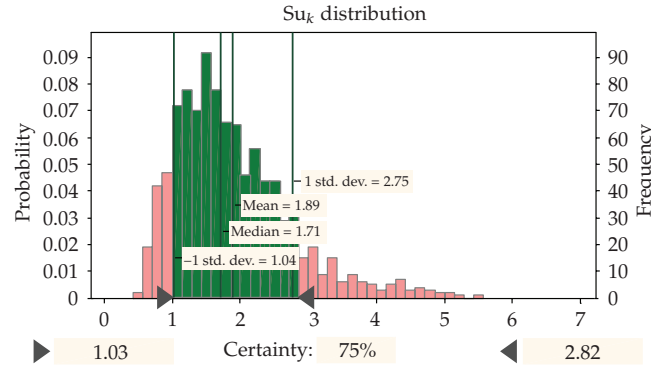
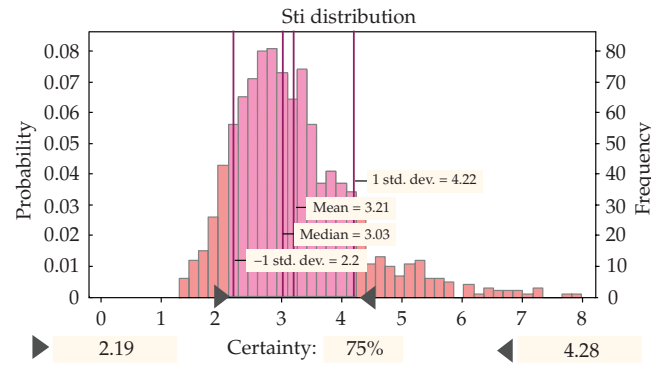
5.3. Fuzzy arithmetic: implementation and application

Implementation

In the computational implementation of the approach using FA, the uncertain variables Su_k and Sti are represented as triangular fuzzy numbers. Therefore, the computational code is altered, and all operations performed with those parameters in the solution procedure (as described in Algorithm 1 and (2.2)–(2.6)) have the traditional arithmetic operators replaced by the fuzzy operators presented in (4.4) to (4.7).

As mentioned in Section 4.2, the fuzzy operations of multiplication and division generate quadratic numbers; however, when their spreads are small, they can be approximated by linear ones. Therefore, although (4.5) to (4.7) are approximations for small spreads, they are feasible for this specific work, since the values of final penetration (dominant value, and the lower and upper bounds) are more important than the shape of the membership function.

Once these fuzzy operators are implemented in the computational code, it remains to determine the values that define the triangular membership functions, which represent Su_k

Figure 12: Definition of bounds for Su_k .Figure 13: Definition of bounds for Sti .

and Sti as fuzzy numbers. As illustrated in Figure 6, these values are the lower and upper bounds a and b , and the dominant value m ; they can be derived by investigating the statistical distribution of the soil parameters, taking the lognormal distribution generated as described in the previous item.

The lower and upper bounds a and b can be assumed as defining an interval of confidence of 75% corresponding to one standard deviation below and above the mean. This criterion provides samples that have consistent values for the uncertain parameters (positive values, Sti greater than 1.0, etc.), and is illustrated in Figures 12 and 13, for Su_k and Sti distributions, respectively.

Regarding the “dominant” value m , the first choice could be to take the mean value; however, since the most representative value of a sample with large dispersion is the median, its value was chosen as m for each parameter. The values thus obtained for a , b , and m that define the membership functions for Su_k and Sti are presented in Table 6 and graphically represented in Figure 14.

Results

Finally, the evaluation of the uncertain response using this FA approach consists simply in performing one analysis with the penetration model. The uncertainties embedded in the fuzzy

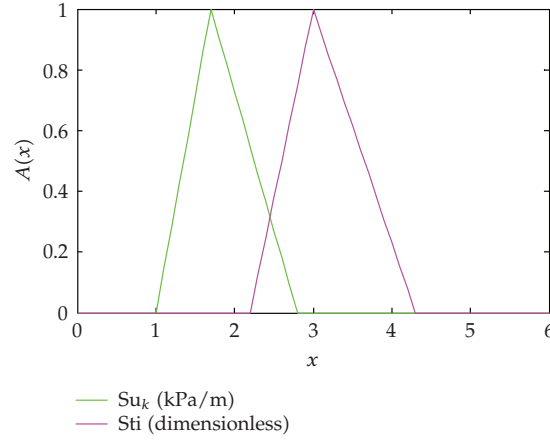


Figure 14: Triangular fuzzy representation for the soil uncertain parameters.

Table 6: Membership functions for the parameters Su_k and Sti .

	Lower bound a	Dominant value m	Upper bound b
Su_k (kPa/m)	1.0	1.7	2.8
Sti (dimensionless)	2.2	3.0	4.3

Table 7: FA approach: results of fuzzy analyses.

	Lower bound	Dominant value	Upper bound
Penetration (m)	30.1	38.6	66.3

numbers that represent the parameters Su_k and Sti are incorporated in the calculation of the terms F_T and F_S defined in (2.6), at the right-hand side of step b.1 of Algorithm 1, and therefore are updated and propagated at each time step of the solution procedure presented in that table. This fact points to the remarkable computational advantage of this approach, compared to the probabilistic MC method with conventional arithmetic that required a total number of 1000 analyses.

The results of the fuzzy analyses, in terms of lower, dominant, and upper bound for the final penetration of the torpedo pile are presented in Table 7.

5.4. Comparison of results

This section compares the results of analyses of the torpedo pile with the penetration model, considering both MC and FA approaches. Before comparing the final pile penetration, Figure 15 presents the full behavior of the pile as it penetrates the soil, in terms of penetration x velocity curves, beginning from the depth of 200 m (that corresponds to the seabed) until it completes the penetration.

Three curves are presented for each approach, corresponding to the “dominant” or “most probable” result, and a lower and upper “bounds” of the response. For the MC simulation, the “most probable” curve is represented by taking the median values of penetration and velocities at each time step of the response; the lower and upper bounds are

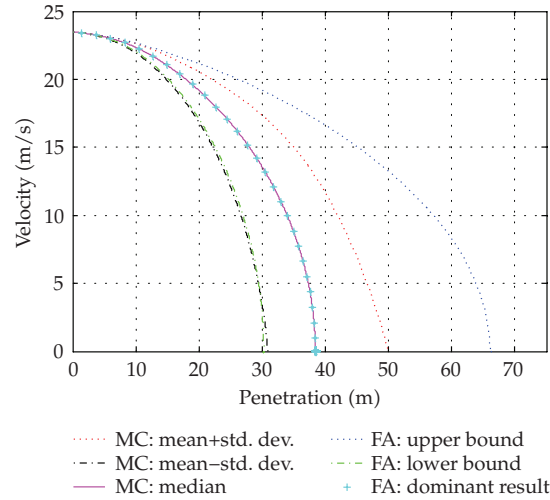


Figure 15: Comparison of results of MC and FA approaches.

Table 8: Comparison of results.

Method	Final penetration (m)		
	Mean – 1 std deviation	Median value	Mean + 1 std deviation
MC	29.7 (–22.9%)	38.5	49.9 (+29.6%)
FA	30.1 (–22.0%)	38.6	66.3 (+71.8%)

determined, respectively, by taking the mean value and subtracting or adding one standard deviation (similarly to the procedure applied to determine the bounds of the fuzzy input parameters).

For the FA approach, the “dominant” curve is represented by taking the “crisp” result, that is, the values corresponding to a degree of membership equal to one. The lower and upper bounds are determined by the support of the fuzzy set defined by the values corresponding to a membership degree greater than zero.

Table 8 summarizes and compares the results presented in Tables 5 and 7 for the MC and fuzzy approaches. Observing this table and also Figure 15, it can be observed that the “dominant” or “most probable” results for the final penetration are practically the same; the difference between the median value of the MC analyses and the dominant value of FA analyses is insignificant.

Regarding dispersion of results, it should be recalled that MC “lower” and “upper” results (defined by subtracting and adding one standard deviation to the mean value) cannot be directly compared to the spreads of the fuzzy results, where lower and upper bounds define the interval where a value can possibly represent the calculated penetration. Anyway, it can be noted that the uncertainties of the soil parameters are quite significant and can have a decisive influence in the design of the torpedo pile.

A better comparison for the final penetration can be graphically assessed in terms of the probability distribution of the MC simulation, and the membership function that characterizes

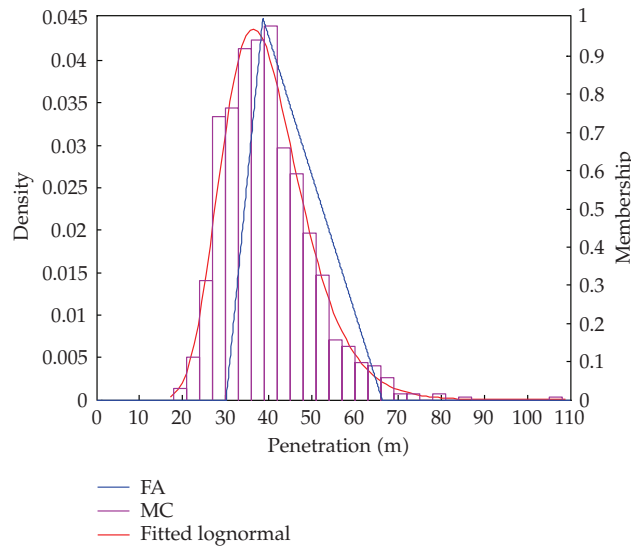


Figure 16: Final penetration obtained from MC and FA approaches.

the fuzzy number for the FA approach. Therefore, Figure 16 compares the results obtained from the MC and FA approaches, in terms of the probability distribution and membership function. For this example, while the assumed supports of the fuzzy input parameters Su_k and St_i corresponded to a certainty interval of 75% of their lognormal distribution, the support of the fuzzy number that represents the final penetration corresponds to a certainty interval of around 80% of the MC distribution.

Finally, the most remarkable comparison in the performance of both methods can be stated in terms of the total CPU time required. While the MC probabilistic approach required 1000 analyses with the penetration model using the solution procedure of Algorithm 1, only one analysis was required for the approach employing FA.

6. Final Remarks and Conclusions

The torpedo pile has been acknowledged as a very promising alternative to anchor mooring systems. It has recently been considered for use not only in mooring lines of floating production systems, but also for mobile offshore drilling units (MODUs) operating in deep and ultradeep waters. Therefore, oil exploitation companies are devoting intense research and design activities in order to deliver efficient mooring solutions using this concept.

One of the main aspects concerning the design of foundation systems are the uncertainties involved in the determination of values for the soil parameters. For conventional onshore systems, this aspect has been tackled by performing a large number of tests with soil samples. However, on deepwater offshore sites the cost of performing such tests may be very expensive, if not prohibitive; therefore, tests may not be performed for every installation site, and sometimes results of tests made at other locations are used to estimate or extrapolate the values of the soil parameters.

This fact can severely affect the effectiveness of the design and analysis of torpedo piles, leading to large discrepancies in the response of the torpedo pile, mainly in terms of

the final depth reached by the pile. Therefore, it is very important to develop and employ methodologies to properly assess the sensitivity of the response to the variation of these parameters, and to incorporate, into the analysis method, techniques for the formal treatment of the uncertainties.

The classical probabilistic Monte Carlo simulation could be considered for this purpose, since it is a sound methodology to estimate the effect of random uncertainties. Nevertheless, in the problem described in this work, there are a great amount of epistemic uncertainties in the model equations and parameters, and therefore, MC simulation results provide only a rough estimation of the uncertainty. In addition, the application of MC simulation requires excessive computational costs, as has been confirmed in the case study considered in this work. More than 1000 simulations were needed to obtain the results.

On the other hand, the computational efficiency of the fuzzy arithmetic approach is outstanding—around three orders of magnitude less. Therefore, the results of the application of the FA approach demonstrated its ability to provide low-cost approximations of the bounds of the uncertainties, and therefore, to comprise an effective design tool for the practitioner.

Future developments

In this study, only two soil parameters, the undrained shear strength and soil sensitivity, were considered as uncertain. Extensions of the fuzzy methodology presented in this work could consider the treatment of other uncertain parameters, such as for instance, the empirical maximum soil strain rate factor (S_e), the empirical soil strain rate factor (C_e), and the drag coefficient C_D considered for the calculation of the soil drag force as the pile penetrates; this latter parameter can vary for different anchor or pile shapes. Also, this work did not consider the uncertainties associated with the penetration model itself. These could also be considered, since it is a mainly empirical model and involves imprecision in its formulation.

Finally, a promising approach for the design of offshore systems would be to incorporate the pile penetration model, associated with the fuzzy methodology, in the implementation of a coupled finite element-based, time domain simulation program. In such implementation, not only the isolated torpedo pile is considered, but also a full finite-element model of all components involved in the installation of the pile (i.e., the mooring line itself and the other lines and chains, illustrated in Figures 2 and 3). The result is a complete 3D model, also submitted to environmental loadings other than dead weight (such as marine current). In such coupled model, there will be no need to “fudge” the drag coefficient C_D , to account for the presence of the mooring line and chain loop.

Such computational tool would therefore comprise an efficient tool for the design of mooring systems based on torpedo piles, and for the simulation of the procedures needed for the installation of such complex offshore system.

Acknowledgments

The authors would like to acknowledge the help of Mr. Cláudio dos Santos Amaral and Dr. Álvaro Maia da Costa, experts in geotechnical engineering from CENPES-Petrobras (Research and Development Center of the Brazilian state oil company), for the invaluable collaboration regarding information and data essential for the completion of this work.

References

- [1] B. R. Danziger, *Dynamic analysis of pile driving*, D.Sc. Thesis, COPPE/Federal University of Rio de Janeiro, Rio de Janeiro, RJ, Brazil, 1991.
- [2] K. Huang and M.-Y. Lee, "Experiences in classification of deepwater mooring systems for floating installations," in *Proceedings of the 30th Annual Offshore Technology Conference (OTC '98)*, vol. 2, pp. 227–236, Houston, Tex, USA, May 1998, paper 8770.
- [3] J.-L. Colliat, "Anchors for deepwater to ultradeepwater moorings," in *Proceedings of the 34th Annual Offshore Technology Conference (OTC '02)*, pp. 2695–2703, Houston, Tex, USA, May 2002, paper 14241.
- [4] P. Sparrevik, "Suction pile technology and installation in deep waters," in *Proceedings of the 20th Annual Offshore Technology Conference (OTC '02)*, pp. 2171–2179, Houston, Tex, USA, May 2002, paper 14241.
- [5] C. J. Medeiros Jr., "Torpedo anchor for deep water," in *Proceedings of the Deep Offshore Technology Conference (DOT '01)*, Rio de Janeiro, RJ, Brazil, October 2001.
- [6] C. J. Medeiros Jr., "Low cost anchor system for flexible risers in deep waters," in *Proceedings of the 20th Annual Offshore Technology Conference (OTC '02)*, pp. 1333–1337, Houston, Tex, USA, May 2002, paper 14151.
- [7] D. G. True, *Undrained vertical penetration into ocean bottom soils*, Ph.D. Thesis, University of California, Berkeley, Calif, USA, 1976.
- [8] Y. Boguslavskii, S. Drabkin, I. Juran, and A. Salman, "Theory and practice of projectile's penetration in soils," *Journal of Geotechnical Engineering*, vol. 122, no. 10, pp. 806–812, 1996.
- [9] C. W. Young, "Depth prediction for earth-penetrating projectiles," *Journal of the Soil Mechanics and Foundations*, vol. 95, no. 3, pp. 803–817, 1969.
- [10] C. W. Young, "An empirical equation for predicting penetration depth into soft sediments," in *Proceedings of the IEEE/MTS Oceans Conference (OCEANS '81)*, vol. 13, pp. 674–677, Boston, Mass, USA, September 1981.
- [11] R. L. McNeill, "Approximate method for estimating the strengths of cohesive materials from penetrator decelerations," in *Proceedings of the IEEE/MTS Oceans Conference (OCEANS '81)*, vol. 13, pp. 688–693, Boston, Mass, USA, September 1981.
- [12] R. M. Beard, "A penetrometer for deep ocean seafloor exploration," in *Proceedings of the IEEE/MTS Oceans Conference (OCEANS '81)*, vol. 13, pp. 668–673, Boston, Mass, USA, September 1981.
- [13] R. M. Beard, "Holding capacity of plate anchors," Tech. Rep. R-882, Civil Engineering Laboratory, Port Hueneme, Calif, USA, 1980.
- [14] J. R. Morison, M. P. O'Brien, J. W. Johnson, et al., "The force exerted by surface waves on piles," *Petroleum Transactions*, vol. 189, pp. 149–154, 1950.
- [15] API Recommended Practice 2A-WSD (RP 2A-WSD), "Recommended Practice for Planning, Designing and Constructing Fixed Offshore Platforms—Working Stress Design," Twenty-First Edition, December 2000.
- [16] A. W. Skempton and R. D. Northey, "The sensitivity of clays," *Geotechnique*, vol. 3, no. 1, pp. 30–53, 1952.
- [17] D. G. True, "Rapid penetration into seafloor soils," in *Proceedings of the 6th Annual Offshore Technology Conference (OTC '74)*, vol. 3, pp. 607–618, Houston, Tex, USA, May 1974.
- [18] J. Chung and J. M. Lee, "A new family of explicit time integration methods for linear and non-linear structural dynamics," *International Journal for Numerical Methods in Engineering*, vol. 37, no. 23, pp. 3961–3976, 1994.
- [19] E. N. Lages, L. C. L. M. Vieira, and A. S. Ramos Jr., "A simplified model for marine soil and anchor line interaction," in *Proceedings of the 25th Iberian Latin-American Congress on Computational Methods in Engineering (XXV CILAMCE '04)*, pp. 1–15, Recife, PE, Brazil, November 2004.
- [20] A. Eltaher, Y. Rajapaksa, and K.-T. Chang, "Industry trends for design of anchoring systems for deepwater offshore structures," in *Proceedings of the Annual Offshore Technology Conference (OTC '03)*, Houston, Tex, USA, May 2003, paper 15265.
- [21] E. Hofer, M. Kloos, B. Krzykacz-Hausmann, J. Peschke, and M. Woltereck, "An approximate epistemic uncertainty analysis approach in the presence of epistemic and aleatory uncertainties," *Reliability Engineering & System Safety*, vol. 77, no. 3, pp. 229–238, 2002.
- [22] K. Durga Rao, H. S. Kushwaha, A. K. Verma, and A. Srividya, "Quantification of epistemic and aleatory uncertainties in level-1 probabilistic safety assessment studies," *Reliability Engineering & System Safety*, vol. 92, no. 7, pp. 947–956, 2007.

- [23] W. L. Oberkampf, S. M. DeLand, B. M. Rutherford, K. V. Diegertd, and K. F. Alvin, "Error and uncertainty in modeling and simulation," *Reliability Engineering & System Safety*, vol. 75, no. 3, pp. 333–357, 2002.
- [24] E. H. Vanmarcke, "Probabilistic modeling of soil profiles," *Journal of the Geotechnical Engineering Division*, vol. 103, no. 11, pp. 1227–1246, 1977.
- [25] B. S. L. P. de Lima, E. C. Teixeira, and N. F. F. Ebecken, "Probabilistic and possibilistic methods for the elastoplastic analysis of soils," *Advances in Engineering Software*, vol. 32, no. 7, pp. 569–585, 2001.
- [26] B. S. L. P. de Lima and N. F. F. Ebecken, "A comparison of models for uncertainty analysis by the finite element method," *Finite Elements in Analysis and Design*, vol. 34, no. 2, pp. 211–232, 2000.
- [27] T. J. Ross, *Fuzzy Logic with Engineering Applications*, John Wiley & Sons, New York, NY, USA, 2nd edition, 2004.
- [28] P. Bratley, L. F. Fox, and L. E. Schrage, *A Guide to Simulation*, Springer, New York, NY, USA, 1983.
- [29] F. Yamazaki and M. Shinozuka, "Neumann expansion for stochastic finite element analysis," *Journal of Engineering Mechanics*, vol. 114, no. 8, pp. 1335–1354, 1988.
- [30] L. A. Zadeh, "Fuzzy sets," *Information and Control*, vol. 8, no. 3, pp. 338–353, 1965.
- [31] W. S. Dester and D. I. Blockley, "Hazard engineering," *Structural Safety*, vol. 16, no. 1-2, pp. 3–12, 1994.
- [32] W. Pedrycz and F. Gomide, *An Introduction to Fuzzy Sets Analysis and Design*, Complex Adaptive Systems, MIT Press, Cambridge, Mass, USA, 1998.

Research Article

Effects of Variations in Nonlinear Damping Coefficients on the Parametric Vibration of a Cantilever Beam with a Lumped Mass

Demian G. Silva¹ and Paulo S. Varoto²

¹ Defense Projects, Empresa Brasileira de Aeronautica (EMBRAER),
Avenue Brigadeiro Faria Lima 2170, 12227-901 São José dos Campos, SP, Brazil

² Mechanical Engineering Department, School of Engineering of São Carlos,
University of São Paulo, Avenue Trabalhador Saocarlene 400, 13566-590 São Carlos, SP, Brazil

Correspondence should be addressed to Paulo S. Varoto, varoto@sc.usp.br

Received 26 March 2008; Accepted 27 June 2008

Recommended by Jose Balthazar

Uncertainties in damping estimates can significantly affect the dynamic response of a given flexible structure. A common practice in linear structural dynamics is to consider a linear viscous damping model as the major energy dissipation mechanism. However, it is well known that different forms of energy dissipation can affect the structure's dynamic response. The major goal of this paper is to address the effects of the turbulent frictional damping force, also known as drag force on the dynamic behavior of a typical flexible structure composed of a slender cantilever beam carrying a lumped-mass on the tip. First, the system's analytical equation is obtained and solved by employing a perturbation technique. The solution process considers variations of the drag force coefficient and its effects on the system's response. Then, experimental results are presented to demonstrate the effects of the nonlinear quadratic damping due to the turbulent frictional force on the system's dynamic response. In particular, the effects of the quadratic damping on the frequency-response and amplitude-response curves are investigated. Numerically simulated as well as experimental results indicate that variations on the drag force coefficient significantly alter the dynamics of the structure under investigation.

Copyright © 2008 D. G. Silva and P. S. Varoto. This is an open access article distributed under the Creative Commons Attribution License, which permits unrestricted use, distribution, and reproduction in any medium, provided the original work is properly cited.

1. Introduction

Characterization and quantification of uncertainties have been a topic of major importance in the context of structural dynamics. Generally speaking, the term uncertainty can be associated to variations of the system's physical parameters due to inaccuracies present either in the system's model or experimental data. In a broad view, the sources of uncertainties can be

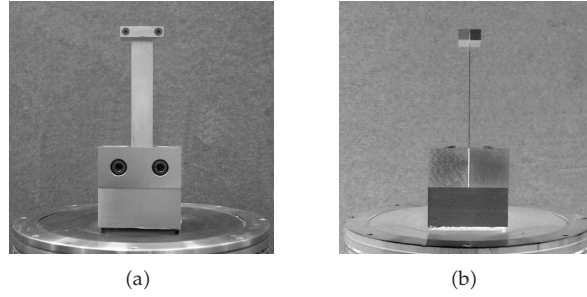


Figure 1: Physical system under investigation: (a) frontal view, (b) lateral view [19, 21, 23].

grouped into two main categories, namely *statistical* and *nonstatistical* [1], where the former is associated to fluctuations in the system's parameter mostly due to variations in material and/or geometry, and the later reflects inaccuracies present in the system's model caused by adoption of inappropriate assumptions or variations in numerical errors, for instance. More recently, a new terminology has been used to this classification by employing the words *aleatory* or *aleatoric* and *epistemic* [2, 3] to refer to these two groups of uncertainties, respectively. Several statistical and fuzzy theory-based procedures have been recently proposed (see [4–8]) to characterize and quantify uncertainties in complex structural systems. Similarly, uncertainties have also been subject of investigation in wave propagations and vibroacoustics (see [9–11]) as well as aerospace structures (see [3, 12, 13]). In the field of nonlinear structural dynamics, a reduced number of works have been reported. Nichols et al. [14] has developed a procedure for the detection of quadratic nonlinearities while Adhikari [2] has discussed uncertainties in damping models.

Parametrically excited cantilever beams have been extensively investigated in the last two decades, specially in the case of the principal parametric resonance [15–18]. Although most of these investigations have dealt with various aspects of the parametric resonance phenomenon, the majority of analysis was done by neglecting the effects of fluid medium. In this work, we perform an experimental and theoretical investigation on the effects of the viscous quadratic damping on the dynamic response of a cantilever beam with tip mass to a principal parametric resonance [19, 20]. To investigate the quadratic damping effect, the structure shown in Figure 1 was built. It is composed of a slender stainless steel ASTM A240 beam, with dimensions of 100 mm in length, 20 mm in width, and 1 mm in thickness. The lumped mass is composed of carbon steel ASTM A36, with dimensions of 10 mm in length, 40 mm in width, and 20 mm in height. The opposite beam's end is clamped to a rigid base built from carbon ASTM A36 steel.

Figure 2 depicts the results of an experiment that was carried out by using the system shown in Figure 1. The experiment consisted of driving the structure into a principal parametric resonance condition through an input base sinusoidal signal. The structure's vibration and interaction with the surrounding fluid medium could be observed through the smoke-wire arrangement [19] as shown in the sequence of pictures of Figure 2. This experiment qualitatively indicates that the drag force plays an important role on the dynamics of the structure under investigation. Thus, this paper is concerned in studying theoretically and experimentally the effects of variations in the quadratic damping coefficients on the lateral vibration of a cantilever beam undergoing a principal parametric excitation.

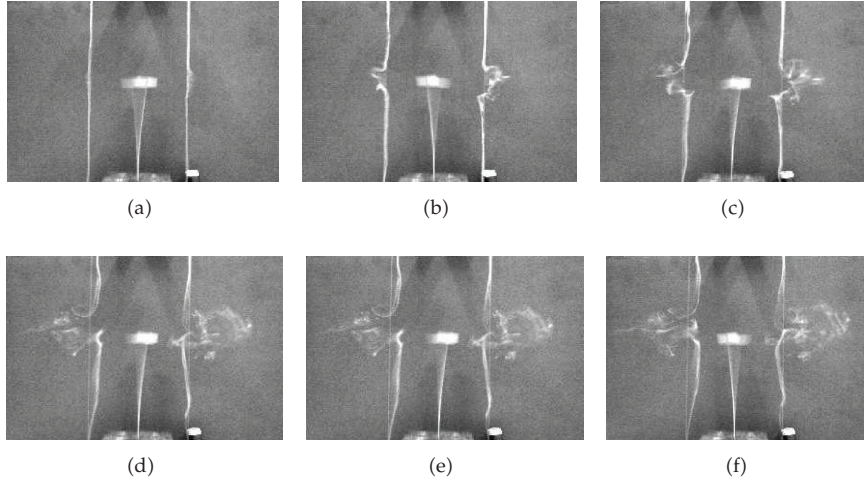


Figure 2: Qualitative effects of quadratic damping on the lateral vibration of the system [19].

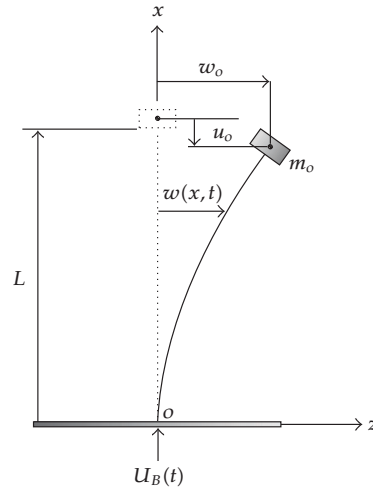


Figure 3: Physical model of the structure under investigation, combined acoustic, and base excitations [19].

2. Mathematical modeling

In a previous work by the authors [21], a general mathematical model for the structure shown in Figure 1 was developed by using the model shown in Figure 3. According to this model, the $OXYZ$ orthogonal coordinates system is fixed at the base of the beam at its unstressed position and directed such that the X axis is taken as the centerline of the beam. The origin O of the coordinate system may be subject to a dynamic displacement $U_B(t)$ in the X direction that represents the external driving signal.

2.1. Energy relationships

The beam is modeled as a continuum solid with displacement field described by u_i ($i = 1, 2, 3$) and u_i^o ($i = 1, 2, 3$). The kinetic energy of the lumped-mass system can be described by

$$T = \frac{1}{2} \int_V \rho \dot{u}_i \dot{u}_i dV + \frac{1}{2} m_o \dot{u}_i^o \dot{u}_i^o \quad (2.1)$$

in which the dot denotes time derivative, ρ and V are, respectively, the material density and volume of the beam, and m_o is the value of the lumped mass. In order to simplify (2.1), the contribution of the distributed mass of the beam will be ignored as well as the rotatory energy of the lumped mass. Hence, the kinetic energy is simplified to

$$T = \frac{1}{2} m_o \left[(\dot{u}_1^o)^2 + (\dot{u}_3^o)^2 \right]. \quad (2.2)$$

The task to find T consists in performing several steps. First, the time derivative of the displacement field must be computed which results in expressions for $(\dot{u}_1)^2$ and $(\dot{u}_3)^2$. Second, the terms in the right-hand side of the expressions of $(\dot{u}_1)^2$ and $(\dot{u}_3)^2$ are described as functions of the $w(x, t)$ and its spatial derivatives. Third, a spatial reduction is necessary so that the deflection on the center of the lumped mass can be obtained. This can be done by using an expression of the form

$$w(x, t) = \phi(x) w_o(t) \quad (2.3)$$

in which $\phi(x)$ represents the first linear natural mode of the structure and $w_o(t)$ represents the modal coordinate associated with this natural mode. As a final result, the expressions for $(\dot{u}_1^o)^2$ and $(\dot{u}_3^o)^2$ are found and truncated to result in nonlinearities of third order as follows:

$$\begin{aligned} (\dot{u}_1^o)^2 &= (A_1)^2 w_o^2 \dot{w}_o^2 - 2A_1 w_o \dot{w}_o \ddot{U}_B + \frac{8}{3} A_2 w_o^3 \dot{w}_o \ddot{U}_B + (\ddot{U}_B)^2, \\ (\dot{u}_3^o)^2 &= \dot{w}_o^2. \end{aligned} \quad (2.4)$$

Substituting the expressions of $(\dot{u}_1^o)^2$ and $(\dot{u}_3^o)^2$ described above into (2.2), the kinetic energy is then given as

$$T = \frac{1}{2} m_o \dot{w}_o^2 + \frac{1}{2} m_o \left[(A_1)^2 w_o^2 \dot{w}_o^2 - 2A_1 w_o \dot{w}_o \ddot{U}_B + \frac{8}{3} A_2 w_o^3 \dot{w}_o \ddot{U}_B + (\ddot{U}_B)^2 \right], \quad (2.5)$$

in which A_1 and A_2 are geometrical constants given as

$$\begin{aligned} A_1 &= \int_0^L \left(\frac{\partial \phi}{\partial x} \right)^2 dx, \\ A_2 &= \int_0^L \left(\frac{\partial \phi}{\partial x} \right)^4 dx, \end{aligned} \quad (2.6)$$

and the first linear mode shape function $\phi(x)$ is given as

$$\phi(x) = 1 - \cos\left(\frac{\pi x}{2L}\right). \quad (2.7)$$

Once the final expression for the kinetic energy is known, the next step towards the derivation of equation of motion is obtaining the system's strain or potential energy which may be written as function of the stress and strain in the X direction as

$$U = \frac{1}{2} \iiint_V \sigma_{xx} \varepsilon_{xx} dV. \quad (2.8)$$

By using the assumption that the material follows the constitutive Hooke law, and ignoring Poisson's effects, (2.8) reduces to

$$U = \frac{1}{2} \iiint_V E \varepsilon_{xx}^2 dV = \frac{1}{2} \int_0^L \int_A E \varepsilon_{xx}^2 dA dx. \quad (2.9)$$

However, u_c is very small when compared to u_r . Therefore, to simplify the analysis, the contributions of u_c and of the gravitational field to the strain energy are ignored, thus giving

$$U = \frac{1}{2} \int_0^L \int_A E \left[z^2 (w'')^2 - z^2 (w'')^2 (w')^2 \right] dA dx. \quad (2.10)$$

By writing $w(x, t)$ as a function of $\phi(x)$ and $w_o(t)$ (see (2.3)), the final expression for the strain energy truncated cubic terms in the system's equation of motion is given by

$$U = \frac{1}{2} E I_y B_1 w_o^2 - \frac{3}{2} E I_y B_2 w_o^4 + \dots, \quad (2.11)$$

where I_y is the area moment of inertial about the Y axis, and the geometrical constants B_1 and B_2 are given as

$$\begin{aligned} B_1 &= \int_0^L (\phi'')^2 dx, \\ B_2 &= \int_0^L (\phi'')^2 (\phi')^2 dx. \end{aligned} \quad (2.12)$$

The last step before deriving the system's equation of motion consists in obtaining the expression for the nonconservative forces acting on the system. Herein, it will be considered the action of two nonconservative forces. The first is the structural damping force which is modeled in terms of the generalized coordinates as $c_1 \dot{w}_o$. The second is the aerodynamic drag damping force acting on the system (when in motion) and is proportional to the squared of the generalized velocity $c_2 \dot{w}_o |\dot{w}_o|$. Both damping forces act in the negative direction of the virtual transversal displacement δw_o . Therefore, the nonconservative virtual work δW_{nc} which is done on the system is given by

$$\delta W_{nc} = (-c_1 \dot{w}_o - c_2 \dot{w}_o |\dot{w}_o|) \delta w_o. \quad (2.13)$$

Since the nonconservative virtual work is defined as a function of the nonconservative generalized force Q_{nc} as $\delta W_{nc} = Q_{nc} \delta w_o$, the generalized force Q_{nc} is obtained as

$$Q_{nc} = \frac{\delta W_{nc}}{\delta w_o} = -c_1 \dot{w}_o - c_2 \dot{w}_o |\dot{w}_o|. \quad (2.14)$$

2.2. Equation of motion

In the earlier section, the expressions for the kinetic energy T , strain energy U , and nonconservative generalized force Q_{nc} were obtained. From these results, it is possible to derive the system's equation of motion by using the well-known Lagrange equation [22] which, in turn, for the system under investigation is written as

$$\frac{d}{dt} \left(\frac{\partial T}{\partial \dot{w}_o} \right) - \frac{\partial T}{\partial w_o} + \frac{\partial U}{\partial w_o} = Q_{nc}. \quad (2.15)$$

Through the computation of each term of Lagrange's equation and substitution of the result (2.15), the following result is obtained:

$$\begin{aligned} & \left(1 + \underline{A_1^2 w_o^2} \right) \ddot{w}_o + \left(\frac{c_1}{m_o} + \frac{c_2}{m_o} |\dot{w}_o| \right) \dot{w}_o + \left(\underline{A_1^2 \dot{w}_o^2} - \underline{A_1 \ddot{U}_B} + \frac{EI_y B_1}{m_o} \right) w_o \\ & + \left[\underline{\underline{\frac{4}{3} A_2 \ddot{U}_B}}} - \left(\underline{\underline{\frac{6EI_y B_2}{m_o}}} \right) \right] w_o^3 = \frac{F(t)}{m_o}. \end{aligned} \quad (2.16)$$

Equation (2.16) represents an ordinary inhomogeneous nonlinear time-dependent differential equation. In addition, this equation holds both the axial contraction and the curvature nonlinear effects. If both the underlined and double underlined terms are ignored, this equation reduces to a classical linear damped forced model. On the other hand, if only the double underlined terms are ignored, this equation reduces to the same equation obtained in [23] plus a forced term. Still, if the double underlined terms plus the nonlinear damping were ignored, this equation reduces to the same model obtained in [24] plus a forced term.

Since the present work is focused on the dynamic response of a structure under parametric sinusoidal excitation, it is considered that this excitation can be written as

$$\ddot{U}_B(t) = -Q\lambda^2 \cos(\lambda t + \varphi) = -Q_o \cos(\lambda t + \varphi) \quad (2.17)$$

in which Q_o is the magnitude of the input base acceleration, λ is the parametric excitation frequency, and φ is a phase shift. Then, (2.16) can be rewritten in the dimensional final form as

$$\begin{aligned} & (1 + A_1^2 w_o^2) \ddot{w}_o + \left(\frac{c_1}{m_o} + \frac{c_2}{m_o} |\dot{w}_o| \right) \dot{w}_o + \left(A_1^2 \dot{w}_o^2 + A_1 Q_o \cos(\lambda t + \varphi) + \frac{EI_y B_1}{m_o} \right) w_o \\ & + \left[-\frac{4}{3} A_2 Q_o \cos(\lambda t + \varphi) - \frac{6EI_y B_2}{m_o} \right] w_o^3 = 0. \end{aligned} \quad (2.18)$$

From the numerical viewpoint, it is interesting to work with the differential equation in dimensionless form. Therefore, by setting new dimensionless variables $w_o^* = A_1 w_o$ and $t^* = t/T_n$ in which T_n is the period of free vibration, the system's equation of motion is given by

$$(1 + w_o^{*2}) \ddot{w}_o^* + H_1 \dot{w}_o^* + H_2 \dot{w}_o^* |\dot{w}_o^*| + [1 + \dot{w}_o^{*2} + H_3 \cos(\Theta t^* + \varphi)] w_o^* - [H_5 + H_4 \cos(\Theta t^* + \varphi)] w_o^{*3} = 0 \quad (2.19)$$

in which

$$\begin{aligned} H_1 &= \frac{c_1 T_n}{m_o}, & H_2 &= \frac{c_2}{m_o A_1}, & H_3 &= Q_o A_1 T_n^2, \\ H_4 &= \frac{4 A_2 Q_o T_n^2}{3 A_1^2}, & H_5 &= \frac{6 B_2 E I_y T_n^2}{m_o A_1^2}, \\ \Theta &= \lambda T_n, & \Psi &= \Omega T_n. \end{aligned} \quad (2.20)$$

Further, we will discuss the effects of variations of the dimensionless quadratic damping coefficient H_2 on the response of the parametrically driven cantilever beam.

3. Perturbation analysis and numerical simulations

In order to address the effects of the quadratic damping (H_2) on the structure's response, a solution of the (2.19) is required. Such a solution is here developed by employing the method of multiple scales (MME) [19]. For that purpose, it is more convenient to rewrite (2.19) in a slight different way by considering zero-order (ε^0) and first-order (ε^1) terms as follows:

$$\begin{aligned} \varepsilon^0 \ddot{w}_o^* + \varepsilon^0 (2\pi)^2 w_o^* &= -\varepsilon^1 w_o^{*2} \ddot{w}_o^* - \varepsilon^1 \dot{w}_o^{*2} \dot{w}_o^* - \varepsilon^1 H_1 \dot{w}_o^* - \varepsilon^1 H_2 \dot{w}_o^* |\dot{w}_o^*| \\ &\quad - \varepsilon^1 H_3 \cos(\Theta t^* + \varphi) w_o^* + \varepsilon^1 H_4 \cos(\Theta t^* + \varphi) w_o^{*3} + \varepsilon^1 H_5 w_o^{*3} \end{aligned} \quad (3.1)$$

in which the dimensionless coefficients $\varepsilon^1 H_1, \varepsilon^1 H_2, \dots, \varepsilon^1 H_5$ are defined according to (2.20). To apply the MME technique, first we express w_o^* as

$$w_o^*(\varepsilon; t^*) = w_0(T_0, T_1) + \varepsilon w_1(T_0, T_1), \quad (3.2)$$

where $T_0 = t$ is the fast time scale associated with changes occurring at the frequency Θ and $T_1 = \varepsilon^1 t$ is a slow time scale associated with the modulations in amplitude and phase.

As it is known, the principal parametric resonance occurs when the parametric excitation Θ assumes a value that is equal to twice the undamped natural frequency ω_n . Therefore, the normalized undamped natural frequency $\bar{\omega}_n = 2\pi$ can be written as

$$(2\pi)^2 = \left(\frac{1}{2}\Theta\right)^2 - \varepsilon\sigma \quad (3.3)$$

in which $\varepsilon\sigma$ is a tuning parameter that flags the proximity of the principal parametric resonance.

By carrying out the standard details of the method of multiple scales, the first approximation to the solution of (3.1) is obtained as

$$w_o^* = a(T_1) \cos[2\pi T_0 + \beta(T_1)] + O(\varepsilon) \quad (3.4)$$

in which $a(T_1)$ and $\beta(T_1)$ are given by

$$\begin{aligned} a' &= \left(-\frac{1}{4\Theta} \varepsilon H_4 a^3 + \frac{1}{2\Theta} \varepsilon H_3 a \right) \sin(2\beta) - \frac{1}{2} \varepsilon H_1 a - \frac{2}{3\pi} \varepsilon H_2 \Theta a^2, \\ a\beta' &= \left(-\frac{1}{2\Theta} \varepsilon H_4 a^3 + \frac{1}{2\Theta} \varepsilon H_3 a \right) \cos(2\beta) + \frac{\varepsilon}{8\Theta} (-6H_5 - \Theta^2) a^3 - \frac{\varepsilon\sigma a}{\Theta} \end{aligned} \quad (3.5)$$

and (3.5) are known as modulation equations. As stated in [19], steady state motions correspond to fixed points (constant solutions) of these modulation equations. Mathematically, this condition is reached when $a'_i = \beta'_i = 0$. Hence, in steady-state condition the modulation equations are rewritten as

$$\begin{aligned} \left(-\frac{1}{4\Theta}\varepsilon H_4 \bar{a}^3 + \frac{1}{2\Theta}\varepsilon H_3 \bar{a} \right) \sin(2\beta) - \frac{1}{2}\varepsilon H_1 \bar{a} - \frac{2}{3\pi}\varepsilon H_2 \Theta \bar{a}^2 &= 0, \\ \left(-\frac{1}{2\Theta}\varepsilon H_4 \bar{a}^3 + \frac{1}{2\Theta}\varepsilon H_3 \bar{a} \right) \cos(2\beta) + \frac{1}{8\Theta}(-6\varepsilon H_5 - \Theta^2)\bar{a}^3 - \frac{\varepsilon \sigma \bar{a}}{\Theta} &= 0, \end{aligned} \quad (3.6)$$

where \bar{a} describes the steady-state vibration amplitude. Trivial solutions of this system of equations are immediately apparent and correspond to the case where $\bar{a} = 0$. Nontrivial solutions ($\bar{a} \neq 0$) are obtained by solving (3.6) in terms of the amplitude \bar{a} and phase angle β . The solution process for these quantities is laborious and can be found in detail in the work by da Silva [19]. The final expression for \bar{a} is given as

$$\bar{a} = \pm \frac{\sqrt{-2E_4 E_2 \pm 2E_4 \sqrt{E_2^2 - 4E_4 E_0}}}{2E_4}, \quad (3.7)$$

where the E_i are given as

$$\begin{aligned} E_4 &= -9\pi^2 \varepsilon H_4 \varepsilon H_3 \Theta^2 \varepsilon \sigma - 54\pi^2 \varepsilon H_4 \varepsilon H_3 \varepsilon H_5 \varepsilon \sigma + 9\pi^2 \varepsilon H_4^2 \varepsilon \sigma^2 - \frac{117}{4}\pi^2 \varepsilon H_4^2 \varepsilon H_3^2 \\ &\quad - 32\Theta^4 \varepsilon H_4 \varepsilon H_3 \varepsilon H_2^2 + \frac{9}{16}\pi^2 \varepsilon H_3^2 \Theta^4 + \frac{81}{4}\pi^2 \varepsilon H_3^2 \varepsilon H_5^2 + \frac{27}{4}\pi^2 \varepsilon H_3^2 \varepsilon H_5 \Theta^2, \\ E_2 &= 27\pi^2 \varepsilon H_4 \varepsilon H_3^3 + 54\pi^2 \varepsilon H_3^2 \varepsilon H_5 \varepsilon \sigma + 16\Theta^4 \varepsilon H_3^2 \varepsilon H_2^2 + 9\pi^2 \varepsilon H_3^2 \Theta^2 \varepsilon \sigma - 36\pi^2 \varepsilon H_4 \varepsilon H_3 \varepsilon \sigma^2, \\ E_0 &= 36\pi^2 \varepsilon H_3^2 \varepsilon \sigma^2 - 9\pi^2 \varepsilon H_3^4, \end{aligned} \quad (3.8)$$

and the phase angle β is written as

$$\beta = \frac{1}{2} \tan^{-1} \left(\frac{G_1}{G_2} \right) \quad (3.9)$$

with coefficients G_1 and G_2 given as

$$\begin{aligned} G_1 &= 8\Theta(4\varepsilon H_2 \Theta \varepsilon H_4 \bar{a}^3 - 4\varepsilon H_2 \Theta \varepsilon H_3 \bar{a}), \\ G_2 &= 3\pi(6\varepsilon H_5 \varepsilon H_4 \bar{a}^4 + \varepsilon H_4 \Theta^2 \bar{a}^4 + 8\varepsilon H_4 \varepsilon \sigma \bar{a}^2) \\ &\quad + 3\pi(-12\varepsilon H_3 \varepsilon H_5 \bar{a}^2 - 2\varepsilon H_3 \Theta^2 \bar{a}^2 - 16\varepsilon H_3 \varepsilon \sigma). \end{aligned} \quad (3.10)$$

Hence, the solution for the modulation equations is given as a function of the parametric excitation frequency Θ , the frequency tuning parameter $\varepsilon \sigma$, and the dimensionless coefficients H_i . Particularly, we are interested in investigating the effects of variations of the dimensionless quadratic damping coefficient H_2 on the amplitude of the response. For that purpose, a series of simulations were performed by varying this parameter on the above equations and computing

the resulting response. Figure 4 shows the computed response \bar{a} from (3.7) for different values of εH_2 . It is seen that variations of this parameter do not alter the critical points C and E . Additionally the nonsymmetric shape of the amplitude-frequency curve tends to decrease as εH_2 increases. It is also noticed that two characteristics of the response are strongly influenced by variations on the quadratic damping coefficient, namely, the amplitude of the response and stability of the nontrivial ramification CG . The maximum value of the amplitude of response \bar{a}_{\max} represents an important information of the system under investigation. In this sense, it is equally important to assess the influence of variations of the nonlinear damping coefficient on \bar{a}_{\max} . Figure 5 shows the behavior of this parameter when variations on εH_2 are introduced. The results were obtained for three different values of the amplitude of the parametric excitation, represented by the dimensionless coefficient εH_3 . Figure 5(a) shows that for small values of εH_2 ($0 < \varepsilon H_2 < 0.1$), \bar{a}_{\max} is relatively insensitive to variations on εH_2 . The largest impact of εH_2 on \bar{a}_{\max} occurs in the $0.2 < \varepsilon H_2 < 0.5$ range, becoming less sensitive as εH_2 approaches the end of the range. Figure 5(b) shows essentially the same trend where the values of the relative reduction of the amplitude are depicted. As previously pointed out in Figure 4, the stability of the nontrivial ramification CG is strongly affected by the nonlinear quadratic damping since it involves the definition of the bifurcation shown in point G . This bifurcation is responsible for the jump phenomenon when the values of the tuning parameter $\varepsilon \sigma$ are varied in the ascending order. From the numerical solution of (3.7) we can identify critical values of εH_2 in the response-frequency curve that will make the bifurcation disappear. These critical values can be found from the following expression:

$$\varepsilon H_2^{\text{crit}} = -0.012\varepsilon H_3^2 + 0.14\varepsilon H_3 + 0.14 \quad (3.11)$$

and they are represented in Figure 6. Hence, from this equation it is possible to estimate values for the εH_2 for a given known excitation condition (εH_3) that would make the jump phenomenon to completely disappear from the system's response. Figure 7 shows the effects of variations of the εH_2 in the system's response when the excitation amplitude is varied. It can be seen that the critical point C is not affected by the different values of εH_2 . On the other hand, the vibration amplitude and the stability of the nontrivial ramification CF are strongly affected when varying the values of the quadratic damping coefficient. It is also interesting to observe in Figure 7 the magnitude of the response at D and F , here referred to as \bar{a}_D and \bar{a}_F , respectively. The value of \bar{a}_D indicates the minimum value of the vibration amplitude as soon as the parametric resonance occurs, or, if the critical point C is exceeded. The value of \bar{a}_F reflects the minimum value of the amplitude at the moment that the principal parametric resonance condition ceases. The variation of \bar{a}_D and \bar{a}_F with respect to εH_2 is shown in Figure 8.

3.1. Response-nonlinear damping curves

In the previous analysis, a series of numerically simulated results have shown in detail how the nonlinear quadratic damping affects the response of the cantilever beam under parametric excitation. In this section, we continue to explore these effects from the numerical standpoint by defining the response-nonlinear damping curves. This curve is obtained from a specific vibration condition imposed to the structure under test by the excitation mechanism, and Figure 9 defines three distinct operating regions (marked as I, II, and III) that differ essentially in terms of the excitation frequency imposed to the system as well as resulting vibration

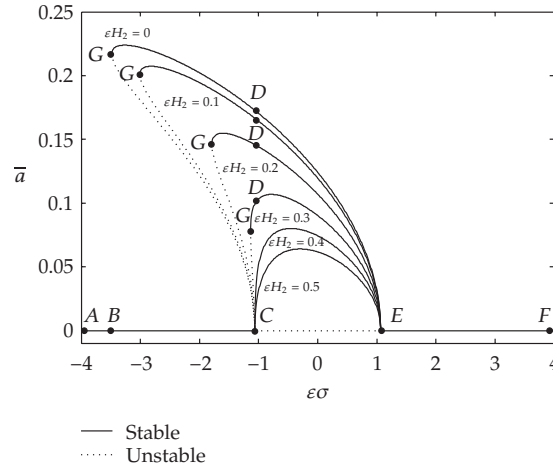


Figure 4: Typical response-frequency curve showing the effects of varying the quadratic dimensionless term H_2 and $\varepsilon H_1 = 0.0$ (nontrivial), $\varepsilon H_1 = 0.016$ (trivial), $\varepsilon H_3 = 2.1352$, $\varepsilon H_4 = 3.4674$, $\varepsilon H_5 = 62.7218$ [19].

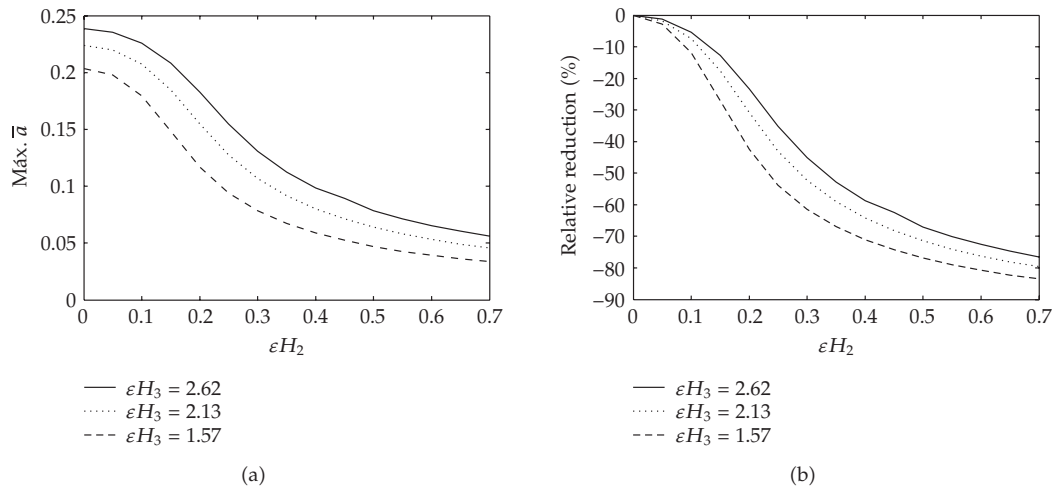


Figure 5: Influence of quadratic damping variation on the nontrivial response solution \bar{a} : (a) variation of the maximum value of \bar{a} with the nonlinear damping and (b) percent reduction of the maximum value of \bar{a} for vacuum operation. Curves obtained for (—) $\varepsilon H_1 = 0.0$, $\varepsilon H_3 = 2.62$, $\varepsilon H_4 = 4.25$, $\varepsilon H_5 = 62.72$; (···) $\varepsilon H_1 = 0.0$, $\varepsilon H_3 = 2.13$, $\varepsilon H_4 = 3.46$, $\varepsilon H_5 = 62.72$; (---) $\varepsilon H_1 = 0.0$, $\varepsilon H_3 = 1.57$, $\varepsilon H_4 = 2.55$, $\varepsilon H_5 = 62.72$ [19].

amplitude. Two operation points $P1$ and $P2$ are chosen in regions I and II, respectively, with corresponding amplitudes given by \bar{a}_{P1} and \bar{a}_{P2} . Figure 10 shows how variations on εH_2 affect the amplitude \bar{a}_{P1} . Two ramifications form this curve, one stable (solid line) and one unstable (dashed line). In case εH_2 is decreased to the value $\varepsilon H_2 = 0$, the structure still remains vibrating but with an amplitude approximately 4% larger. Similarly, if εH_2 increases beyond point $P1$, the vibration amplitude decreases on the stable nontrivial ramification until point C is reached. At this point, \bar{a}_{P1} is reduced by 19%. If εH_2 exceeds point C , the nontrivial stable solution

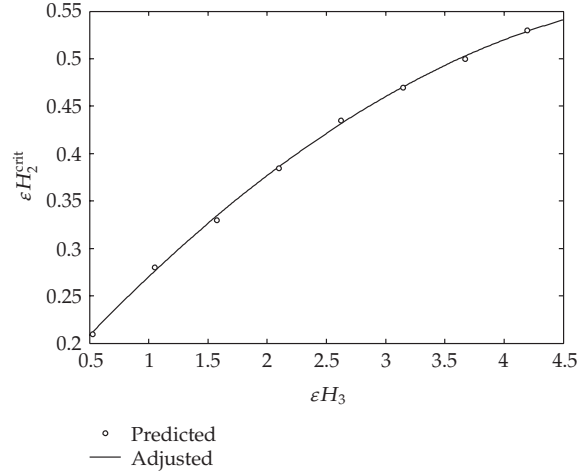


Figure 6: Critical values of εH_2 as a function of εH_3 [19].

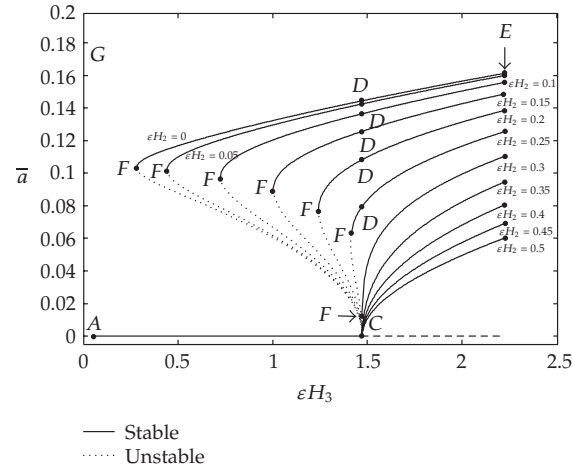


Figure 7: Typical response-amplitude curve demonstrating the effects of varying the quadratic nonlinear damping term (εH_2) for $\varepsilon \sigma = -0.73$. Also $\varepsilon H_1 = 0.0$ (nontrivial), $\varepsilon H_1 = 0.016$ (trivial), and $\varepsilon H_5 = 62.7218$ [19].

looses stability through a bifurcation and the vibration is extinct. When the structure vibrates according to point P_2 , the magnitude of the response is given by \bar{a}_{P_2} . Figure 11 shows the effects on the system's response \bar{a}_{P_2} produced by varying the values of εH_2 . In this case, a single stable ramification is observed, and independently on how εH_2 is varied the response continues being nontrivial and stable. On the other hand, there is a strong reduction in the value of \bar{a}_{P_2} .

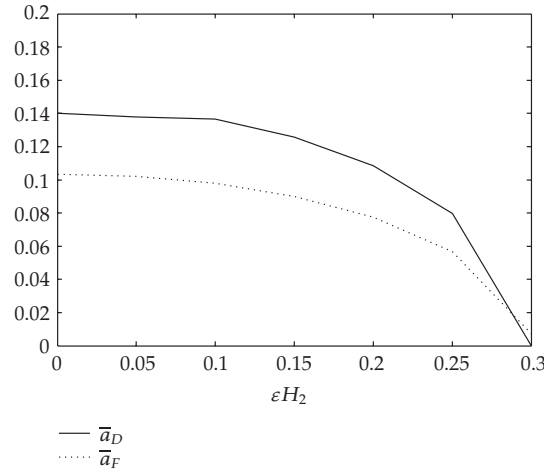


Figure 8: Typical plots showing the effects of the nonlinear quadratic damping on points D and F . Results obtained with $\epsilon\sigma = -0.73$, $\epsilon H_1 = 0.0$ (nontrivial), $\epsilon H_1 = 0.016$ (trivial), and $\epsilon H_5 = 62.7218$ [19].

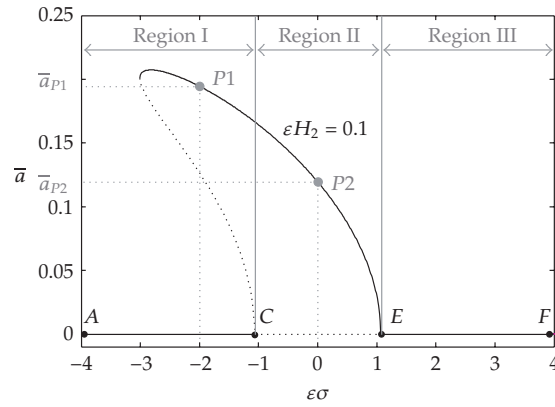


Figure 9: Typical response-frequency curve showing two specific operation points, designated as $P1$ and $P2$. Results obtained with $\epsilon H_1 = 0.0$ (nontrivial), $\epsilon H_1 = 0.016$ (trivial), $\epsilon H_2 = 0.1$, $\epsilon H_3 = 2.1352$, $\epsilon H_4 = 3.4674$, $\epsilon H_5 = 62.7218$ [19].

4. Experimental analysis

This section describes an experimental analysis that was performed on the structure shown in Figure 1. Initially some basic properties of the cantilever beam-mass system such as first bending damped natural frequency and modal damping ratio were obtained by standard modal testing procedures. In this case, the step relaxation method was employed to excite the system in order to get the driving point frequency response function (FRF) at the beam's end point [25]. The resulting values found for the first bending damped natural frequency and viscous modal damping ratio were $\omega_d = 18.066$ Hz and $\zeta_m = 0.1272\%$, respectively. These results were used to correlate the experimental results with the analytical prediction as well as in the planning of nonlinear tests. A detailed explanation of this procedure can be found in [19, 23].

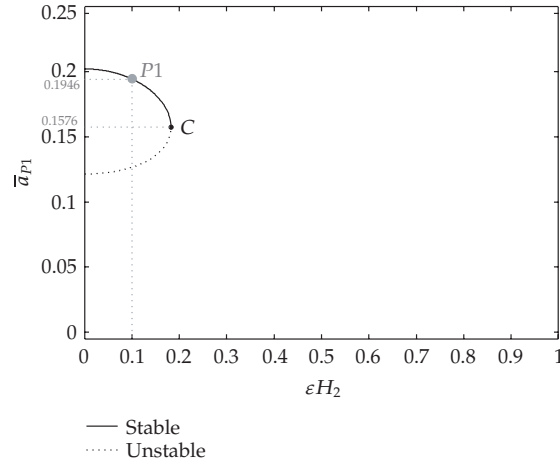


Figure 10: Typical response-quadratic damping curve showing the effects of variations of εH_2 on the magnitude of the response. Results obtained with $\varepsilon H_1 = 0.0$ (nontrivial), $\varepsilon H_1 = 0.016$ (trivial), $\varepsilon H_3 = 2.1352$, $\varepsilon H_4 = 3.4674$, $\varepsilon H_5 = 62.7218$, and $\varepsilon \sigma = -2$ [19].

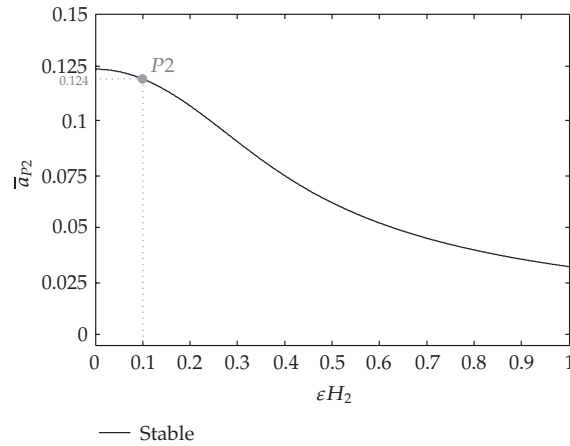


Figure 11: Typical response-quadratic damping curve showing the effects of variations of εH_2 on the magnitude of the response. Results obtained with $\varepsilon H_1 = 0.0$ (nontrivial), $\varepsilon H_1 = 0.016$ (trivial), $\varepsilon H_3 = 2.1352$, $\varepsilon H_4 = 3.4674$, $\varepsilon H_5 = 62.7218$, and $\varepsilon \sigma = 0$ [19].

Once these basic linear characteristics were found, the system of Figure 1 was subjected to a base driven test according to the experimental setup shown in Figure 12. The beam carrying the lumped mass at one end is first attached at the opposite end to a steel block in order to properly simulate the fixed end boundary condition. This assembly is then mounted on the vibrating table of a B&K type 4810 electrodynamic vibration exciter that will drive the system in the vertical direction. The excitation signal is provided by the HP Agilent E1432A data acquisition board that is controlled by the MTS I-Deas 10 modal testing software. The sinusoidal input signal was first sent to a B&K power amplifier type 2707

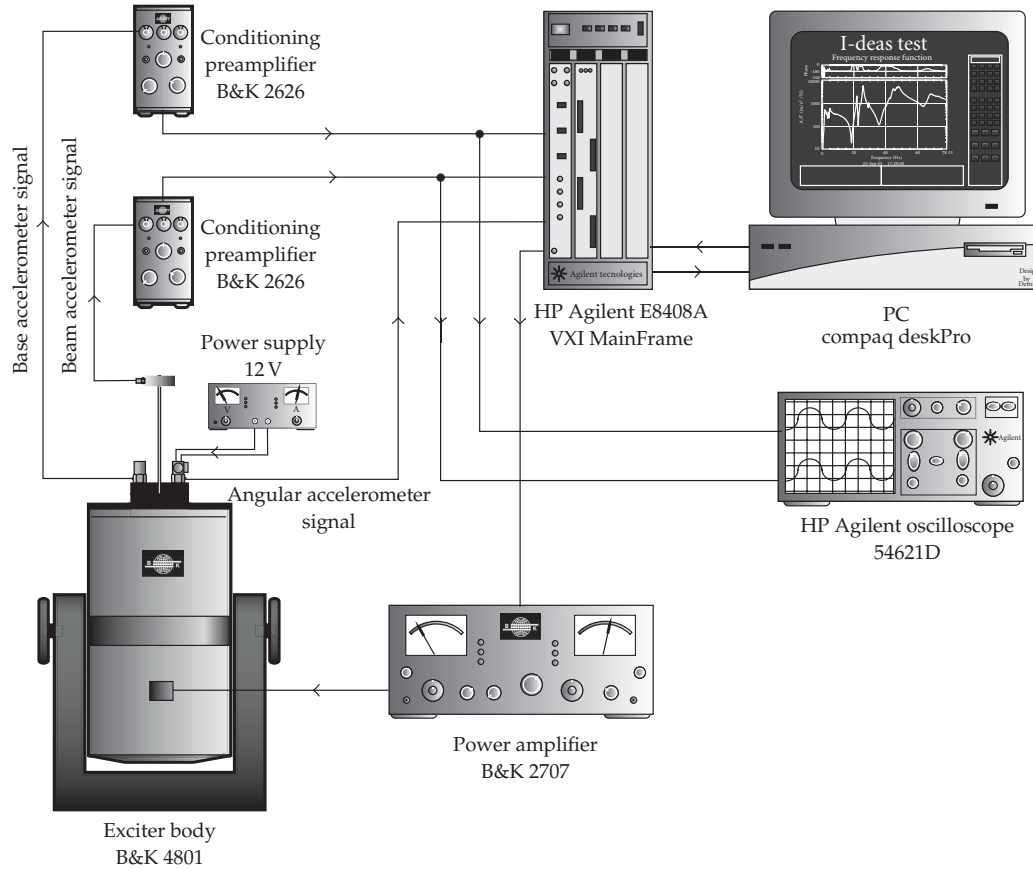


Figure 12: Experimental layout employed to obtain the experimental frequency-response and amplitude-response curves [19–21].

and further sent to a B&K type 4810 electrodynamic vibration exciter. The beam's transverse output signal was monitoring using an HP Agilent oscilloscope type 54621D. To minimize the rocking and translation, the shaker was clamped securely to the floor in the testing room. The sensing mechanism employed is three piezoelectric accelerometers, two for monitoring the base's motion and one for the beam-mass-system's motion. The base's linear translation motion was measured using an accelerometer B&K model 4371 (9.84 pC/g), and possible rocking motion about Y axis was measured using a Kistler angular accelerometer model 8836M01 ($34 \mu \text{ V/rad/s}^2$). The beam-mass-system's translation motion was measured using an accelerometer B&K model 4374 (1.06 pC/g) and mass of 0.64 g .

In order to perform a coherent comparative analysis with the theoretical results, four experimental tests were conducted. In two of these tests, the amplitude of the base excitation acceleration was maintained constant at 39.24 m/s^2 and the sinusoidal excitation signal was slowly varied upward and downward in the frequency range of interest. The remaining tests were performed by keeping the excitation frequency constant at 36.132 Hz , and then increasing the amplitude of the input excitation signal in the power amplifier. It should be noticed that the excitation frequency of 36.132 Hz corresponds to the so-called principal parametric excitation

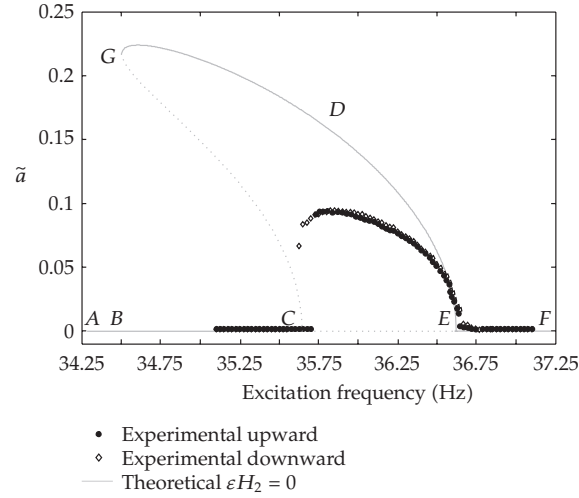


Figure 13: Experimental and theoretical response-frequency curves of the first flexural mode when $\epsilon H_2 = 0.00$ and for $\epsilon H_1 = 0.0160$ (trivial), $\epsilon H_1 = 0.0160$ (nontrivial), $\epsilon H_3 = 2.1352$; $\epsilon H_4 = 3.4674$; $\epsilon H_5 = 62.7218$. Experimental results for parametric excitation frequency at 36.132 Hz and 39.24 m/s². (—) stable solution; (···) unstable solution [20].

frequency since it is approximately twice the system's first bending natural frequency thus satisfying the 2 : 1 relationship that is required to drive such a system into a principal parametric resonance condition [26].

The process of obtaining the experimental frequency-response curve consists of varying the excitation frequency while keeping the magnitude of the input base acceleration constant. The input base acceleration was maintained constant during the tests. A similar process was used to obtain the amplitude-response curves, however the frequency of excitation was kept constant and the amplitude was changed in small increments.

Figure 13 shows the experimental and theoretical frequency-response curves for the first bending mode. The theoretical curve was obtained in the absence of quadratic damping (i.e., $\epsilon H_2 = 0.00$), while the experimental was obtained in atmospheric conditions.

The theoretical results in the upward direction show that by increasing the excitation frequency starting at point A, the trivial solution loses stability at point C, which corresponds to the critical value $\epsilon \sigma = -\epsilon H_3/2$, through a subcritical pitchfork bifurcation and jumps up to point D. This point belongs to the nontrivial stable branch GDE. From point D, the steady-state amplitude of parametric response \tilde{a} decreases as the excitation frequency is increased, until point E is reached. From this point, the nontrivial solution loses stability through a supercritical pitchfork bifurcation and the trivial solution is reached again.

On the other hand, theoretical results in the downward direction show that decreasing the frequency of excitation from point F, the trivial solution loses stability at point E, corresponding to the critical value $\epsilon \sigma = \epsilon H_3/2$, through a supercritical pitchfork bifurcation, and the nontrivial stable branch GDE is reached. From the point E, the response amplitude \tilde{a} increases as the frequency is decreased. The solution loses stability through a turning point at point G and the response amplitude jumps down to point B where only the trivial solution exists thereafter.

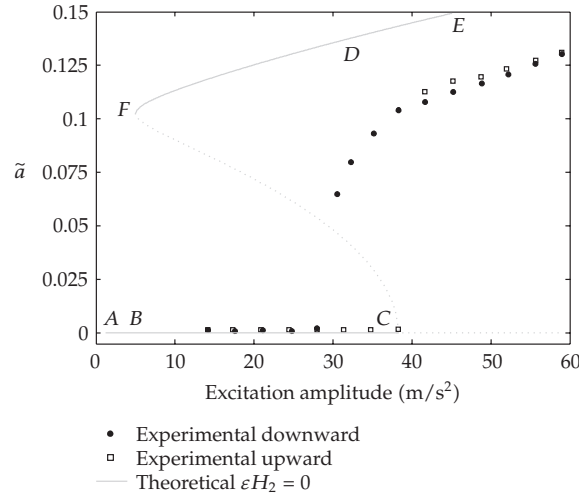


Figure 14: Experimental and theoretical amplitude-response curves of the first flexural mode when $\varepsilon H_2 = 0.00$ and for $\varepsilon H_1 = 0.0160$ (trivial), $\varepsilon H_1 = 0.0160$ (nontrivial), $\varepsilon H_3 = 2.2236$; $\varepsilon H_4 = 3.6109$; $\varepsilon H_5 = 62.7218$ and $\varepsilon \sigma = -0.725$. Experimental results for parametric excitation frequency at 36.132 Hz. (—) stable solution; (···) unstable solution [20].

When the theoretical behavior described above is confronted with the experimental results, it can be claimed that a good qualitative match between theory and experiment exists, mainly in the vicinity of the bifurcation frequencies. However, quantitatively there is an enormous difference between the amplitudes of theoretical and experimental results. The maximum theoretical value for the response amplitude is about $\tilde{a} \approx 0.225$, while the maximum experimental value is about $\tilde{a} \approx 0.1$, that is, about 125% smaller. This difference suggests the existence of important dissipative forces acting on the structure.

From this last result, it can be seen that by introducing the nonlinear quadratic damping a strong reduction of response amplitude has been achieved. Particularly, by using $\varepsilon H_2 = 0.333$, an excellent agreement between the experimental and theoretical results was obtained. However, a slight discrepancy was observed in terms of the bifurcation points mainly in the upward sweep. Consequently, there is no exact agreement around point C. An analogous result was obtained for bifurcation point E.

Figure 14 shows the experimental and theoretical amplitude-response curves also for the first bending mode. Since an exact resonance condition ($\varepsilon \sigma = 0$) is difficult to be achieved, the theoretical curve was obtained for $\varepsilon \sigma < 0$. In addition, the result shown was obtained in the absence of quadratic damping (i.e., $\varepsilon H_2 = 0.00$) while the experimental result was obtained in atmospheric conditions.

The theoretical results in the upward direction shows that by increasing the excitation amplitude from point A, the trivial solution loses stability at point C, corresponding to the critical value $\varepsilon H_3 = \sqrt{4\varepsilon \sigma^2 + \varepsilon H_1^2 \Theta^2}$, through a subcritical pitchfork bifurcation and jumps up to point D. This point belongs to the nontrivial stable branch FDE. A further increase in the excitation amplitude leads to higher response amplitudes tracing the branch DE.

On the other hand, the theoretical results in the downward direction shows that by decreasing the excitation amplitude from point E, the amplitude response continually

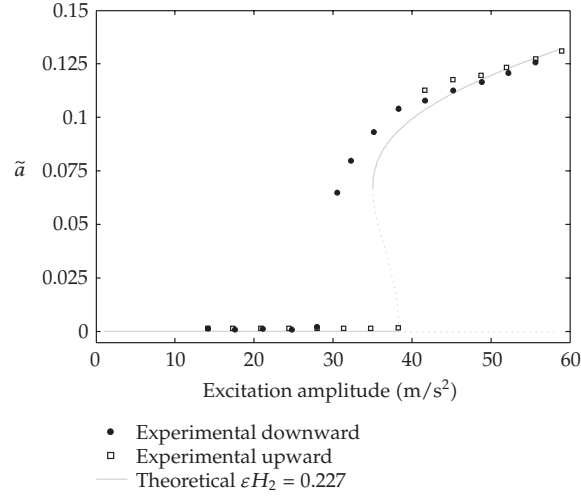


Figure 15: Experimental and theoretical amplitude-response curves of the first flexural mode when $\epsilon H_2 = 0.227$ and for $\epsilon H_1 = 0.0160$ (trivial), $\epsilon H_1 = 0.00$ (nontrivial), $\epsilon H_3 = 2.2236$, $\epsilon H_4 = 3.6109$, $\epsilon H_5 = 62.7218$, and $\epsilon \sigma = -0.725$. Experimental results for parametric excitation frequency at 36.132 Hz. (—) stable solution; (---) unstable solution [20].

decreases until point F is reached. Then, the nontrivial solution loses stability through a turning point bifurcation, leading to a jump down to point B whereby only the trivial solution exists thereafter.

When the theoretical behavior described above is confronted with the experimental results, a very good qualitative as well as quantitative disagreement between them exists. These two characteristics also suggest the existence of important dissipative force acting on the structure. In order to prove this point, an additional theoretical amplitude-response curve was obtained, but now, including the nonlinear quadratic damping effects. The results are shown in Figure 15.

In this last figure, it can be claimed that by introducing the nonlinear quadratic damping a much better match between theory and experiment was obtained, specially when $\epsilon H_2 = 0.227$ is used. However, some discrepancies related to response amplitude, as well as with the bifurcation point F , were observed. A close view in region between 30 m/s^2 and 50 m/s^2 revealed 20% difference in the amplitude response. On the other hand, this discrepancy tends to decrease with the increase of the excitation amplitude. Also, there is a discrepancy related with the bifurcation point F . In the theoretical prediction, it occurs about 35 m/s^2 , whereas in the experimental results it is shown at 30 m/s^2 showing a 17% difference.

5. Concluding remarks

This article addressed numerically and experimentally the effects of viscous fluid medium on the dynamic response of a cantilever beam carrying a lumped mass. Numerically simulated results showed the effects of variations induced in the nonlinear damping on the acceleration response of the test structure when it undergoes a principal parametric resonance condition. Experimental assessment on the effects of quadratic damping due to frictional turbulent force on the structure's dynamic response has been obtained. Generally speaking, good agreement

between experimental and numerically simulated results was achieved in terms of frequency and amplitude response curves. It was observed that the quadratic damping due to frictional turbulent force plays an important role in the response of parametrically excited cantilever beam carrying a lumped mass. The inclusion of the quadratic damping significantly improves the theoretical predictions, and it should be included in the mathematical models when the problem involves the principal parametric response. Although the results shown in this paper were obtained for the first bending mode, similar conclusions may be obtained for higher natural frequencies.

References

- [1] R. A. Ibrahim, "Structural dynamics with parameter uncertainties," *Applied Mechanics Reviews*, vol. 40, no. 3, pp. 309–328, 1987.
- [2] S. Adhikari, "On the quantification of damping model uncertainty," *Journal of Sound and Vibration*, vol. 306, no. 1-2, pp. 153–171, 2007.
- [3] J. Guo and X. Du, "Sensitivity analysis with mixture of epistemic and aleatory uncertainties," *AIAA Journal*, vol. 45, no. 9, pp. 2337–2349, 2007.
- [4] J. R. Fonseca, M. I. Friswell, J. E. Mottershead, and A. W. Lees, "Uncertainty identification by the maximum likelihood method," *Journal of Sound and Vibration*, vol. 288, no. 3, pp. 587–599, 2005.
- [5] C. Soize, "A comprehensive overview of a non-parametric probabilistic approach of model uncertainties for predictive models in structural dynamics," *Journal of Sound and Vibration*, vol. 288, no. 3, pp. 623–652, 2005.
- [6] D. Moens and D. Vandepitte, "A fuzzy finite element procedure for the calculation of uncertain frequency-response functions of damped structures—part 1: procedure," *Journal of Sound and Vibration*, vol. 288, no. 3, pp. 431–462, 2005.
- [7] H. De Gerssem, D. Moens, W. Desmet, and D. Vandepitte, "A fuzzy finite element procedure for the calculation of uncertain frequency response functions of damped structures—part 2: numerical case studies," *Journal of Sound and Vibration*, vol. 288, no. 3, pp. 463–486, 2005.
- [8] C. Chen, D. Duhamel, and C. Soize, "Probabilistic approach for model and data uncertainties and its experimental identification in structural dynamics: case of composite sandwich panels," *Journal of Sound and Vibration*, vol. 294, no. 1-2, pp. 64–81, 2006.
- [9] A. Carcaterra, "Ensemble energy average and energy flow relationships for nonstationary vibrating systems," *Journal of Sound and Vibration*, vol. 288, no. 3, pp. 751–790, 2005.
- [10] P. J. Shorter and R. S. Langley, "Vibro-acoustic analysis of complex systems," *Journal of Sound and Vibration*, vol. 288, no. 3, pp. 669–699, 2005.
- [11] V. Cotoni, R. S. Langley, and M. R. F. Kidner, "Numerical and experimental validation of variance prediction in the statistical energy analysis of built-up systems," *Journal of Sound and Vibration*, vol. 288, no. 3, pp. 701–728, 2005.
- [12] L. G. Crespo, D. P. Giesy, and S. P. Kenny, "Robustness analysis and robust design of uncertain systems," *AIAA Journal*, vol. 46, no. 2, pp. 388–396, 2008.
- [13] C. L. Pettit, "Uncertainty quantification in aeroelasticity: recent results and research challenges," *Journal of Aircraft*, vol. 41, no. 5, pp. 1217–1229, 2004.
- [14] J. M. Nichols, P. Marzocca, and A. Milanese, "On the use of the auto-bispectral density for detecting quadratic nonlinearity in structural systems," *Journal of Sound and Vibration*, vol. 312, no. 4-5, pp. 726–735, 2008.
- [15] N. HaQuang, D. T. Mook, and R. H. Plaut, "A nonlinear analysis of the interactions between parametric and external excitations," *Journal of Sound and Vibration*, vol. 118, no. 3, pp. 425–439, 1987.
- [16] N. HaQuang, D. T. Mook, and R. H. Plaut, "Non-linear structural vibrations under combined parametric and external excitations," *Journal of Sound and Vibration*, vol. 118, no. 2, pp. 291–306, 1987.
- [17] A. H. Nayfeh and L. D. Zavodney, "Experimental observation of amplitude- and phase-modulated responses of two internally coupled oscillators to a harmonic excitation," *Journal of Applied Mechanics*, vol. 55, no. 3, pp. 706–710, 1988.

- [18] T. J. Anderson, A. H. Nayfeh, and B. Balachandran, "Experimental verification of the importance of the nonlinear curvature in the response of a cantilever beam," *Journal of Vibration and Acoustics*, vol. 118, no. 1, pp. 21–27, 1996.
- [19] D. G. da Silva, *Nonlinear vibrations in resonant beam type structures*, Ph.D. thesis, Department of Mechanical Engineering, University of São Paulo, Campus of São Carlos, Sao Carlos, Brazil, 2005.
- [20] P. S. Varoto and D. G. da Silva, "On the role of quadratic damping in the parametric response of a cantilever beam with tip mass: experimental investigation," in *Proceedings of the 5th Euromech Nonlinear Dynamics Conference (ENOC '05)*, pp. 1–13, University of Technology, Eindhoven, The Netherlands, August 2005.
- [21] P. S. Varoto and D. G. da Silva, "Nonlinear dynamic behavior of a flexible structure to combined external acoustic and parametric excitation," *Shock and Vibration*, vol. 13, no. 4-5, pp. 233–254, 2006.
- [22] L. Meirovitch, *Methods of Analytical Dynamics*, McGraw-Hill, New York, NY, USA, 1970.
- [23] D. G. da Silva and P. S. Varoto, "On the sufficiency of classical response models in predicting the dynamic behavior of flexible structures," in *Proceeding of the 12th International Modal Analysis Conference (IMAC '04)*, pp. 1–21, SEM, Dearborn, Mich, USA, January 2004.
- [24] M. Cartmell, *Introduction to Linear, Parametric and Nonlinear Vibrations*, Chapman and Hall, London, UK, 1990.
- [25] K. G. McConnell, *Vibration Testing: Theory and Practice*, John Wiley & Sons, Chichester, UK, 1995.
- [26] A. H. Nayfeh and D. T. Mook, *Nonlinear Oscillations*, Pure and Applied Mathematic, John Wiley & Sons, New York, NY, USA, 1979.

Research Article

Influence of Uncertainties on the Dynamic Buckling Loads of Structures Liable to Asymmetric Postbuckling Behavior

Paulo B. Gonçalves¹ and Donald Mark Santee²

¹ *Departamento de Engenharia Civil, Pontifícia Universidade Católica do Rio de Janeiro (PUC-Rio),
Rua Marquês de São Vicente 225, Gávea, 22453-900 Rio de Janeiro, RJ, Brazil*

² *Department of Mathematics, Federal University of Goiás (UFG), Campus of Catalão,
75705-220 Catalão, GO, Brazil*

Correspondence should be addressed to Paulo B. Gonçalves, paulo@civ.puc-rio.br

Received 26 February 2008; Accepted 9 April 2008

Recommended by Jose Balthazar

Structural systems liable to asymmetric bifurcation usually become unstable at static load levels lower than the linear buckling load of the perfect structure. This is mainly due to the imperfections present in real structures. The imperfection sensitivity of structures under static loading is well studied in literature, but little is known on the sensitivity of these structures under dynamic loads. The aim of the present work is to study the behavior of an archetypal model of a harmonically forced structure, which exhibits, under increasing static load, asymmetric bifurcation. First, the integrity of the system under static load is investigated in terms of the evolution of the safe basin of attraction. Then, the stability boundaries of the harmonically excited structure are obtained, considering different loading processes. The bifurcations connected with these boundaries are identified and their influence on the evolution of safe basins is investigated. Then, a parametric analysis is conducted to investigate the influence of uncertainties in system parameters and random perturbations of the forcing on the dynamic buckling load. Finally, a safe lower bound for the buckling load, obtained by the application of the Melnikov criterion, is proposed which compares well with the scatter of buckling loads obtained numerically.

Copyright © 2008 Paulo B. Gonçalves and D. M. Santee. This is an open access article distributed under the Creative Commons Attribution License, which permits unrestricted use, distribution, and reproduction in any medium, provided the original work is properly cited.

1. Introduction

During the past few decades, a considerable effort within the engineering sciences has been directed towards understanding the behavior of structures that exhibit unstable postbuckling behavior [1–3]. The main motivation for this comes from a notorious and persistent discrepancy between theoretical and experimental results of the buckling loads of several slender structures, being that the experimental results are lower than the theoretical ones.

A general explanation for this upsetting behavior is given by Koiter in his pioneering work on the general theory of buckling and postbuckling behavior of elastic structures [4]. He showed that imperfections in the geometry or in the load might decrease substantially the load carrying capacity of these structures under slow variation of the applied load. This scenario becomes even worse if the unavoidable uncertainties in system parameters are also taken into account. Elishakoff [5] and Kounadis [6], among others, studied imperfection-sensitive structures under a step load. Because the expressions for the critical load are developed from a static equilibrium analysis, they actually calculate an upper bound for the load carrying capacity of the real structure, since they do not take into account the disturbances imposed upon the imperfect structure during its service life [7]. The influence of these disturbances on the integrity of the structure can be evaluated by analyzing the evolution of the basin of attraction of the stable equilibrium configuration as a function of the system parameters. To take indirectly into account these deleterious effects, lower bounds of buckling loads have been proposed for design. They are usually based on the scatter of experimental buckling loads [8, 9]. However, in the past decades researchers have sought to deduce theoretically well-founded lower bounds for imperfection-sensitive structures under static load. Croll [8] developed the so-called reduced stiffness method based on the elimination in the potential energy of the structure of the energy components mostly eroded by the imperfections. Based on this idea, reliable lower bounds have been deduced for a series of structures [8, 9].

The estimation of the dynamic buckling load of structures with unstable postbuckling branches—the load corresponding to escape from the safe prebuckling well—considering the effects of uncertainties and imperfections is a much more difficult task. Structures under dynamic loads may exhibit both local and global bifurcations that affect in different ways the load carrying capacity and degree of safety of the structure. Global bifurcations are particularly important since they control, as shown by Thompson et al. [10–13], the evolution of the basins of attraction of the solutions in phase space. In addition, compared with the static case, the number of load control parameters is higher. Finally, experimental results of dynamic buckling loads of slender structures are rather scarce in literature [14, 15]. Therefore, little is known on the effects of uncertainties on the load carrying capacity of structures liable to unstable static buckling. Therefore, the aim of the present work is to shed some light on this problem by analyzing the behavior of an archetypal model of a harmonically forced structure liable to asymmetric bifurcation under increasing static load.

First, the evolution of the basin of attraction of the static equilibrium configuration is studied. Then, the dynamic buckling load under different loading conditions is evaluated and the different types of bifurcation connected with the instability boundaries in force control space are identified. Next, a detailed parametric analysis clarifies the influence of uncertainties in load and system parameters on the dynamic buckling load. Based on these results, a lower bound is proposed which compares favorably with the scatter of buckling loads obtained in the analysis.

The evolution of the basins of attraction of these systems is governed in a large extent by the evolution of the stable and unstable manifolds of the saddle connected with the hilltop that separates the pre- and postbuckling wells. Thompson et al. have studied this connection in detail [10–13]. They show that the erosion and stratification of the basin of attraction increases significantly after the first crossing of the stable and unstable manifolds. The load level associated with such event can be obtained by the application of the Melnikov criterion, which measures the distance between the manifolds [16, 17]. It can be applied to lightly

damped system, which is usually the case of slender structures found in structural engineering. The present work shows that the zeros of the Melnikov function can be used as a basis for the deduction of safe lower bounds that can be used effectively in design. Rega and Lenci [18] discussed recently the use of integrity measures in nonlinear mechanical oscillators based on the evolution of basins of attraction.

A classical example that illustrates asymmetric buckling behavior in structural system is the plane frame studied by Roorda [1–3, 19]. Recently, Galvão et al. [20] published a detailed parametric analysis of this frame structure showing the influence of the system parameters on its postbuckling behavior and imperfection sensitivity. Another system is the perfect shallow spherical cap under lateral pressure [21].

Analyses of the dynamics of structures liable to asymmetric bifurcations have been studied by, among others, Virgin [22] and Donescu et al. [23]. General analyses of the static buckling behavior of systems with asymmetric postbuckling behavior have been conducted recently by Ohaki [24] and Banchio and Godoy [25].

2. Formulation of the problem

Consider an SDOF system with quadratic nonlinearity that exhibits under the variation of a static load parameter a transcritical bifurcation point. The equation of motion of such a system can be written as

$$\ddot{x} + 2\eta\omega_0\dot{x} + \varepsilon + \omega_0^2x + \beta x^2 = F\cos(\Omega t) \quad (2.1)$$

where η is the viscous damping parameter, $\omega_0 = \sqrt{(\lambda_{cr} - \lambda)/m}$ is the natural frequency of the statically loaded structure in which λ_{cr} is a critical load parameter, λ is an applied load parameter and m is the mass (this expression describes the load frequency, leading to $\omega_0^2 = 0$ at $\lambda = \lambda_{cr}$), ε is an imperfection parameter, β is a nonlinearity parameter, F is the magnitude of the externally applied load, and Ω is the excitation frequency. The dots indicate derivation with respect to time t .

Equation (2.1) is sometimes called Helmholtz equation [26], meaning a single-well potential with one escape direction. It applies also to other fields of mechanics such as the rolling of asymmetric vessels, in which case the critical threshold corresponds to overturning [10]. In fact, (2.1) is the archetypal model of an asymmetric bifurcation where the parameter ε is the perturbation responsible for the unfolding [27, 28]. As an example, (2.1) is derived in the appendix for a structural system liable to asymmetric bifurcation [1–3].

2.1. Analysis of the autonomous system

For the autonomous undamped system, there are two fixed points. They are

$$x_{(eq1)} = \frac{1}{2} \frac{-\omega_0^2 + \sqrt{\omega_0^4 - 4\beta\varepsilon}}{\beta}, \quad (2.2a)$$

$$x_{(eq2)} = \frac{1}{2} \frac{-\omega_0^2 - \sqrt{\omega_0^4 - 4\beta\varepsilon}}{\beta}. \quad (2.2b)$$

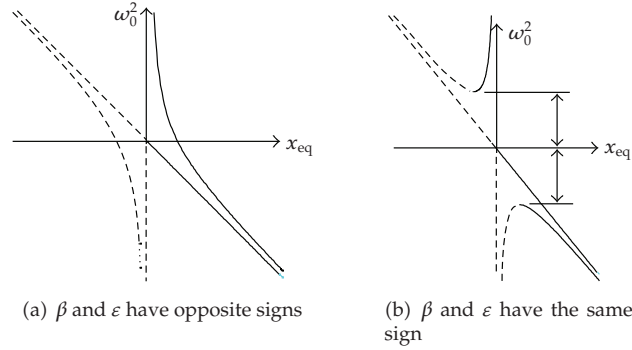


Figure 1: Equilibrium paths of the perfect and imperfect structures ($\beta = 1$).

For the equilibrium branch described by (2.2a), the eigenvalues are

$$\begin{aligned}\mu_1 &= \sqrt{-\sqrt{\omega_0^4 - 4\beta\varepsilon}}, \\ \mu_2 &= -\sqrt{-\sqrt{\omega_0^4 - 4\beta\varepsilon}}.\end{aligned}\tag{2.3}$$

For the equilibrium solution (2.2b), the eigenvalues are

$$\begin{aligned}\mu_1 &= \sqrt{\sqrt{\omega_0^4 - 4\beta\varepsilon}}, \\ \mu_2 &= -\sqrt{\sqrt{\omega_0^4 - 4\beta\varepsilon}}.\end{aligned}\tag{2.4}$$

Figure 1 shows, for $\beta > 0$, the variation of ω_0^2 as a function of the equilibrium position x_{eq} . Continuous lines correspond to stable equilibrium paths, and dashed lines correspond to unstable paths. A similar figure, symmetric with respect to the ω_0^2 axis, is obtained for $\beta < 0$. For the perfect system and for the imperfect system when β and ε have opposite signs, there are for any load level two equilibrium positions, a center and a saddle. For the imperfect system, when β and ε have the same sign, there is a region below and above the critical value ($\omega_0^2 = 0$ or $\lambda = \lambda_{cr}$) where no solution occurs. This region is bounded by two limit loads corresponding to saddle-node bifurcations. The limit load defines thus the load carrying capacity of a real imperfect system. The limit load parameter is given by

$$\lambda_{lim} = \lambda_{cr} - 2\sqrt{\beta\varepsilon}.\tag{2.5}$$

The limit load may be attained only in a slowly evolving, quasistatic, system. Nonzero initial conditions will further decrease the buckling load. In fact, the limit load is but an upper bound of the load carrying capacity of the imperfect system under static loading. The area of the basin of attraction at the critical point is zero. Therefore, any small disturbance leads to buckling. A good measure of the integrity and safety of the system is the area and topology of

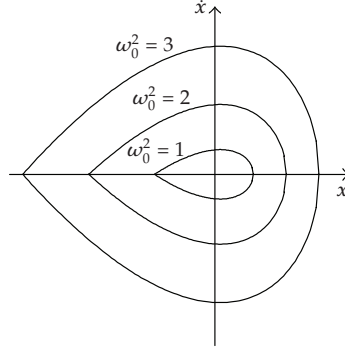


Figure 2: Variation of the safe region defined by the homoclinic orbit of the saddle corresponding to the unstable equilibrium point. $\varepsilon = 0, \beta = -1$.

the basin of attraction [18]. For the undamped autonomous system, bounded solution only occurs for initial condition within the area defined by the homoclinic orbit of the saddle connected with the unstable solution in Figure 1. The area enclosed by the homoclinic orbit is given by

$$A = 2 \int_{x_{\min}}^{x_{\max}} \sqrt{2 \left(E_{\text{saddle}} - \varepsilon x - \frac{1}{2} \omega_0^2 x^2 - \frac{1}{3} \beta x^3 \right)} dx, \quad (2.6)$$

where E_{saddle} is the total energy of the system at the saddle point, x_{\min} is the coordinate corresponding to the saddle, given by (2.2b), and x_{\max} is given by

$$x_{\max} = \frac{2\sqrt{\omega_0^4 - \beta\varepsilon - \omega_0^2}}{2\beta}. \quad (2.7)$$

The variation of this area with ω_0^2 is illustrated in Figure 2. By expanding (2.6) in Taylor series, one obtains as a first approximation

$$A = \frac{6\omega_0^5}{5\beta^2} - \frac{6\omega_0\varepsilon}{\beta} \quad (2.8)$$

which shows clearly the influence of the nonlinearity, β , and imperfection, ε , on the safe area.

The variation of the safe region with the load parameter λ and the imperfection ε is illustrated in Figure 3. The curve on the λ - ε plane is the so-called imperfection sensitivity curve [1–3].

As the load level approaches the critical value, there is not only a swift decrease of the safe area but also a decrease in the depth of the safe potential well, h , which is given by

$$h = \frac{\sqrt{(\omega_0^4 - 4\beta\varepsilon)^3}}{6\beta^2}. \quad (2.9)$$

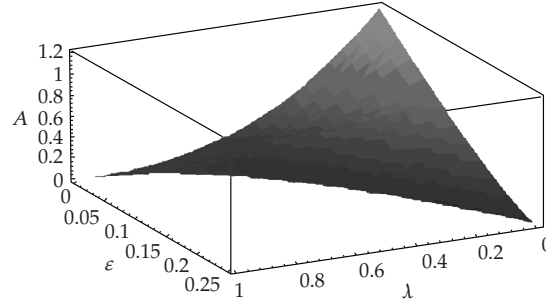


Figure 3: Variation of the safe region as a function of the load parameter λ and the imperfection ε . $\beta = -1$.

The degree of safety of a given autonomous undamped system can be established by defining at the stage of design the magnitude of the safe area A . The maximum load, λ_{\max} , that can be applied to the structure with a prescribed safe area A is given approximately by [7]

$$\lambda_{\max} = \lambda_{\text{cr}} - \sqrt{5\beta\varepsilon} - \frac{5^{1/4} A \beta \sqrt{\sqrt{\beta\varepsilon}}}{12\varepsilon}. \quad (2.10)$$

The consideration of viscous damping changes the eigenvalues but not the equilibrium solutions of (2.1). For the damped case, the eigenvalues connected with the stable solution (2.2a) become

$$\begin{aligned} \mu_1 &= -\eta\omega_0 + \sqrt{\eta^2\omega_0^2 - \sqrt{\omega_0^4 - 4\beta\varepsilon}}, \\ \mu_2 &= -\eta\omega_0 - \sqrt{\eta^2\omega_0^2 - \sqrt{\omega_0^4 - 4\beta\varepsilon}}. \end{aligned} \quad (2.11)$$

So, for positive damping, the equilibrium is asymptotically stable. For solutions (2.2b), the eigenvalues are

$$\begin{aligned} \mu_1 &= -\eta\omega_0 + \sqrt{\eta^2\omega_0^2 + \sqrt{\omega_0^4 - 4\beta\varepsilon}}, \\ \mu_2 &= -\eta\omega_0 - \sqrt{\eta^2\omega_0^2 + \sqrt{\omega_0^4 - 4\beta\varepsilon}}, \end{aligned} \quad (2.12)$$

which is a saddle.

The basin of attraction of the lightly damped system is illustrated in Figure 4, where gray corresponds to bounded solutions and white to unbounded solutions. Disregarding the infinite tail that corresponds to initially large amplitude motions, the area of this basin of attraction is only slightly higher than the area enclosed by the homoclinic orbit. So, (2.6) can be used as a safe measure of the basin area [7].

Figure 5 shows the variation of the basin area of the damped ($\eta = 0.05$) autonomous system with the nonlinear parameter β and the imperfection magnitude ε .

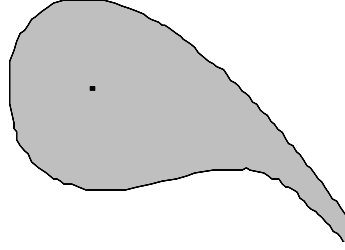


Figure 4: Basin of attraction of the damped autonomous system. Gray area: bounded solutions.

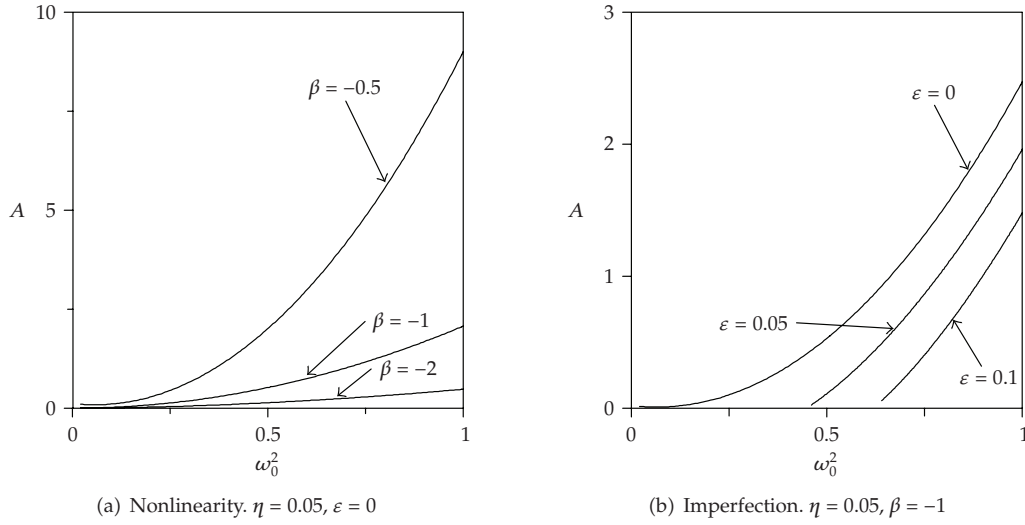


Figure 5: Variation of the basin area as a function of the nonlinearity and imperfections.

2.2. The forced system

This section addresses the problem of calculating the dynamic buckling load of imperfection-sensitive structures under a harmonic load. Actually, because of the resonance phenomenon this is one of the worst possible types of dynamic load.

The solution set of (2.1) can be classified in bounded and unbounded solutions. Unbounded solutions indicate ruin of the structure, as its displacements become increasingly large and incompatible with the structure's use and hypotheses embodied into the mathematical modeling. Unbounded solutions are also called *escape solutions*, or simply *escape*. In this work, as in, for example, the works of Malasoma et al. [29], Thompson [10], and Szemplińska-Stupnicka [30], one is interested in the values of F and Ω that lead to escape from a given potential well. The minimum value of F at which escape occurs, when all other parameters are maintained fixed, is called the *escape load*, F_e . The underlying dynamics that ultimately leads to escape can be very complex. Consequently, the *escape boundary*, which is the set of escape loads in the parameter space, is rather involved and can even be of fractal nature [7].

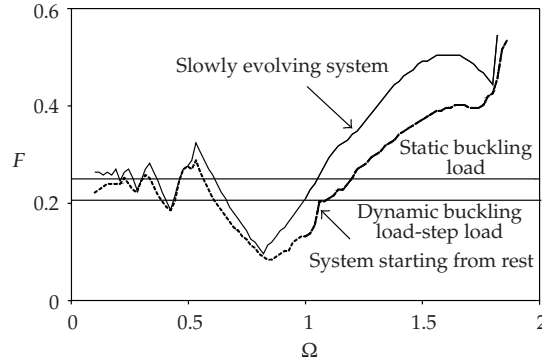


Figure 6: Stability boundaries in force control space. System under harmonic and constant load. $\eta = 0.05$, $\varepsilon = 0$, $\omega_0 = 1$, and $\beta = -1$.

Figure 6 shows the escape load, F_e , as a function of the forcing frequency, Ω , for $\eta = 0.05$, $\varepsilon = 0$, $\omega_0 = 1$, and $\beta = -1$. Two loading processes are considered: a *suddenly applied harmonic load* (dashed line) and a *gradually increasing harmonic load* (continuous line). For the suddenly applied harmonic load, after each load increment, (2.1) is integrated numerically considering zero initial position and velocity, that is, after each increment the system starts from rest. For the gradually increasing harmonic load, for a given excitation frequency, the final position and velocity of the previous load level are taken as the initial conditions for the current load level (here, a load step of 0.001 is considered). For comparison purposes, Figure 6 also shows the *escape load* for a structure under a step load of infinite duration as well as the *static critical load*. As the value of the forcing frequency Ω varies, there is a series of valleys associated to super harmonics of various orders culminating with a deep valley around the natural frequency. For higher excitation frequencies, the escape load increases and can be, due to the appearance of new attractors, many times larger than the corresponding static critical load.

The escape is connected with a series of local bifurcations, as illustrated in the bifurcation diagrams depicted in Figure 7. In the main resonance region, for excitation frequencies smaller than those corresponding to the minimum escape load, escape occurs due to a saddle-node (S-N) bifurcation, as illustrated in Figure 7(a) for $\Omega = 0.70$. After this minimum, the initially stable period one solution undergoes a stable period doubling bifurcation (D_1) and escape occurs just after this solution becomes unstable, as shown in Figure 7(b), for $\Omega = 1.00$. As the forcing frequency increases, the period doubling bifurcation becomes unstable and initially escape occurs at this point, as illustrated in Figure 7(c), for $\Omega = 1.50$. Finally, as the forcing frequency increases even further, a secondary stable branch appears along the bifurcated path after a saddle-node bifurcation. This solution also becomes unstable (D_2). If the bifurcation load D_2 is higher than the bifurcation load D_1 , the escape load of the slowly evolving system is then controlled by D_2 , as illustrated in Figure 7(d), for $\Omega = 1.90$. Here, after D_1 , escape becomes unpredictable [10–13]. Figure 8 shows a summary of the bifurcation events connected with the escape boundary of the slowly evolving system.

The influence of the geometric imperfection parameter ε on the escape load is illustrated in Figure 9 that depicts the stability boundaries for increasing values of ε . The stability boundaries show a shift to the lower frequency range as ε increases. This is due to the decrease in the natural frequency caused by the imperfection. For comparison, the static buckling

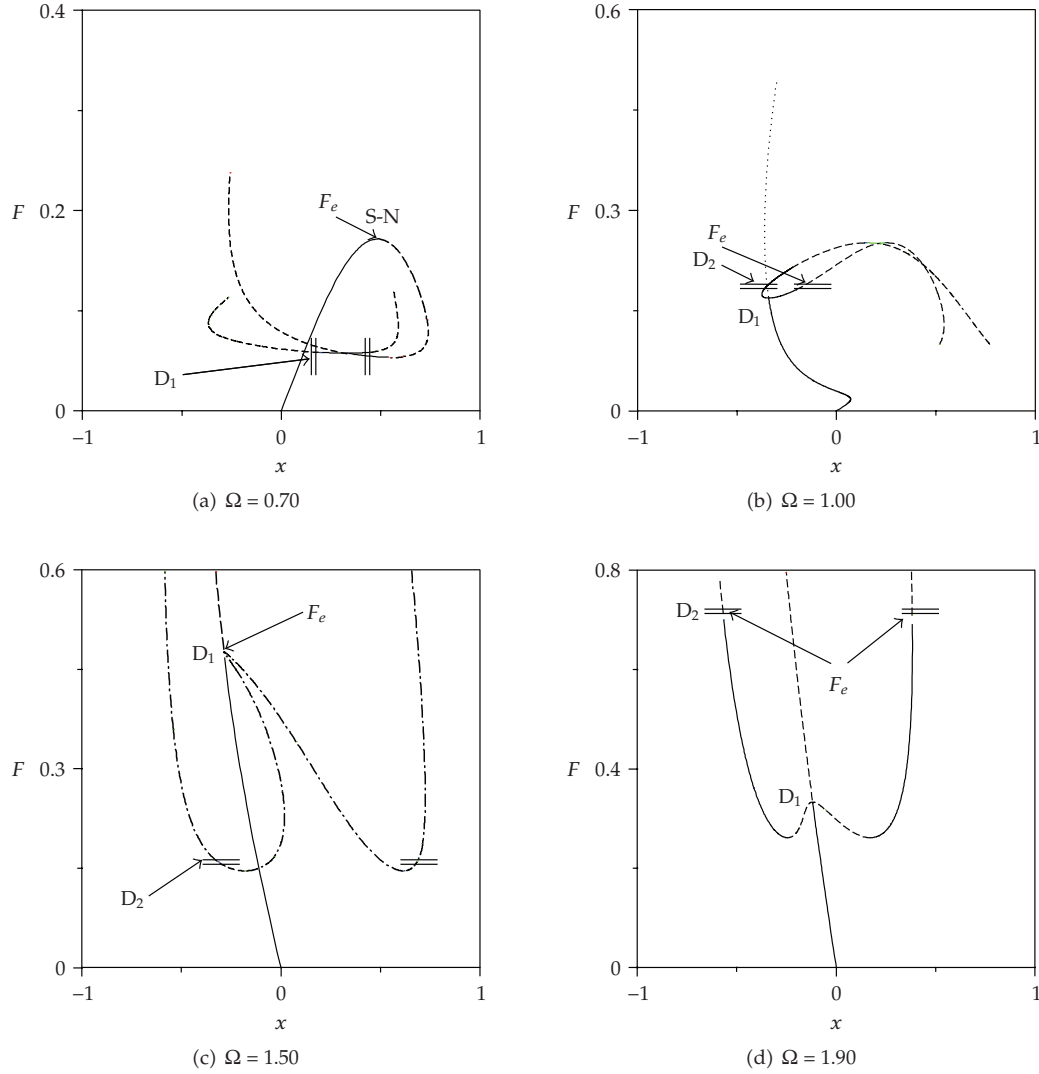


Figure 7: Bifurcation diagrams of the slowly evolving system for selected values of the excitation frequency, Ω . Bifurcations connected with the stability boundaries in force control space: S-N: saddle-node bifurcation; D_1 : first period doubling bifurcation; D_2 : second period doubling bifurcation; F_e : escape load. $\eta = 0.05$, $\varepsilon = 0$, $\omega_0 = 1$, and $\beta = -1$.

load of the imperfect system is also shown in Figure 9. While in some frequency ranges the imperfection sensitivity of the escape load is of the same order or even higher than that of the static case, in other regions the escape load is almost insensitive to imperfections. However, the escape load of the slowly evolving system represents only an upper bound of the actual load bearing capacity of the structure under harmonic loading. Because of dynamic perturbations, an imperfection-sensitive structure can escape at load levels much lower than at the escape load, as will be shown herein through the analysis of the basins of attraction.

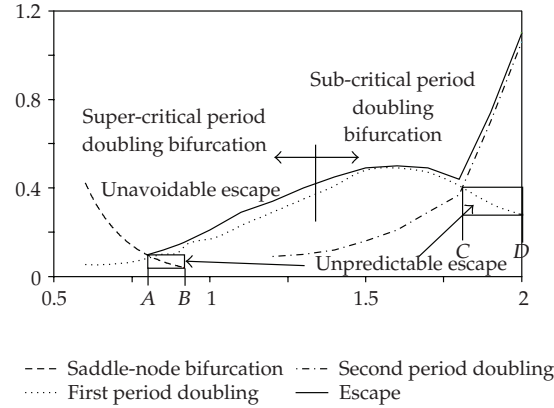


Figure 8: Summary of the bifurcations connected with the escape boundary. $\eta = 0.05$, $\varepsilon = 0$, $\omega_0 = 1$, and $\beta = -1$.

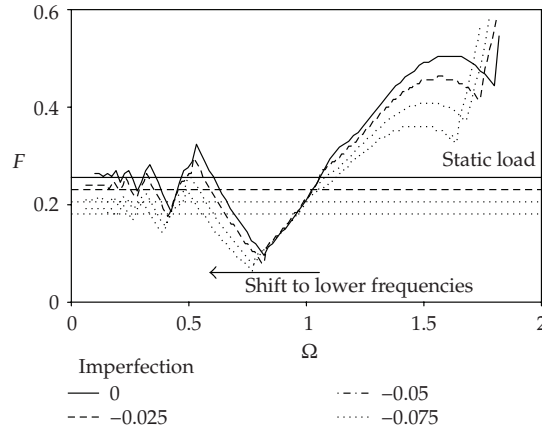


Figure 9: Influence of the imperfection parameter ε on the static and dynamic buckling loads.

3. Basin of attraction of the forced system and structural stability

Mathematically, the *basin of attraction* of a periodic solution is the set of all initial conditions that lead to a solution (attractor) as time goes to infinity. This means that if a periodic solution has a large compact basin of attraction, it will be stable under finite perturbations. On the other hand, if it has a small, or fragmented, basin of attraction, small finite perturbations can lead the solution to escape even if the solution is stable. Thus, a measure of the stability of the structure, in particular its safety, has to be based on a global view of the behavior of the structure. This global view can be expressed mathematically by the characteristics of the basin of attraction and its boundary.

The concept of basin of attraction is based on the limit $t \rightarrow \infty$. Because of limitations in the numerical integration, a practical concept for basin of attraction is used. This practical concept is the basin of r -attraction [10–13]. A *basin of r -attraction* is the set of all initial conditions

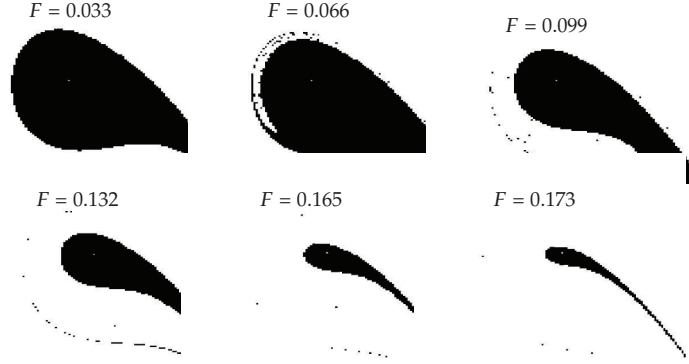


Figure 10: Variation of the basin area of the damped forced system. Black: steady-state bounded solutions. White: unbounded solutions. $\eta = 0.05$, $\varepsilon = 0$, $\omega_0^2 = 1$, $\beta = -1$, and $\Omega = 0.68$.

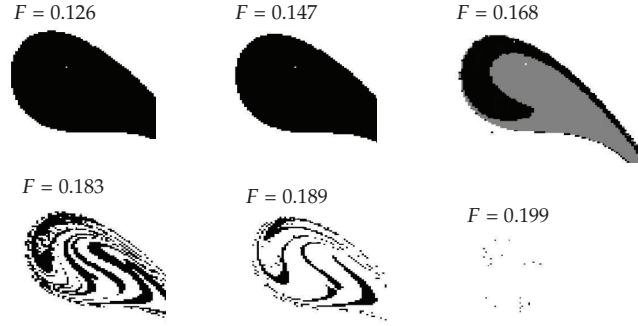


Figure 11: Variation of the basin area of the damped forced system. Black and gray: steady-state bounded solutions. White: unbounded solutions. $\eta = 0.5$, $\varepsilon = 0$, $\omega_0^2 = 1$, $\beta = -1$, and $\Omega = 0.43$.

that lead to the neighborhood of the respective periodic solution in r times the forcing period $T = 2\pi/\Omega$. As the integration time increases, the basin of r -attraction tends asymptotically to the basin of attraction. Our experience has shown that a basin of 32-attraction is a reasonable approximation.

Numerical explorations have shown that the way the basin of attraction changes as the load level F increases can be classified into one of two groups: (a) it gradually decreases until it vanishes completely; (b) its shape remains the same as the load level increases, until it suddenly becomes fractal [7]. In these two types of basin of attraction evolution, the area decreases as the load increases and becomes zero at $F = F_e$. The two types of behavior are illustrated in Figures 10 and 11. One important fact to note is that, even at the eminence of escape, when the basin of attraction is very small, the periodic solution represented by the fixed point of the Poincaré map is a stable solution. This shows that when one uses the stability of the periodic solution as a measure of the structure's stability, this value furnishes only an upper bound to the true stable load.

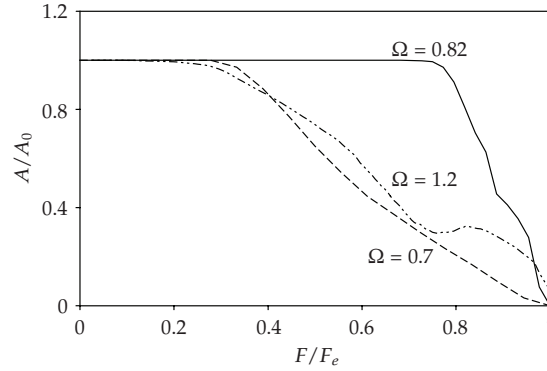


Figure 12: Variation of the basin area as a function of the excitation magnitude for selected values of the forcing frequency.

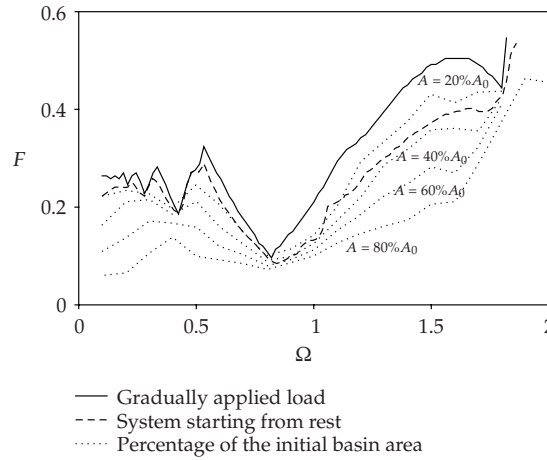


Figure 13: Variation of the basin area as a function of the load control parameters. Curves of constant parameterized area.

Figure 12 shows the variation of the basin area parameterized by the basin area of the corresponding unloaded system, A/A_0 , as a function of the force ratio F/F_e , for three different values of Ω .

For higher and lower values of the excitation frequency, the variation of the basin area becomes smoother, decreasing the relative length of the initial plateau. The variation of the basin area, as will be shown in the next item, is closely related to the sensitivity of the dynamic buckling loads to perturbations and uncertainties.

As a safety measure, the designer can specify a maximum erosion level with respect to the initial safe area of the structure, A_0 , and determine the corresponding maximum load that can be applied during the service life of the structure. In the autonomous case, this load level is given by (2.8). For the system under harmonic excitation, curves of constant A/A_0 ratio, obtained numerically, are depicted in Figure 13 and compared with the previously deduced escape boundaries. From Figures 12 and 13, one can conclude that the erosion of the safe basin

area varies with the value the forcing frequency. For the excitation frequency corresponding to the lowest escape load ($\Omega \cong 0.82$), the safe area remains practically constant up to the critical value and then drops suddenly to zero.

4. Influence of uncertainties in system parameters on the dynamic buckling load

4.1. Nondeterministic force

The analysis conducted up to this point considered a harmonic excitation. This is rarely true in practical situations where loads do not lend themselves to explicit time description, being random or including at least some kind of noise. So, it is important to know how departures from an ideally perfect harmonic excitation may affect the performance of the system. Consider that the applied load is composed of a harmonic deterministic portion plus a random term such that

$$F_t(t) = F \cos(\Omega t) + G(t; F, \Omega), \quad (4.1)$$

where the random term $G(t; F, \Omega)$ depends on the deterministic parameters F and Ω .

For the numerical simulation, the following hypotheses about G are adopted in the present work [7, 31].

(i) A force that varies randomly in time is mathematically a stochastic process. A stochastic process is a random variable where the probability distribution depends on a parameter. If the parameter is continuous, the process is called continuous. In the present case, this parameter is time. If the statistics of the process (mean and variance) are time-independent, the process is called stationary.

(ii) An *ergodic process* is a process where the statistics of the random variable $G(t; F, \Omega)$ are the same as the statistics of only a sample of the random process taken along time. An ergodic process is always stationary, but a stationary process may not be ergodic. In this work, it is assumed that the random term $G(t; F, \Omega)$ is an ergodic process and, consequently, stationary.

Another hypothesis is that G has expected value zero, that is,

$$E[G(t; F, \Omega)] = 0. \quad (4.2)$$

The description of a stochastic process is usually made in the frequency domain. Here, it is assumed that the random term has a spectral density function given by

$$\Phi_{GG}(\omega) = \frac{\sigma_{GG}^2}{2\omega_l} \quad \text{for } \Omega - \frac{\omega_l}{2} < \omega < \Omega + \frac{\omega_l}{2}, \quad (4.3)$$

where σ_{GG}^2 is the variance of the random force amplitude and ω_l is the frequency bandwidth.

Additionally, it is considered that the standard deviation of the random force amplitude is proportional to the deterministic force amplitude, thus

$$\sigma_{GG} = aF, \quad (4.4)$$

where a is the standard deviation parameter. Here, the random force depends on the frequency and amplitude of the deterministic term.

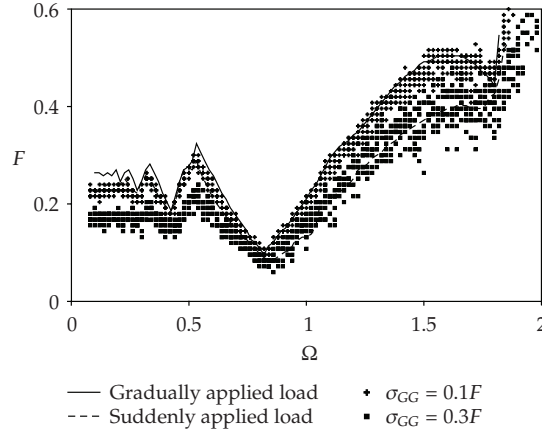


Figure 14: Influence of the standard deviation parameter of the random force, σ_{GG} , on the dynamic buckling load of the structure. Comparison with the dynamic buckling load of the system under deterministic harmonic forcing.

Physically, the random term is a noise that increases with an increase in the applied force. Another point to be emphasized is that the random term depends on two prescribed parameters: the standard deviation parameter a with respect to the deterministic force amplitude F , and the frequency bandwidth ω_l around the forcing frequency Ω . The numerical methodology used to generate the random force in time domain is presented in the appendix.

The influence of the random noise on the dynamic buckling load is studied considering the following system parameters: $\eta_0 = 0.05$, $\omega_0^2 = 1.00$, and $\beta_0 = -1$. For each excitation frequency, five to ten load samples are considered, depending on the dispersion, and the dynamic buckling load, F_e , is computed numerically. The results considering two values of the standard deviation parameter a ($0.1F$ and $0.3F$) are shown in Figure 14 and compared with the results obtained for the deterministic load. Figure 15 shows the results considering two values of the bandwidth ω_l (0.1 and 0.3).

The real values of the systems parameters, such as mass, damping, and stiffness, are dependent on the quality of the fabrication process. They can be, and usually are, different from the value assumed at the design stage. In order to quantify the influence of variations on system parameters in the vicinity of the design values on the dynamic buckling load, a parametric analysis is carried out herein.

Uncertainties in the following system parameters are considered: ε , η , ω_0^2 , and β . For each control parameter, the following probability density function is assumed:

$$f(\alpha) = \begin{cases} \frac{100}{2\alpha_0 Q}, & \text{if } \alpha_0 - \frac{\alpha_0 Q}{100} < \alpha < \alpha_0 + \frac{\alpha_0 Q}{100}, \\ 0, & \text{otherwise,} \end{cases} \quad (4.5)$$

where α is the system parameter, α_0 is the mean value of the chosen parameter, and Q is a parameter which expresses the quality of the fabrication process as a percentage of the mean value, α_0 .

The mean values (design values) considered in the analysis are $\varepsilon_0 = -0.05$, $\eta_0 = 0.05$, $\omega_0^2 = 1.00$, $\beta_0 = -1$, and $Q = 10$ (10%). In the parametric analysis, for each excitation frequency,

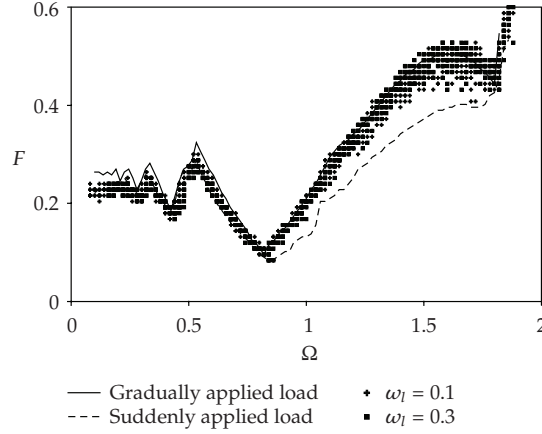


Figure 15: Influence of the bandwidth parameter of the random force, ω_l , on the dynamic buckling load of the structure. Comparison with the dynamic buckling load of the system under deterministic harmonic forcing

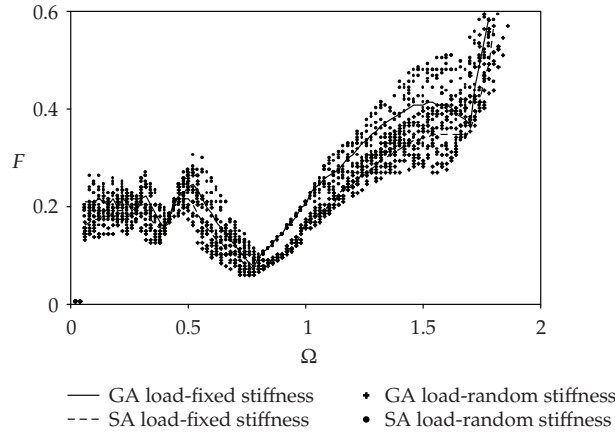


Figure 16: Influence of uncertainties in the stiffness parameter, $\omega_0 = \sqrt{(\lambda_{cr} - \lambda)/m}$, on the dynamic buckling load. GA load: gradually applied harmonic load. SA load: suddenly applied harmonic load.

ten samples of the perturbed parameter are considered and the escape load is computed considering both a gradually applied harmonic load and a suddenly applied harmonic load, as in the previous deterministic analysis. An example of such analysis is shown in Figure 16 where the influence of small variations on the system stiffness parameter, and, consequently, natural frequency ($\omega_0 = \sqrt{(\lambda_{cr} - \lambda)/m}$), is considered. Similar distribution is observed when the other parameters are considered. The scatter of results shows the strong influence of the stiffness value on the dynamic buckling load and the sensitivity of the load carrying capacity of the structure to small variations in system parameters.

It is interesting to notice that the scatter of results presented in Figures 14–16 follows the pattern of variation of the basin area shown in Figure 13. So, it becomes clear that there is a close relation between the variation of the basin of attraction and the scatter of dynamic

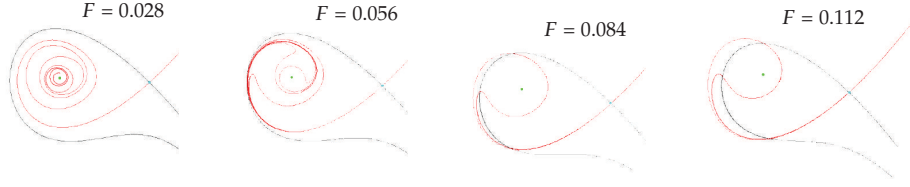


Figure 17: The change in the stable and unstable manifolds as the load F increases.

buckling loads. It is also clear that, in the present case, the scatter is a function of the excitation frequency. The results show that the escape load of the perturbed system is mostly lower than the escape load under deterministic harmonic forcing. One can also observe that the scatter of buckling loads is highly dependent on the forcing frequency.

5. Stable and unstable manifolds: Melnikov criterion

When an imperfection-sensitive damped structure described by (2.1) is unloaded ($F = 0$), the system has only one stable equilibrium point and one saddle point. In this situation, the saddle point's stable manifold goes smoothly around the stable equilibrium point defining the boundary of the basin of attraction of this point. One of the branches of the unstable manifold lies inside the safe basin of attraction, converging to the stable equilibrium solution. The other branch lies outside the basin of attraction and tends to infinity.

Figure 17 shows how the stable and unstable manifolds change as a function of the load. As the load increases, they approach each other and, at a certain load level F^M , the stable and unstable manifolds cross transversally. When the stable and unstable manifolds cross transversally at one point, they cross at an infinite number of points, thus this crossing indicates the beginning of the erosion of the basin of attraction [16, 17].

The prediction of the first crossing of the stable and unstable manifolds can be obtained by the *Melnikov function*. This function gives a measure of the distance of the stable and unstable manifolds, when this distance is small [16, 17]. It applies to problems where the damping is small, which is usually the case of slender structures, and when the algebraic expressions for the stable and unstable manifolds for zero damping are known.

When both the damping and the externally applied forces are small, the vector field of the system can be expressed generically as [16]

$$\begin{aligned}\dot{x} &= \frac{\partial E}{\partial v} + \xi g_1, \\ \dot{v} &= -\frac{\partial E}{\partial x} + \xi g_2,\end{aligned}\tag{5.1}$$

where the vector $g = g(x, v, t) = (g_1, g_2)$, ξ is a small parameter, and $E(x, v)$ is the total energy of the unforced, undamped system ($\xi = 0$). Also admit that $g(t)$ is periodic, that is, it satisfies the relation

$$g(t + T) = g(t).\tag{5.2}$$

The Melnikov function is given by

$$M(t_0) = \int_{-\infty}^{\infty} g^* \cdot \nabla E(x^*, v^*) dt \quad (5.3)$$

where $g^* = g(x^*, v^*, t + t_0)$. $x^*(t)$ and $v^*(t)$ are the algebraic expressions of position and velocity of the stable and unstable manifolds of the conservative system.

The two manifolds cross when this distance is zero, that is,

$$M(t_0) = 0. \quad (5.4)$$

Equation (5.4) leads to an algebraic expression that can be used to calculate the load level F^M at which the tangling of the stable and unstable manifolds first occurs. Next, we apply the Melnikov method to imperfection-sensitive structures whose motion is described by (2.1).

In the case of structures liable to asymmetric bifurcation with no imperfection ($\varepsilon = 0$), it is possible to obtain an analytic solution for the homoclinic orbit using the law of conservation of energy [7]. The solution is

$$x_p(t) = -\frac{\omega_0^2 e^{2\omega_0 t} - 4 e^{\omega_0 t} + 1}{\beta e^{2\omega_0 t} + 2 e^{\omega_0 t} + 1}. \quad (5.5)$$

The effect of the imperfection parameter ε can be introduced by observing that it does not change qualitatively the solution (the homoclinic orbit continues to be a homoclinic orbit), but changes only the position of the center and saddle points. Thus, the approximate solution can be expressed by

$$x(t) = A(\varepsilon) + L(\varepsilon) x_p[a(\varepsilon) t]. \quad (5.6)$$

The coefficients A and L in (5.6) can be obtained by the restrictions

$$\begin{aligned} \lim_{t \rightarrow \infty} x(t) &= x_{\text{saddle}}, \\ x(0) &= x_{\text{max}}. \end{aligned} \quad (5.7)$$

This leads to

$$\begin{aligned} A(\varepsilon) &= -\frac{\varepsilon}{\omega_0^2}, \\ L(\varepsilon) &= 1 - \frac{2\beta\varepsilon}{\omega_0^4}. \end{aligned} \quad (5.8)$$

The time scale coefficient $a(\varepsilon)$ in (5.6) can be obtained by applying Galerkin method on the residue

$$R(t) = \frac{1}{2}\dot{x}^2 + \frac{1}{2}\omega_0^2 x^2 + \varepsilon x + \frac{1}{3}\beta x^3 - E_{\text{saddle}} \quad (5.9)$$

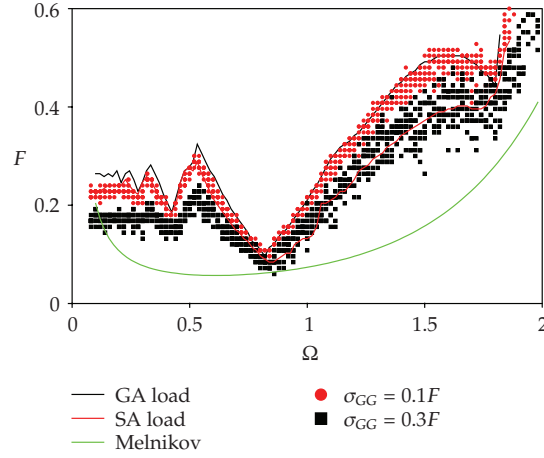


Figure 18: Comparison of the scatter of buckling load with the Melnikov load $\omega_l = 0.1$ and two values of σ_{GG} .

and by using the weight function $\delta x = x(t)$. This leads to

$$a(\varepsilon) = 1 - \frac{\beta \varepsilon}{\omega_0^4}. \quad (5.10)$$

Remembering that $v = dx/dt$, the Melnikov function becomes

$$M(t_0) = \int_{-\infty}^{\infty} \bar{F} v \cos[\Omega(t + t_0)] dt - 2\bar{\eta}\omega_0 \int_{-\infty}^{\infty} v^2 dt. \quad (5.11)$$

In (5.11), $F = \xi \bar{F}$, $\eta = \xi \bar{\eta}$, and ξ is the small perturbation parameter. By substituting $x(t)$ into (5.11) and calculating the integrals, one obtains

$$M(t_0) = \bar{F} \sin(\Omega t_0) \left[-\frac{6L\pi\Omega^2}{a^2\beta \sinh(\pi\Omega/a\omega_0)} \right] - 2\bar{\eta}\omega_0 \left[\frac{6La\omega_0^5}{5\beta^2} \right]. \quad (5.12)$$

Thus, the first crossing occurs when $M(t_0) = 0$, which leads to

$$F^M = \frac{\eta}{\pi} \left[\frac{2\omega_0^6}{5\beta\Omega^2} - \frac{\varepsilon\omega_0^2}{\Omega^2} \right] \sinh \left[\frac{\pi\Omega}{\omega_0} + \frac{\pi\Omega\beta\varepsilon}{\omega_0^5} \right]. \quad (5.13)$$

This expression can thus be used to calculate the load level above which the structure's basin of attraction starts to loose its integrity.

6. Melnikov lower bound

The algebraic expressions for the Melnikov load given by (5.13) allows the prediction of the load above which the stable solution's basin of attraction begins to loose its integrity by the tangling of the stable and unstable manifolds of the respective saddle point. Figure 18

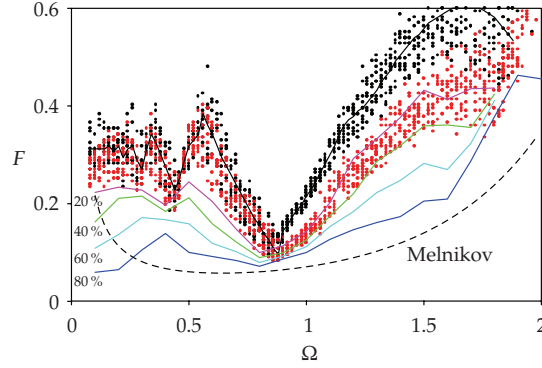


Figure 19: Comparing Melnikov load with the buckling load of a realistic imperfection-sensitive structure.

compares the Melnikov load with the scatter of the dynamic buckling results shown in Figure 14. As one can observe, all results lie above the Melnikov load, indicating that (5.13) can be considered as a safe lower bound in the whole range of excitation frequencies considered in the present work. Reference [7] presents similar comparisons considering uncertainties in all parameters. In all cases, the scatter of results, considering reliable deviations from design values, lies above the present lower bound.

The uncertainties in the structure's parameters (stiffness, nonlinearity, natural frequency, etc.) and random deviations of the applied load make real structures become nondeterministic. In this sense, the random perturbation of the parameters is a numerical simulation of a real structure. Note that the random perturbation of 10% of the actual design value generates a large scatter in the values of the escape loads. Despite the large variation of the escape loads, the Melnikov load is always smaller indicating that it is a safe lower bound.

Finally, in Figure 19, the lower bound is compared with the curves of constant basin area, already shown in Figure 13, and the scatter of buckling loads obtained considering uncertainties in all system parameters, except the external load ($Q = 10$). The results corroborate the lower bound character of the Melnikov load. However, if a good quality control is considered at the fabrication stage, the designer may use a less conservative estimate of the dynamic buckling load based on the safe basin area. In fact, one can observe in Figure 19 that almost all results in this numerical experiment are above the curve corresponding to a safe basin with an area equal to 40% of the reference basin of the unloaded system A_0 .

7. Conclusions

For a structure liable to asymmetric bifurcation, the critical load of the perfect or imperfect structure is an upper bound of its buckling load, since it corresponds to a safe basin with null area. So, any disturbance, however small, leads to buckling. To preserve the integrity of the structure, the designer should prescribe a nonzero compact basin surrounding the fixed point of the desired solution. In this paper, initially, the integrity of the structure under static load is investigated by the variation of the safe basin of attraction as a function of the system parameters, including initial imperfections. The results show that the safe basin decreases exponentially as one approaches the critical value. Next, the behavior of the harmonically excited structure is analyzed and the stability boundaries in force control

space are obtained considering different loading histories. The results show that uncertainties in system parameters or small random perturbations of the applied load lead to dynamic buckling loads that are mostly lower than the load of the unperturbed ideal system. The scatter of results varies with the forcing frequency and is governed by the variation of the safe basin of attraction. The variation of the safe basin is dictated by the evolution of the stable and unstable manifolds of the saddle connected with the safe basin boundary. Melnikov developed a procedure to determine an approximation for the first crossing of the stable and unstable manifolds of the saddle-point related to the fundamental stable solution. When the stable and unstable manifolds cross transversally at one point, they cross transversally at an infinite number of discrete points. Since the unstable manifold is the fundamental solution's basin of attraction boundary, this indicates that the basin of attractions becomes, at least partially, fractal. Thus, the load level at which the tangling of the stable and unstable manifolds first occurs can be taken as the load that marks the beginning of the loss of stability of the structure, consequently a lower bound for the structure load carrying capacity. The proposed lower bound, based on a mathematical reasoning that accounts for the effects of imperfection and dynamical perturbations on the structure, compares well with the scatter of dynamic buckling loads and can be used as a safe design recommendation for imperfection-sensitive structures under periodic loads. Finally, the proposed procedure can be applied to a variety of imperfection-sensitive structures, in particular structural systems liable to unstable symmetric or asymmetric bifurcation.

Appendices

A. Simulation of the random force

In the following, the theoretical fundamentals and methodology used to generate the random force in time domain are presented [7].

The idea of an algorithm to generate a stochastic process sample $G(t)$ comes from the expression of the process variance in terms of the spectral density function

$$\sigma_{GG}^2 = \int_{-\infty}^{\infty} \Phi_{GG}(\omega) d\omega \quad (\text{A.1})$$

Assuming that the process is ergodic, the variance can also be calculated in time domain as

$$\sigma_{GG}^2 = \lim_{T_0 \rightarrow \infty} \frac{1}{T_0} \int_0^{T_0} g^2(t) dt \cong \frac{1}{T_0} \int_0^{T_0} g^2(t) dt, \quad (\text{A.2})$$

where T_0 is the force duration and $g(t)$ is a sample of the stochastic process $G(t)$.

Based on (A.1) and (A.2), the following relation between the time function $g(t)$ and the spectral density function is obtained:

$$\frac{1}{T_0} \int_0^{T_0} g^2(t) dt \cong \int_{-\infty}^{\infty} \Phi_{GG}(\omega) d\omega. \quad (\text{A.3})$$

Discretizing (A.3), one obtains

$$\frac{1}{N} \sum_{m=0}^{N-1} g^2(m\Delta t) \cong 2 \sum_{k=1}^{N/2} \Phi_{GG}(k\omega_0) \omega_0, \quad (\text{A.4})$$

where $\Delta t = T_0/N$ and $\Delta\omega = \omega_0 = 2\pi/T_0$.

Parseval theorem [31], which relates the amplitude of a stochastic process in time with the process amplitude on frequency domain, states that

$$\frac{1}{N} \sum_{m=0}^{N-1} g^2(m\Delta t) \cong \sum_{k=0}^{N-1} |C_g(k\Delta\omega)|^2, \quad (\text{A.5})$$

where $C_g(\omega)$ is the discrete Fourier transform (DFT) coefficient of the process sample $g(t)$.

Substituting (A.5) on the right-hand side of (A.4) and remembering that, for $g(t)$ to be real, it is necessary that $C_g(N/2 + i) = C_g^*(N/2 - i)$, (A.4) can be rewritten as

$$2 \sum_{k=1}^{N/2} |C_g(k\omega_0)|^2 \cong 2 \sum_{k=1}^{N/2} \Phi_{GG}(k\omega_0) \omega_0. \quad (\text{A.6})$$

The above expression is true if

$$|C_g(k\omega_0)| = \sqrt{\Phi_{GG}(k\omega_0) \omega_0}, \quad k = 1, \dots, \frac{N}{2}. \quad (\text{A.7})$$

This expression allows determining the modulus of the coefficients C_g of a discrete Fourier transform sample of the stochastic process $G(t)$ in a way that it has a specified spectral density function. Finally, each DFT coefficient of $g(t)$ can be calculated from

$$C_g(k\omega_0) = |C_g(k\omega_0)| \cos(\theta_k) + i |C_g(k\omega_0)| \sin(\theta_k), \quad (\text{A.8})$$

where the phase angles θ_k are random variables with constant distribution between 0 and 2π . Samples of the random variables can be obtained using a random number generator. In order to use expression (A.8), the following initial values are necessary:

- (i) T_0 : random process duration,
- (ii) N : number of points analyzed on the process,
- (iii) $\Phi_{GG}(\omega)$: specified spectral density function.

B. Structural system liable to asymmetric bifurcation

Consider the well-known SDOF structural system shown in Figure 20 comprising an inverted pendulum of length L and mass m , supported laterally by a linear spring of stiffness K in both tension and compression and inclined initially at 45 degrees. The structure is loaded by a vertical dead load of magnitude P (which includes the weight of the mass m). To generate a family of imperfect systems, a small perturbation moment M is applied to the system. This can be caused, for example, by a small load eccentricity, or any other moment generating

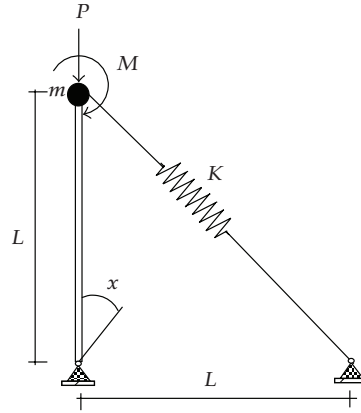


Figure 20: Laterally supported inverted pendulum submitted to an axial force P and a small disturbance M .

disturbance. The effects of various imperfections on the response of the model are very similar. The rotation of the inverted pendulum is denoted by x .

The potential energy of the system in terms of the rotation x is given by

$$V = KL^2 \left[\sqrt{1 + \sin(x)} - 1 \right]^2 - PL[1 - \cos(x)] - Mx. \quad (\text{B.1})$$

The kinetic energy of the pendulum is

$$T = \frac{mL^2}{2} \dot{x}^2. \quad (\text{B.2})$$

By expanding the potential energy in Taylor series and retaining all terms up to the third order, one obtains the following nonlinear equilibrium equation:

$$-M + \left[\frac{KL^2}{2} - PL \right] x - \frac{3KL^2}{8} x^2 = 0. \quad (\text{B.3})$$

If the load imperfection M is not considered in the analysis, one obtains from the linearized equilibrium equation the following critical load:

$$P_{\text{cr}} = \frac{KL^2}{2}. \quad (\text{B.4})$$

The associated equation of motion is given by

$$mL^2 \ddot{x} - M + L[P_{\text{cr}} - P]x - \frac{3KL^2}{8} x^2 = 0. \quad (\text{B.5})$$

By introducing the following auxiliary parameters (notice that we use the usual symbols found in literature for load, imperfection, and nonlinearity parameters):

$$\lambda_{\text{cr}} = \frac{P_{\text{cr}}}{L}, \quad \lambda = \frac{P}{L}, \quad \varepsilon = -\frac{M}{mL^2}, \quad \beta = -\frac{3K}{8m}, \quad (\text{B.6})$$

the following equation of motion is obtained:

$$\ddot{x} + \varepsilon + \omega_0^2 x + \beta x^2 = 0, \quad (\text{B.7})$$

where

$$\omega_0 = \sqrt{\frac{\lambda_{\text{cr}} - \lambda}{m}}. \quad (\text{B.8})$$

The term $K_{\text{ef}} = (\lambda_{\text{cr}} - \lambda)$ is usually referred to as effective stiffness in the technical literature and the parameter λ is usually referred to as load parameter.

References

- [1] J. G. A. Croll and A. C. Walker, *Elements of Structural Stability*, John Wiley & Sons, New York, NY, USA, 1972.
- [2] J. M. T. Thompson and G. W. Hunt, *A General Theory of Elastic Stability*, John Wiley & Sons, London, UK, 1973.
- [3] Z. P. Bažant and L. Cedolin, *Stability of Structures*, Oxford University Press, Oxford, UK, 1991.
- [4] W. T. Koiter, *On the stability of elastic equilibrium*, Ph.D. dissertation, Technological University of Delft, Delft, The Netherlands, 1945, English Translation, NASA, TTF-10833, 1967.
- [5] I. Elishakoff, "Remarks on the static and dynamic imperfection-sensitivity of nonsymmetric structures," *Journal of Applied Mechanics*, vol. 47, no. 1, pp. 111–115, 1980.
- [6] A. N. Kounadis, "Recent advances on postbuckling analyses of thin-walled structures: beams, frames and cylindrical shells," *Journal of Constructional Steel Research*, vol. 62, no. 11, pp. 1101–1115, 2006.
- [7] D. M. Santee, *Non-linear vibrations and instabilities of imperfection-sensitive structural elements*, D.Sc. Thesis, Civil Engineering Department, Catholic University, PUC-Rio, Rio de Janeiro, Brazil, 1999.
- [8] J. G. A. Croll, "Stability in shells," *Nonlinear Dynamics*, vol. 43, no. 1-2, pp. 17–28, 2006.
- [9] R. C. Batista and P. B. Gonçalves, "Non-linear lower bounds for shell buckling design," *Journal of Constructional Steel Research*, vol. 29, no. 2, pp. 101–120, 1994.
- [10] J. M. T. Thompson, "Chaotic phenomena triggering the escape from a potential well," *Proceedings of the Royal Society of London. Series A*, vol. 421, no. 1861, pp. 195–225, 1989.
- [11] M. S. Soliman and J. M. T. Thompson, "Integrity measures quantifying the erosion of smooth and fractal basins of attraction," *Journal of Sound and Vibration*, vol. 135, no. 3, pp. 453–475, 1989.
- [12] J. M. T. Thompson and M. S. Soliman, "Indeterminate jumps to resonance from a tangled saddle-node bifurcation," *Proceedings of the Royal Society of London. Series A*, vol. 432, no. 1884, pp. 101–111, 1991.
- [13] A. N. Lansbury, J. M. T. Thompson, and H. B. Stewart, "Basin erosion in the twin-well Duffing oscillator: two distinct bifurcation scenarios," *International Journal of Bifurcation and Chaos*, vol. 2, no. 3, pp. 505–532, 1992.
- [14] L. N. Virgin, *Introduction to Experimental Nonlinear Dynamics*, Cambridge University Press, Cambridge, UK, 2000.
- [15] M. Amabili, *Nonlinear Vibrations and Stability of Shells and Plates*, Cambridge University Press, Cambridge, UK, 2008.
- [16] J. Guckenheimer and P. Holmes, *Nonlinear Oscillations, Dynamical Systems, and Bifurcations of Vector Fields*, vol. 42 of *Applied Mathematical Sciences*, Springer, New York, NY, USA, 1983.
- [17] S. Wiggins, *Introduction to Applied Nonlinear Dynamical Systems and Chaos*, vol. 2 of *Texts in Applied Mathematics*, Springer, New York, NY, USA, 1990.
- [18] G. Rega and S. Lenci, "Identifying, evaluating, and controlling dynamical integrity measures in non-linear mechanical oscillators," *Nonlinear Analysis: Theory, Methods & Applications*, vol. 63, no. 5–7, pp. 902–914, 2005.
- [19] J. Roorda, *Instability of imperfect elastic structures*, Ph.D. Thesis, University College London, London, UK, 1965.
- [20] A. S. Galvão, P. B. Gonçalves, and R. A. M. Silveira, "Postbuckling behavior and imperfection sensitivity of L-frames," *International Journal of Structural Stability and Dynamics*, vol. 5, no. 1, pp. 19–35, 2005.

- [21] P. B. Gonçalves and J. G. A. Croll, "Axisymmetric buckling of pressure-loaded spherical caps," *Journal of Structural Engineering*, vol. 118, no. 4, pp. 970–985, 1992.
- [22] L. N. Virgin, "On the harmonic response of an oscillator with unsymmetric restoring force," *Journal of Sound and Vibration*, vol. 126, no. 1, pp. 157–165, 1988.
- [23] P. Donescu, L. N. Virgin, and J. J. Wu, "Periodic solutions of an unsymmetric oscillator including a comprehensive study of their stability characteristics," *Journal of Sound and Vibration*, vol. 192, no. 5, pp. 959–976, 1996.
- [24] M. Ohsaki, "Maximum load factor corresponding to a slightly asymmetric bifurcation point," *International Journal of Mechanical Sciences*, vol. 46, no. 11, pp. 1621–1634, 2004.
- [25] E. G. Banchio and L. A. Godoy, "A new approach to evaluate imperfection sensitivity in asymmetric bifurcation buckling analysis," *Journal of the Brazilian Society of Mechanical Sciences*, vol. 23, no. 1, pp. 23–40, 2001.
- [26] S. Lenci and G. Rega, "A unified control framework of the non-regular dynamics of mechanical oscillators," *Journal of Sound and Vibration*, vol. 278, no. 4-5, pp. 1051–1080, 2004.
- [27] A. H. Nayfeh and B. Balachandran, *Applied Nonlinear Dynamics: Analytical, Computational, and Experimental Methods*, Wiley Series in Nonlinear Science, John Wiley & Sons, New York, NY, USA, 1995.
- [28] Y. A. Kuznetsov, *Elements of Applied Bifurcation Theory*, vol. 112 of *Applied Mathematical Sciences*, Springer, New York, NY, USA, 3rd edition, 2004.
- [29] J.-M. Malasoma, C.-H. Lamarque, and L. Jezequel, "Chaotic behavior of a parametrically excited nonlinear mechanical system," *Nonlinear Dynamics*, vol. 5, no. 2, pp. 153–160, 1994.
- [30] W. Szemplińska-Stupnicka, "The analytical predictive criteria for chaos and escape in nonlinear oscillators: a survey," *Nonlinear Dynamics*, vol. 7, no. 2, pp. 129–147, 1995.
- [31] A. Preumont, *Random Vibration and Spectral Analysis*, Kluwer Academic Publishers, Dordrecht, The Netherlands, 1994.

Research Article

Model Validation Using Coordinate Distance with Performance Sensitivity

Jiann-Shiun Lew

Center of Excellence in Information Systems, Tennessee State University, Nashville, TN 37209, USA

Correspondence should be addressed to Jiann-Shiun Lew, lew@coe.tsuniv.edu

Received 21 February 2008; Accepted 20 July 2008

Recommended by Paulo Gonçalves

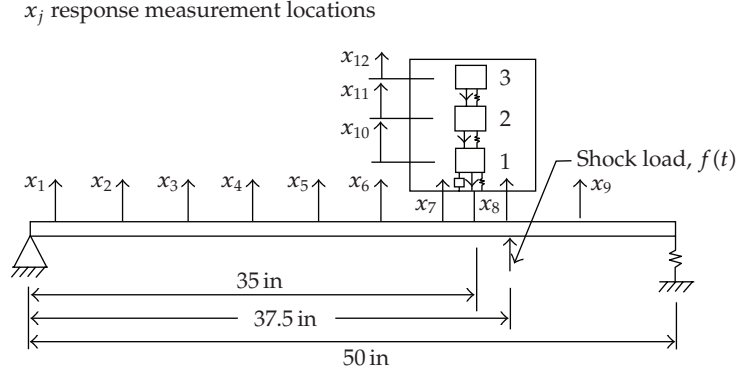
This paper presents an innovative approach to model validation for a structure with significant parameter variations. Model uncertainty of the structural dynamics is quantified with the use of a singular value decomposition technique to extract the principal components of parameter change, and an interval model is generated to represent the system with parameter uncertainty. The coordinate vector, corresponding to the identified principal directions, of the validation system is computed. The coordinate distance between the validation system and the identified interval model is used as a metric for model validation. A beam structure with an attached subsystem, which has significant parameter uncertainty, is used to demonstrate the proposed approach.

Copyright © 2008 Jiann-Shiun Lew. This is an open access article distributed under the Creative Commons Attribution License, which permits unrestricted use, distribution, and reproduction in any medium, provided the original work is properly cited.

1. Introduction

Model validation of structural dynamics is of great interest to both government and industry [1]. Recently, a model validation workshop [2, 3] was organized by Sandia National Laboratories to address the problem of certification of structures under various forms of uncertainty. Following their formulation, an integrated system consisting of a beam structure and an attached subsystem, shown in Figure 1, is the test structure used for study. In this model the physical elements of the attached three degrees of freedom subsystem are the only ones exhibiting significant parameter variations, all other parameters are known. The substructure, along with its nonlinear connection, is considered for calibration, and data are provided as a basis for the calibration of the substructure model [2].

In the process of certifying structures for use in harsh dynamic environments, it is often required that not only the main structure be capable of withstanding the loads but also all the attached substructures. To ensure survivability of all the substructures, Sandia in [2] has chosen a performance metric in terms of the maximum acceleration magnitude of mass 3, top of the substructure, under a shock force at position x_8 . For this study, the uncertain



parameters are the identified modal parameters (frequency, damping, and mode shape) of subsystem, 15 parameters total.

This paper presents a model validation methodology based on an interval modeling technique for the structural dynamics problem proposed by Sandia [2]. A singular value decomposition technique [4] is applied to extract the principal components of parameter change, where the sensitivity of performance is included in the SVD process. From this process, an interval model is generated and each interval corresponds to one identified bounded uncertainty parameter with its associated principal direction. This interval modeling technique can precisely quantify the uncertainty of a system with significant parameter uncertainty [4]. The coordinate vector, corresponding to the identified principal directions, of the validation system can be computed. The coordinate distance between the validation system and the identified interval model is used as the metric for model validation [5].

2. Model validation

In the model validation process, first an interval modeling technique, given in the appendix, is applied for uncertainty quantification. The data used for model uncertainty quantification are based on the identified modal parameters from 60 virtual experiments [2], generated from 20 identical systems selected from a virtual pool and three levels of random excitation applied at mass 2. The modal parameter vector of the subsystem is defined as

$$p = [\omega_1 \ \omega_2 \ \omega_3 \ \xi_1 \ \xi_2 \ \xi_3 \ \phi_{11} \ \phi_{21} \ \phi_{31} \ \phi_{12} \ \cdots \ \phi_{33}]^T, \quad (2.1)$$

where ω_i is the i th natural frequency, ξ_i is the i th damping ratio, and ϕ_{ji} is the j th component of the i th mode shape. The interval modeling technique in the appendix is applied to generate an interval model as

$$P = \left\{ p \mid p = p_0 + \sum_{j=1}^{15} \alpha_j q_j, \alpha_j \in [\alpha_j^-, \alpha_j^+] \right\}, \quad (2.2)$$

where p_0 is the nominal parameter vector, and α_j is the j th identified bounded uncertainty parameter corresponding to the basis vector q_j . The coordinate vector of any validation system with parameter vector p^v can be computed as

$$\beta^v = U^{-1} \Delta p^v, \quad (2.3)$$

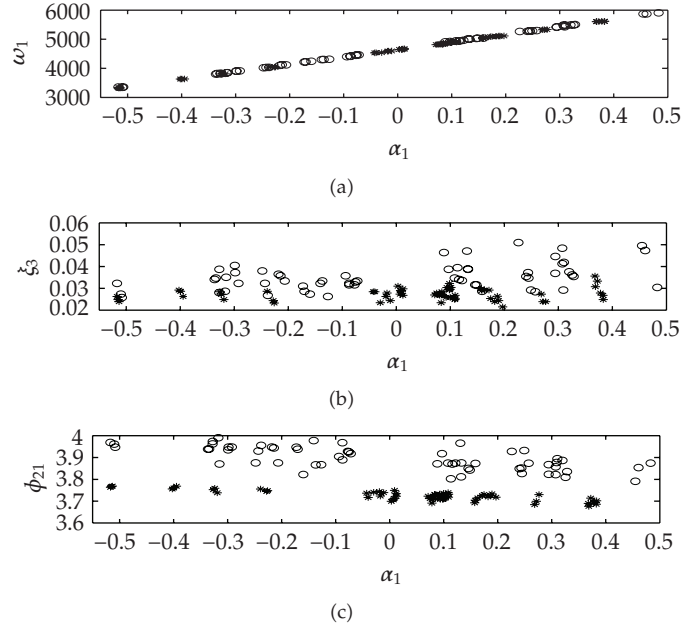


Figure 2: Modal parameters of subsystems: (a) natural frequency (rad/sec) of 1st mode, (b) damping ratio of 3rd mode, (c) 2nd mode shape coefficient of 1st mode. (circels) 60 calibration systems; (asterisks) 60 validation systems.

with

$$\Delta p^v = p^v - p_0, \quad U = [q_1 \ \cdots \ q_{15}], \quad (2.4)$$

where U is the basis matrix. The coordinate distance between a validation system and the interval model is defined as

$$d^v = \min \left\{ \sqrt{[\beta^v - \beta(p)]^T [\beta^v - \beta(p)]}, p \in P \right\}, \quad (2.5)$$

where $\beta(p)$ is the coordinate vector of the subsystem with parameter vector p . This distance represents a metric of performance deviation between a validation system and the identified interval model since the weighting of performance sensitivity is included in SVD process [4, 5].

3. Discussion of results

There are 60 sets of identified modal parameters used for model validation [2], generated from 20 identical systems selected from a virtual pool with three levels of shock input at mass 1. Figure 2 shows three modal parameters of 60 calibration systems and 60 validation systems as functions of the first uncertainty parameter α_1 . Variations in the natural frequencies are significant, around 100%, and increase linearly as the first uncertainty parameter α_1 increases. Natural frequencies of calibration systems and validation systems share same variation characteristics. Damping and mode shape coefficients of validation systems show bias from those of calibration systems. For example, the mean value of ξ_3 of the validation systems

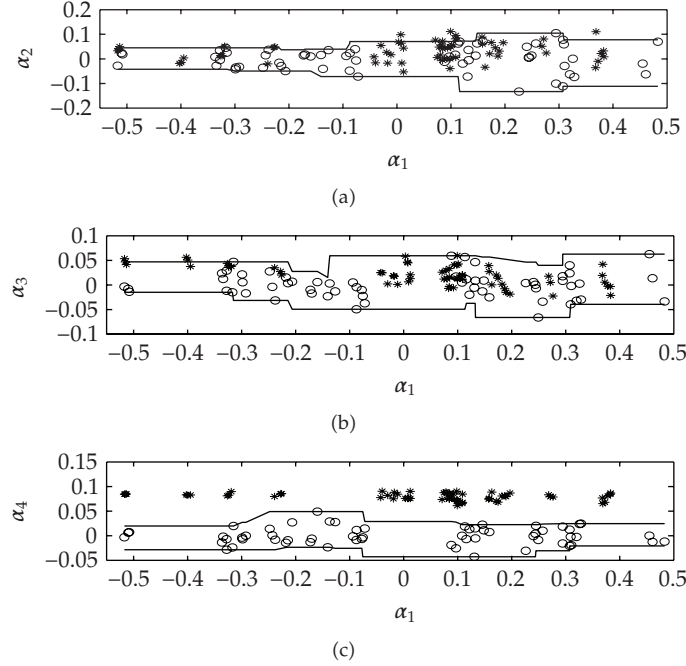


Figure 3: Coordinates and parameter bounds of uncertainty parameters: (a) 2nd uncertainty parameter, (b) 3rd uncertainty parameter, (c) 4th uncertainty parameter. (circles) 60 calibration systems; (asterisks) 60 validation systems; — parameter bounds of interval model.

is around 30% lower than that of the calibration systems when α_1 is 0.1. For the second mode shape coefficient of the first mode in Figure 2, the mean value for the validation systems is always around 5% lower than that of the calibration systems. Figure 3 shows the uncertainty parameters α_2 – α_4 and the identified interval bounds as functions of the first uncertainty parameter α_1 . The third interval length, normalized to the first interval length (i.e., $\alpha_1 = 1$), drops to less than 10% (see Figure 3) of the first interval length [4]. The model uncertainty is dominated by the first uncertainty parameter α_1 . Natural frequency variations are the dominant uncertainty corresponding to variations in α_1 . In contrast to frequency variations, damping and mode shape variations behave more like random variables, and they correspond to secondary uncertainties [4]. All α_2 and α_3 of validation systems are inside the bounds or close to the boundary of the identified interval model. All α_4 of validation systems are outside the bounds of the interval model, and this bias is mainly contributed from the bias of mode shape and damping. Figure 4 shows the coordinate distance of 60 validation systems from interval model. The distance is mainly due to the bias of α_4 .

Figure 5 shows the performance sensitivity to the identified uncertainty parameters α_i . The sensitivity of performance to the j th uncertainty parameters α_j of the i th chosen subsystem p^i is defined as

$$s_{ij}^a = \frac{1}{a(p^i)} \left| \frac{\partial a(p^i)}{\partial \alpha_j} \right|, \quad i = 1, \dots, n_s, \quad (3.1)$$

where $a(p^i)$ is the maximum acceleration magnitude of the integrated system with subsystem parameter vector p^i , and n_s is the number of parameter vectors. This sensitivity represents a

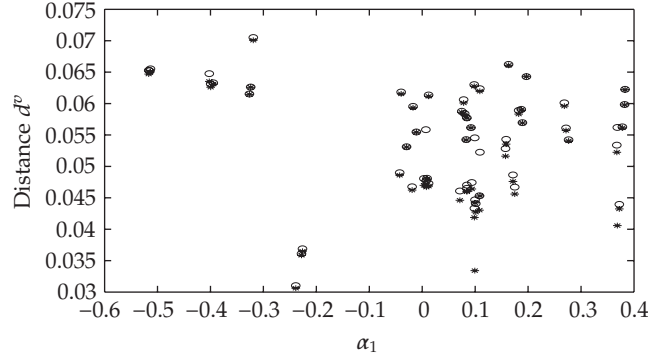


Figure 4: Coordinate distance of 60 validation systems from interval model: (circles) distance from interval model; (asterisks) distance contributed from α_4 bias.

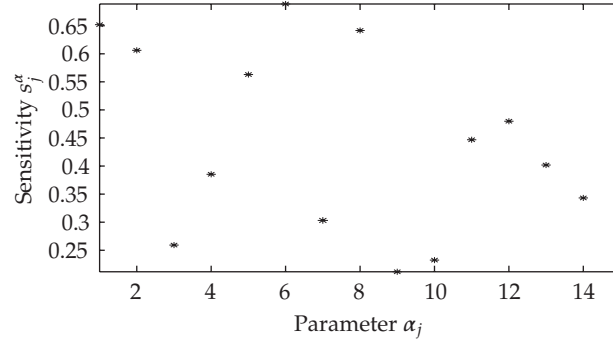


Figure 5: Sensitivity of performance to identified uncertainty parameters α_j .

percentage change. The average sensitivity corresponding to the j th uncertainty parameters α_j is defined as

$$s_j^\alpha = \frac{1}{n_s} \sum_{i=1}^{n_s} |s_{ij}^\alpha|. \quad (3.2)$$

Figure 5 shows that this sensitivity is between 21% and 69%, corresponding to the original maximum acceleration magnitude, and the sensitivity to α_4 is 39% of the maximum acceleration. Coordinate distance of all the validation systems is between 0.03 and 0.07. This means that the maximum acceleration deviation between the validation system and a system in interval model is insignificant (around 1% to 3%), based on the sensitivity in Figure 5. All the validation systems are acceptable, based on the coordinate distance corresponding to performance index of maximum acceleration.

Figure 6 shows the maximum acceleration of the integrated systems with the identified interval model, 60 calibration systems, and 60 validation systems when an impulse force is applied at x_8 position. The results show that the identified interval model well represents and covers 60 calibration systems. The maximum acceleration of all the validation systems is inside the envelope or close to the boundary of the interval model. As expected, the validation systems are acceptable, based on the coordinate distance results shown in Figure 4. This

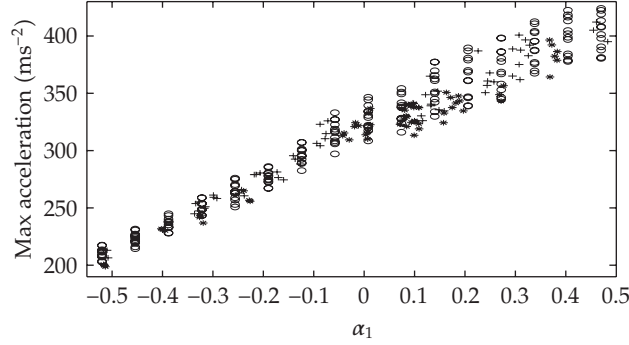


Figure 6: Maximum acceleration with impulse input: (circles) interval system; + 60 calibration systems; (asterisks) 60 validation systems.

coordinate distance represents a metric of the maximum acceleration deviation (percentage difference) between a validation system and the identified interval model.

4. Concluding remarks

This paper presents a novel approach for model validation of a system with an attached subsystem that is exhibiting significant parameter uncertainty. An interval modeling technique is applied for uncertainty quantification with the performance sensitivity weighting in SVD process. The coordinate distance, between the validation system and the identified interval model, is defined as a metric for model validation. This distance represents a metric of the possible performance deviation of the validation system from a system in interval model. The results show that all the validation systems provided by Sandia are acceptable, based on this distance metric. This demonstrates an efficient tool for model validation, based on the interval model analysis. The proposed technique in this paper can be extended to probability framework.

Appendix

Model uncertainty quantification

The sensitivity of performance index a , such as maximum acceleration magnitude, to the j th component of the i th chosen subsystem p^i is defined as

$$s_{ij} = \frac{1}{a(p^i)} \left| \frac{\partial a(p^i)}{\partial p^{ij}} \right| \sigma_j, \quad i = 1, \dots, n_s, \quad (\text{A.1})$$

where p^{ij} is the j th component of parameter vector p^i , and σ_j is the standard deviation of the j th vector component. This sensitivity represents a percentage change including the factor σ_j to account for the size of the parameter variation. The average sensitivity corresponding to the j th vector component is defined as

$$s_j = \frac{1}{n_s} \sum_{i=1}^{n_s} |s_{ij}|. \quad (\text{A.2})$$

To quantify the parameter uncertainty, an uncertainty matrix is defined as

$$\Delta P = [\Delta p_1 \ \Delta p_2 \ \cdots \ \Delta p_n], \quad (\text{A.3})$$

with

$$\Delta p_j = p_j - p_0, \quad j = 1, \dots, n, \quad p_0 = \frac{1}{n} \sum_{j=1}^n p_j, \quad (\text{A.4})$$

where p_j is the j th identified parameter vector, and p_0 is the nominal parameter vector, which is computed as the average from $n = 60$ experiments.

A singular value decomposition (SVD) technique [4] is used to generate an optimal linear interval model. This SVD process involves the following computational steps.

- (1) Compute an initial weighting matrix as

$$\Delta P^1 = W_1^{-1} \Delta P, \quad (\text{A.5})$$

where W_1 is a diagonal matrix with its j th diagonal element as the standard deviation σ_j .

- (2) Compute the weighting matrix including sensitivity as

$$\Delta P^W = W_2 \Delta P^1, \quad (\text{A.6})$$

where W_2 is a diagonal matrix with its j th diagonal element s_j .

- (3) Use SVD to compute the basis matrix U^W for ΔP^W ,

$$\Delta P^W = U^W S V^T, \quad S = \text{diag} [d_1 \ \cdots \ d_{15}]. \quad (\text{A.7})$$

- (4) Compute the basis matrix U for ΔP ,

$$U = W_1 W_2^{-1} U^W, \quad U = [q_1 \ \cdots \ q_{15}]. \quad (\text{A.8})$$

The singular values d_j are in descending order, this leads to a descending order of perturbation distribution in q_j .

- (5) Compute the coordinate vector of Δp_i corresponding to the basis vectors q_j ,

$$\beta_i = U^{-1} \Delta p_i. \quad (\text{A.9})$$

- (6) Represent each parameter vector as

$$p_i = p_0 + \sum_{l=1}^{15} \beta_i(l) q_l, \quad (\text{A.10})$$

where $\beta_i(l)$ is the l th element of the coordinate vector β_i .

- (7) Compute the parameter bounds as

$$\begin{aligned} \alpha_j^+ &= \max \{ \beta_1(j), \beta_2(j), \dots, \beta_n(j) \}, \\ \alpha_j^- &= \min \{ \beta_1(j), \beta_2(j), \dots, \beta_n(j) \}. \end{aligned} \quad (\text{A.11})$$

All the basis vectors, coordinates, and parameter bounds are normalized to the first interval length [6].

References

- [1] B. H. Thacker, "The role of nondeterminism in computational model verification and validation," in *Proceedings of the 46th AIAA/ASME/ASCE/AHS/ASC Structures, Structural Dynamics and Materials Conference (AIAA '05)*, vol. 2, pp. 1237–1250, Austin, Tex, USA, April 2005.
- [2] J. R. Red-Horse and T. L. Paez, "Sandia national laboratories validation workshop: structural dynamics application," *Computer Methods in Applied Mechanics and Engineering*, vol. 197, no. 29–32, pp. 2578–2584, 2008.
- [3] L. G. Horta, S. P. Kenny, K. B. Elliot, K. B. Lim, L. Crespo, and J.-S. Lew, "NASA langley approach towards a solution of the Sandia's structural dynamics challenge problem," in *Proceedings of the Validation Methodology Workshop at Sandia National Laboratories*, Albuquerque, NM, USA, May 2006.
- [4] J.-S. Lew and L. G. Horta, "Uncertainty quantification using interval modeling with performance sensitivity," *Journal of Sound and Vibration*, vol. 308, no. 1-2, pp. 330–336, 2007.
- [5] J.-S. Lew, "Model validation using interval modeling with performance sensitivity," in *Proceedings of the 48th AIAA/ASME/ASCE/AHS/ASC Structures, Structural Dynamics, and Materials Conference (AIAA '07)*, vol. 8, pp. 7760–7770, Honolulu, Hawaii, USA, April 2007.
- [6] J.-S. Lew, L. G. Horta, and M. C. Reaves, "Uncertainty quantification of an inflatable/rigidizable torus," *Journal of Sound and Vibration*, vol. 294, no. 3, pp. 615–623, 2006.

Research Article

Guaranteed Performance Robust Kalman Filter for Continuous-Time Markovian Jump Nonlinear System with Uncertain Noise

Jin Zhu, Junhong Park, Kwan-Soo Lee, and Maksym Spiriyagin

Department of Mechanical Engineering, Hanyang University, 17 Haengdang-dong, Seongdong-gu, Seoul 133-791, South Korea

Correspondence should be addressed to Jin Zhu, jinzhu@ustc.edu

Received 29 January 2008; Accepted 13 July 2008

Recommended by Paulo Gonçalves

Robust Kalman filtering design for continuous-time Markovian jump nonlinear systems with uncertain noise was investigated. Because of complexity of Markovian jump systems, the statistical characteristics of system noise and observation noise are time-varying or unmeasurable instead of being stationary. In view of robust estimation, maximum admissible upper bound of the uncertainty to noise covariance matrix was given based on system state estimation performance. As long as the noise uncertainty is limited within this bound via noise control, the Kalman filter has robustness against noise uncertainty, and stability of dynamic systems can be ensured. It is proved by game theory that this design is a robust mini-max filter. A numerical example shows the validity of this design.

Copyright © 2008 Jin Zhu et al. This is an open access article distributed under the Creative Commons Attribution License, which permits unrestricted use, distribution, and reproduction in any medium, provided the original work is properly cited.

1. Introduction

Optimal filtering problem has been a hot topic in past decades, within which Kalman filtering is one of the most popular estimation approaches and considerable effort has been devoted to its theory and applications. The applications of Kalman filtering theory may be found in a large spectrum of different fields ranging from various engineering problems to biology, geoscience, economics, and management [1]. For standard Kalman filtering, one of the key assumptions is that system noise and observation noise are Gaussian, whose covariances are known and stationary. However, in many actual problems, the statistical characteristics (covariances) of noise may be time-varying instead of being stationary, and in some cases it is impossible to get the exact measurement values, which means that the noise covariances are uncertain instead of being exactly known; for this reason, the stochastic noise is called “uncertain.” Consequently, the standard Kalman filter may not be robust

against modeling uncertainty and disturbances. Thus, the study of a robust state estimation approach is of practical importance and has been attracting more interest over the past few years. A useful approach is to use a game-theoretic formulation with which one minimizes the worst performance stimulated by uncertain factors, and some corresponding results of robust filtering for linear systems with uncertain noise have been addressed in [2–4].

On the other hand, Markovian jump systems, which are convenient tools for representing many real-world systems [5], have aroused much attention in recent years. In the case of fault detection, fault-tolerant control, and multimodal control, discrete jumps in the continuous dynamics are used to model component failures and sudden switch of system dynamics. With further study of Markovian jump systems, many achievements have been made in the last decade on stability analysis [6, 7], filtering [8, 9], and controller design [10, 11]. Among the efforts towards filtering, Shi et al. [12] and Mahmoud et al. [13] gave Kalman filtering equations for continuous-time and discrete-time Markovian jump linear systems with structure uncertainty, respectively. However, in the above-referred contributions, all the research work is facing the same problem as that of nonjump systems; both the state equation and output measurement are subjected to *stationary* Gaussian noise so that an optimal filtering gain is obtained based on the stationary noise covariance matrix. But this is only an ideal assumption for Markovian jump systems. As we know, Markovian jump systems are used to represent a class of systems which are usually accompanied by sudden changes of working environment or system dynamics. For this reason, noise uncertainty occurs more frequently or with more probability than in nonjump systems. Moreover, with the uncertainty to noise covariance matrix increasing, the estimation of system state tends to be inaccurate or false, which may cause errors in control signals and in worst case may lead to breakdown of the whole dynamic systems.

To avoid this tragical situation, a direct way dealing with this problem is to redesign Kalman filter for jump systems by using new noise covariance matrix. But as we have pointed out above, it is almost impossible to get the real-time information of noise covariance matrix since it is time-varying or unmeasurable; therefore we could not update Kalman filter gain online. Another feasible way is to give an admissible bound for estimation performance of system state so that the predesigned Kalman filter will remain effective and the system operates in the course of nature as long as the real-time estimation error is within this precision. To achieve this purpose, we perform the following design method. By using the view of robust estimation, a maximum bound of noise covariance matrix uncertainty is obtained through calculation according to admissible bias for estimation performance of system state. If we could ensure the noise uncertainty to be within this bound via technical method such as noise control, the estimation of system state can be within a desired precision, and thus stability of the whole dynamic process can be achieved. It should be noted that in this research work, we do not mean to eliminate the effect of noise entirely because it is almost impossible or highly costly to do so in practical environment. Our work focuses on the upper bound of noise change level; thus it means only that the change to noise covariance matrix is required to be limited within this bound no matter what the stationary covariance matrix is.

In this paper, robust Kalman filtering for continuous-time Markovian jump nonlinear systems with uncertain noise is considered. Firstly, we give some assumptions so that the nonlinear jump systems can be modeled as a linear one by local linearization. Secondly, we seek the maximum upper bound of nonstructural uncertainty to noise covariance matrix such that the deviation of performance can be within a prescribed precision. Then, we discuss the analytical solution of maximum bound using *Lagrange* method. Finally, we prove the establishment of saddle inequality, and show that this filter design is a mini-max robust

filter using game theory. At the end of the paper, an illustrative example is used to show the validity of our method.

2. Problem Description

Throughout the paper, unless otherwise specified, we denote by $(\Omega, \mathcal{F}, \{\mathcal{F}_t\}_{t \geq 0}, \mathbf{P})$ a complete probability space with filtration $\{\mathcal{F}_t\}_{t \geq 0}$ satisfying the usual conditions (i.e., it is right-continuous, and \mathcal{F}_0 contains all p -null sets). Let $|x|$ stand for the usual Euclidean norm for a vector x , and let $|X|$ denote the Frobenius norm of a matrix X defined by $|X| = \lambda_{\max}^{1/2}(XX^T)$, where $\lambda_{\max}(\cdot)$ is the maximum eigenvalue of matrix and the superscript T represents transpose. Operator $\text{Tr}(\cdot)$ denotes the matrix trace, and we denote by $X > 0$ (≥ 0) that matrix X is positive definite (semipositive definite). Let $\{r(t), t \geq 0\}$ be a right-continuous Markov process on the probability space taking values in finite state space $S = \{1, 2, \dots, N\}$ with $\Pi = [\pi_{ij}]$ being the chain generator, an $N \times N$ matrix. The entries π_{ij} , $i, j \in S$, are interpreted as transition rates such that

$$\mathbf{P}(r(t+dt) = j \mid r(t) = i) = \begin{cases} \pi_{ij}dt + o(dt) & \text{if } i \neq j, \\ 1 + \pi_{ii}dt + o(dt) & \text{if } i = j, \end{cases} \quad (2.1)$$

where $dt > 0$ and $\lim_{dt \rightarrow 0} (o(dt)/dt) = 0$. Here, $\pi_{ij} > 0$ ($i \neq j$) is the transition rate from i to j . Notice that the total probability axiom imposes $\pi_{ii} < 0$ and

$$\sum_{j=1}^N \pi_{ij} = 0, \quad \forall i \in S. \quad (2.2)$$

Consider the following continuous-time Markovian jump nonlinear system with uncertain noise:

$$\begin{aligned} \dot{x} &= f(x, r(t)) + \omega^0, \\ y &= h(x, r(t)) + v^0, \end{aligned} \quad (2.3)$$

where $x \in \mathbf{R}^n$ is state vector, and $y \in \mathbf{R}^m$ is measurement output. $f(\cdot, \cdot) \in \mathbf{R}^n$ and $h(\cdot, \cdot) \in \mathbf{R}^m$ are nonlinear vector functions. ω^0 and v^0 are n -dimensional and m -dimensional white noises and satisfy the following assumption.

Assumption 2.1. For any given time $s, t \geq 0$, there are

- (1) $E[\omega_t^0] = 0, E[v_t^0] = 0,$
- (2) $\text{Cov}[\omega_t^0, \omega_s^0] = W^0 \delta_{t,s} = (W + \Delta W) \delta_{t,s}, W \geq 0, \Delta W \geq 0,$
- (3) $\text{Cov}[v_t^0, v_s^0] = V^0 \delta_{t,s} = (V + \Delta V) \delta_{t,s}, V > 0, \Delta V \geq 0,$
- (4) $E\left[\begin{pmatrix} \omega_t^0 \\ v_t^0 \end{pmatrix} \cdot (\omega_s^{0T} v_s^{0T})\right] = \begin{bmatrix} W^0 \delta_{t,s} & 0 \\ 0 & V^0 \delta_{t,s} \end{bmatrix}.$

In Assumption 2.1, $W^0 \in \mathbf{R}^{n \times n}$ and $V^0 \in \mathbf{R}^{m \times m}$ consist of two parts, where W and V denote the stationary noise covariance matrix, whose values are exactly known. ΔW and ΔV denote the noise uncertainty caused by time-varying or sudden switch of system dynamics; they are unknown but norm-bounded. $\delta(\cdot, \cdot)$ is a *Dirac* function taking values in $\{0, 1\}$. For the deduction of robust Kalman filter, we introduce the following assumption.

Assumption 2.2. For any fixed system mode $r(t) = i \in S$ and vector $\sigma \in \mathbf{R}^n$, the nonlinear vector functions $f(\cdot, \cdot)$, $h(\cdot, \cdot)$ are assumed to satisfy $f(0, i) = h(0, i) = 0$ and

$$\begin{aligned} |f(x + \sigma, i) - f(x, i) - A(i)\sigma| &\leq |\Delta A(i)| |\sigma|, \\ |h(x + \sigma, i) - h(x, i) - C(i)\sigma| &\leq |\Delta C(i)| |\sigma|, \end{aligned} \quad (2.4)$$

where $A(i)$, $C(i)$ are Jacobian matrices of $f(\cdot, \cdot)$, $h(\cdot, \cdot)$, and $\Delta A(i)$, $\Delta C(i)$ satisfy

$$\begin{aligned} \Delta A(i) &= H_1(i)F(i)E(i), \\ \Delta C(i) &= H_2(i)F(i)E(i), \end{aligned} \quad (2.5)$$

where $H_1(i)$, $H_2(i)$, and $E(i)$, $i \in S$, are known constant matrices, and $F(i)$, $i \in S$, is unknown matrix satisfying $F^T(i)F(i) \leq I$. Establishing Assumption 2.2, the Markovian jump nonlinear system could be transformed to a nominal linear model via local linearization technique:

$$\begin{aligned} \dot{x} &= [A(r(t)) + \Delta A(r(t))]x + \omega^0, \\ y &= [C(r(t)) + \Delta C(r(t))]x + v^0. \end{aligned} \quad (2.6)$$

For simplification, we denote $A(r(t) = i)$, $H_1(r(t) = i)$, $H_2(r(t) = i)$, $E(r(t) = i)$, $\Delta A(r(t) = i)$, $C(r(t) = i)$, and $\Delta C(r(t) = i)$ by A_i , H_{1i} , H_{2i} , E_i , ΔA_i , C_i , and ΔC_i .

Theorem 2.3. Consider stochastically stable Markovian jump system (2.6), and assume that the noise is stationary, which means that $\Delta W = \Delta V = 0$. Then, one has the following standard Kalman filter (see [12]):

$$\hat{\hat{x}} = \hat{A}_i \hat{x} + K_i [y - \hat{C}_i \hat{x}], \quad (2.7)$$

where filtering gain K_i is given by the following coupled Riccati equations:

$$\begin{aligned} \hat{A}_i &= A_i + \left(\frac{1}{\epsilon_i} H_{1i} H_{1i}^T + W \right) P_i^{-1}, \\ \hat{C}_i &= \frac{1}{\epsilon_i} H_{2i} H_{1i} P_i^{-1} + C_i, \\ A_i P_i + P_i A_i^T + \epsilon_i P_i E_i^T E_i P_i + \sum_{j=1}^N \pi_{ij} P_j + \frac{1}{\epsilon_i} H_{1i} H_{1i}^T + W &= 0, \\ K_i &= \left(Q_i \hat{C}_i^T + \frac{1}{\epsilon_i} H_{1i} H_{2i}^T \right) \left(\frac{1}{\epsilon_i} H_{2i} H_{2i}^T + V \right)^{-1}, \\ (\hat{A}_i - K_i \hat{C}_i) Q_i + Q_i (\hat{A}_i - K_i \hat{C}_i)^T + K_i V K_i^T + \sum_{j=1}^N \pi_{ij} Q_j + \frac{1}{\epsilon_i} H_{1i} H_{1i}^T + W &= 0. \end{aligned} \quad (2.8)$$

Here, matrices $P_i > 0$, $Q_i > 0$ and scalar ϵ_i are chosen so that $\text{tr}(Q_i)$ reaches the minimum.

With the above standard Kalman filter gain K_i adopted, the state estimation error is

$$E \left\{ (x - \hat{x})^T (x - \hat{x}) \right\} \leq \max_{j \in S} \text{tr}(Q_j). \quad (2.9)$$

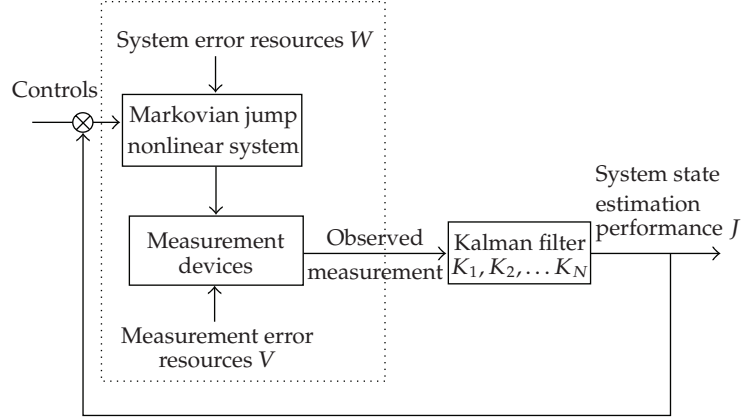


Figure 1: Standard Kalman filter with stationary noise.

Define the estimation error performance as

$$J(K_1, K_2, \dots, K_N, W, V) = \max_{j \in S} \text{tr}(Q_j). \quad (2.10)$$

According to Theorem 2.3 and the quality of Kalman filtering, if the noise is stationary ($\Delta W = \Delta V = 0$), the estimation error performance can achieve the minimum value by adopting standard Kalman filtering (2.7).

Now, we consider that the noise is not stationary, which means that $\Delta W \neq 0$ and $\Delta V \neq 0$; thus the new covariance matrix of noise is W^0, V^0 . If we still adopt the former predesigned standard Kalman filter gain K_i , the new state estimation error should be Q_i^0 , which satisfies

$$(\hat{A}_i - K_i \hat{C}_i)Q_i^0 + Q_i^0(\hat{A}_i - K_i \hat{C}_i)^T + K_i V^0 K_i^T + \sum_{j=1}^N \pi_{ij} Q_j^0 + \frac{1}{\epsilon_i} H_{1i} H_{1i}^T + W^0 = 0. \quad (2.11)$$

Therefore, the new estimation error performance is

$$J(K_1, K_2, \dots, K_N, W^0, V^0) = \max_{j \in S} \text{tr}(Q_j^0). \quad (2.12)$$

According to (2.10) and (2.12), the deviation of estimation error performance yielded by noise uncertainty ($\Delta W, \Delta V$) can be written as

$$\begin{aligned} \Delta J(K_1, K_2, \dots, K_N, \Delta W, \Delta V) &= J(K_1, \dots, K_N, W^0, V^0) - J(K_1, \dots, K_N, W, V) \\ &= \max_{j \in S} \text{tr}(Q_j^0) - \max_{j \in S} \text{tr}(Q_j) \leq r, \end{aligned} \quad (2.13)$$

where $r > 0$ is a parameter which is given according to detailed precision request of practical dynamic process.

Our design purpose is shown in Figures 1 and 2. Suppose that the noise is stationary with covariance matrix W, V , and that the system filtering performance is J with standard filtering gain K_i adopted as shown in Figure 1. But now noise is with uncertainty ($\Delta W, \Delta V$);

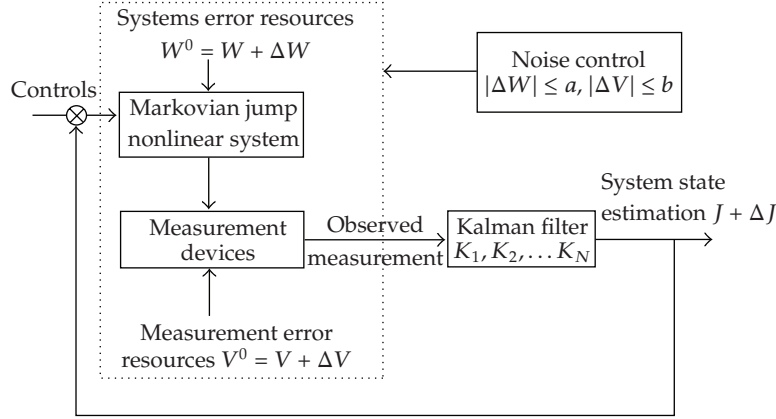


Figure 2: Robust Kalman filter with uncertain noise.

the former designed Kalman filter gain K_i will no longer be an optimal one. If we still want to get the precise estimation of system state so that the dynamic system could remain stable, there are two choices. One is to update the Kalman filter gain K_i according to new noise covariance matrix $(W + \Delta W, V + \Delta V)$, but this way is impossible or highly costly. Another way is to still adopt the former designed filtering gain K_i and take some actions in noise control. Based on this idea, the new estimation performance is $J + \Delta J$ with K_i adopted, and a deviation ΔJ occurs resulting from noise uncertainty (see Figure 2). For the robustness of system, which means that ΔJ is less than an admissible precision r , there must become limitation to noise uncertainty. Using the view of robust estimation, we are trying to find a maximum upper bound a, b for the uncertainty to noise covariance matrix. As long as the noise uncertainty is controlled to satisfy $|\Delta W| \leq a, |\Delta V| \leq b$ via noise control, we will achieve deviation of estimation performance to be within the admissible precision r , which means that $\Delta J \leq r$; thus the general system has robustness to noise uncertainty, and stability of the whole dynamic process can be maintained whatever the original stationary noise covariance matrix (W, V) is. In the following part of this paper, we seek the solution of maximum upper bound a, b .

3. Upper Bound of Nonstructural Noise Uncertainty

3.1. Mathematical Expression of Upper Bound

According to (2.8) and (2.11), we have

$$(\hat{A}_i - K_i \hat{C}_i) \Delta Q_i + \Delta Q_i (\hat{A}_i - K_i \hat{C}_i)^T + \sum_{j=1}^N \pi_{ij} \Delta Q_j + \Delta W + K_i \Delta V K_i^T = 0, \quad (3.1)$$

where $\Delta Q_i = Q_i^0 - Q_i$. From the above equation, it is easily seen that $\text{tr}(\Delta Q_i)$ is a linear mapping of $(\Delta W, \Delta V)$. Define a compact convex set as $\Xi = \{(\Delta W, \Delta V) : 0 \leq \Delta W \leq \Delta W^*, 0 \leq \Delta V \leq \Delta V^*\}$; thus the deviation of performance $\Delta J(K_1, K_2, \dots, K_N, \Delta W, \Delta V)$ is a mapping from Ξ to \mathbf{R}^1 , and it has the following facts.

Fact 1. For any given noise uncertainty $(\Delta W_j, \Delta V_j) \in \Xi$, $j = 1, 2$, if $\Delta W_1 \leq \Delta W_2$ and $\Delta V_1 \leq \Delta V_2$, one has

$$\Delta J(K_1, K_2, \dots, K_N, \Delta W_1, \Delta V_1) \leq \Delta J(K_1, K_2, \dots, K_N, \Delta W_2, \Delta V_2). \quad (3.2)$$

Fact 2. Define the maximum admissible deviation of estimation performance r as

$$r = \max_{(\Delta W, \Delta V) \in \Xi} \Delta J(K_1, K_2, \dots, K_N, \Delta W, \Delta V). \quad (3.3)$$

Thus, r could be achieved only by maximum noise uncertainty $(\Delta W^*, \Delta V^*)$, which means that

$$r = \Delta J(K_1, K_2, \dots, K_N, \Delta W^*, \Delta V^*). \quad (3.4)$$

The purpose of the following work is to construct a maximal compact convex set Ξ^* , as long as the noise uncertainty satisfies $(\Delta W, \Delta V) \in \Xi^*$, (2.13) is sure to establish. According to the finity of mode S , (2.13) is equivalent to

$$\text{tr}(Q_i^0) \leq r + \max_{j \in S} \text{tr}(Q_j). \quad (3.5)$$

Therefore, for each mode $i \in S$, there is

$$\text{tr}(\Delta Q_i) = \text{tr}(Q_i^0) - \text{tr}(Q_i) \leq r + \max_{j \in S} \text{tr}(Q_j) - \text{tr}(Q_i). \quad (3.6)$$

Define the maximum upper bound of noise uncertainty as $|\Delta W| \leq a$, $|\Delta V| \leq b$; thus

$$0 \leq \Delta W \leq aI_n, \quad 0 \leq \Delta V \leq bI_m. \quad (3.7)$$

Substituting the above inequalities into (3.1) and (3.6), one has

$$a \text{tr}(D_i) + b \text{tr}(G_i) \leq r + \max_{j \in S} \text{tr}(Q_j) - \text{tr}(Q_i), \quad \forall i \in S, \quad (3.8)$$

where matrices $D_i, G_i > 0$, $i \in S$, satisfy the following coupled Riccati equations:

$$\begin{aligned} (\hat{A}_i - K_i \hat{C}_i) D_i + D_i (\hat{A}_i - K_i \hat{C}_i)^T + \sum_{j=1}^N \pi_{ij} D_j + I_n &= 0, \\ (\hat{A}_i - K_i \hat{C}_i) G_i + G_i (\hat{A}_i - K_i \hat{C}_i)^T + \sum_{j=1}^N \pi_{ij} G_j + K_i K_i^T &= 0. \end{aligned} \quad (3.9)$$

According to the above analysis, seeking a maximum upper bound of noise uncertainty $(\Delta W, \Delta V)$ is equivalent to obtaining the optimal solution of a , b :

$$\begin{aligned} \max \quad & a \cdot b \\ \text{s.t.} \quad & a \cdot \text{tr}(D_i) + b \cdot \text{tr}(G_i) \leq r + \max_{j \in S} \text{tr}(Q_j) - \text{tr}(Q_i), \quad a \geq 0, b \geq 0, i \in S. \end{aligned} \quad (3.10)$$

Thus, seeking the optimal solution a , b is transformed to a nonlinear programming problem with linear inequalities' constraints. Now, we discuss how to find the analytical solution of such problem.

3.2. Analytical Solution

Since $\Xi = \{(\Delta W, \Delta V)\}$ is a compact convex set and the inequalities' constraints in (3.10) compose a compact set on which $a \cdot b$ is defined as a continuous function, thus the nonlinear programming problem must have optimal solution a^* , b^* and the existence of solution is proved. Next, we will seek the analytical solution a^* , b^* .

Decompose the original nonlinear programming problem (see (3.10)) into N subproblems:

$$\begin{aligned}
 & \max \quad a_1 \cdot b_1 \\
 & \text{s.t.} \quad a_1 \cdot \text{tr}(D_1) + b_1 \cdot \text{tr}(G_1) \leq r + \max_{j \in S} \text{tr}(Q_j) - \text{tr}(Q_1) \\
 & \max \quad a_2 \cdot b_2 \\
 & \text{s.t.} \quad a_2 \cdot \text{tr}(D_2) + b_2 \cdot \text{tr}(G_2) \leq r + \max_{j \in S} \text{tr}(Q_j) - \text{tr}(Q_2) \\
 & \quad \vdots \\
 & \max \quad a_N \cdot b_N \\
 & \text{s.t.} \quad a_N \cdot \text{tr}(D_N) + b_N \cdot \text{tr}(G_N) \leq r + \max_{j \in S} \text{tr}(Q_j) - \text{tr}(Q_N).
 \end{aligned} \tag{3.11}$$

By using *Lagrange* method, we have the optimal analytical solution for each subproblem as

$$\begin{aligned}
 a_i^* &= \frac{r + \max_{j \in S} \text{tr}(Q_j) - \text{tr}(Q_i)}{2 \text{tr}(D_i)}, \\
 b_i^* &= \frac{r + \max_{j \in S} \text{tr}(Q_j) - \text{tr}(Q_i)}{2 \text{tr}(G_i)}.
 \end{aligned} \tag{3.12}$$

Thus, the analytical solution for the original nonlinear programming problem (see (3.10)) is given as

$$\begin{aligned}
 a^* &= \min_{i \in S} a_i^* = \min_{i \in S} \left\{ \frac{r + \max_{j \in S} \text{tr}(Q_j) - \text{tr}(Q_i)}{2 \text{tr}(D_i)} \right\}, \\
 b^* &= \min_{i \in S} b_i^* = \min_{i \in S} \left\{ \frac{r + \max_{j \in S} \text{tr}(Q_j) - \text{tr}(Q_i)}{2 \text{tr}(G_i)} \right\}.
 \end{aligned} \tag{3.13}$$

Remark 3.1. The analytical solution of the nonlinear programming problem is given by the above analysis; however, it is only an optimal solution for each subproblem. This analytical solution in (3.13) is local optimal, but global suboptimal. For the global optimal solution, we could only get the numerical solution using “fmincon” function in MATLAB software. The optimal analytical solution of such nonlinear programming problem is still an open problem in mathematics for further exploration.

Theorem 3.2. Consider Markovian jump system (2.6). If one adopts state estimator (2.7) and Kalman filter gain (2.8), there exists a maximum admissible compact set Ξ . As long as the uncertainty to noise covariance matrix satisfies $(\Delta W, \Delta V) \in \Xi$, the deviation of system state estimation error performance ΔJ is within a given precision r .

Remark 3.3. Take into account the existence of noise uncertainty, and the new noise covariance matrix is given as $(W + \Delta W, V + \Delta V)$. Thus, the former predesigned optimal Kalman filter gain K_i , which is deduced from stationary noise (W, V) , will no longer be optimal and may cause distortion of control signals. But, this does not mean that we need to redesign Kalman filter. According to the above analysis, if we can successfully limit noise uncertainty $(\Delta W, \Delta V)$ to be within an admissible compact set Ξ , the predesigned Kalman filter gain K_i can still be effective though it is not optimal. Moreover, the deviation of estimation performance is ensured to be within a desirable precision r .

4. Mini-Max Robust Filter

Let $K_1^*, K_2^*, \dots, K_N^*$ denote the standard Kalman filtering gain according to new noise covariance matrix pair $(W^*, V^*) = (W + \Delta W^*, V + \Delta V^*)$, which corresponds to the maximum admissible noise uncertainty $(\Delta W^*, \Delta V^*)$; thus $K_1^*, K_2^*, \dots, K_N^*$ satisfy

$$\begin{aligned} A_i P_i^* + P_i^* A_i^T + \epsilon_i P_i^* E_i^T E_i P_i^* + \sum_{j=1}^N \pi_{ij} P_j^* + \frac{1}{\epsilon_i} H_{1i} H_{1i}^T + W^* &= 0, \\ K_i^* &= \left(Q_i^* \hat{C}_i^T + \frac{1}{\epsilon_i} H_{1i} H_{2i}^T \right) \left(\frac{1}{\epsilon_i} H_{2i} H_{2i}^T + V^* \right)^{-1}, \\ (\hat{A}_i - K_i^* \hat{C}_i) Q_i^* + Q_i^* (\hat{A}_i - K_i^* \hat{C}_i)^T + K_i^* V^* K_i^{*T} + \sum_{j=1}^N \pi_{ij} Q_j^* + \frac{1}{\epsilon_i} H_{1i} H_{1i}^T + W^* &= 0. \end{aligned} \quad (4.1)$$

According to the least-square quality of standard Kalman filtering, we have

$$\Delta J(K_1^*, K_2^*, \dots, K_N^*, \Delta W^*, \Delta V^*) \leq \Delta J(K_1, K_2, \dots, K_N, \Delta W^*, \Delta V^*). \quad (4.2)$$

On the other hand, with the establishment of Fact 1, there is

$$\Delta J(K_1^*, K_2^*, \dots, K_N^*, \Delta W, \Delta V) \leq \Delta J(K_1^*, K_2^*, \dots, K_N^*, \Delta W^*, \Delta V^*). \quad (4.3)$$

Thus, we have the following saddle-point inequality:

$$\begin{aligned} \Delta J(K_1^*, K_2^*, \dots, K_N^*, \Delta W, \Delta V) &\leq \Delta J(K_1^*, K_2^*, \dots, K_N^*, \Delta W^*, \Delta V^*) \\ &\leq \Delta J(K_1, K_2, \dots, K_N, \Delta W^*, \Delta V^*). \end{aligned} \quad (4.4)$$

By game theory, we have

$$\min_{K_i} \max_{(\Delta W, \Delta V) \in \Xi} \Delta J(K_1, K_2, \dots, K_N, \Delta W, \Delta V) = \max_{(\Delta W, \Delta V) \in \Xi} \min_{K_i} \Delta J(K_1, K_2, \dots, K_N, \Delta W, \Delta V). \quad (4.5)$$

This means that the optimal estimation under the worst situation is a mini-max filter. It cannot only minimize the estimation performance under the largest noise uncertainty $(a^* I_n, b^* I_m)$, but can also ensure the deviation to be within a given precision r . For this reason, this Kalman filter design is a robust mini-max filter.

Remark 4.1. Traditional Kalman filtering design is performed on the basis that noise covariance matrix is stationary and exactly known, and it will fail when the noise covariance matrix is unknown or has uncertainty. In our method, the filter design could be divided into two steps. Firstly, we design standard Kalman filter according to the stationary noise covariance matrix (W, V) , then via some technical methods such as noise control we impose the noise uncertainty to be within the given bound $(\Delta W^*, \Delta V^*)$, which could be presented in the form of nonstructural $(a^* I_n, b^* I_m)$. In practical dynamic process, when the noise uncertainty reaches the maximum, the ideal deviation of performance is $\Delta J(K_1^*, K_2^*, \dots, K_N^*, \Delta W^*, \Delta V^*)$, and this deviation is less than the worst case $\Delta J(K_1, K_2, \dots, K_N, \Delta W^*, \Delta V^*) \leq r$, which ensures the estimation of system states and control signals to be precise to some extent, and the synthetical system to be robust and stable. For this reason, the Kalman filter design has robustness to noise uncertainty, and according to (4.5), this filter is also a mini-max filter.

5. Simulation

Consider the following two-mode Markovian jump system.

Let the system mode $r(t) = 1$ be given by

$$\begin{aligned}\dot{x}_1 &= -0.6x_1 + 0.5x_2 + 0.01 \sin(x_1 + x_2) + \omega_1^0, \\ \dot{x}_2 &= 0.7x_1 + 0.02 \cos(x_1 - x_2) + \omega_2^0, \\ y &= x_1 + 0.5x_2 + v^0.\end{aligned}\tag{5.1}$$

Let the system mode $r(t) = 2$ be given by

$$\begin{aligned}\dot{x}_1 &= -x_1 + 0.6x_2 + 0.02 \sin x_2 + \omega_1^0, \\ \dot{x}_2 &= 0.8x_1 - 1.1x_2 + 0.02 \cos x_1 + \omega_2^0, \\ y &= x_1 + v^0,\end{aligned}\tag{5.2}$$

where uncertain state and measurement noise are $\omega^0 = [\omega_1^0 \ \omega_2^0]^T$ and v^0 ; its stationary covariance matrix is known as $W = \begin{bmatrix} 1 & 0 \\ 0 & 1 \end{bmatrix}$, $V = 1$; system mode transition matrix is $\Pi = \begin{bmatrix} -0.6 & 0.6 \\ 0.9 & -0.9 \end{bmatrix}$; the admissible bound of performance deviation is $r = 0.3$.

The detailed algorithm is as follows.

- (1) By applying Assumption 2.1, we have $A_1 = \begin{bmatrix} -0.6 & 0.5 \\ 0.7 & 0 \end{bmatrix}$, $C_1 = [1 \ 0.5]$, $A_2 = \begin{bmatrix} -1 & 0.6 \\ 0.8 & -1.1 \end{bmatrix}$, $C_2 = [1 \ 0]$, $H_{11} = [0.1 \ 0.2]^T$, $E_1 = [0.1 \ 0.1]$, $H_{12} = [0.1 \ 0.1]^T$, $E_2 = [0.2 \ 0.2]$.

Notice that $\Delta C_i \equiv 0$; thus $H_{21} = H_{22} = 0$.

- (2) Solve (2.8) and get Q_1, Q_2 and K_1, K_2 : $Q_1 = \begin{bmatrix} 2.6058 & 1.4207 \\ 1.4207 & 3.1934 \end{bmatrix}$, $Q_2 = \begin{bmatrix} 2.6573 & 1.4181 \\ 1.4181 & 2.8473 \end{bmatrix}$, $K_1 = \begin{bmatrix} 0.8748 \\ 1.0921 \end{bmatrix}$, $K_2 = \begin{bmatrix} 0.6567 \\ 0.4866 \end{bmatrix}$.
- (3) Substitute the result to (3.10), using *Lagrange* method; the upper bound of noise uncertainty is given as

$$a^* = 0.1014, \quad b^* = 0.1701.\tag{5.3}$$

- (4) Let the new noise covariance matrix correspond to the maximum uncertainty:

$$\begin{aligned} W^* &= W + \Delta W = W + a^* \cdot I_2, \\ V^* &= V + \Delta V = V + b^* \cdot I_1. \end{aligned} \quad (5.4)$$

- (5) Repeat step (2), and we have the correspondent Q_1^* , Q_2^* , K_1^* , K_2^* for new noise covariance matrix (W^*, V^*) :

$$\begin{aligned} Q_1^* &= \begin{bmatrix} 2.7641 & 1.4417 \\ 1.4417 & 3.2688 \end{bmatrix}, & Q_2^* &= \begin{bmatrix} 2.6788 & 1.4458 \\ 1.4458 & 2.9011 \end{bmatrix}, \\ K_1^* &= \begin{bmatrix} 0.8977 \\ 1.3021 \end{bmatrix}, & K_2^* &= \begin{bmatrix} 0.7012 \\ 0.5041 \end{bmatrix}. \end{aligned} \quad (5.5)$$

- (6) Applying the robust Kalman filtering, there is saddle-point inequality:

$$\begin{aligned} \Delta J(K_1^*, K_2^*, \Delta W, \Delta V) &\leq \Delta J(K_1^*, K_2^*, \Delta W^*, \Delta V^*) \\ &= \max\{\text{tr}(Q_1^*), \text{tr}(Q_2^*)\} - \max\{\text{tr}(Q_1), \text{tr}(Q_2)\} \\ &= 0.2337 < 0.3 \\ &= \Delta J(K_1, K_2, \Delta W^*, \Delta V^*). \end{aligned} \quad (5.6)$$

From the above simulation, it is seen that with the noise uncertainty being limited within the upper bound a^* , b^* via noise control, the deviation of system estimation performance is less than the admissible precision r . Because the analytical solution a^* , b^* is global suboptimal, the deviation of system estimation performance (0.2337) is obviously less than admissible precision (0.3), which means that this solution is a conservative one and the global optimal solution of a , b could be a little greater than a^* , b^* . Thus, this method allows flexibility to the designer to some extent.

6. Conclusion

In this paper, robust Kalman filter for continuous-time Markovian jump nonlinear systems with uncertain noise is considered. For the stability of dynamic system when statistical information of noise is unavailable, a new design method is given by obtaining the maximum admissible bound of uncertainty to noise covariance matrix. Based on this, the deviation of system estimation performance is thus guaranteed to be within a given precision. Furthermore, the worst performance yielded by noise uncertainty can be minimized by this method since it is a mini-max robust filter. The analytical solution of the bound to noise uncertainty is also discussed in this paper, which is a global, suboptimal, and conservative solution using *Lagrange* method. The simulation results show the validity of this design.

Acknowledgment

This work has been funded by BK21 research project: Switching Control of Systems with Structure Uncertainty and Noise.

References

- [1] B. D. O. Anderson and J. B. Moore, *Optimal Filtering*, Prentice-Hall, Englewood Cliffs, NJ, USA, 1979.
- [2] V. Poor and D. P. Looze, "Minimax state estimation for linear stochastic systems with noise uncertainty," *IEEE Transactions on Automatic Control*, vol. 26, no. 4, pp. 902–906, 1981.
- [3] S. Sangsuk-lam and T. E. Bullock, "Analysis of continuous-time Kalman filtering under incorrect noise covariances," *Automatica*, vol. 24, no. 5, pp. 659–669, 1988.
- [4] Y.-L. Chen and B.-S. Chen, "Minimax robust deconvolution filters under stochastic parametric and noise uncertainties," *IEEE Transactions on Signal Processing*, vol. 42, no. 1, pp. 32–45, 1994.
- [5] M. Mariton, *Jump Linear Systems in Automatic Control*, Marcel-Dekker, New York, NY, USA, 1990.
- [6] Y. Ji and H. J. Chizeck, "Controllability, stabilizability, and continuous-time Markovian jump linear quadratic control," *IEEE Transactions on Automatic Control*, vol. 35, no. 7, pp. 777–788, 1990.
- [7] X. Feng, K. A. Loparo, Y. Ji, and H. J. Chizeck, "Stochastic stability properties of jump linear systems," *IEEE Transactions on Automatic Control*, vol. 37, no. 1, pp. 38–53, 1992.
- [8] F. Dufour and P. Bertrand, "The filtering problem for continuous-time linear systems with Markovian switching coefficients," *Systems & Control Letters*, vol. 23, no. 6, pp. 453–461, 1994.
- [9] C. E. de Souza, A. Trofino, and K. A. Barbosa, "Mode-independent H_∞ filters for Markovian jump linear systems," *IEEE Transactions on Automatic Control*, vol. 51, no. 11, pp. 1837–1841, 2006.
- [10] S. K. Nguang and P. Shi, "Robust H_∞ output feedback control design for Takagi-Sugeno systems with Markovian jumps: a linear matrix inequality approach," *Journal of Dynamic Systems, Measurement and Control*, vol. 128, no. 3, pp. 617–625, 2006.
- [11] J. Zhu, H. Xi, H. Ji, and B. Wang, "A robust adaptive controller for Markovian jump uncertain nonlinear systems with Wiener noises of unknown covariance," *International Journal of Control, Automation and Systems*, vol. 5, no. 2, pp. 128–137, 2007.
- [12] P. Shi, E.-K. Boukas, and R. K. Agarwal, "Kalman filtering for continuous-time uncertain systems with Markovian jumping parameters," *IEEE Transactions on Automatic Control*, vol. 44, no. 8, pp. 1592–1597, 1999.
- [13] M. S. Mahmoud, P. Shi, and A. Ismail, "Robust Kalman filtering for discrete-time Markovian jump systems with parameter uncertainty," *Journal of Computational and Applied Mathematics*, vol. 169, no. 1, pp. 53–69, 2004.

Research Article

GA-Based Fuzzy Sliding Mode Controller for Nonlinear Systems

P. C. Chen,¹ C. W. Chen,² and W. L. Chiang¹

¹ Department of Civil Engineering, National Central University, Chung-li 32011, Taiwan

² Department of Logistics Management, College of Management, Shu-Te University, Kaohsiung 82445, Taiwan

Correspondence should be addressed to C. W. Chen, cwchen@mail.stu.edu.tw

Received 20 February 2008; Revised 4 June 2008; Accepted 8 August 2008

Recommended by Paulo Gonçalves

Generally, the greatest difficulty encountered when designing a fuzzy sliding mode controller (FSMC) or an adaptive fuzzy sliding mode controller (AFSMC) capable of rapidly and efficiently controlling complex and nonlinear systems is how to select the most appropriate initial values for the parameter vector. In this paper, we describe a method of stability analysis for a GA-based reference adaptive fuzzy sliding model controller capable of handling these types of problems for a nonlinear system. First, we approximate and describe an uncertain and nonlinear plant for the tracking of a reference trajectory via a fuzzy model incorporating fuzzy logic control rules. Next, the initial values of the consequent parameter vector are decided via a genetic algorithm. After this, an adaptive fuzzy sliding model controller, designed to simultaneously stabilize and control the system, is derived. The stability of the nonlinear system is ensured by the derivation of the stability criterion based upon *Lyapunov's* direct method. Finally, an example, a numerical simulation, is provided to demonstrate the control methodology.

Copyright © 2008 P. C. Chen et al. This is an open access article distributed under the Creative Commons Attribution License, which permits unrestricted use, distribution, and reproduction in any medium, provided the original work is properly cited.

1. Introduction

Over the past few years, fuzzy control (FC) can be designed without needing an exact mathematical model of the system to be controlled, and can efficiently control complex continuous unmodeled or partially modeled processes [1, 2]. There have been significant research efforts devoted to the analysis and control designs for fuzzy systems (see [3, 4] and the references therein). The main motivation for this development has been applied to practical nonlinear systems and engineering problems (see [5–7] and the references therein). Undoubtedly, *Lyapunov's* theory is one of the most common approaches for dealing with the stability analysis of systems. However, to overcome the conservatism that arises from the use of *Lyapunov's* methods, it has been necessary to develop a number of more effective methods, for example, fuzzy *Lyapunov* functions [8, 9]. There are also many important issues that have

advanced results for T-S fuzzy control systems, such as time delays [10–13], H^∞ performance [3–15], robustness [16, 17], neural networks (NNs), and genetic algorithms (GAs) [18–21]. Furthermore, much work has been published on the design of fuzzy sliding mode controllers (FSMCs) [22, 23]. An FSMC is composed of an FC and a sliding mode controller (SMC) [24–26]. An FSMC is a powerful and robust control strategy for the treatment of modeling uncertainties and external disturbances. Although control performance is good, one still has to decide on the parameters. This is one of the most important issues in their design.

In the so-called *adaptive FSMC* (AFSMC), [27–29], an adaptive algorithm is utilized to find the best high-performance parameters for the FSMC [30, 31]. In recent years, adaptive fuzzy control system designs have attracted a good deal of attention as a promising way to approach nonlinear control problems [30, 31]. For adaptive fuzzy control, one initially constructs a fuzzy model to describe the dynamic characteristics of the controlled system; then, an FSMC is designed based on the fuzzy model to achieve the control objectives. After this, adaptive laws are designed (with Lyapunov's synthesis approach) for tuning the adjustable parameters of the fuzzy models, and analyzing the stability of the overall system.

Deciding on the fuzzy rules and the initial parameter vector values for the AFSMC is very important. A genetic algorithm [32–34] is usually used as an optimization technique in the self-learning or training strategy for deciding on the fuzzy control rules and the initial values of the parameter vector. This GA-based AFSMC should improve the immediate response, the stability, and the robustness of the control system.

Another common problem encountered when switching the control input of the FSMC system is the so-called “chattering” phenomenon. Chattering is eliminated by smoothing the control discontinuity inside a thin boundary layer, which essentially acts as a low-pass filter structure for the local dynamics [25]. The boundary-layer function is introduced into these updated laws to cover parameter and modeling errors, and to guarantee that the state errors converge within a specified error bound.

In this study, we focus on the design of robust tracking control for a class of nonlinear uncertain system involving plant uncertainties and external disturbances. First, the nonlinear system for the tracking of a reference trajectory for the plant [35] is described via fuzzy models with fuzzy rules. A genetic algorithm is used to find the initial values of the parameter vector. Then the designed adaptive control laws of the reference adaptive fuzzy sliding mode controller (RAFSMC) are updated. This GA-based RAFSMC would improve the immediate response, the stability, and the robustness of the control system. Finally, both the tracking error and the modeling error approach zero.

2. Reference modeling of a nonlinear dynamic system

The plant is a single-input/single-output n th-order system with $n \geq 1$:

$$\begin{aligned}\dot{x}_1 &= x_2, \\ &\vdots \\ \dot{x}_{n-1} &= x_n, \\ \dot{x}_n &= f(x) + g(x) \cdot u + d, \\ y &= x_1,\end{aligned}\tag{2.1}$$

where $x = [x_1, x_2, \dots, x_{n-1}, x_n]^T \in R^n$ is the state vector of the system; $u \in R$ is the control

signal; f, g are smooth nonlinear functions; d denotes the external disturbance $d(t)$ which is unknown but usually bounded.

The states $x = [x_1, x_2, \dots, x_{n-1}, x_n]^T$ are assumed to be available. For example, a single robot can be represented in the form of (2.1), with $n = 2$ and $x(x_1 = \theta, x_2 = \dot{\theta})$ being measurable. Differentiating the output with respect to time for n times (till the control input u appears), one obtains the input/output form of (2.1):

$$\overset{(n)}{y} = f(x) + g(x) \cdot u + d(t). \quad (2.2)$$

The system is said to have a relative degree n , if $g(x)$ is bounded away from zero.

Assumption 2.1. $g(x)$ is bounded away from zero over a compact set $\zeta \subset R^n$,

$$|g(x)| \geq b > 0, \quad \forall x \in \zeta. \quad (2.3)$$

If the control goal is for the plant output y to track a reference trajectory y_r , the reference control input r can be defined by the following reference model:

$$r = \overset{(n)}{y}_r + \alpha_{n-1} \overset{(n-1)}{y}_r + \alpha_{n-2} \overset{(n-2)}{y}_r + \dots + \alpha_1 \dot{y}_r + \alpha_0 y_r, \quad (2.4)$$

where $\alpha_{n-1}, \alpha_{n-2}, \dots, \alpha_1, \alpha_0$ are chosen such that the polynomial $\ell^n + \alpha_{n-1}\ell^{n-1} + \alpha_{n-2}\ell^{n-2} + \dots + \alpha_1\ell + \alpha_0$ is Hurwitz, and ℓ here denotes the complex Laplace variable.

If $f(x), g(x)$ are known, and assumption 2.1 is satisfied, the control law can defined by

$$u = \frac{-f(x) - d(x) - \left(\alpha_{n-1} \overset{(n-1)}{y} + \dots + \alpha_1 \dot{y} + \alpha_0 y \right) + r}{g(x)}, \quad \forall x \in S. \quad (2.5)$$

Substituting (2.5) into (2.1), the linearized system becomes

$$\left(\overset{(n)}{y}_r - \overset{(n)}{y} \right) + \alpha_{n-1} \left(\overset{(n-1)}{y}_r - \overset{(n-1)}{y} \right) + \dots + \alpha_1 (\dot{y}_r - \dot{y}) + \alpha_0 (y_r - y) = 0. \quad (2.6)$$

If we define $e = y_r - y$ as the tracking error, then the reference control input (2.4) results in the following error equation:

$$\overset{(n)}{e} + \alpha_{n-1} \overset{(n-1)}{e} + \dots + \alpha_1 \dot{e} + \alpha_0 e = 0. \quad (2.7)$$

It is clear that e will approach zero if $\alpha_{n-1}, \alpha_{n-2}, \dots, \alpha_1, \alpha_0$ are chosen, such that the polynomial $\ell^n + \alpha_{n-1}\ell^{n-1} + \alpha_{n-2}\ell^{n-2} + \dots + \alpha_1\ell + \alpha_0$ is Hurwitz.

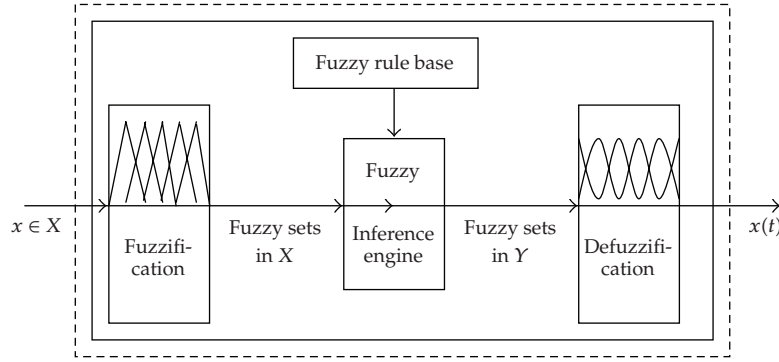


Figure 1: The fuzzy logic controller system.

3. Development of a GA-based FSMC

In general, people describe the decision-making process using linguistic statements, such as “IF something happens, THEN do a certain action.” For example, let us look at a rule: “IF the temperature is high, THEN the power of the heater is low.” In this statement both “high” and “low” are linguistic terms. Although this kind of linguistic rule is not precise, humans can use them to make correct decisions. To utilize such fuzzy information in a scientific way, mathematical representation of the fuzzy information is needed. Fuzzy set theory and approximate reasoning are two ways that such linguistic information can be dealt with mathematically. A review of the literature provides the theoretical foundation for the developed fuzzy logic controller. The configuration of the fuzzy logic controller is shown in Figure 1.

The basic concepts for fuzzy sets and fuzzy logic are briefly described below.

(1) *Fuzzy set, fuzzifier, and membership function.* Let X denote the universe of discourse. A fuzzy set A in X is characterized by a membership function $\mu_A : X \rightarrow [0, 1]$, with $\mu_A(x)$ representing the grade of membership of $x \in X$ in fuzzy set A . For example, the Gaussian-shaped membership function is represented as $\mu_A(x) = \exp(-((x - m)/\sigma)^2)$, where m is the center and σ denotes the spread of the membership function.

(2) *Fuzzy rule base and fuzzy inference engine.* Each rule R_j in the fuzzy rule base can be expressed as

$$R_j : \text{IF } x_1 \text{ is } A_{1j} \text{ and } \cdots x_n \text{ is } A_{nj}, \text{ THEN } y \text{ is } B_j; \text{ and } \mu_{R_j}(\chi) = \prod_{i=1}^n \mu_{A_{ij}}(x_i). \quad (3.1)$$

(3) *Defuzzifier.* The defuzzifier maps a fuzzy set A in X to a crisp point $x \in X$. There are several defuzzification methods described in the literature. The most popular is the weighted average defuzzification method defined as $y = \sum_{j=1}^N \theta_j \cdot \mu_{R_j}(\chi) / \sum_{j=1}^N \mu_{R_j}(\chi)$.

The FSMC is composed of a sliding mode controller and an FLC. This makes it a powerful and robust control strategy for the treatment of modeling uncertainties and external disturbances. The sliding mode plant combined with the FLC is shown in Figure 2.

Genetic algorithms (GAs) are parallel, global search techniques derived from the concepts of evolutionary theory and natural genetics. They emulate biological evolution by means of genetic operations such as reproduction, crossover, and mutation. GAs are usually

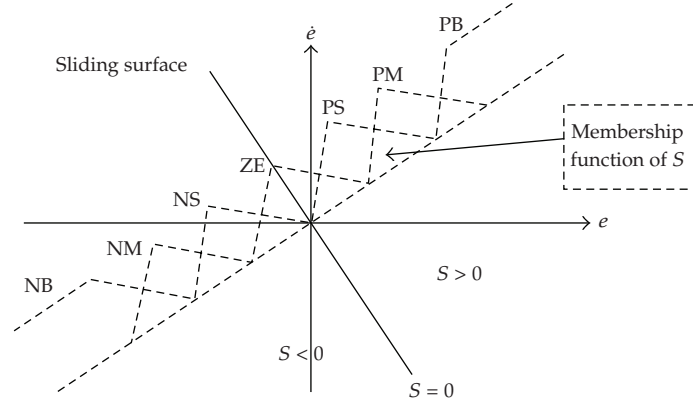


Figure 2: The sliding mode plant combined with the FLC.

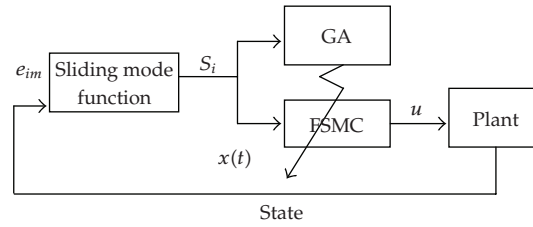


Figure 3: GA-based FSMC.

used as optimization techniques and it has been shown that they also perform well with multimodal functions (i.e., functions which have multiple local optima).

Genetic algorithms work with a set of artificial elements (binary strings, e.g., 0101010101) called a population. An individual (string) is referred to as a chromosome, and a single bit in the string is called a gene. A new population (called offspring) is generated by the application of genetic operators to the chromosomes in the old population (called parents). Each iteration of the genetic operation is referred to as a generation.

A fitness function, specifically the function to be maximized, is used to evaluate the fitness of an individual. The offspring may have better fitness than their parents. Consequently, the value of the fitness function increases from generation to generation. In most genetic algorithms, mutation is a random-work mechanism to avoid the problem of being trapped in a local optimum. Theoretically, a global optimal solution can be found.

Offspring are generated from the parents until the size of the new population is equal to that of the old population. This evolutionary procedure continues until the fitness reaches the desired specifications. However, in a specific application, the fitness specification might be used to stop the evolutionary process. In most applications, the optimal fitness value is totally unknown. In this case, the evolutionary process is interrupted either by stabilization of the fitness value (the variation is below a specific value) or by reaching the maximum number of generations.

Knowledge acquisition is the most important task in the fuzzy sliding mode controller design. The initial values of the entries in the consequent parameter vector are decided by the self-organizing of FSMC system which developed based on GA. The configuration of this system is shown in Figure 3.

The learning procedure for the GA-based FSMC is summarized as follows.

(1) The fuzzy rule base of FSMC (with fixed premise parts and random consequence parts) is constructed. For example, FSMC for system (2.1):

$$\text{FSMC} : \begin{cases} R_1^{(i)} : \text{IF } S \text{ is } PB(4, 0.424) & \text{THEN } u \text{ is } \hat{u}_1^{(i)}(\hat{\theta}_1^{(i)}), \\ R_2^{(i)} : \text{IF } S \text{ is } PM(3.2, 0.424) & \text{THEN } u \text{ is } \hat{u}_2^{(i)}(\hat{\theta}_2^{(i)}), \\ \vdots \\ R_N^{(i)} : \text{IF } S \text{ is } PB(-4, 0.424) & \text{THEN } u \text{ is } \hat{u}_N^{(i)}(\hat{\theta}_N^{(i)}), \end{cases} \quad (3.2)$$

where $\hat{u}_j^{(i)}$ is an unknown linguistic label for the control u ; $\hat{\theta}_j^{(i)}$ is the adjustable parameter, which have to be encoded as binary strings for genetic operations.

(2) Encode each parameter, $\hat{\theta}_j^{(i)}$ ($i = 1, 2, \dots, M$; $j = 1, 2, \dots, N$), to a d -bit binary code, $P_j^{(i)}(h) = (b_j^1 b_j^2 \dots b_j^d)(h) = \text{enc}(\hat{\theta}_j^{(i)}(h))$, where $b_j^1, b_j^2, \dots, b_j^d \in \{0, 1\}$ and $\text{enc}(\ast)$ denote the encoding operator which encodes the real values to the corresponding binary codes and synthesizes the chromosome of the i th individual.

(3) Establish the population for generation h , $P_j(h) = \{P_j^{(1)}(h), P_j^{(2)}(h), \dots, P_j^{(M)}(h)\}$, where M is the population size, and every individual $P_j^{(i)}(h)$ corresponds to a binary-code parameter of an FSMC candidate.

(4) Evaluate the fitness value of each individual. The fitness function F is defined as $F = 1/(w\|s(k)\| + v\|u(k)\| + \varepsilon_0)$, where $k = \text{int}(t/\Delta t)$ denotes the iteration instance; Δt is the sampling period; $\text{int}(\ast)$ is the rounding off operator; w and v are positive weights; ε_0 is a very small positive constant used to avoid the numerical error of dividing by zero.

(5) Based on the fitness value of the individual, keep the best and apply the genetic operators. Assuming that the population size M is 12, pick the top ten-fitted individuals in $P_j(h)$ to apply as genetic operators, that is, reproduction, crossover, mutation (assuming the mutation rate is 0.03125), and keep the top two fitted individuals to generate a new population $P_j(h+1)$, as the offspring of $P_j(h)$.

(6) Decode each binary code to its real value and use this to calculate the control u , then apply u to the system (2.1).

(7) Set $h = h + 1$; go to Step 2, and repeat the aforementioned procedure until $F \geq F_M$ or $h \geq H$, where F_M and H denote an acceptable specific fitness value and the top generation number, respectively, as specified by the designer.

In general, there are at least four methods for the construction of a fuzzy rule base: (1) from expert knowledge or operator experience; (2) modeling an operator's control action; (3) modeling a process; (4) generating fuzzy rules by training, self-organizing, and self-learning algorithms. In Figure 3, GA is used as the learning and training mechanism. The use of the GA means that the second, third, and fourth approaches also provide an efficient way to obtain a fuzzy rule base. Although there are several methods that can provide excellent results in this kind of modeling [36–38], we are convinced that GAs are the most advantageous way to extract an optimal, or at least suboptimal fuzzy rule base for the initial values of the consequent parameter vector of the FSMC or AFSMC.

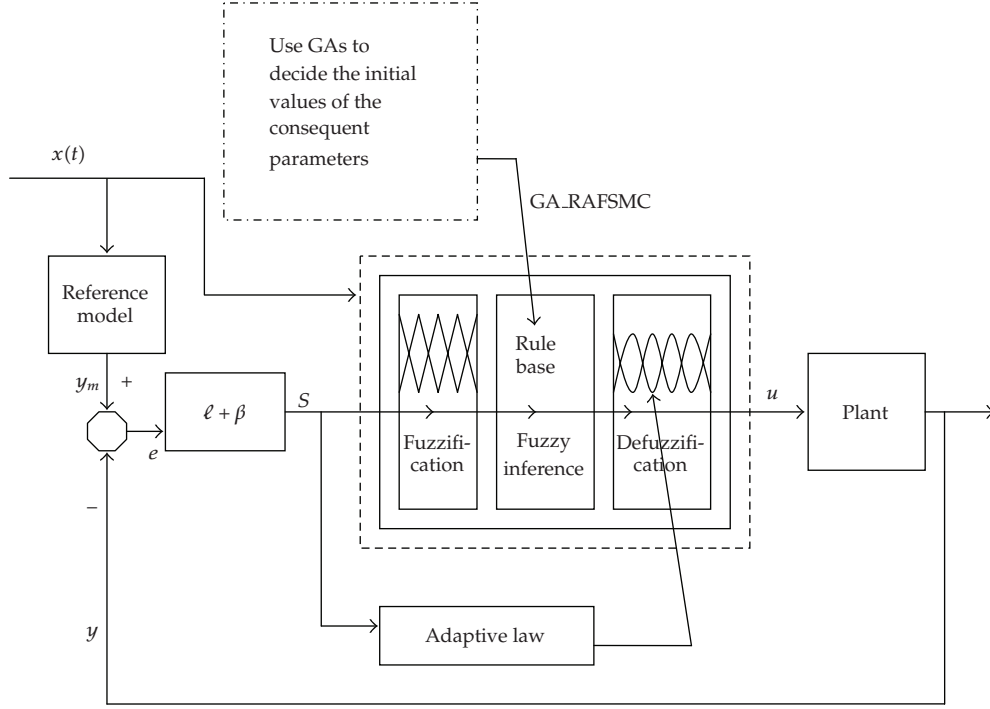


Figure 4: GA-RAFSMC system.

4. GA-based RAFSMC for nonlinear systems

A schematic representation of the GA-RAFSMC system is shown in Figure 4. If $f(x)$, $g(x)$ are known, we can design the FLC (4.1) to approximate u :

$$\bar{u}(\bar{\theta}) = \sum_{k=1}^m R_k \left(- \left(\frac{\|S_i - C_{ki}\|}{\beta} \right)^2 \right) \cdot \bar{\theta}_k, \quad (4.1)$$

where m is the sum of the fuzzy rules, $\bar{\theta}_k$, that is, $|\bar{\theta}_k| \leq \theta_{\max}$ indicate the adjustable consequent parameters of the FLC, and $R(S) = [R_1(S), R_2(S), \dots, R_m(S)]^T$ is the vector of fuzzy basis function [23] which is defined as

$$R_k(S) = R_k(\|S_i - C_{ki}\|) = \frac{\prod_{i=1}^n \mu_k(\|S_i - C_{ki}\|)}{\sum_{k=1}^m \left[\prod_{i=1}^n \mu_k(\|S_i - C_{ki}\|) \right]}, \quad (4.2)$$

where $k = 1, \dots, m$ and $i = 1, \dots, n$ with μ_k represent the degree of membership. The S_i in μ_k can be chosen by

$$\mu_k(\|S_i - C_{ki}\|) = \exp \left(- \left(\frac{\|S_i - C_{ki}\|}{\beta} \right)^2 \right). \quad (4.3)$$

Since here n , the sum of input variables, is only one, we know that

$$R_k(S) = \frac{\mu_k(S - C_k)}{\sum_{k=1}^m \mu_k(S - C_k)}, \quad (4.4)$$

where $k = 1, \dots, m$ with μ_k represent the degree of membership. The S in μ_k can be chosen by $\mu_k(\|S - C_k\|) = \exp(-(\|S - C_k\|/\beta)^2)$.

From the approximation property of the fuzzy system, an uncertain and nonlinear plant can be well approximated and described via a fuzzy model with FLC rules to achieve the control object [14, 39, 40].

Assumption 4.1. For $x \in \zeta \subset R^n$, there exists an adjustable parameter vector $\bar{\theta} = [\bar{\theta}_1, \bar{\theta}_2, \dots, \bar{\theta}_m]^T$ such that the fuzzy system $\bar{u}(S, \bar{\theta}) = \bar{\theta}^T R(S)$ can approximate a continuous function u with accuracy ε_{\max} over the set ζ , that is, $\exists \bar{\theta}$, such that

$$\sup |\bar{u}(S, \bar{\theta}) - u(S)| \leq \varepsilon_{\max}, \quad \forall S \in \zeta. \quad (4.5)$$

Let $\hat{\theta}$ denote the estimate of $\bar{\theta}$ at time t . Now, we can define the estimated control output $\hat{u}(S, \hat{\theta})$ by

$$\hat{u}(S, \hat{\theta}) = \sum_{k=1}^m \hat{\theta}_k \cdot R_k(S) = \hat{\theta}^T R(S), \quad (4.6)$$

and decide on the initial values of the consequent parameter vector $\hat{\theta} = [\hat{\theta}_1, \hat{\theta}_2, \dots, \hat{\theta}_m]^T$ based on the genetic algorithm.

First, define the parameter error vector at time t by $\tilde{\theta} = \bar{\theta} - \hat{\theta}$, and then

$$\tilde{\theta}^T R(S) = \bar{u}(S, \bar{\theta}) - \hat{u}(S, \hat{\theta}). \quad (4.7)$$

According to assumption 4.1, we can define the modeling error

$$\varepsilon = u - \bar{u}(S, \bar{\theta}), \quad (4.8)$$

where $|\varepsilon| \leq \varepsilon_{\max}$.

We can say that

$$u = \hat{u}(S, \hat{\theta}) + \tilde{\theta}^T R(S) + \varepsilon. \quad (4.9)$$

Now, by substituting (4.9) into (2.5), we obtain the error dynamic equation:

$$e^{(n)} + \alpha_{n-1} e^{(n-1)} + \dots + \alpha_1 \dot{e} + \alpha_0 e = g(x) \cdot (\tilde{\theta}^T R(S) + \varepsilon). \quad (4.10)$$

We now define the augmented error as

$$S = \beta_{n-1} e^{(n-1)} + \cdots + \beta_1 \dot{e} + \beta_0 e, \quad (4.11)$$

where $\beta_{n-1}, \dots, \beta_1, \beta_0$ in (4.11), and $\alpha_{n-1}, \dots, \alpha_1, \alpha_0$ in (4.10) are chosen such that

$$\widehat{M}(\ell) = \frac{\beta_{n-1} \ell^{n-1} + \cdots + \beta_1 \ell + \beta_0}{\ell^n + \alpha_{n-1} \ell^{n-1} + \cdots + \alpha_1 \ell + \alpha_0} = \frac{N(\ell)}{D(\ell)} \quad (4.12)$$

is strictly positive real (SPR) transfer function, and $N(\ell)$ and $D(\ell)$ are coprime. Now, S and $g(x) \cdot (\tilde{\theta}^T R(S) + \varepsilon)$ can be related by

$$L\{S(t)\} = \widehat{M}(\ell) \cdot L\{g(x) \cdot (\tilde{\theta}^T R(S) + \varepsilon)\}, \quad (4.13)$$

where $L\{\cdot\}$ is the *Laplace* transform of the function, and ℓ denotes the complex *Laplace* transform variable.

If we define $e_m = [e, \dots, e^{(n-1)}]^T$ as the states of (4.10), then (4.10) can be realized as

$$\dot{e}_m(t) = \Lambda \cdot e_m(t) + b \cdot [g(x) \cdot (\tilde{\theta}^T R(S) + \varepsilon)], \quad (4.14)$$

$$S(t) = c^T e_m(t), \quad (4.15)$$

where

$$\Lambda = \begin{bmatrix} 0 & 1 & 0 & \cdots & 0 & 0 \\ 0 & 0 & 1 & \cdots & 0 & 0 \\ \vdots & \vdots & \vdots & \ddots & \vdots & \vdots \\ 0 & 0 & 0 & \cdots & 1 & 0 \\ 0 & 0 & 0 & \cdots & 0 & 1 \\ -\alpha_0 & -\alpha_1 & -\alpha_2 & \cdots & -\alpha_{n-2} & -\alpha_{n-1} \end{bmatrix}_{n \times n}, \quad b = \begin{bmatrix} 0 \\ 0 \\ \vdots \\ 0 \\ 0 \\ 1 \end{bmatrix}_{n \times 1}, \quad (4.16)$$

$$c = [\beta_0 \ \beta_1 \ \cdots \ \beta_{n-1}]^T, \quad \text{let } \beta_{n-1} = 1.$$

According to the *Kalman-Yakubovich* lemma, when $\widehat{M}(\ell)$ is SPR, there exist symmetric and positive definite matrices P and Q such that

$$P\Lambda + \Lambda^T P = -Q, \quad (4.17)$$

$$Pb = c, \quad \text{for } i = 1, \dots, p.$$

Next, we investigate the asymptotic stability of the origin using *Lyapunov's* function candidates. First, define a *Lyapunov* candidate function as

$$V(e_m, \tilde{\theta}) = \eta \cdot e_m^T P e_m + \tilde{\theta}^T H_{11} \tilde{\theta}, \quad (4.18)$$

where η is a positive constant representing the learning rate

$$\begin{aligned} \tilde{\theta} &= [\tilde{\theta}_1 \ \tilde{\theta}_2 \ \cdots \ \tilde{\theta}_m]^T, \quad H_{11} = g(x) \cdot I_{m \times m}, \\ \tilde{\theta}^T H_{11} &= \begin{bmatrix} g(x) \cdot \tilde{\theta}_1 & 0 & \cdots & 0 \\ 0 & g(x) \cdot \tilde{\theta}_2 & \cdots & 0 \\ \vdots & \vdots & \ddots & 0 \\ 0 & 0 & \cdots & g(x) \cdot \tilde{\theta} \end{bmatrix}_{m \times m}, \quad m : \text{the sum of the fuzzy rules.} \end{aligned} \quad (4.19)$$

If $e_m^T P e_m > \phi^2$, the derivate of $V(e_m, \tilde{\theta})$ along the trajectories of the system should be negative definite for all nonlinearities that satisfy a given sector condition (*Lyapunov's stability*):

$$\dot{V}(e_m, \tilde{\theta}) = \eta \cdot (\dot{e}_m^T P e_m + e_m^T P \dot{e}_m) + 2\tilde{\theta}^T H_{11} \dot{\tilde{\theta}}. \quad (4.20)$$

As mentioned above $\tilde{\theta} = \bar{\theta} - \hat{\theta}$, and we can infer that $\dot{\tilde{\theta}} = -\dot{\hat{\theta}}$, and

$$\begin{aligned} \dot{V} &= \eta \cdot (e_m^T \Lambda^T P e_m + e_m^T P \Lambda e_m) + 2\eta \cdot e_m^T P b \cdot [g(x) \cdot (\tilde{\theta}^T R(S) + \varepsilon)] + 2 \cdot \tilde{\theta}^T H_{11} (-\dot{\hat{\theta}}) \\ &= \eta \cdot e_m^T (-Q) e_m + 2\eta \cdot S \cdot [g(x) \cdot (\tilde{\theta}^T R(S) + \varepsilon)] + 2 \cdot \tilde{\theta}^T H_{11} (-\dot{\hat{\theta}}). \end{aligned} \quad (4.21)$$

In general, chattering must be eliminated for the controller to perform properly. This can be achieved by smoothing out control discontinuity in a thin boundary layer neighboring the switching surface. To amend the modeling error ε and the chattering phenomenon, we propose a modified adaptive law (4.22) with which to tune the adjustable consequent parameters of the RAFSMC:

$$\dot{\hat{\theta}} = \eta \cdot |S| \cdot R(S) \cdot \text{sat}\left(\frac{S}{\Phi}\right). \quad (4.22)$$

The thin boundary layer function $\text{sat}(S/\Phi)$ is defined as

$$\text{sat}\left(\frac{S}{\Phi}\right) = \begin{cases} 1, & \text{if } \left(\frac{S}{\Phi}\right) > 1, \\ \left(\frac{S}{\Phi}\right), & \text{if } -1 \leq \left(\frac{S}{\Phi}\right) \leq 1, \\ -1, & \text{if } \left(\frac{S}{\Phi}\right) < -1, \end{cases} \quad (4.23)$$

where $\Phi > 0$ is the thickness of the boundary layer.

If we substitute (4.22) into (4.21), then (4.21) becomes

$$\dot{V} = -\eta \cdot e_m^T Q e_m + 2\eta \cdot S \cdot [g(x) \cdot (\tilde{\theta}^T R(S) + \varepsilon)] - 2\eta \cdot |S| \cdot [g(x) \cdot \tilde{\theta}^T R(S)] \cdot \text{sat}\left(\frac{S}{\Phi}\right). \quad (4.24)$$

When $|S| > \Phi$, then

$$\begin{aligned}\dot{V} &= -\eta \cdot e_m^T Q e_m + 2\eta \cdot e_m^T c \cdot (g(x) \cdot \varepsilon) \\ &\leq -\eta \cdot \|e_m\|^2 \cdot Q + 2\eta \cdot \|e_m\| \cdot \|c\| \cdot \|g(x) \cdot \varepsilon\| \\ &\leq -\eta \cdot \|e_m\| \cdot [\|e_m\| \cdot Q - 2\|c\| \cdot \|g(x) \cdot \varepsilon\|].\end{aligned}\quad (4.25)$$

If μ is positive and small enough, then $\phi > 0$ and $\sigma > 0$, such that

$$\left\{ \frac{\phi Q}{\sqrt{P}} - 2\|c\| \cdot \|g(x) \cdot \varepsilon\| \right\} > \sigma, \quad (4.26)$$

where $e_m^T P e_m > \phi^2$.

It is real that $\dot{V} \leq -\eta \cdot \|e_m\| \cdot \sigma$ if $e_m^T P e_m > \phi^2$ and $|S| > \Phi$, and hence $\dot{V} < 0$. Thus V will gradually converge to zero as all the ς .

Based on the above inference and *Lyapunov's* stability theory, e_m will gradually converge inside the bounded zone $|e_m| \leq (\phi/\sqrt{P}, \Phi/\beta_0)$. The tracking error and the modeling error will then both approach zero.

Theorem 4.2. Consider a nonlinear uncertain system $\overset{(n)}{y} = f(x) + g(x) \cdot u + d$ that satisfies the assumptions $(\bar{\theta}, \hat{\theta})$. Suppose that the unknown control input u can be approximated by $\hat{u}(S, \hat{\theta})$ as in (4.6). Now, S is given by (4.15), and Q is a symmetric positive definite weighting matrix.

5. Numerical simulation

In this section, the proposed GA-based RAFSMC is demonstrated with an example of the control methodology.

Consider the problem of balancing an inverted pendulum on a cart as shown in Figure 5. The dynamic equations of motion of the pendulum are given below [27]:

$$\begin{aligned}\dot{x}_1 &= x_2, \\ \dot{x}_2 &= \frac{g \cdot \sin(x_1) - a m l x_2^2 \sin(2x_1)/2 - a \cos(x_1) \cdot u}{4l/3 - a m l \cos^2(x_1)},\end{aligned}\quad (5.1)$$

where x_1 denotes the angle (in radian) of the pendulum from the vertical; and x_2 is the angular vector. Thus the gravity constant $g = 9.8 \text{ m/s}^2$, where m is the mass of the pendulum, M is the mass of the cart, l is the length of F (input force), s is the force applied to the cart (in Newtons), and $a = 1/(m + M)$. The parameters chosen for the pendulum in this simulation are $m = 0.1 \text{ kg}$, $M = 1 \text{ kg}$, and $l = 0.5 \text{ m}$.

The control objective in this example is to balance the inverted pendulum in the approximate range $x \in (-\pi/2, \pi/2)$. The GA-based RAFSMC designed based on the procedure discussed above will have the following steps.

Step 1. Specify the response of the control system by defining a suitable sliding surface

$$S = c^T e_m = 5e + \dot{e} \quad [27]. \quad (5.2)$$

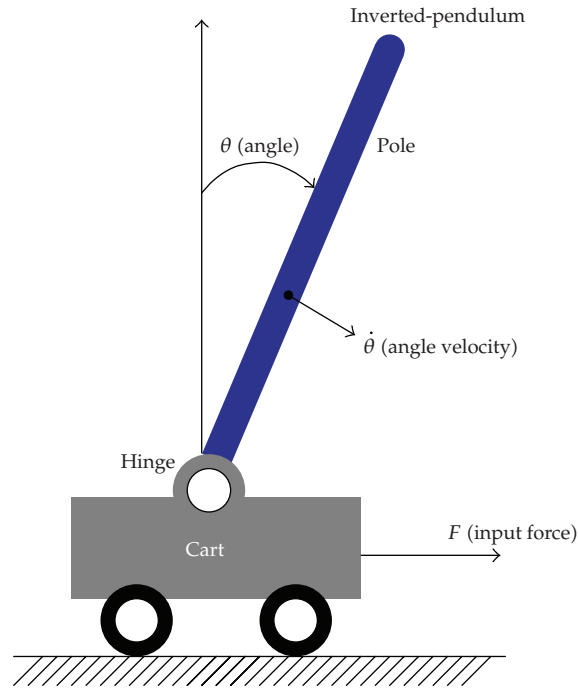


Figure 5: Inverted pendulum system.

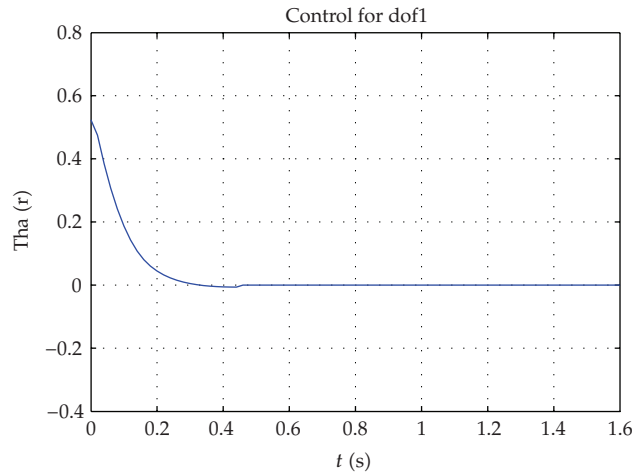


Figure 6: Angle response of the pendulum with the initial condition $x_1(0) = 30^\circ$.

Step 2. Construct the fuzzy rule base (3.2) and the fuzzy models (4.6) based on the genetic algorithm. After carrying out the abovementioned genetic-based learning procedure, the number of individual strings is 10, the size of population M is 12, the crossover rate is 0.8333, the mutation rate is 0.03125, and the maximum number of the generations H is 15. Now, the

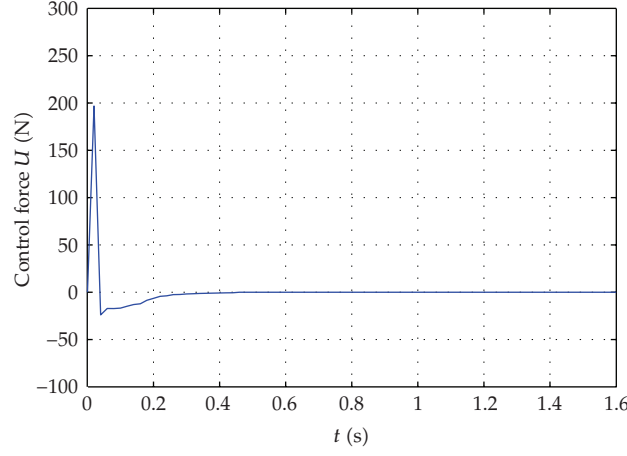


Figure 7: Control force in the pendulum system with the initial $x_1(0) = 30^\circ$.

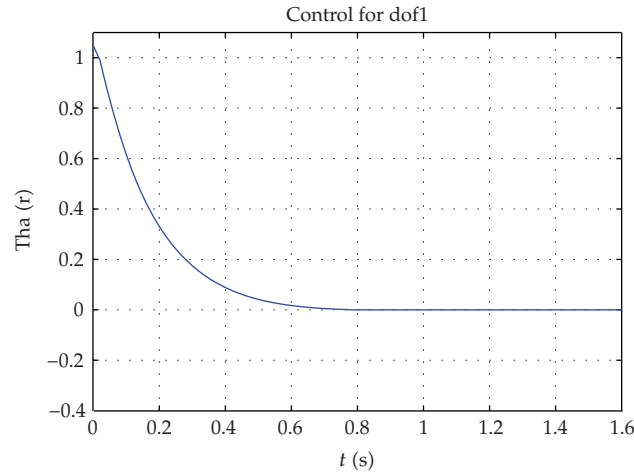


Figure 8: Angle response of the pendulum with the initial condition $x_1(0) = 60^\circ$.

initial values of the consequent parameter vector $\hat{\theta}$ for the GA-based RAFSMC can be chosen as follows:

$$[1, 0.6263, 0.4113, 0.2100, 0.0850, 0, -0.0850, -0.2100, -0.4113, -0.6263, -1]^T. \quad (5.3)$$

Step 3. Apply the controller as given by (4.6) to control the nonlinear system (2.1). Now, let $\eta = 10$, $\Phi = 0.3$, and adjust $\hat{\theta}$ by the adaptive law as given by (4.22).

Therefore, based on Theorem 4.2, the proposed GA-based RAFSMC can asymptotically stabilize the inverted pendulum. The simulation results are illustrated in Figures 6–9. The initial conditions are $x_1(0) = 30^\circ$, 60° , and $x_2(0) = 0$.

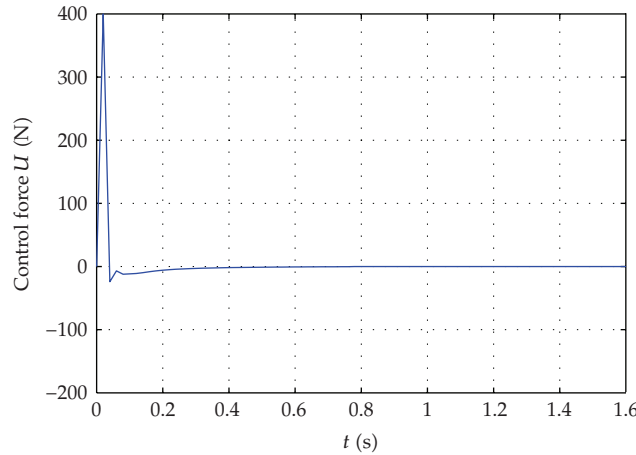


Figure 9: Control force in the pendulum system with the initial condition $x_1(0) = 60^\circ$.

Figures 6–9 show that the inverted pendulum system (compare with Yoo and Ham [27]) is rapidly, asymptotically stable because the system trajectory starts from any nonzero initial state, to rapidly and asymptotically approach the origin.

6. Conclusion

The stability analysis of a GA-based reference adaptive fuzzy sliding model controller for a nonlinear system is discussed. First, we track the reference trajectory for an uncertain and nonlinear plant. We make sure that it is well approximated and described via the fuzzy model involving FLC rules. Then we decide on the initial values of the consequent parameter vector $\hat{\theta}$ via a GA. Next, an adaptive fuzzy sliding model controller is proposed to simultaneously stabilize and control the system. A stability criterion is also derived from *Lyapunov's* direct method to ensure stability of the nonlinear system. Finally, we discuss an example and provide a numerical simulation. From this example, we see that the stability of the inverted pendulum system is ensured because the trajectories from nonzero initial states approach to zero by proposed controller design, and the results demonstrate that with this control methodology we can rapidly and efficiently control a complex and nonlinear system.

Acknowledgments

The authors would like to thank the National Science Council of the Republic of China, Taiwan for financial support of this research under Contract no. NSC 96-2628-E-366-004-MY2. The authors are also most grateful for the kind assistance of Professor Balthazar, Editor of special issue, and the constructive suggestions from anonymous reviewers all of which has led to the making of several corrections and suggestions that have greatly aided us in the presentation of this paper.

References

- [1] G. J. Klir and B. Yuan, *Fuzzy Sets and Fuzzy Logic: Theory and Applications*, Prentice Hall, Upper Saddle River, NJ, USA, 1995.

- [2] W.-J. Wang and H.-R. Lin, "Fuzzy control design for the trajectory tracking on uncertain nonlinear systems," *IEEE Transactions on Fuzzy Systems*, vol. 7, no. 1, pp. 53–62, 1999.
- [3] X.-J. Ma, Z.-Q. Sun, and Y.-Y. He, "Analysis and design of fuzzy controller and fuzzy observer," *IEEE Transactions on Fuzzy Systems*, vol. 6, no. 1, pp. 41–51, 1998.
- [4] T. Takagi and M. Sugeno, "Fuzzy identification of systems and its applications to modeling and control," *IEEE Transactions on Systems, Man and Cybernetics*, vol. 15, no. 1, pp. 116–132, 1985.
- [5] F.-H. Hsiao, C. W. Chen, Y.-H. Wu, and W.-L. Chiang, "Fuzzy controllers for nonlinear interconnected TMD systems with external force," *Journal of the Chinese Institute of Engineers*, vol. 28, no. 1, pp. 175–181, 2005.
- [6] T.-Y. Hsieh, M. H. L. Wang, C. W. Chen, et al., "A new viewpoint of s-curve regression model and its application to construction management," *International Journal on Artificial Intelligence Tools*, vol. 15, no. 2, pp. 131–142, 2006.
- [7] C.-H. Tsai, C. W. Chen, W.-L. Chiang, and M.-L. Lin, "Application of geographic information system to the allocation of disaster shelters via fuzzy models," *Engineering Computations*, vol. 25, no. 1, pp. 86–100, 2008.
- [8] C. W. Chen, W.-L. Chiang, C.-H. Tsai, C.-Y. Chen, and M. H. L. Wang, "Fuzzy Lyapunov method for stability conditions of nonlinear systems," *International Journal on Artificial Intelligence Tools*, vol. 15, no. 2, pp. 163–171, 2006.
- [9] K. Tanaka, T. Hori, and H. O. Wang, "A multiple Lyapunov function approach to stabilization of fuzzy control systems," *IEEE Transactions on Fuzzy Systems*, vol. 11, no. 4, pp. 582–589, 2003.
- [10] B. Chen, X. Liu, and S. Tong, "New delay-dependent stabilization conditions of T-S fuzzy systems with constant delay," *Fuzzy Sets and Systems*, vol. 158, no. 20, pp. 2209–2224, 2007.
- [11] C. W. Chen, C.-L. Lin, C.-H. Tsai, C.-Y. Chen, and K. Yeh, "A novel delay-dependent criterion for time-delay T-S fuzzy systems using fuzzy Lyapunov method," *International Journal on Artificial Intelligence Tools*, vol. 16, no. 3, pp. 545–552, 2007.
- [12] F.-H. Hsiao, J.-D. Hwang, C. W. Chen, and Z.-R. Tsai, "Robust stabilization of nonlinear multiple time-delay large-scale systems via decentralized fuzzy control," *IEEE Transactions on Fuzzy Systems*, vol. 13, no. 1, pp. 152–163, 2005.
- [13] K. Yeh, C.-Y. Chen, and C. W. Chen, "Robustness design of time-delay fuzzy systems using fuzzy Lyapunov method," *Applied Mathematics and Computation*, vol. 205, no. 2, pp. 568–577, 2008.
- [14] C. W. Chen, K. Yeh, W.-L. Chiang, C.-Y. Chen, and D.-J. Wu, "Modeling, H^∞ control and stability analysis for structural systems using Takagi-Sugeno fuzzy model," *Journal of Vibration and Control*, vol. 13, no. 11, pp. 1519–1534, 2007.
- [15] G. Feng, C.-L. Chen, D. Sun, and Y. Zhu, " H^∞ controller synthesis of fuzzy dynamic systems based on piecewise Lyapunov functions and bilinear matrix inequalities," *IEEE Transactions on Fuzzy Systems*, vol. 13, no. 1, pp. 94–103, 2005.
- [16] F.-H. Hsiao, C. W. Chen, Y.-W. Liang, S.-D. Xu, and W.-L. Chiang, "T-S fuzzy controllers for nonlinear interconnected systems with multiple time delays," *IEEE Transactions on Circuits and Systems I*, vol. 52, no. 9, pp. 1883–1893, 2005.
- [17] S. Xu and J. Lam, "Robust H^∞ control for uncertain discrete-time-delay fuzzy systems via output feedback controllers," *IEEE Transactions on Fuzzy Systems*, vol. 13, no. 1, pp. 82–93, 2005.
- [18] C. W. Chen, "Modeling and control for nonlinear structural systems via a NN-based approach," *Expert Systems with Applications*. In press.
- [19] C.-Y. Chen, J. R.-C. Hsu, and C. W. Chen, "Fuzzy logic derivation of neural network models with time delays in subsystems," *International Journal on Artificial Intelligence Tools*, vol. 14, no. 6, pp. 967–974, 2005.
- [20] P. C. Chen, C. W. Chen, and W. L. Chiang, "GA-based modified adaptive fuzzy sliding mode controller for nonlinear systems," *Expert Systems with Applications*. In press.
- [21] S. Limanond and J. Si, "Neural-network-based control design: an LMI approach," *IEEE Transactions on Neural Networks*, vol. 9, no. 6, pp. 1422–1429, 1998.
- [22] R. Palm, "Robust control by fuzzy sliding mode," *Automatica*, vol. 30, no. 9, pp. 1429–1437, 1994.
- [23] L. X. Wang, *A Course in Fuzzy Systems and Control*, Prentice Hall, Englewood Cliffs, NJ, USA, 1997.
- [24] V. I. Utkin, *Sliding Modes and Their Application in Variable Structure Systems*, MIR Publishers, Moscow, Russia, 1978.

- [25] J. J. E. Slotine and W. Li, *Applied Nonlinear Control*, Prentice Hall, Englewood Cliffs, NJ, USA, 1991.
- [26] Y. Xia and Y. Jia, "Robust sliding-mode control for uncertain time-delay systems: an LMI approach," *IEEE Transactions on Automatic Control*, vol. 48, no. 6, pp. 1086–1092, 2003.
- [27] B. Yoo and W. Ham, "Adaptive fuzzy sliding mode control of nonlinear system," *IEEE Transactions on Fuzzy Systems*, vol. 6, no. 2, pp. 315–321, 1998.
- [28] S. Tong and H.-X. Li, "Fuzzy adaptive sliding-mode control for MIMO nonlinear systems," *IEEE Transactions on Fuzzy Systems*, vol. 11, no. 3, pp. 354–360, 2003.
- [29] S. Labiod, M. S. Boucherit, and T. M. Guerra, "Adaptive fuzzy control of a class of MIMO nonlinear systems," *Fuzzy Sets and Systems*, vol. 151, no. 1, pp. 59–77, 2005.
- [30] L. X. Wang, *Adaptive Fuzzy Systems and Control: Design and Stability Analysis*, Prentice Hall, Englewood Cliffs, NJ, USA, 1994.
- [31] G. Feng, S. G. Cao, and N. W. Rees, "Stable adaptive control for fuzzy dynamic systems," *Fuzzy Sets and Systems*, vol. 131, no. 2, pp. 217–224, 2002.
- [32] D. E. Goldberg, *Genetic Algorithms in Search, Optimization, and Machine Learning*, Addison-Wesley, Reading, Mass, USA, 1989.
- [33] S. C. Lin, *Stable self-learning optimal fuzzy control system design and application*, Ph.D. dissertation, Department of Electrical Engineering, National Taiwan University, Chung-li, Taiwan, 1997.
- [34] P. C. Chen, *Genetic algorithm for control of structure system*, M.S. thesis, Department of Civil Engineering, Chung Yuan University, Taipei, Taiwan, 1998.
- [35] C. C. Liu and F. C. Chen, "Adaptive control of nonlinear continuous-time systems using neural networks—general relative degree and MIMO cases," *International Journal of Control*, vol. 58, no. 2, pp. 317–335, 1993.
- [36] J.-S. R. Jang, C.-T. Sun, and E. Mizutani, *Neuro-Fuzzy and Soft Computing: A Computational Approach to Learning and Machine Intelligence*, Prentice-Hall, Upper Saddle River, NJ, USA, 1997.
- [37] J.-S. R. Jang, "ANFIS: adaptive-network-based fuzzy inference system," *IEEE Transactions on Systems, Man and Cybernetics*, vol. 23, no. 3, pp. 665–685, 1993.
- [38] F. J. de Souza, M. M. R. Velasco, and M. A. C. Pacheco, "Hierarchical neuro-fuzzy quadtree models," *Fuzzy Sets and Systems*, vol. 130, no. 2, pp. 189–205, 2002.
- [39] C. W. Chen, W. L. Chiang, and F. H. Hsiao, "Stability analysis of T-S fuzzy models for nonlinear multiple time-delay interconnected systems," *Mathematics and Computers in Simulation*, vol. 66, no. 6, pp. 523–537, 2004.
- [40] C. W. Chen, "Stability conditions of fuzzy systems and its application to structural and mechanical systems," *Advances in Engineering Software*, vol. 37, no. 9, pp. 624–629, 2006.

Research Article

Experimental Active Vibration Control in Truss Structures Considering Uncertainties in System Parameters

Douglas Domingues Bueno, Clayton Rodrigo Marqui, Rodrigo Borges Santos, Camilo Mesquita Neto, and Vicente Lopes Jr.

Grupo de Materiais e Sistemas Inteligentes (GMSINT), Departamento de Engenharia Mecânica (DEM), Faculdade de Engenharia de Ilha Solteira (FEIS), Universidade Estadual Paulista (UNESP), Avenida Brasil Centro 56, 15385-000 Ilha Solteira, SP, Brazil

Correspondence should be addressed to Vicente Lopes Jr., vicente@dem.feis.unesp.br

Received 16 October 2007; Revised 11 June 2008; Accepted 9 August 2008

Recommended by Paulo Gonçalves

This paper deals with the study of algorithms for robust active vibration control in flexible structures considering uncertainties in system parameters. It became an area of enormous interest, mainly due to the countless demands of optimal performance in mechanical systems as aircraft, aerospace, and automotive structures. An important and difficult problem for designing active vibration control is to get a representative dynamic model. Generally, this model can be obtained using finite element method (FEM) or an identification method using experimental data. Actuators and sensors may affect the dynamics properties of the structure, for instance, electromechanical coupling of piezoelectric material must be considered in FEM formulation for flexible and lightly damping structure. The nonlinearities and uncertainties involved in these structures make it a difficult task, mainly for complex structures as spatial truss structures. On the other hand, by using an identification method, it is possible to obtain the dynamic model represented through a state space realization considering this coupling. This paper proposes an experimental methodology for vibration control in a 3D truss structure using PZT wafer stacks and a robust control algorithm solved by linear matrix inequalities.

Copyright © 2008 Douglas Domingues Bueno et al. This is an open access article distributed under the Creative Commons Attribution License, which permits unrestricted use, distribution, and reproduction in any medium, provided the original work is properly cited.

1. Introduction

Lightweight space structures are the future of space vehicles and satellite technology. Possessing ideal space launching characteristics, such as minimal storage volume and minimal mass, these lightweight structures will propel the space industry into the next generation. Space satellites must be expertly controlled from a vibration standpoint because signal transmission to and from the earth mandates tight tolerances. Vibration control is critical to mission success as well as satellite longevity [1].

Large and light space structures are basically flexible due to their low stiffness and damping. These characteristics may cause problems since flexible structures present many vibration modes within or beyond the bandwidth of the controller. When only a few modes are dealt in the controller, spillover may occur because uncontrolled higher modes or unmodeled modes may become excited. The effects of spillover can occur where structure, sensors, or actuators are poorly modeled, and the numbers of sensors and actuators are low.

In order to achieve better dynamic properties, great attention has been paid to the control of structural vibration using intelligent structures. So, the application of active vibration control in flexible structures has been increasingly used as a solution for space structures to achieve the degree of vibration suppression required for precision pointing accuracy and to guarantee the stability.

In truss structures, active members are integrated because of their multiple functions. They serve as structural elements, and as load device. As actuators, the active member exerts internal forces, and as sensor elements, it allows measurement of the elastic strains. The piezoelectric stack actuators are remarkable because they are light weight, high force, and low power consumption [2].

Several researchers have proposed the use of piezoelectric material for active vibration control. In truss structures, the control force can be accomplished by piezoelectric active members, known as "PZT wafer stacks," that are mechanically linked in series producing an axial force in the bar that are positioned.

State space realization is used in modern control formulation to obtain the dynamic model, but in many cases this model has significant uncertainties in relation to the real system. These uncertainties can be caused, for instance, by parameter variation during the operation, or by dynamic uncertainties (nonlinearities, higher modes, noises, etc.). So, for an efficient experimental control design, it is important to qualify and quantify the uncertainties.

In this context, this paper proposes a methodology for robust control design considering uncertainties in the dynamic model, represented by state space realization. It is designed as an active controller to attenuate vibrations in a truss structures. The active members are composed by PZT wafer stacks actuators, and the control design is based on linear quadratic regulator solved through linear matrix inequalities (LMIs). LMI presents advantages when compared to conventional techniques, and it has contributed to overcome many difficulties in control design [3]. In the last decade, LMI has been used to solve many problems that until then were unfeasible through other methodologies, mainly due to the emergence of powerful algorithms to solve convex optimization problem, for instance, the interior point method (see Boyd et al. [4] and Gahinet et al. [5]). Sarracini and Serpa [6] apply H_{infinite} control approach solved through LMI for model reduction. Silva et al. [7] present a consistent formulation for control design based on LMI approach. Chen and Zhu [8] present a formulation based on H_2 , H_∞ , and mixed H_2/H_∞ control strategies for a flexible rotor system under seismic excitation by means of linear matrix inequality (LMI) to attenuate the transient vibration of the flexible rotor system under a nonstationary seismic excitation and to improve robust performance of the flexible rotor system.

In the present work, the numerical method of subspace and the Kalman estimator were used to identify the dynamic model with experimental data and to estimate the state vector, respectively. Experimental results, obtained through dSPACE control board and the Simulink/Matlab, are shown in order to validate the proposed approach.

2. Dynamic modeling of robust control

Modern linear control formulation is based on the state space realization. Using this formulation, the design of a vibration control for multi-input multioutput (MIMO) system is similar of simple-input simple-output (SISO) system approach. This realization is appropriate for experimental applications because there are many numerical methods to solve it in real time, as for instance, the numerical method of Runge-Kutta. A linear differential inclusion (LDI) system, in modal state space form, considering the matrices with appropriate dimensions and assumed to be known, is given by

$$\begin{aligned}\dot{\mathbf{x}}(t) &= \mathbf{A}(t)\mathbf{x}(t) + \mathbf{B}_w(t)\mathbf{w}(t) + \mathbf{B}_u(t)\mathbf{u}(t) + \mathbf{E}_{in}\mathbf{v}_{in}(t), \\ \mathbf{y}(t) &= \mathbf{C}(t)\mathbf{x}(t) + \mathbf{D}\mathbf{u}(t) + \mathbf{E}_{out}\mathbf{v}_{out}(t), \\ \begin{bmatrix} \mathbf{A}(t) & \mathbf{B}_w(t) \\ \mathbf{B}_u(t) & \mathbf{C}(t) \end{bmatrix} &\in \mathbf{\Omega},\end{aligned}\tag{2.1}$$

where $\mathbf{\Omega}$ is a polytope that is described by a list of vertexes in a convex space, $\mathbf{A}(t)$ is the dynamic matrix, $\mathbf{B}_w(t)$ is the matrix of disturbance, $\mathbf{B}_u(t)$ is the matrix of control input, $\mathbf{C}(t)$ is the output matrix, $\mathbf{w}(t)$ is the vector of disturbance input, $\mathbf{u}(t)$ is the vector of control input, $\mathbf{y}(t)$ is the output vector, and $\mathbf{v}_{in}(t)$ and $\mathbf{v}_{out}(t)$ are stationary zero-mean Gaussian white process and measurement noises vectors with unit intensity, respectively. In this paper, some variables, as the matrices in (2.1), are represented as time function to emphasize the uncertainties in the system parameters. The vectors \mathbf{E}_{in} and \mathbf{E}_{out} are the process and measurement noise vectors, respectively.

The state vector $\mathbf{x}(t)$ of the modal coordinates system consists of n independent components, $\mathbf{x}_i(t)$, that represent a state of each mode, where n is the number of modes. The $\mathbf{x}_i(t)$ (i th state component), related to (2.3), is defined as [9]

$$\mathbf{x}_i(t) = \begin{Bmatrix} \mathbf{q}_{mi}(t) \\ \mathbf{q}_{moi}(t) \end{Bmatrix}, \quad \text{where } \mathbf{q}_{moi}(t) = \zeta_i(t)\mathbf{q}_{mi}(t) + \frac{\dot{\mathbf{q}}_{mi}(t)}{\omega_i(t)},\tag{2.2}$$

where \mathbf{q}_{mi} and \mathbf{q}_{moi} are named modal displacement and velocity for i th vibration mode, respectively. Using modal coordinates, these parameters have no physical interpretation. Also, ζ_i and ω_i are damping factor and natural frequency of the i th mode. These parameters are represented as time function to emphasize the uncertainties.

The modal state space realization is characterized by the block-diagonal dynamic matrix and the related input and output matrices [9]:

$$\begin{aligned}\mathbf{A}(t) &= \text{diag}(\mathbf{A}_{mi}(t)), \quad \mathbf{B}_w(t) = \begin{bmatrix} \mathbf{B}_{wm1}(t) \\ \mathbf{B}_{wm2}(t) \\ \vdots \\ \mathbf{B}_{wmn}(t) \end{bmatrix}, \quad \mathbf{B}_u(t) = \begin{bmatrix} \mathbf{B}_{um1}(t) \\ \mathbf{B}_{um2}(t) \\ \vdots \\ \mathbf{B}_{umn}(t) \end{bmatrix}, \\ \mathbf{C}(t) &= [\mathbf{C}_{m1}(t) \quad \mathbf{C}_{m2}(t) \quad \cdots \quad \mathbf{C}_{mn}(t)],\end{aligned}\tag{2.3}$$

where $i = 1, 2, \dots, n$; \mathbf{A}_{mi} , \mathbf{B}_{wmi} , \mathbf{B}_{umi} , and \mathbf{C}_{mi} are 2×2 , $2 \times k$, $2 \times s$, and $r \times 2$ blocks, respectively; k is the number of disturbances; s is the number of control inputs; and r is the number of outputs. These blocks can be obtained in several different forms and also it is possible to convert it in another realization through a linear transformation. One possible form to block $\mathbf{A}_{mi}(t)$ is

$$\mathbf{A}_{mi}(t) = \begin{bmatrix} -\zeta_i(t)\omega_i(t) & \omega_i(t) \\ -\omega_i(t)(\zeta_i^2(t) - 1) & -\zeta_i(t)\omega_i(t) \end{bmatrix}. \quad (2.4)$$

The dynamic model of the truss structure was initially identified using experimental data through subspace identification method. $n_I > 1$ identification tests were considered to characterize the uncertainties in the system parameters. The members that include PZT stack actuator are nominated by active members. It is considered a variation in the properties of these members caused by the insertion of these actuators. These uncertainties are described by a polytopic linear differential inclusion (PLDI):

$$\begin{aligned} \mathbf{\Omega} &= \begin{bmatrix} \mathbf{A}_c(t) & \mathbf{B}_{wc}(t) \\ \mathbf{B}_{uc}(t) & \mathbf{C}_c(t) \end{bmatrix}, \\ &\text{Co}\{S_1, \dots, S_v\}, \end{aligned} \quad (2.5)$$

where $S_i = \begin{bmatrix} \mathbf{A}_{ci} & \mathbf{B}_{wci} \\ \mathbf{B}_{uci} & \mathbf{C}_{ci} \end{bmatrix}, \quad i = 1, \dots, v,$

where the subscript c is relative to controlled modes; $\mathbf{\Omega}$ is a polytope described by a list of vertexes in a convex space Co [4], and v is the number of vertexes of the polytopic system. Usually, in practical situations, it is very difficult to define the polytopic vertexes, but these vertexes are not variant in time. So, it is possible to project the vibration control using an invariant model.

A reduced-order model is obtained by truncating the states. Let $\mathbf{x}(t)$ and the state ($\mathbf{A}(t)$, $\mathbf{B}_w(t)$, $\mathbf{B}_u(t)$, $\mathbf{C}(t)$) be partitioned considering the canonical modal decomposition. From the Jordan canonical form, the following can be obtained :

$$\begin{aligned} \begin{Bmatrix} \dot{\mathbf{x}}_c(t) \\ \dot{\mathbf{x}}_r(t) \end{Bmatrix} &= \begin{bmatrix} \mathbf{A}_c(t) & \mathbf{0} \\ \mathbf{0} & \mathbf{A}_r(t) \end{bmatrix} \begin{Bmatrix} \mathbf{x}_c(t) \\ \mathbf{x}_r(t) \end{Bmatrix} + \begin{bmatrix} \mathbf{B}_{wc}(t) \\ \mathbf{B}_{wr}(t) \end{bmatrix} \mathbf{w}(t) + \begin{bmatrix} \mathbf{B}_{uc}(t) \\ \mathbf{B}_{ur}(t) \end{bmatrix} \mathbf{u}(t), \\ \mathbf{y}(t) &= [\mathbf{C}_c(t) \quad \mathbf{C}_r(t)] \begin{Bmatrix} \mathbf{x}_c(t) \\ \mathbf{x}_r(t) \end{Bmatrix}, \end{aligned} \quad (2.6)$$

where $\mathbf{A}_c(t)$ is given by (2.4) and the subscript r is relative to the residual modes. Generally, in practical applications, \mathbf{E}_{in} and \mathbf{E}_{out} are not identified, but there are, always, some process and measurement noises.

3. Control methodology

In this section, a robustness analysis is conducted for understanding the LQR-LMI controller performance. Controller design can be done through rigorous mathematical optimization

techniques. One of these, which was originated in the sixties [10], is called modern optimal control theory that is a time-domain technique.

Control systems robustness is defined as the ability for maintaining satisfactory stability and performance features in the presence of parameters variations and uncertainties [11]. Traditional LQR solved by Riccati's equation can be obtained in text books [12]. In the following, one presents the procedure for the LQR-LMI approach.

Firstly, mathematical definitions of some terms are given, and LQR control problem is defined. Then, the LQR problem is represented as an equivalent eigenvalue problem (EVP) in terms of LMI using the H_2 representation of the LQR problem.

3.1. Basic definitions of LMIs and EVPs

A linear matrix inequality has the form

$$\mathbf{F}(\mathbf{z}) = \mathbf{F}_0 + \sum_{i=1}^m \mathbf{z}_i \mathbf{F}_i > \mathbf{0}, \quad (3.1)$$

where \mathbf{z} is a real vector and \mathbf{F}_0 and \mathbf{F}_i are real symmetric matrices. Inequality (3.1) is shorthand for saying that $\mathbf{F}(\mathbf{z})$ is positive definite. A vector \mathbf{z} that satisfies inequality (3.1) is known as a feasible solution of the LMI.

Inequality (3.1) is a convex constraint on \mathbf{z} . This property is important because powerful numerical techniques are available for the solution of problems involving convex LMIs [4]. On the other hand, no efficient algorithm is available for the solution of nonconvex problems. Hence, nonconvex inequalities which may arise from a control problem should be converted to convex LMIs to be solvable numerically. One useful example for such manipulations is the LMI representation of the following nonconvex inequalities:

$$\mathbf{Q}(\mathbf{z}) - \mathbf{S}(\mathbf{z})\mathbf{R}(\mathbf{z})^{-1}\mathbf{S}^T(\mathbf{z}) > \mathbf{0}, \quad \mathbf{R}(\mathbf{z}) > \mathbf{0}, \quad (3.2)$$

where \mathbf{Q} , \mathbf{R} , and \mathbf{S} are affine functions of \mathbf{z} , and \mathbf{Q} and \mathbf{R} are symmetric matrix. Inequality (3.2) is equivalent to

$$\begin{bmatrix} \mathbf{Q}(\mathbf{z}) & \mathbf{S}(\mathbf{z}) \\ \mathbf{S}^T(\mathbf{z}) & \mathbf{R}(\mathbf{z}) \end{bmatrix} > \mathbf{0}. \quad (3.3)$$

This transformation can be achieved easily premultiplying inequality (3.3) by

$$\begin{bmatrix} \mathbf{I} & -\mathbf{S}\mathbf{R}^{-1} \\ \mathbf{0} & \mathbf{I} \end{bmatrix} > \mathbf{0} \quad (3.4)$$

and postmultiplying it by its transpose.

One of the concepts related with LMIs and control problems is the eigenvalue problem. An eigenvalue problem may have several representations, one of which is given by

$$\begin{aligned} \min \quad & \mathbf{c}^T \mathbf{z} \\ \text{subject to} \quad & \mathbf{A}(\mathbf{z}) > \mathbf{0}, \end{aligned} \quad (3.5)$$

where $\mathbf{A}(\mathbf{z})$ is a symmetric and affine function of \mathbf{z} . An LQR problem may be transformed into this form of the EVP to be represented in terms of LMIs.

3.2. LQR control problem

There are various representations of LQR problem in the literature. Here, definitions are given in a way that aids the derivation of the specific problem defined above; hence they may not be the most general forms of LQR problem. The LQR problem is to find the control gain \mathbf{K} that satisfies the optimization

$$\begin{aligned} \min_{\mathbf{K}} \quad & E[\mathbf{y}^T \tilde{\mathbf{Q}} \mathbf{y} + \mathbf{u}^T \tilde{\mathbf{R}} \mathbf{u} + \mathbf{y}^T \tilde{\mathbf{N}} \mathbf{u} + \mathbf{u}^T \tilde{\mathbf{N}}^T \mathbf{y}], \\ \text{subject to} \quad & (2.1) \text{ and } \mathbf{u}(t) = -\alpha \mathbf{K} \mathbf{x}(t), \end{aligned} \quad (3.6)$$

where $\tilde{\mathbf{Q}} \geq 0$ and $\tilde{\mathbf{R}} > 0$ are symmetric weighting matrices, $\tilde{\mathbf{N}}$ is the weighting matrix between input and output vectors, and α is a scalar amplifier. Substituting the output equation in (2.1) into the optimization problem (3.6), and assuming \mathbf{E}_{in} and \mathbf{E}_{out} as zero vectors; one obtains another form of the LQR problem

$$\begin{aligned} \min_{\mathbf{K}} \quad & E[\mathbf{x}^T \mathbf{Q} \mathbf{x} + \mathbf{u}^T \mathbf{R} \mathbf{u} + \mathbf{x}^T \mathbf{N} \mathbf{u} + \mathbf{u}^T \mathbf{N}^T \mathbf{x}], \\ \text{subject to} \quad & \dot{\mathbf{x}}(t) = \mathbf{A}(t) \mathbf{x}(t) + \mathbf{B}_w(t) \mathbf{w}(t) + \mathbf{B}_u(t) \mathbf{u}(t), \quad \mathbf{u}(t) = -\alpha \mathbf{K} \mathbf{x}(t), \end{aligned} \quad (3.7)$$

where

$$\mathbf{Q} = \mathbf{C}^T \tilde{\mathbf{Q}} \mathbf{C}, \quad \mathbf{N} = \mathbf{C}^T \tilde{\mathbf{Q}} \mathbf{D} + \mathbf{C}^T \tilde{\mathbf{N}}, \quad \mathbf{R} = \tilde{\mathbf{R}} + \mathbf{D}^T \tilde{\mathbf{Q}} \mathbf{D} + \mathbf{D}^T \tilde{\mathbf{N}} + \tilde{\mathbf{N}} \mathbf{D}. \quad (3.8)$$

3.3. EVP representation of the LQR problem

Lyapunov's stability criteria can be used to state that a system given by (2.1) with control force $\mathbf{u}(t) = -\alpha \mathbf{K} \mathbf{x}(t) = -\mathbf{G} \mathbf{x}(t)$, where $\mathbf{G} = \alpha \mathbf{K}$, is stable if there exists a matrix $\mathbf{S} = \mathbf{S}^T > \mathbf{0}$ that satisfies

$$(\mathbf{A} - \mathbf{B}_u \mathbf{G}) \mathbf{S} + \mathbf{S} (\mathbf{A} - \mathbf{B}_u \mathbf{G})^T + \mathbf{B}_w \mathbf{B}_w^T \leq 0, \quad (3.9)$$

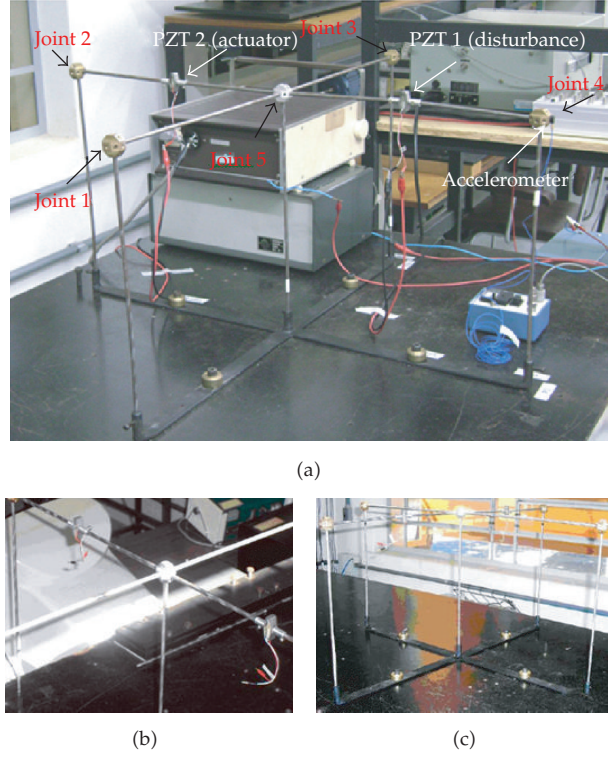


Figure 1: 3D truss structures and PZT wafer stack actuators.

where \mathbf{S} that satisfies inequality (3.9) is the optimal state covariance matrix \mathbf{P} . So, combining (3.7) and (3.9) and optimizing \mathbf{S} , the H_2 optimization problem may be stated as [13]

$$\begin{aligned} \min_{(\mathbf{K}, \mathbf{S})} \quad & \text{Tr}(\mathbf{R}^{1/2} \mathbf{G} \mathbf{S} \mathbf{G}^T \mathbf{R}^{1/2}) + \text{Tr}(\mathbf{Q} \mathbf{S}) - \text{Tr}(\mathbf{G} \mathbf{S} \mathbf{N}) - \text{Tr}(\mathbf{N}^T \mathbf{S} \mathbf{G}^T), \\ \text{subject to} \quad & \mathbf{A} \mathbf{S} - \mathbf{B}_u \mathbf{G} \mathbf{S} + \mathbf{S} \mathbf{A}^T - \mathbf{S} \mathbf{G}^T \mathbf{B}_u^T + \mathbf{B}_w \mathbf{B}_w^T \leq 0, \quad \mathbf{S} = \mathbf{S}^T > 0, \end{aligned} \quad (3.10)$$

where $\text{Tr}()$ is the trace of the matrix. This is not an EVP problem since it is not convex because of the terms involving $\mathbf{G} \mathbf{S}$. To obtain a convex version of the problem, two new variables are introduced $\mathbf{X} = \mathbf{R}^{1/2} \mathbf{G} \mathbf{S} \mathbf{G}^T \mathbf{R}^{1/2}$ and $\mathbf{Y} = \mathbf{G} \mathbf{S}$. Substituting these variables into (3.10) and using the transformation given by (3.2) and (3.3), the EVP representation of LQR problem is obtained as

$$\begin{aligned} \min_{(\mathbf{X}, \mathbf{S}, \mathbf{Y})} \quad & \text{Tr}(\mathbf{X}) + \text{Tr}(\mathbf{Q} \mathbf{S}) - \text{Tr}(\mathbf{Y} \mathbf{N}) - \text{Tr}(\mathbf{N}^T \mathbf{Y}^T), \\ \text{subject to} \quad & \mathbf{A} \mathbf{S} - \mathbf{B}_u \mathbf{Y} + \mathbf{S} \mathbf{A}^T - \mathbf{Y}^T \mathbf{B}_u^T + \mathbf{B}_w \mathbf{B}_w^T \leq 0, \\ & \begin{bmatrix} \mathbf{X} & \mathbf{R}^{1/2} \mathbf{Y} \\ \mathbf{Y}^T \mathbf{R}^{1/2} & \mathbf{S} \end{bmatrix} > 0. \end{aligned} \quad (3.11)$$

Table 1: Physics and geometric properties of the truss structures.

Length of structural element (mm)	30
Diameter of structural element (mm)	5
Young's Modulus (GPa)	210
Density (Kg/m ³)	7800

The optimal control gain is then computed from $\mathbf{G} = \mathbf{Y}\mathbf{S}^{-1}$, so $\mathbf{K} = \alpha\mathbf{Y}\mathbf{S}^{-1}$. For well-posed problem with no additional constraints, the \mathbf{S} that optimizes (3.11) is identical to the optimal state covariance matrix \mathbf{P} . In this paper, LQR in LMI version was implemented using the LMI Toolbox of Matlab.

3.4. Kalman states estimator

The Kalman estimator was named after Rudolf E. Kalman, though Thorvald Nicolai Thiele and Peter Swerling actually developed a similar algorithm earlier. Stanley F. Schmidt is generally credited with developing the first implementation of a Kalman estimator. It was during a visit of Kalman to the NASA Ames Research Center that he saw the applicability of his ideas to the problem of trajectory estimation for the Apollo program, leading to its incorporation in the Apollo navigation computer. The estimator was developed in papers by Swerling [14], Kalman [15], and Kalman and Bucy [16]. In control theory, the Kalman estimator is most commonly referred to as Kalman filter or, mainly, as linear quadratic estimation (LQE). In this paper, the Kalman estimator gain was obtained using the software Matlab through command "lqe."

3.5. Dynamic and modal uncertainties representation

This paper presents a methodology to design a robust control considering dynamic or modal uncertainties in the state space model. The uncertainty ranges in the parameters were quantified through experimental identification considering different excitations. The mathematical model in state space realization was obtained using the numerical method of subspace identification (N4SID). An expressive part of identification methods concerns with computing polynomial models, which, typically, give rise to numerically ill-conditioned mathematical problems, especially for multi-input multioutput systems [17]. N4SID algorithms are then viewed as optimal alternatives. This approach is advantageous, especially for high-order multivariable systems, where the parameterization is not trivial. The parameterization is needed to start up classical identification algorithms, which means that a priori knowledge of the order and of the observability or controllability indices is required [18].

Using n_t ($n_t > 1$) data acquisition tests, it is possible to realize n_t model identification (through N4SID algorithm) and, consequently, n_t dynamic models. Each one can be used as a polytopic vertex, S_i (see (2.5)). In this way, it is possible to define the polytope $\mathbf{\Omega}$ to describe the convex space Co . Considering this convex space to solve the controller, it is possible to obtain a robust gain, and so to get a controller with the ability for maintaining satisfactory stability and performance features in the presence of parameters uncertainties and variations.

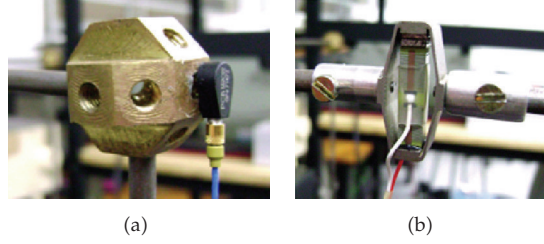


Figure 2: Accelerometer in joint 4 and details of the PZT wafer stack actuator.

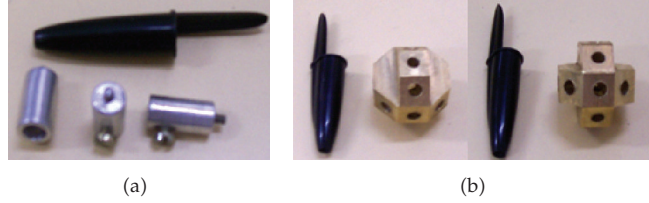


Figure 3: (a) Adapters to connect PZT stacks; (b) structural nodes.

4. Experimental control design

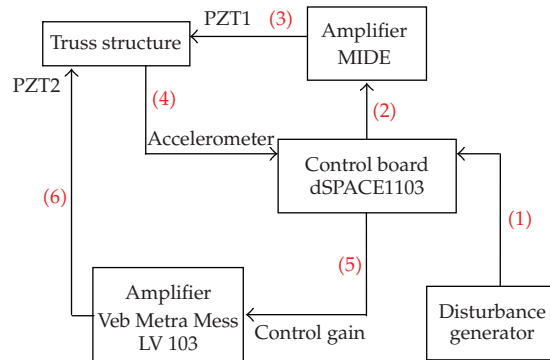
The proposed methodology was experimentally applied in a 3D truss structure, as shown in Figure 1. The physics and geometric properties of the truss are given in Table 1. The properties of the PZT wafer stacks elements are shown in Table 2, and the output signals were obtained with an accelerometer, model 352C22 PCB Piezotronics. Figures 2(a) and 2(b) show the accelerometer in joint 4, and the detail of the PZT wafer actuator, respectively. In this application, the PZT 1 was used to apply the disturbance input, $\mathbf{w}(t)$, and PZT 2 was used as control force input, $\mathbf{u}(t)$.

The connections of the piezoelectric actuators in the structural elements were made through adapters, shown in Figure 3(a). Figure 2(b) shows details of this connection. These adapters were made using aluminum rod in order to connect the structural part and the PZT wafer actuator. This kind of actuator amplifies the displacement in the axial direction of the structural member, and it is named active member. The joint connections were made of copper, with 24 mm of diameter in the geometric format of eight sides, as shown in Figure 3(b).

The dynamic model represented through state space realization was identified using the N4SID algorithm considering $n_t = 6$. Therefore, the dynamic uncertainties were considered through identification of six models, then, the convex space was obtained with six vertexes (S_1, S_2, \dots, S_6). The order of the model (dimension of state vector) was chosen as 2, so the first mode was identified. Using the first identified mode, the Kalman estimator gain was computed by the "lqe" command of the Matlab software. It was computed as $\mathbf{L} = [463, 9982 \ 65, 8124]^T$. Considering the weighting matrices \mathbf{Q} and \mathbf{R} as $5 \cdot \mathbf{I}$ and $1 \cdot \mathbf{I}$, respectively, where \mathbf{I} is the identity matrix, the controller gain was obtained as $\mathbf{G} = [-1, 5426 \ 2, 5514]$. The scalar amplifier α was chosen as 80 to the first mode. The controller was designed to the first mode, however, at the practice test, it was verified that the second mode also had a significant attenuation in the vibration amplitude.

Table 2: Physics and geometric properties of PZT wafer stack actuators, based on material designation APA60 M (Amplified Piezo Actuators, CEDRAT).

Property	Unit	APA60 M
Displacement	(μm)	80
Blocked Force	(N)	110
Stiffness	(N/ μm)	1,38
Resonance Frequency (Free-Free)	(Hz)	10400
Response Time (Free-Free)	(ms)	0,05
Resonance Frequency (Blocked-Free)	(Hz)	2800
Response Time (Blocked-Free)	(ms)	0,18
Voltage Range	(V)	$-20 \dots 150$
Capacitance	(μF)	1,55
Resolution	(nm)	0,8
Thermo-Mechanical Behaviour	($\mu\text{m}/\text{K}$)	1,02
Height H (in actuation direction)	(mm)	13,0
Length	(mm)	26,9
Width (ind. Edges, wires)	(mm)	11,5
Mass	(g)	20,0
Standard Mechanical Interface [TH]	2 flat surface $5 \times 10 \text{ mm}^2$ with M2.5 threaded hole	
Standard Electrical Interface	2 PTFE insulated AWG30 wires 100 mm long with $\varnothing 1$ banana plug	

**Figure 4:** Disposition of the experimental setup.

To verify the results of the active vibration control, two cases were considered. Figure 4 shows the configuration of the experimental setup used. In the first case, the disturbance input was a sine signal with frequency of 16 Hz (approximately the first natural frequency). Figure 5 shows the output signal with and without control obtained in joint 4. Figure 6 shows the experimental output measured using the accelerometer in joint 4 and the estimated output through Kalman estimator algorithm. These results were obtained using the dSPACE 1103 control board and the Simulink/Matlab.

In the second case, a disturbance input was considered as a sine signal with frequency of 26 Hz (approximately the second natural frequency). Figure 7 shows the response in time domain for the uncontrolled and controlled systems. The controller was applied approximately after 4.5 seconds. Figures 8 and 9 show the control force in the PZT stack

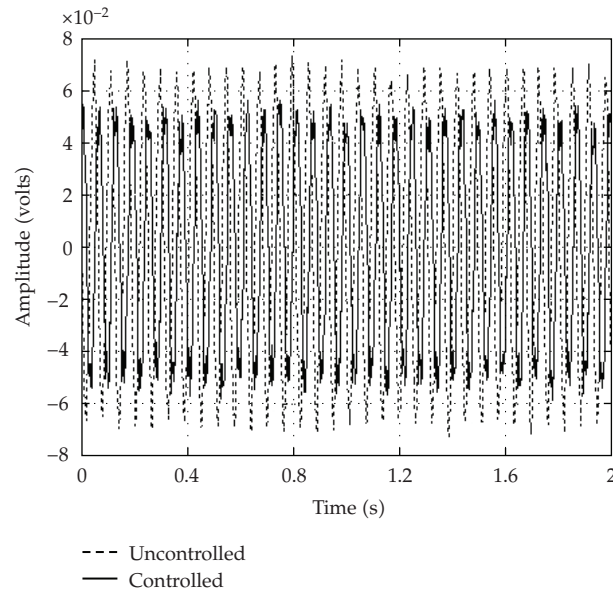


Figure 5: Output signal measured in the joint 4 using accelerometer-controlled and uncontrolled systems.

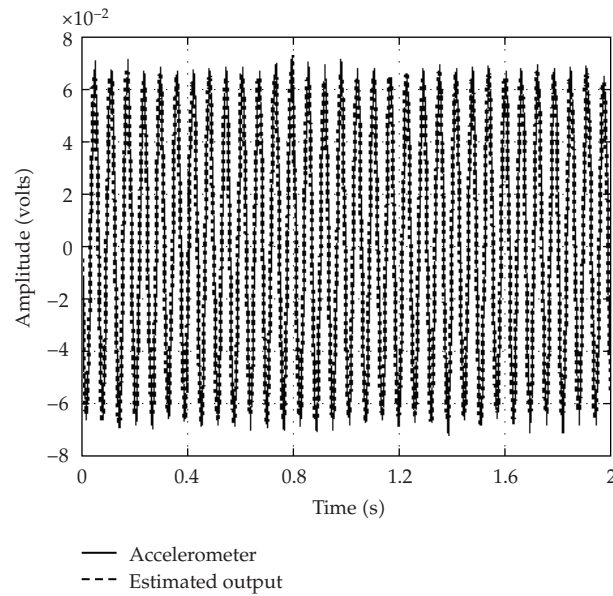


Figure 6: Estimated output signal in joint 4 through Kalman Estimator and experimental output.

actuator 2 and the output estimated through Kalman estimator, respectively. Figure 10 shows the frequency response function (FRF) of the uncontrolled and controlled truss structures. It was attenuated approximately by 6 dB and 9 dB to the first and second modes, respectively.

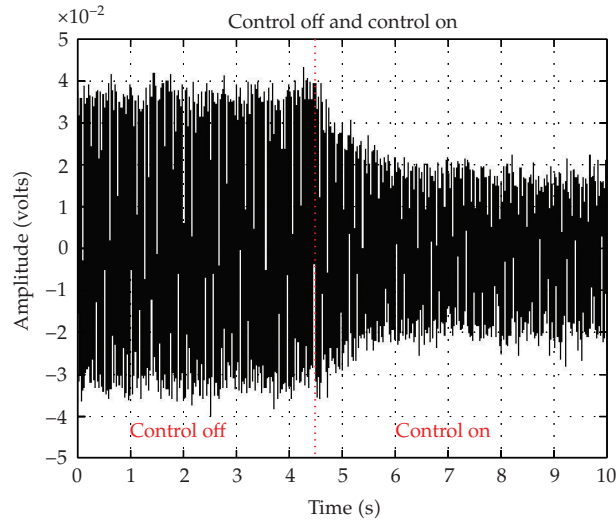


Figure 7: Experimental output signal of uncontrolled and controlled truss structure in joint 4.

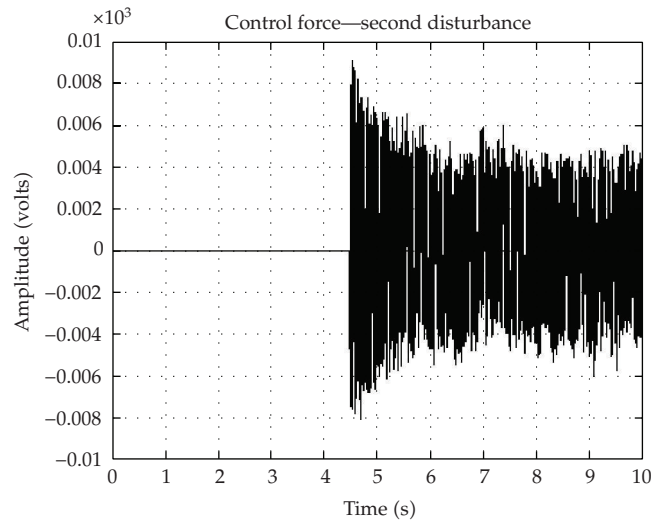


Figure 8: Control force applied by PZT wafer stack 2 for the second case of disturbance.

5. Final remarks

Over the last two decades, the use of piezoceramics as actuators and sensors has increased considerably, since they provide an effective means of high-quality actuation and sensing mechanism. Piezoceramics have been considered as an alternative due features as low-cost, light weight, and easy-to-implement for active control of structural vibration.

In this paper, the subspace identification method was used to obtain the parameters of the system and to characterize the uncertainty ranges present in the model. In the experimental application, the uncertainties were defined in a polytopic with six vertexes. The system identification technique was used to identify the model in the state space

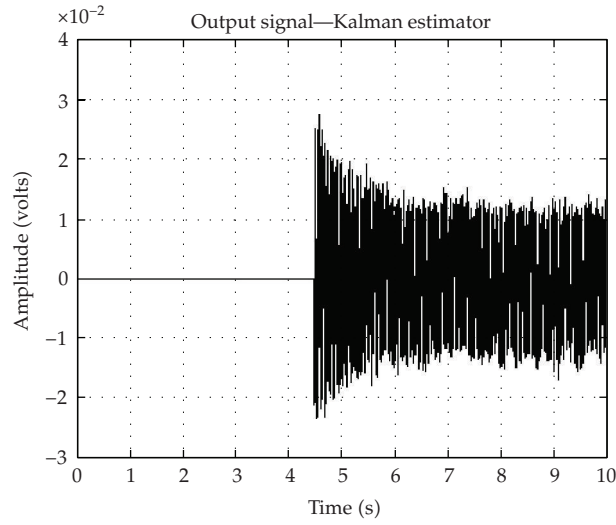


Figure 9: Output signal estimated through Kalman Estimator algorithm for the second case of disturbance (sine signal with 26 Hz).

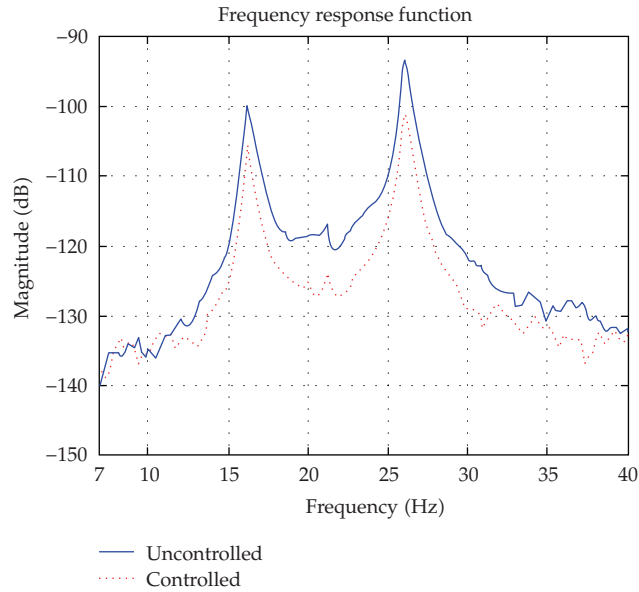


Figure 10: Frequency response function of uncontrolled and controlled system.

realization that was converted to modal coordinates. The LQR controller solved through LMI was experimentally implemented and applied in a 3D truss structure that contains nonlinearities and uncertainties. The disturbance was applied through PZT wafer stack. LMI techniques that are classified by some authors as postmodern control present many advantages, mainly due to the facilities of solving numerical problems for complex structure, where the analytical solution should be difficult to implement. Uncertainties in the dynamic matrix were considered in order to design a robust active vibration control. However, any

other uncertain parameter should be added, for instance, damping coefficients. In this case, it is only needed to consider new vertexes in the box with all uncertain parameters and write the respective LMIs. The proposed approach showed that an efficient robust controller design can be obtained for complex structures with nonlinearities and uncertainties.

Acknowledgment

The authors acknowledge the support of the Research Foundation of the State of São Paulo (FAPESP, Brazil).

References

- [1] E. J. Ruggiero, *Active dynamic analysis and vibration control of gossamer structures using smart materials*, M.S. thesis, Virginia Polytechnic Institute and State University, Blacksburg, Va, USA, 2002.
- [2] Y. J. Yan and L. H. Yam, "A synthetic analysis on design of optimum control for an optimized intelligent structure," *Journal of Sound and Vibration*, vol. 249, no. 4, pp. 775–784, 2002.
- [3] K. M. Grigoriadis and R. E. Skelton, "Low-order control design for LMI problems using alternating projection methods," *Automatica*, vol. 32, no. 8, pp. 1117–1125, 1996.
- [4] S. Boyd, L. El Ghaoui, E. Feron, and V. Balakrishnan, *Linear Matrix Inequalities in System and Control Theory*, vol. 15 of *SIAM Studies in Applied Mathematics*, SIAM, Philadelphia, Pa, USA, 1994.
- [5] P. Gahinet, A. Nemirovski, A. J. Laub, and M. Chiliali, "LMI Control Toolbox User's Guide," The Mathworks Inc., Natick, Mass, USA, 1995.
- [6] F. Sarracini Jr. and A. L. Serpa, "Reduced model in H^∞ vibration control using linear matrix inequalities," *Shock and Vibration*, vol. 13, no. 4-5, pp. 469–484, 2006.
- [7] S. Da Silva, V. Lopes Jr., and M. J. Brennan, "Design of a control system using linear matrix inequalities for the active vibration control of a plate," *Journal of Intelligent Material Systems and Structures*, vol. 17, no. 1, pp. 81–93, 2006.
- [8] Y. Chen and C. Zhu, "Active vibration control based on linear matrix inequality for rotor system under seismic excitation," *Journal of Sound and Vibration*, vol. 314, no. 1-2, pp. 53–69, 2008.
- [9] W. K. Gawronski, *Dynamics and Control of Structures: A Modal Approach*, Mechanical Engineering Series, Springer, New York, NY, USA, 1998.
- [10] R. E. Kalman, "Contributions to the theory of optimal control," *Boletín de la Sociedad Matemática Mexicana*, vol. 5, pp. 102–119, 1960.
- [11] A. Kumar, F. Wu, M. Lin, et al., "Potential Applications of Smart Layer® Technology for Homeland Security," Acellent Technologies, Inc. 155 C-3 Moffett Park Drive, Sunnyvale, CA e National Institute of Standards and Technology, 2004.
- [12] K. Ogata, *Modern Control Engineering*, Prentice Hall, Upper Saddle River, NJ, USA, 1997.
- [13] E. A. Johnson and B. Erkus, "Structural control with dissipative damping devices," in *Proceedings of the American Control Conference (ACC '02)*, vol. 3, pp. 2463–2468, Anchorage, Alaska, USA, May 2002.
- [14] P. Swerling, "A proposed stagewise differential correction procedure for satellite tracking and prediction," Tech. Rep. P-1292, RAND, Santa Monica, Calif, USA, January 1958.
- [15] R. E. Kalman, "A new approach to linear filtering and prediction problems," *Journal of Basic Engineering*, vol. 82, pp. 35–45, 1960.
- [16] R. E. Kalman and R. S. Bucy, "New results in linear filtering and prediction theory," *Journal of Basic Engineering*, vol. 83, pp. 95–108, 1961.
- [17] P. Van Overschee and B. De Moor, "N4SID: subspace algorithms for the identification of combined deterministic-stochastic systems," *Automatica*, vol. 30, no. 1, pp. 75–93, 1994.
- [18] L. Ljung, *System Identification: Theory for the User*, Prentice Hall Information and System Sciences Series, Prentice Hall, Upper Saddle River, NJ, USA, 1987.

Research Article

Sliding Mode Control of Uncertain Neutral Stochastic Systems with Multiple Delays

Dilan Chen^{1,2} and Weidong Zhang¹

¹ Department of Automation, Shanghai Jiaotong University, Shanghai 200030, China

² Department of Mathematics, Shanghai Maritime University, Shanghai 200135, China

Correspondence should be addressed to Dilan Chen, dlchen@dbc.shmtu.edu.cn

Received 31 August 2007; Accepted 4 March 2008

Recommended by Paulo Gonçalves

This paper is concerned with the sliding mode control for uncertain stochastic neutral systems with multiple delays. A switching surface is adopted first. Then, by means of linear matrix inequalities (LMIs), a sufficient condition is derived to ensure the global stochastic stability of the stochastic system in the sliding mode for all admissible uncertainties. The synthesized sliding mode controller guarantees the existence of the sliding mode.

Copyright © 2008 D. Chen and W. Zhang. This is an open access article distributed under the Creative Commons Attribution License, which permits unrestricted use, distribution, and reproduction in any medium, provided the original work is properly cited.

1. Introduction

Time delay occurs due to the finite capabilities of information processing and data transmission among various parts of the system. The phenomena of time delay are often encountered in various relevant systems, such as HIV infection with drug therapy, aircraft stabilization, chemical engineering systems, inferred grinding model, manual control, neural network, nuclear reactor, population dynamic model, rolling mill, ship stabilization, and systems with lossless transmission lines. It is well known that time delay factors always lead to poor performance. Hence, problems of stability analysis and stabilization of dynamical systems with time delays in the state variables and/or control inputs have received considerable interest for more than three decades [1–6].

In practice, systems are almost always innately “noisy”. Therefore, in order to model a system realistically, a degree of randomness must be incorporated into the model. Thus, a class of stochastic systems has received great attention in the past decade [7]. On the other hand, it has been shown that a lot of practical systems can be modeled by using functional differential equations of the neutral type [8, 9]. However, the mathematical model always contains some

uncertain elements. Therefore, uncertain systems have been extensively studied in the past years [10–12].

To cope with the problem of stability of uncertain stochastic neutral delay systems, most of the research focused on the retarded functional differential equations and it also seems that few results are available on the variable structure control.

Sliding mode control (SMC) is a particular type of variable structure control. It provides an effective alternative to deal with the nonlinear dynamic systems. The main feature of SMC is its easy realization, control of independent motion, insensitivity to variation in plant parameters or external perturbations, and wide variety of operational models [13–15].

The purpose of this paper lies in the design of SMC for a class of uncertain stochastic neutral delay systems. A switching surface, which makes it easy to guarantee the stability of the uncertain stochastic neutral delay systems in the sliding mode, is first proposed. By means of linear matrix inequalities (LMIs), a sufficient condition is given such that the stochastic dynamics in the specified switching surface is globally stochastically stable. And then, based on this switching surface, a synthesized SMC law is derived to guarantee the existence of the composite sliding motion. Finally, a numerical example is illustrated to demonstrate the validity of the proposed SMC.

2. Problem formulation

Consider the following neutral stochastic system with uncertainties and multiple delays:

$$\begin{aligned} d[Ex(t) - Cx(t - \tau)] &= [(A + \Delta A(t))x(t) + (A_d + \Delta A_d(t))x(t - h(t)) + Bu(t)]dt \\ &\quad + [\Delta E(t)x(t) + \Delta E_d(t)x(t - h(t))]dw(t), \\ x(t) &= \phi(t), \quad t \in [-H, 0], \end{aligned} \quad (2.1)$$

where $x(t) \in \mathbb{R}^n$ is the state, $u(t) \in \mathbb{R}^m$ is the control input, τ is the constant delay, $h(t)$ is the time-varying differentiable bounded delay satisfying $0 \leq h(t) \leq h_M$, $\Delta h(t) \leq h_D < 1$, $w(t)$ is an m -dimensional Brownian motion, $H = \max\{\tau, h_M\}$. It is assumed that $\phi(t)$ is the initial condition which is continuous, $t \in [-H, 0]$. In system (2.1), $E \in \mathbb{R}^{n \times n}$, $C \in \mathbb{R}^{n \times n}$, $A \in \mathbb{R}^{n \times n}$, $A_d \in \mathbb{R}^{n \times n}$, $B \in \mathbb{R}^{n \times m}$ are known real constant matrices. $\Delta A(t)$, $\Delta A_d(t)$, $\Delta E(t)$, and $\Delta E_d(t)$ represent the structured uncertainties in (2.1), which are assumed to be of the forms

$$\begin{aligned} \Delta A(t) &= MF_1(t)N_A, \quad \Delta A_d(t) = MF_2(t)N_{A_d}, \\ [\Delta E(t), \Delta E_d(t)] &= MF_3(t)[N_E, N_{E_d}], \end{aligned} \quad (2.2)$$

M , N_A , N_{A_d} , N_E , and N_{E_d} are some given constant matrices, $F_l(t)$ ($l = 1, 2, 3$) are unknown real time-varying matrices which have the following structure:

$$F_l(t) = \text{blockdiag}\{\delta_{l_1}(t)I_{r_1}, \dots, \delta_{l_k}(t)I_{r_k}, F_{l_1}(t), \dots, F_{l_s}(t)\}, \quad \delta_{l_i} \in \mathbb{R}, |\delta_{l_i}| \leq 1, 1 \leq i \leq k, \text{ and } F_{l_j}^\top F_{l_j} \leq I, 1 \leq j \leq s.$$

We define the sets Δ_l as

$$\Delta_l = \left\{ F_l^\top(t)F_l(t) \leq I, F_l N_l = N_l F_l, \forall N_l \in \Sigma_l \right\}, \quad (2.3)$$

where $\Sigma_l = \{N_l = \text{blockdiag}[N_{l_1}, \dots, N_{l_k}, n_{l_1}I_{f_{l_1}}, \dots, n_{l_s}I_{f_{l_s}}]\}$, N_{l_i} are invertible for $1 \leq i \leq k$, and $n_{l_j} \in \mathbb{R}$, $n_{l_j} \neq 0$ for $1 \leq j \leq s$.

The following useful lemmas will be used to derive the desired LMI-based stability criteria.

Lemma 2.1 (see [1]). *The LMI $\begin{bmatrix} S_{11} & S_{12} \\ * & S_{22} \end{bmatrix} < 0$, with $S_{11} = S_{11}^\top$, $S_{22} = S_{22}^\top$, is equivalent to*

$$S_{22} < 0, \quad S_{11} - S_{12}S_{22}^{-1}S_{12}^\top < 0. \quad (2.4)$$

Lemma 2.2 (see [11]). *Let D, E, F_l be real matrices of appropriate dimensions and $F_l \in \Delta_l$. Then for any block-structured matrix $N_l \in \Sigma_l$,*

$$DF_lE + (DF_lE)^\top \leq D(N_lN_l^\top)D^\top + E^\top(N_lN_l^\top)^{-1}E. \quad (2.5)$$

Lemma 2.3 (see [11]). *Let A, D, E, F_l , and P be real matrices of appropriate dimensions with $P = P^\top > 0$ and $F_l \in \Delta_l$. Then for any block-structured matrix $N_l \in \Sigma_l$ satisfying $P^{-1} - D(N_lN_l^\top)D^\top > 0$, one has*

$$(A + DF_lE)^\top P(A + DF_lE) \leq A^\top(P^{-1} - DN_lN_l^\top D^\top)^{-1}A + E^\top(N_lN_l^\top)^{-1}E. \quad (2.6)$$

Lemma 2.4 (see [11]). *For any $z, y \in \mathbb{R}^n$ and for any symmetric positive-definite matrix $X \in \mathbb{R}^{n \times n}$,*

$$-2z^\top y \leq z^\top X^{-1}z + y^\top Xy. \quad (2.7)$$

Definition 2.5 (see [14]). *The nominal stochastic time-delay system of form (2.1) with $u(t) = 0$ is said to be mean-square asymptotically stable if*

$$\lim_{t \rightarrow \infty} \mathbb{E}|x(t)|^2 = 0. \quad (2.8)$$

Definition 2.6 (see [14]). *The uncertain time delay system of the form (2.1) is robustly mean square stabilized if the nominal system is mean-square asymptotically stable for all admissible uncertainties.*

In order to simplify the treatment of the problem, the operator $\mathfrak{J} : C([- \tau, 0], \mathbb{R}^n) \rightarrow \mathbb{R}^n$ is defined to be

$$\mathfrak{J}(x_t) = Ex(t) - Cx(t - \tau). \quad (2.9)$$

The stability of the operator \mathfrak{J} is defined as follows.

Definition 2.7 (see [9]). *The operator \mathfrak{J} is said to be stable if the zero solution of the homogeneous difference equation*

$$\begin{aligned} \mathfrak{J}(x_t) &= 0, \quad t \geq 0, \\ X_0 &= \varphi \in \{\varphi \in C[-\tau, 0] : \mathfrak{J}\varphi = 0\} \end{aligned} \quad (2.10)$$

is uniformly asymptotically stable.

If $\text{rank}(E) = m < n$, then it is easy to find that there exist nonsingular constant matrices K and S , such that

$$KES^{-1} = \begin{pmatrix} E_1 & 0 \\ 0 & 0 \end{pmatrix}, \quad KCS^{-1} = \begin{pmatrix} C_1 & 0 \\ 0 & C_2 \end{pmatrix}, \quad (2.11)$$

where E_1 is an $m \times m$ nonsingular matrix, C_1 and C_2 are $m \times m$ and $(n - m) \times (n - m)$ constant matrices, respectively.

Lemma 2.8 (see [9]). *The operator \mathfrak{J} is stable if $\|E_1^{-1}C_1\| < 1$ and $|C_2| \neq 0$, where E_1 , C_1 , and C_2 are defined as in (2.11) and $\|\cdot\|$ is any matrix norm.*

3. Switching surface and controller design

In this work, we choose the switching function as follows:

$$S(t) = D[Ex(t) - Cx(t - \tau)] + \sigma(t), \quad (3.1)$$

where the auxiliary variable $\sigma(t)$ satisfies the following:

$$d\sigma = -D[(A + BK)x(t) + A_d x(t - h(t))]dt - D[\Delta Ex(t) + \Delta E_d x(t - h(t))]dw(t), \quad (3.2)$$

where $D \in \mathbb{R}^{m \times n}$ and $K \in \mathbb{R}^{m \times n}$ are constant matrices. The matrix K is chosen such that the matrix $A + BK$ is Hurwitz, and the matrix D is to be designed later so that DB is nonsingular. As long as the system operates in the sliding mode, it satisfies the equations $S(t) = 0$ and $\dot{S}(t) = 0$ [13].

Therefore, the equivalent control $u_{eq}(t)$ in the sliding manifold is given by

$$u_{eq} = -(DB)^{-1}D[(\Delta A(t) - BK)x(t) + \Delta A_d(t)x(t - h(t))]. \quad (3.3)$$

Substituting (3.3) into system (2.1), the following equivalent sliding mode dynamics can be obtained:

$$\begin{aligned} d[Ex(t) - Cx(t - \tau)] = & \left[(A + BK + \Delta A(t) - B(DB)^{-1}D\Delta A(t))x(t) \right. \\ & + \left(A_d + \Delta A_d(t) - B(DB)^{-1}D\Delta A_d(t) \right)x(t - h(t))]dt \\ & + [\Delta Ex(t) + \Delta E_d x(t - h(t))]dw(t). \end{aligned} \quad (3.4)$$

Now, we proceed to the first task which is to analyze the robustly stochastic stability of the sliding motion described by (3.4), and derive a sufficient condition by means of the linear matrix inequality method.

4. Robust stabilization in the mean square sense

Theorem 4.1. Consider the equivalent sliding mode dynamics (3.4). If the operator \mathfrak{I} is stable and there exist symmetric positive-definite matrices $X, Q_1, Q_2, T_1, T_2, T_3, T_4, T_5$, and T_6 satisfying the following LMIs:

$$\Pi = \begin{bmatrix} \Pi_{11} & \Pi_{12} & \Pi_{13} & E^\top XB & E^\top XM & E^\top XM & 0 & 0 & 0 \\ * & \Pi_{22} & -C^\top XA_d & 0 & 0 & 0 & C^\top XB & C^\top XM & C^\top XM \\ * & * & \Pi_{33} & 0 & 0 & 0 & 0 & 0 & 0 \\ * & * & * & -\frac{B^\top XB}{2} & 0 & 0 & 0 & 0 & 0 \\ * & * & * & * & -T_1 & 0 & 0 & 0 & 0 \\ * & * & * & * & * & -T_2 & 0 & 0 & 0 \\ * & * & * & * & * & * & -\frac{B^\top XB}{2} & 0 & 0 \\ * & * & * & * & * & * & * & -T_3 & 0 \\ * & * & * & * & * & * & * & 0 & -T_4 \end{bmatrix} < 0, \quad (4.1)$$

where $\Pi_{11} = E^\top X(A + BK) + (A + BK)^\top XE + Q_1 + Q_2 + N_A^\top(T_1 + T_3 + T_5)N_A + N_E^\top T_6 N_E$, $\Pi_{12} = -(A + BK)^\top XC$, $\Pi_{13} = E^\top XA_d + N_{E_d}^\top T_4 N_{E_d}$, $\Pi_{22} = -Q_1 + N_A^\top T_2 N_A$, $\Pi_{33} = -(1 - h_D)Q_1 + N_{A_d}^\top(T_1 + T_3 + T_5)N_{A_d} + N_{E_d}^\top T_4 N_{E_d}$,

$$\begin{bmatrix} -X & XM \\ * & -T_6 \end{bmatrix} < 0, \quad (4.2)$$

$$\begin{bmatrix} -\frac{X}{2} & XM \\ * & -T_5 \end{bmatrix} < 0, \quad (4.3)$$

then the uncertain time delay system of the form (2.1) with the switching surface (3.1) is robustly stochastically stable and sliding mode matrix $D = B^\top X$. In the above LMIs, T takes the form of $N_l N_l^\top$ for $N_l \in \Sigma_l$.

Proof. Choose a Lyapunov functional candidate $V(x(t), t)$ as

$$V(x_t) = (\mathfrak{I}x_t)^\top(t)P(\mathfrak{I}x_t) + \int_{t-\tau}^t x^\top(s)Q_1x(s)ds + \int_{t-h(t)}^t x^\top(s)Q_2x(s)ds. \quad (4.4)$$

Then, the averaged derivative is given by the following expression:

$$\begin{aligned} \mathbb{L}V(x_t) &= 2[Ex(t) - Cx(t - \tau)]^\top X[(A + BK + \Delta A(t) - B(DB)^{-1}D\Delta A(t))x(t) \\ &\quad + (A_d + \Delta A_d(t) - B(DB)^{-1}D\Delta A_d(t))x(t - h(t))] \\ &\quad + [\Delta E(t)x(t) + \Delta E_d(t)x(t - h(t))]^\top P[\Delta E(t)x(t) + \Delta E_d(t)x(t - h(t))] \\ &\quad + x^\top(t)Q_1x(t) - x^\top(t - \tau)Q_1x(t - \tau) + x^\top(t)Q_2x(t) \\ &\quad - (1 - \frac{\Delta}{h}(t))x^\top(t - h(t))Q_2x(t - h(t)). \end{aligned} \quad (4.5)$$

Using Lemma 2.1, inequality (4.2) is equivalent to

$$X^{-1} - MT_6^{-1}M^T > 0. \quad (4.6)$$

Hence, it follows from Lemma 2.3 that

$$\begin{aligned} & [\Delta E(t)x(t) + \Delta E_d(t)x(t-h(t))]^T X [\Delta E(t)x(t) + \Delta E_d(t)x(t-h(t))] \\ &= \{MF_3(t)[N_E x(t) + N_{E_d} x(t-h(t))]\}^T X \{MF_3(t)[N_E x(t) + N_{E_d} x(t-h(t))]\} \\ &\leq [N_E x(t) + N_{E_d} x(t-h(t))]^T T_6 [N_E x(t) + N_{E_d} x(t-h(t))] \\ &= x^T(t) N_E^T T_6 N_E x(t) + x^T(t) N_E^T T_6 N_{E_d} x(t-h(t)) + x^T(t-h(t)) N_{E_d}^T T_6 N_E x(t) \\ &\quad + x^T(t-h(t)) N_{E_d}^T T_6 N_{E_d} x(t-h(t)). \end{aligned} \quad (4.7)$$

Note that $D = B^T X$, and it follows from Lemma 2.4 that

$$\begin{aligned} & -2x^T(t) E^T X B (DB)^{-1} D \Delta A(t) x(t) \leq x^T [E^T X B (B^T X B)^{-1} B^T X E + \Delta A^T(t) X \Delta A(t)] x(t), \\ & -2x^T(t) E^T X B (DB)^{-1} D \Delta A_d(t) x(t-h(t)) \\ & \leq x^T E^T X B (B^T X B)^{-1} B^T X E x(t) + x^T(t-h(t)) \Delta A_d^T(t) X \Delta A_d(t) x(t-h(t)), \\ & 2x^T(t-\tau) C^T X B (DB)^{-1} D \Delta A(t) x(t) \\ & \leq x^T(t-\tau) C^T X B (B^T X B)^{-1} B^T X C x(t-\tau) + x^T(t) \Delta A^T(t) X \Delta A(t) x(t), \\ & 2x^T(t-\tau) C^T X B (DB)^{-1} D \Delta A_d(t) x(t-h(t)) \\ & \leq x^T(t-\tau) C^T X B (B^T X B)^{-1} B^T X C x(t-\tau) + x^T(t-h(t)) \Delta A_d^T(t) X \Delta A_d(t) x(t-h(t)). \end{aligned} \quad (4.8)$$

Substituting (4.7) and (4.8) into (4.5), we obtain

$$LV(x(t)) \leq X^T(t) \Xi X(t), \quad (4.9)$$

where $\Xi = \Xi_1 + M_1 F_1(t) N_1 + N_1^T F_1(t) M_1^T + M_1 F_2(t) N_2 + N_2^T F_2(t) M_1^T + M_2 F_1(t) N_1 + N_1^T F_1(t) M_2^T + M_2 F_2(t) N_2 + N_2^T F_2(t) M_2^T$, $X = [x^T(t), x^T(t-\tau), x^T(t-h(t))]^T$,

$$\begin{aligned} \Xi_1 &= \begin{bmatrix} \Xi_{11} & -(A+BK)^T X C & E^T X A_d + N_{E_d}^T T_6 N_{E_d} \\ * & \Xi_{22} & -C^T X A_d \\ * & * & \Xi_{33} \end{bmatrix}, \\ \Xi_{11} &= E^T X (A+BK) + (A+BK)^T X E + N_E^T T_6 N_E + 2\Delta A^T(t) X \Delta A(t) + Q_1 + Q_2 \\ &\quad + 2E^T X B (B^T X B)^{-1} B^T X E, \end{aligned} \quad (4.10)$$

$$\Xi_{22} = -Q_1 + 2C^T X B (B^T X B)^{-1} B^T X C,$$

$$\Xi_{33} = -(1-h_D)Q_2 + 2\Delta A_d^T(t) X \Delta A_d(t) + N_{E_d}^T T_6 N_{E_d},$$

$$M_1 = \begin{bmatrix} E^T X M \\ 0 \\ 0 \end{bmatrix}, \quad M_2 = \begin{bmatrix} 0 \\ -C^T X M \\ 0 \end{bmatrix}, \quad N_1 = \begin{bmatrix} N_A & 0 & 0 \end{bmatrix}, \quad N_2 = \begin{bmatrix} 0 & 0 & N_{A_d} \end{bmatrix}.$$

Using Lemmas 2.1 and 2.2, we have

$$\begin{aligned}
& \Xi \leq \Xi' \\
& = \begin{bmatrix} \Xi'_{11} & \Pi_{12} & \Pi_{13} & E^\top XB & E^\top XM & E^\top XM & 0 & 0 & 0 & 0 & 0 \\ * & \Pi_{22} & -C^\top XA_d & 0 & 0 & 0 & C^\top XB & C^\top XM & C^\top XM & 0 & 0 \\ * & * & \Xi'_{33} & 0 & 0 & 0 & 0 & 0 & 0 & 0 & 0 \\ * & * & * & -\frac{B^\top XB}{2} & 0 & 0 & 0 & 0 & 0 & 0 & 0 \\ * & * & * & * & -T_1 & 0 & 0 & 0 & 0 & 0 & 0 \\ * & * & * & * & * & -T_2 & 0 & 0 & 0 & 0 & 0 \\ * & * & * & * & * & * & -\frac{B^\top XB}{2} & 0 & 0 & 0 & 0 \\ * & * & * & * & * & * & * & -T_3 & 0 & 0 & 0 \\ * & * & * & * & * & * & * & * & -T_4 & 0 & 0 \\ * & * & * & * & * & * & * & * & * & -\frac{X}{2} & 0 \\ * & * & * & * & * & * & * & * & * & 0 & -\frac{X}{2} \end{bmatrix} \\
& \quad + M_3 \bar{F}(t) N_3 + N_3^\top \bar{F}^\top(t) M_3^\top, \\
& \Xi'_{11} = E^\top X(A+BK) + (A+BK)^\top XE + Q_1 + Q_2 + N_A^\top (T_1 + T_3) N_A + N_E^\top T_6 N_E, \\
& \Xi'_{33} = -(1-h_D)Q_1 + N_{A_d}(T_2 + T_4)N_{A_d} + N_{E_d}^\top T_6 N_{E_d}, \\
& M_3 = \begin{bmatrix} N_A & 0 & 0 & 0 & 0 & 0 & 0 & 0 & 0 & 0 & 0 \\ 0 & 0 & N_{A_d} & 0 & 0 & 0 & 0 & 0 & 0 & 0 & 0 \end{bmatrix}^\top, \quad \bar{F}(t) = \begin{bmatrix} F_1^\top(t) & 0 \\ 0 & F_2^\top(t) \end{bmatrix}, \\
& N_3 = \begin{bmatrix} 0 & 0 & 0 & 0 & 0 & 0 & 0 & 0 & 0 & M^\top X & 0 \\ 0 & 0 & 0 & 0 & 0 & 0 & 0 & 0 & 0 & 0 & M^\top X \end{bmatrix}.
\end{aligned} \tag{4.11}$$

With Lemma 2.1, we can see that $\Xi' < 0$ is equivalent to LMIs (4.1)–(4.3).

According to Itô's formula, system (2.1) is robustly stochastically stable. This completes the proof. \square

5. Sliding mode control

We now design an SMC law such that the reachability of the specified switching surface is ensured.

Theorem 5.1. *Consider the uncertain stochastic time delay system (2.1). Suppose that the switching function is given as (3.1) with $D = B^\top X$, where X is the solution of LMIs (4.1)–(4.3). Then the reachability of the sliding surface $s(t) = 0$ can be guaranteed by the following SMC law:*

$$u(t) = Kx(t) - \rho(t)\text{sgn}(s(t)), \tag{5.1}$$

where the switching gain $\rho(t)$ is given as

$$\rho(t) = \lambda + \|(DB)^{-1}DM\| \times (\|N_A x(t)\| + \|N_{A_d} x(t - h(t))\|) \quad (5.2)$$

with $\lambda > 0$.

Proof. A Lyapunov functional candidate $V(t)$ is defined as

$$V(t) = \frac{1}{2} S^\top(t)(DB)^{-1}S(t). \quad (5.3)$$

Hence we have

$$\begin{aligned} \dot{V}(t) &= S^\top(t)(DB)^{-1} \dot{S}(t) \\ &= S^\top(t)(DB)^{-1}D[\Delta A(t)x(t) + \Delta A_d(t)x(t - h(t)) - B\rho(t) \operatorname{sgn}(s(t))] \\ &\leq \|S(t)\| \|(DB)^{-1}DM\| \times (\|N_A x(t)\| + \|N_{A_d} x(t - h(t))\|) - \rho(t)\|S(t)\| \\ &\leq -\lambda\|S(t)\| < 0 \quad \text{for } \|S(t)\| \neq 0. \end{aligned} \quad (5.4)$$

This completes the proof. \square

6. An illustrative example

Consider neutral stochastic systems (2.1) with

$$\begin{aligned} A &= \begin{bmatrix} 2.3 & 1.2 \\ 2 & 3.4 \end{bmatrix}, \quad B = \begin{bmatrix} 1 & 0 \\ 0 & 1 \end{bmatrix}, \quad C = \begin{bmatrix} 0.1 & 0.3 \\ 0 & 0.1 \end{bmatrix}, \\ M &= \begin{bmatrix} 0.2 & 0 \\ 0.3 & -0.01 \end{bmatrix}, \quad E = I, \quad A_d = \begin{bmatrix} 0.5 & 0 \\ 0.2 & 0.3 \end{bmatrix}, \\ N_A &= \begin{bmatrix} 0.1 & 0 \\ 0.1 & 0.2 \end{bmatrix}, \quad N_{A_d} = \begin{bmatrix} -0.1 & 0 \\ 0.3 & 0.3 \end{bmatrix}, \quad N_E = \begin{bmatrix} 0.4 & 0 \\ -0.01 & 0.4 \end{bmatrix}, \\ N_{E_d} &= \begin{bmatrix} 0.21 & 0 \\ 0.1 & -0.1 \end{bmatrix}, \quad h(t) = 0.1 \sin t. \end{aligned} \quad (6.1)$$

We select matrix $K = \begin{bmatrix} -11.3000 & -1.2000 \\ -2.0000 & -12.4000 \end{bmatrix}$. Using Matlab LMI control toolbox to solve the LMIs (4.1)–(4.3), we obtain the following:

$$\begin{aligned} X &= \begin{bmatrix} 0.1752 & -0.0038 \\ -0.0038 & 0.1985 \end{bmatrix}, \quad Q_1 = \begin{bmatrix} 1.1255 & -0.0186 \\ -0.0186 & 1.2138 \end{bmatrix}, \quad Q_2 = \begin{bmatrix} 1.0613 & -0.0605 \\ -0.0605 & 1.2145 \end{bmatrix}, \\ T_1 &= \begin{bmatrix} 1.1670 & 0.0001 \\ 0.0001 & 1.1623 \end{bmatrix}, \quad T_2 = \begin{bmatrix} 1.1661 & -0.0007 \\ -0.0007 & 1.1652 \end{bmatrix}, \quad T_3 = \begin{bmatrix} 1.1670 & 0.0001 \\ 0.0001 & 1.1623 \end{bmatrix}, \\ T_4 &= \begin{bmatrix} 1.1647 & 0.0025 \\ 0.0025 & 1.1700 \end{bmatrix}, \quad T_5 = \begin{bmatrix} 1.1670 & 0.0001 \\ 0.0001 & 1.1623 \end{bmatrix}, \quad T_6 = \begin{bmatrix} 1.1580 & -0.0046 \\ -0.0046 & 1.1705 \end{bmatrix}. \end{aligned} \quad (6.2)$$

7. Conclusions

In this paper, we have investigated the sliding mode control problem for uncertain stochastic neutral systems with multiple delays. The stability criteria are expressed by means of LMIs, which can be readily tested by some standard numerical packages. Therefore, the developed result is practical.

Acknowledgments

This work is supported in part by National Science Foundation of China (60474031), NCET (04-0383), National 973 Key Fundamental Research Program (2002cb312200-3), and Australia-China Special Fund for Scientific and Technological Cooperation.

References

- [1] M. S. Mahmoud, *Robust Control and Filtering for Time-Delay Systems*, vol. 5 of *Control Engineering*, Marcel Dekker, New York, NY, USA, 2000.
- [2] J. Sun, "Delay-dependent stability criteria for time-delay chaotic systems via time-delay feedback control," *Chaos, Solitons & Fractals*, vol. 21, no. 1, pp. 143–150, 2004.
- [3] J. Cao, "Global stability conditions for delayed CNNs," *IEEE Transactions on Circuits and Systems I*, vol. 48, no. 11, pp. 1330–1333, 2001.
- [4] K. Zhang, "Stability analysis of linear neutral systems with multiple time delays," *Mathematical Problems in Engineering*, vol. 2005, no. 2, pp. 175–183, 2005.
- [5] J. Cao and J. Wang, "Delay-dependent robust stability of uncertain nonlinear systems with time delay," *Applied Mathematics and Computation*, vol. 154, no. 1, pp. 289–297, 2004.
- [6] F. Ren and J. Cao, "Novel α -stability criterion of linear systems with multiple time delays," *Applied Mathematics and Computation*, vol. 181, no. 1, pp. 282–290, 2006.
- [7] E.-K. Boukas, *Stochastic Hybrid Systems: Analysis and Design*, Birkhäuser, Boston, Mass, USA, 2005.
- [8] D. Ya. Khusainov, "Investigation of interval stability of linear systems of neutral type of Lyapunov function method," *Journal of Applied Mathematics and Stochastic Analysis*, vol. 15, no. 1, pp. 71–81, 2002.
- [9] H. Li, H.-B. Li, and S.-M. Zhong, "Stability of neutral type descriptor system with mixed delays," *Chaos, Solitons & Fractals*, vol. 33, no. 5, pp. 1796–1800, 2007.
- [10] M. S. Mahmoud and L. Xie, "Passivity analysis and synthesis for uncertain time-delay systems," *Mathematical Problems in Engineering*, vol. 7, no. 5, pp. 455–484, 2001.
- [11] B. Lee and J. G. Lee, "Robust stability and stabilization of linear delayed systems with structured uncertainty," *Automatica*, vol. 35, no. 6, pp. 1149–1154, 1999.
- [12] W. Yu and J. Cao, "Robust control of uncertain stochastic recurrent neural networks with time-varying delay," *Neural Processing Letters*, vol. 26, no. 2, pp. 101–119, 2007.
- [13] C. Edwards and S. K. Spurgeon, *Sliding Mode Control: Theory and Applications*, Taylor & Francis, New York, NY, USA, 1998.
- [14] Y. Niu, D. W. C. Ho, and J. Lam, "Robust integral sliding mode control for uncertain stochastic systems with time-varying delay," *Automatica*, vol. 41, no. 5, pp. 873–880, 2005.
- [15] L. Boutat-Baddas, J. P. Barbot, D. Boutat, and R. Tauleigne, "Sliding mode observers and observability singularity in chaotic synchronization," *Mathematical Problems in Engineering*, vol. 2004, no. 1, pp. 11–31, 2004.

Research Article

Performance of Composite Implicit Time Integration Scheme for Nonlinear Dynamic Analysis

William Taylor Matias Silva and Luciano Mendes Bezerra

Department of Civil Engineering, University of Brasília, 70910-900 Brasília, Brazil

Correspondence should be addressed to William Taylor Matias Silva, taylor@unb.br

Received 26 February 2008; Accepted 12 May 2008

Recommended by Paulo Gonçalves

This paper presents a simple implicit time integration scheme for transient response solution of structures under large deformations and long-time durations. The authors focus on a practical method using implicit time integration scheme applied to structural dynamic analyses in which the widely used Newmark time integration procedure is unstable, and not energy-momentum conserving. In this integration scheme, the time step is divided in two substeps. For too large time steps, the method is stable but shows excessive numerical dissipation. The influence of different substep sizes on the numerical dissipation of the method is studied throughout three practical examples. The method shows good performance and may be considered good for nonlinear transient response of structures.

Copyright © 2008 W. T. Matias Silva and L. Mendes Bezerra. This is an open access article distributed under the Creative Commons Attribution License, which permits unrestricted use, distribution, and reproduction in any medium, provided the original work is properly cited.

1. Introduction

In the last four decades, the computational mechanics community has accomplished many researches trying to propose effective methods for nonlinear dynamic analysis in the framework of the finite element method. For fast transient analyses, for example, impact problems, explicit methods are largely used. However, for methods conditionally stable, very small time steps are required to get reasonable solutions. For transient analyses of long-time duration, as in vibration problems of structural systems, the implicit methods are more effective. According to Bathe [1], the first implicit integration procedures used are Houbolt, Newmark, and Wilson- θ . Among these methods, the Newmark method and its particular case, the trapezoidal rule, became very popular and effective for linear dynamic analysis of practical problems. The trapezoidal rule scheme is the most effective one because it is a second-order method and uses single time step. However, in nonlinear dynamic analysis, the trapezoidal rule becomes considerably unstable. Such instability is due to the pathological growth of the

total potential energy and angular momentum. The trapezoidal rule integration scheme does not guarantee the conservation of the energy-momentum along the time duration. To overcome this adverse characteristic, many implicit algorithms were additionally proposed based on the following ideas explained by Kuhl and Crisfield in [2]: (a) numeric dissipation [3]; (b) conservation of energy-momentum throughout the use of Lagrange multipliers [4]; and (c) imposition, in the algorithm, of energy-momentum conservation [5].

The present work analyzes the application of the trapezoidal rule to nonlinear dynamic analyses. To keep the conservation of the energy-momentum, the trapezoidal rule is combined to the three-point backward Euler method. This combination is very much employed in numerical procedures to solve ordinary and partial differential equations (o.d.e.s and p.d.e.s) [6]. Bank et al. [7] use this combination to solve first-order o.d.e.s to simulate the behavior of silicon devices and circuits. Recently, Bathe [8], Bathe and Baig [9] utilized these mixed algorithms to get solutions of second-order p.d.e.s describing the dynamic equilibrium of structural systems. They obtained transient responses for beams and plates discretizing them with solid 2D finite elements. The beams and plates studied by such authors were subjected to large translations and rotations due to rigid-body motions. In the next sections, the coupling of the trapezoidal rule and the three-point backward Euler method is explained in details, and the numerical dissipation is studied in front of different substeps.

2. The implicit-composed algorithm

The equation of motion of a deformable body discretized by the finite element method may be expressed by the following matricial equation:

$$M\ddot{u} + C\dot{u} + f(u, t) = p(t), \quad (2.1)$$

where M is the mass matrix, C is the damping matrix, f is the vector of internal forces, and $p(t)$ is the vector of external forces. Moreover, \ddot{u} , \dot{u} , and u are, respectively, the vectors of acceleration, velocity, and displacement. We assume that M and C are constant matrices and we observe that (2.1) is a nonlinear equation because the internal force vector f is a function of the displacement vector u . Vectors and vector components are hereafter written with the same notation without loss of meaning. In general, time integration algorithms to solve (2.1) are formulated throughout the finite difference schemes and such schemes show numerical dissipation. In computational mechanics, numerical dissipation means an unexpected lost of energy in the numerical solution. This dissipation property may be good in getting better numerical stabilization for such integration schemes. The implicit-composed scheme divides the time step in two substeps. In the first substep, the trapezoidal rule is applied while in the second substep, we make use of the three-point backward Euler method. As the application of the algorithm aims to nonlinear analyses, it is necessary to establish an incremental-iterative strategy to get the final solution. In this work, the Newton-Raphson method, in the iterative phase, is used to dissipate the residual forces. The equation of motion may be written as a function of the displacements, developed in a Taylor's series up to the first-order terms, and an incremental-iterative strategy is established for the time-step dynamic analysis.

3. First substep

At first, it is assumed that the solution of the equation of motion is known at time t_n and we wish to get a solution at time t_{n+1} , such that $t_{n+1} = t_n + \Delta t$. Consider $t_{n+\gamma} = t_n + \gamma\Delta t$ as

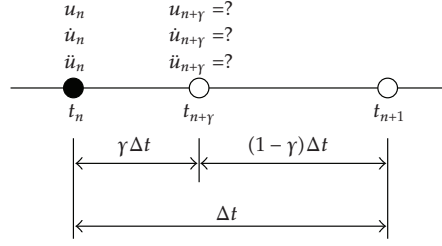


Figure 1: Generalized substep sizes.

a time instance between t_n and t_{n+1} , with $\gamma \in (0, 1)$ according to Figure 1. Applying now the trapezoidal rule over the time step, $\gamma\Delta t$, we can get the velocities and displacements for the time $t_{n+\gamma}$, by means of the following finite difference equations, respectively:

$$\dot{u}_{n+\gamma} = \dot{u}_n + \frac{\ddot{u}_n + \ddot{u}_{n+\gamma}}{2} \gamma \Delta t, \quad (3.1)$$

$$u_{n+\gamma} = u_n + \frac{\dot{u}_n + \dot{u}_{n+\gamma}}{2} \gamma \Delta t. \quad (3.2)$$

Substituting (3.1) into (3.2), we obtain

$$u_{n+\gamma} = u_{n+\gamma}^* + \frac{\gamma^2 \Delta t^2}{4} \ddot{u}_{n+\gamma} \quad (3.3)$$

with

$$u_{n+\gamma}^* = u_n + \gamma \Delta t \dot{u}_n + \frac{\gamma^2 \Delta t^2}{4} \ddot{u}_n. \quad (3.4)$$

On the other hand, (3.1) may be rewritten as

$$\dot{u}_{n+\gamma} = \dot{u}_{n+\gamma}^* + \frac{\gamma \Delta t}{2} \ddot{u}_{n+\gamma} \quad (3.5)$$

with

$$\dot{u}_{n+\gamma}^* = \dot{u}_n + \frac{\gamma \Delta t}{2} \ddot{u}_n. \quad (3.6)$$

Therefore, using (3.3) and (3.5), the accelerations and velocities may be obtained as

$$\ddot{u}_{n+\gamma} = \frac{4}{\gamma^2 \Delta t^2} (u_{n+\gamma} - u_{n+\gamma}^*), \quad (3.7)$$

$$\dot{u}_{n+\gamma} = \dot{u}_{n+\gamma}^* + \frac{2}{\gamma \Delta t} (u_{n+\gamma} - u_{n+\gamma}^*). \quad (3.8)$$

The equation of motion (2.1) at time $t + \gamma \Delta t$ may be rewritten as

$$M \ddot{u}_{n+\gamma} + C \dot{u}_{n+\gamma} + f_{n+\gamma}(u_{n+\gamma}) = p_{n+\gamma}. \quad (3.9)$$

With (3.7), (3.8), and (3.9), the residual force vector $r_{n+\gamma}$ is defined as

$$r_{n+\gamma} = \frac{4}{\gamma^2 \Delta t^2} M(u_{n+\gamma} - u_{n+\gamma}^*) + C \left[\dot{u}_{n+\gamma}^* + \frac{2}{\gamma \Delta t} (u_{n+\gamma} - u_{n+\gamma}^*) \right] + f_{n+\gamma} - p_{n+\gamma}. \quad (3.10)$$

Expanding the resulting equation (3.10) into a Taylor's series as a function of the displacements $u_{n+\lambda}$ and considering only the first-order terms, we can get

$$\begin{aligned} & \left(K_{n+\gamma}^i + \frac{4}{\gamma^2 \Delta t^2} M + \frac{2}{\gamma \Delta t} C \right) \Delta u_{n+\gamma}^{i+1} \\ & = P_{n+\gamma} - \left\{ f_{n+\gamma}^i + M \left[\frac{4}{\gamma^2 \Delta t^2} (u_{n+\gamma}^i - u_{n+\gamma}^*) \right] + C \left[\dot{u}_{n+\gamma}^* + \frac{2}{\gamma \Delta t} (u_{n+\gamma}^i - u_{n+\gamma}^*) \right] \right\} \end{aligned} \quad (3.11)$$

with $u_{n+\gamma}^{i+1} = u_{n+\gamma}^i + \Delta u_{n+\gamma}^{i+1}$ and $K_{n+\gamma}^i = \partial f_{n+\gamma}^i / \partial u_{n+\gamma}^i$ being the consistent tangent stiffness matrix at the configuration corresponding to the displacements $u_{n+\gamma}^i$.

Once the displacements are determined, the accelerations and velocities may be obtained by means of (3.7) and (3.8), respectively. For more details, see the incremental-iterative flow diagram described in Figure 2.

4. Second substep

Let the derivative [6] of a continuous function g at time $t + \Delta t$ be written in terms of the derivatives of the function g at times t , $t + \gamma \Delta t$ and $t + \Delta t$ as

$$\dot{g}_{n+1} = c_1 \dot{g}_n + c_2 \dot{g}_{n+\gamma} + c_3 \dot{g}_{n+1}. \quad (4.1)$$

In this case, the constants [6] c_1 , c_2 , and c_3 may be expressed as

$$c_1 = \frac{(1-\gamma)}{\gamma \Delta t}; \quad c_2 = \frac{-1}{(1-\gamma)\gamma \Delta t}; \quad c_3 = \frac{(2-\gamma)}{(1-\gamma)\Delta t}. \quad (4.2)$$

Thus, the velocities as functions of the displacements, and the accelerations as functions of velocities at time $t + \Delta t$ may be determined by the following equations in the same order:

$$\begin{aligned} \dot{u}_{n+1} &= c_1 \dot{u}_n + c_2 \dot{u}_{n+\gamma} + c_3 \dot{u}_{n+1}, \\ \ddot{u}_{n+1} &= c_1 \ddot{u}_n + c_2 \ddot{u}_{n+\gamma} + c_3 \ddot{u}_{n+1}. \end{aligned} \quad (4.3)$$

Figure 3 illustrates the three-point Backward Euler method in which the quantities at t_{n+1} are calculated from the values at t_n and $t_{n+\gamma}$. These equations may be rewritten as

$$\dot{u}_{n+1} = \dot{u}_{n+\gamma}^* + c_3 \dot{u}_{n+1}, \quad (4.4)$$

$$\ddot{u}_{n+1} = \ddot{u}_{n+\gamma}^* + c_3 \ddot{u}_{n+1} \quad (4.5)$$

with

$$\dot{u}_{n+1}^* = c_1 \dot{u}_n + c_2 \dot{u}_{n+\gamma}, \quad (4.6)$$

$$\ddot{u}_{n+1}^* = c_1 \ddot{u}_n + c_2 \ddot{u}_{n+\gamma}.$$

Substituting (4.4) into (4.5), we obtain

$$\ddot{u}_{n+1} = \ddot{u}_{n+1}^* + c_3 \ddot{u}_{n+1}^* + c_3^2 \ddot{u}_{n+1}. \quad (4.7)$$

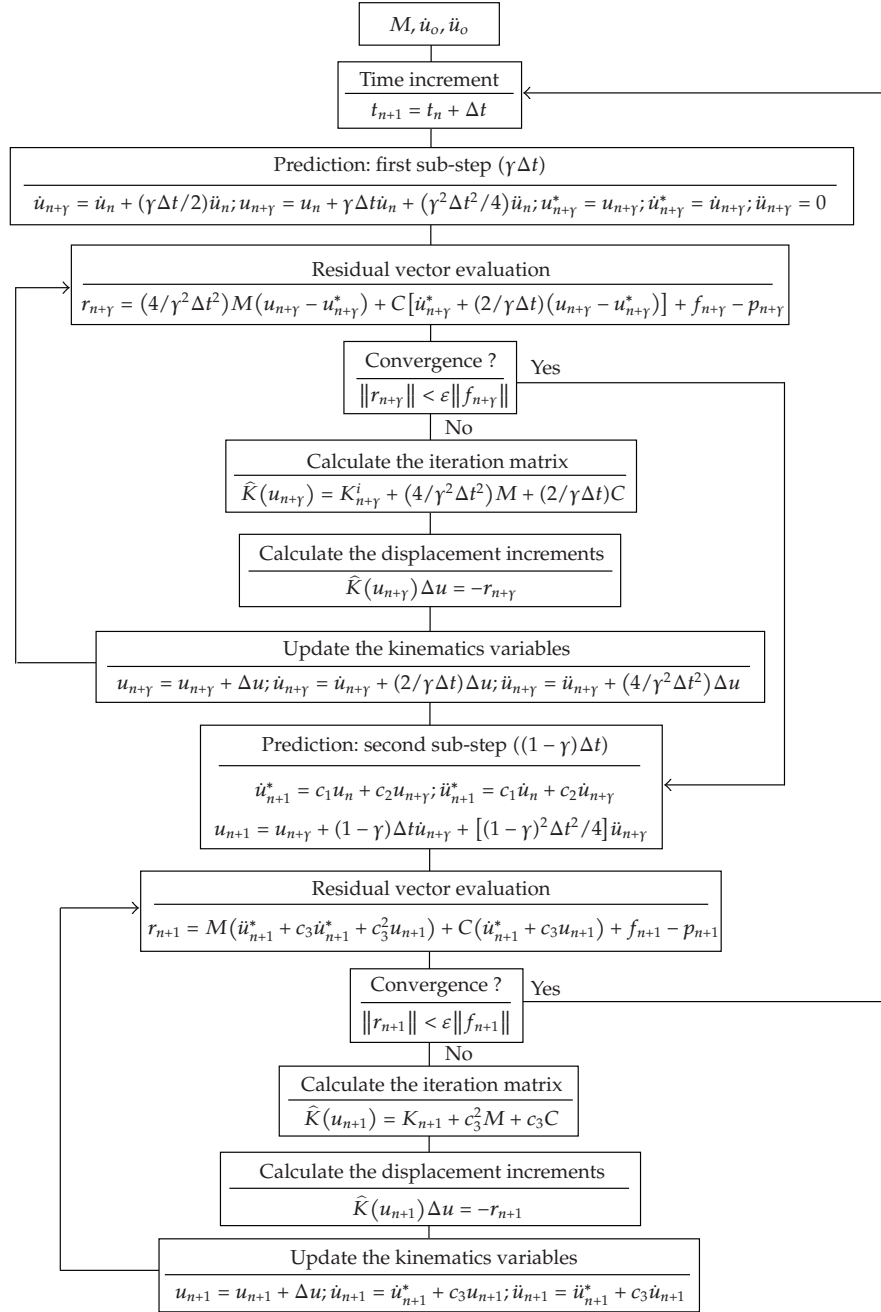


Figure 2: Incremental-iterative scheme of the implicit-composed algorithm.

Equation (2.1) at time $t + \Delta t$ may be rewritten as

$$M\ddot{u}_{n+1} + C\dot{u}_{n+1} + f_{n+1}(u_{n+1}) = P_{n+1}. \quad (4.8)$$

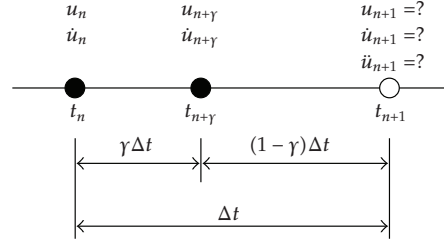


Figure 3: Three-point backward Euler method.

Putting (4.4) and (4.5) into (4.8), the residual force vector is defined as

$$r_{n+1} = M(\ddot{u}_{n+1}^* + c_3 \dot{u}_{n+1}^* + c_3^2 u_{n+1}) + C(\dot{u}_{n+1}^* + c_3 u_{n+1}) + f_{n+1} - p_{n+1}. \quad (4.9)$$

Expanding the resulting equation (4.9) in a Taylor's series up to the first-order terms, as a function of the displacements u_{n+1} , we obtain

$$(K_{n+1}^i + c_3^2 M + c_3 C) \Delta u_{n+1}^{i+1} = P_{n+1} - \{f_{n+1}^i + M(\ddot{u}_{n+1}^* + c_3 \dot{u}_{n+1}^* + c_3^2 u_{n+1}) + C(\dot{u}_{n+1}^* + c_3 u_{n+1})\} \quad (4.10)$$

with $u_{n+1}^{i+1} = u_{n+1}^i + \Delta u_{n+1}^{i+1}$. The tangent stiffness matrix $K_{n+1}^i = \partial f_{n+1}^i / \partial u_{n+1}^i$ and the internal forces f_{n+1}^i are obtained in a consistent way at the configuration corresponding to the displacements u_{n+1}^i . Once the displacements are determined, the velocities and accelerations may be calculated according to (4.4) and (4.5), respectively. For more details, examine the incremental-iterative flow diagram represented in Figure 2. In [8, 9], the prediction displacement adopted in the first iteration of the second substep is not clear. In the present paper, the trapezoidal rule is employed to obtain the prediction displacement as

$$u_{n+1} = u_{n+\gamma} + (1-\gamma)\Delta t \dot{u}_{n+\gamma} + \frac{(1-\gamma)^2 \Delta t^2}{4} \ddot{u}_{n+\gamma}. \quad (4.11)$$

In short, the method has the following main characteristics: (a) it has no additional variables, like Lagrange multipliers, are used; (b) it is suitable to elastic and inelastic analyses; (c) it has symmetry of the tangent stiffness matrix.

5. Numerical examples

In the following examples, one finite element in 2D space representing a biarticulated bar is used. The internal forces' vector and the stiffness matrix of such finite element are obtained from a total Lagrangian formulation. For more details of such formulation, see [10]. The mass matrix in the following examples considers the mass of the bar element as massless and lumped masses concentrated at the two end nodes.

To find the transient response, the incremental iterative scheme illustrated in Figure 2 is used with a convergence tolerance of 10^{-5} on the norm of the residual forces. The mid-point time step varies according to different values $\gamma = 0.4, 0.45, 0.5, 0.55, 0.6$. The objective here is to exam the performance of the implicit-composed algorithm described in Section 2

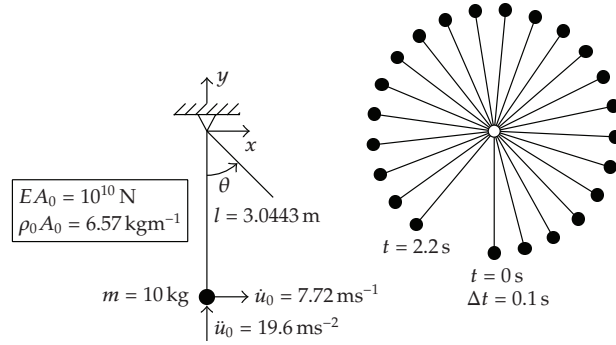


Figure 4: Rigid pendulum. Data and initial conditions.

for varying γ and when different time step is adopted for long-time duration. With this in mind, it is important to analyze if the algorithm presents the following undesirable aspects: (1) excessive errors in the period and in the amplitude of the transient response, (2) strong growth of the total potential energy and the angular momentum, (3) strong decay of the total potential energy and the angular momentum, and (4) lack of convergence during the iterative process.

5.1. Rigid pendulum

Among other authors, Crisfield and Shi [11], Kuhl and Crisfield [2] and Bathe [8] analyzed this example. The geometrical and physical characteristics of the rigid pendulum, the initial conditions, the boundary conditions and other data of the problem are in Figure 4. The rigid pendulum was discretized with one biarticulated finite element bar in 2D space with a very high-axial stiffness. The pendulum has two degrees of freedom restrained and two degrees of freedom released.

The rigid pendulum has an axial stiffness of $EA = 10^{10}$ N. The pendulum displacement is treated as a rigid body rotation around a fixed axis and with a constant angular velocity, where $\dot{\theta} = \omega_o$, $\dot{u}_o = \dot{\theta}l$ and $\ddot{u}_o = \dot{\theta}^2 l = \dot{u}_o^2 / l$. Consider also the energy conservation, $m\dot{u}_o^2/2 = mgl$. Therefore, the initial velocity is given by $\dot{u}_o = \sqrt{2gl} = 7.72$ m/s, and the initial acceleration is $\ddot{u}_o = 2g = 19.6$ m/s². No external force is applied at the free end-node of the pendulum. Therefore, the total potential energy and the angular momentum are kept constants. The value of total potential energy is $\pi_o = m\dot{u}_o^2/2 = 298$ Nm, and the angular momentum $H_o = lm\dot{u}_o$. The period of this pendulum is give by $T = \pi\sqrt{2l/g} = 2.47$ seconds, which corresponds to an angle of 360°, that is, 1 cycle or a complete turnaround in 2.47 seconds.

Three time steps are taken: $\Delta t = 0.01$ second, $\Delta t = 0.1$ second, and $\Delta t = 0.6$ seconds, corresponding to the following ratios to the period $\Delta t/T = 0.004, 0.04$, and 0.24 ; and also to the following angles: 1.45°, 14.5° and 87.3°, respectively. Correspondingly, these angles represent small, moderate, and large rotations. The transient analysis is carried out for a total time duration of 50 seconds which means 20 cycles. Figure 5(a) shows the mass trajectories for the three different time steps adopted; observe the coincidence between the trajectories. Examining Figure 5(b), for $\Delta t = 0.01$ second, the numerical dissipation detected is clearly negligible either for the total potential energy as well as for the angular momentum.

However, for $\Delta t = 0.1$ second, the numerical dissipations along the time are noticeable. On the other hand, for $\Delta t = 0.6$ seconds, an excessive numerical dissipation of the total

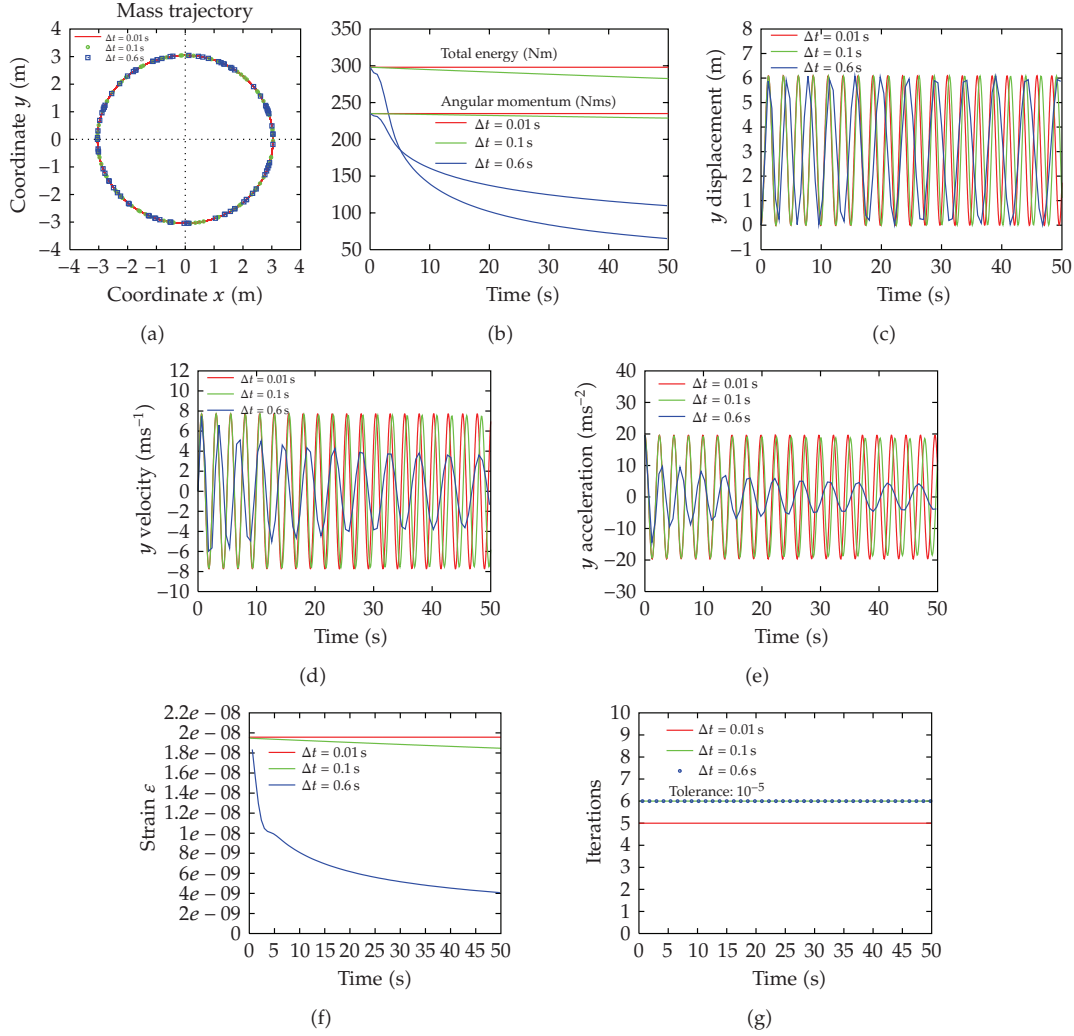


Figure 5: Rigid pendulum. Solution with the implicit-composed algorithm.

potential energy and the angular momentum is observed. Consequently, errors of great magnitude in the period and in the amplitude response may be observed in Figures 5(c), 5(d), and 5(e), respectively, for displacements, velocities, and accelerations. Errors in the periods of the displacements may be noticed for time steps of $\Delta t = 0.1$ second and $\Delta t = 0.6$ seconds from the seventh cycle on. Those errors increase along the next cycles.

With respect to velocity and acceleration, it may be observed that there are errors in the period and in the amplitude for $\Delta t = 0.1$ second, and errors increase from the seventh cycle on. For $\Delta t = 0.6$ seconds, the errors are meaningful and the transient responses are short of precision to represent the physical model under analysis. In Figure 5(f), the magnitude of axial strains do not exceed $\epsilon \leq 2 \times 10^{-8}$ due to the hypothesis of rigid-body motion. Figure 5(g) shows the evolution of the number of iterations along the time necessary to get convergence. It

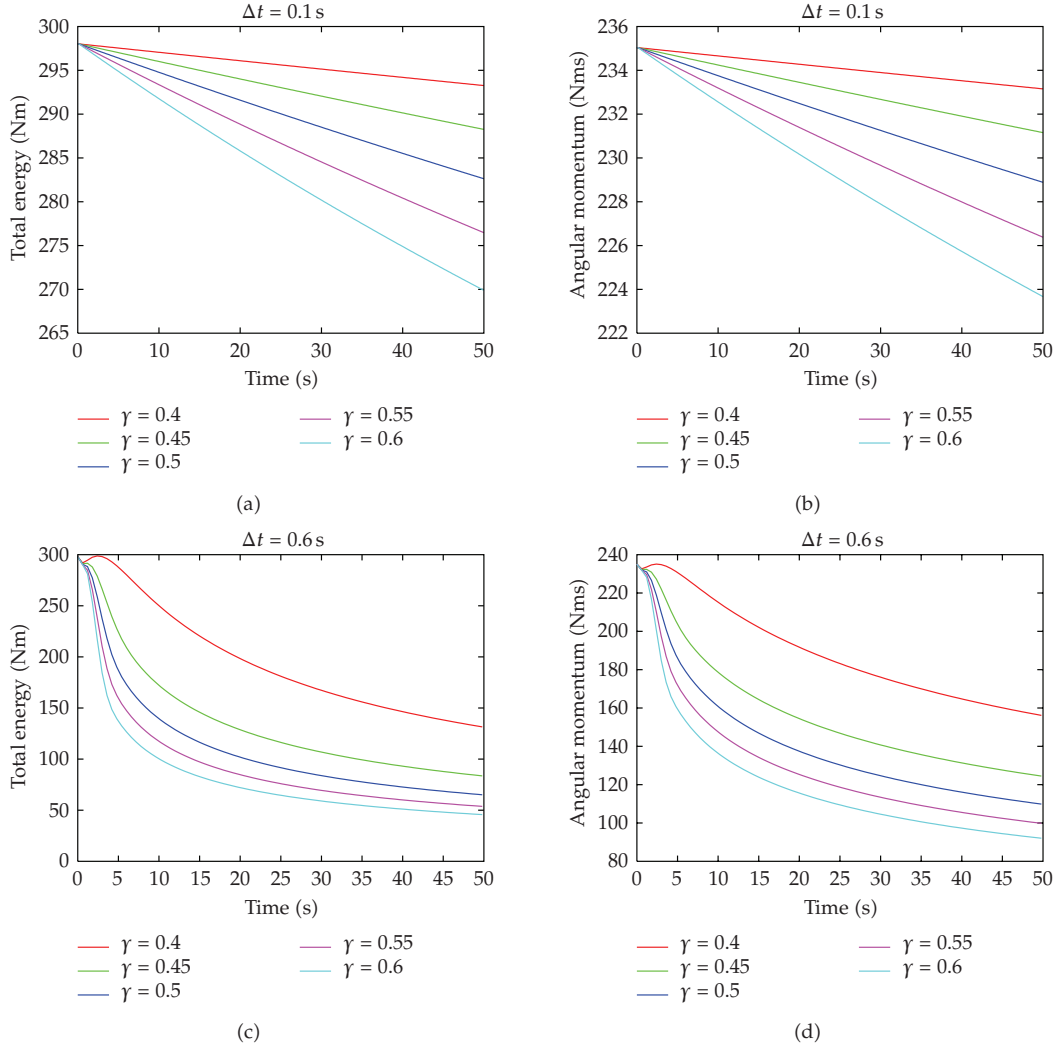


Figure 6: Rigid pendulum. Energy-momentum decaying with different substep sizes.

is important to point out that such figure deals with the sum of the iterations corresponding to the two substeps, that is, $[t_n; t_{n+\gamma}]$ and $[t_{n+\gamma}; t_{n+1}]$ with $\gamma = 0.5$. Finally, it is worth mentioning that the algorithm presented here showed numerical stability even when too large time step is used, for example, for $\Delta t = 0.6$ seconds. In this case, no growth was observed for the energy momentum of the system, as can be seen in Figure 5(b).

To study the influence of the substeps' sizes $\gamma\Delta t$ and $(1 - \gamma)\Delta t$ over the numerical dissipation generated by the method, the analysis of this problem is performed with $\gamma = 0.4$, $\gamma = 0.45$, $\gamma = 0.5$, $\gamma = 0.55$, and $\gamma = 0.6$. For time step $\Delta t = 0.1$ second, the energy-momentum decays are shown in Figures 6(a) and 6(b), respectively. In both figures, it is noticed that the numerical dissipations grow proportional to the γ values. In Table 1, such decays are reported for $t = 50$ seconds and a time step $\Delta t = 0.1$ second. In that table, one can observe how small such

Table 1: Energy-momentum decaying at $t = 50$ seconds with $\Delta t = 0.1$ second.

γ	Total energy	Angular momentum
0.40	1.59%	0.79%
0.45	3.27%	1.64%
0.50	5.16%	2.60%
0.55	7.22%	3.67%
0.60	9.43%	4.82%

Table 2: Energy-momentum decaying at $t = 50$ seconds with $\Delta t = 0.6$ seconds.

γ	Total energy	Angular momentum
0.40	55.86%	33.56%
0.45	71.95%	47.03%
0.50	78.15%	53.25%
0.55	81.96%	57.52%
0.60	84.66%	60.83%

decays are. For time step $\Delta t = 0.6$ seconds, the decays of the total potential energy and of the angular momentum, illustrated in Figures 6(c) and 6(d), also grow with γ . Table 2 shows that such decays are excessive which means that the solution for this case is inaccurate. Even for $\gamma < 0.5$, the numerical dissipation continues high. Therefore, one can conclude the following. (a) For $\gamma < 0.5$, the numerical dissipation is reduced. (b) For $\gamma > 0.5$, the numerical dissipation grows. (c) For $\Delta t = 0.1$ second, there are minor decreases for the potential energy and angular momentum. (d) For $\Delta t = 0.6$ seconds, there are strong decreases for the potential energy and angular momentum.

5.2. System with five spheres connected with massless rigid rods

Crisfield and Shi [11] analyzed this example. Figure 7(a) shows a chain of pinned bars (truss element) that is free to fly in the absence of gravity. Initially, the bars lie horizontally with no velocity in the x -direction but a linear distribution of vertical velocity. Under such conditions, the chain should remain straight moving downwards and rotating at the same time. The system is made of 5 spherical masses connected by massless rigid rods.

The geometrical and physical characteristics of the five connected spheres, the initial conditions, the boundary conditions, and other applicable data are summarized in Figure 7(a). The initial conditions of the system are (a) an angular velocity of $\omega_o = \dot{\theta}_o = 1.0$ rad/s around the axis at pole B (node 5) parallel to the z -axis which is equivalent to a linear distribution of vertical velocities, and (b) a zero-angular acceleration $\alpha_o = \ddot{\theta}_o = 0$.

This system was discretized with four finite elements, biarticulated bar elements in the 2D space. The finite element model has five nodes making a total of 10 degrees of freedom. There are no constraint nodes. Gravitational forces are not considered, and therefore the total potential energy and the angular momentum are kept constant along the time considered for the analysis of this problem, that is, $t = 50$ seconds. Due to the mass symmetry, the center of mass of the system is in middle of the bar length. Therefore, the system of five concentrated masses is subjected to large translations and rotations in the xy -plane. The total potential energy is given by the expression $\pi = 22ml^2\omega_o^2 = 0.11 \times 10^8$ N·cm, and the angular momentum,

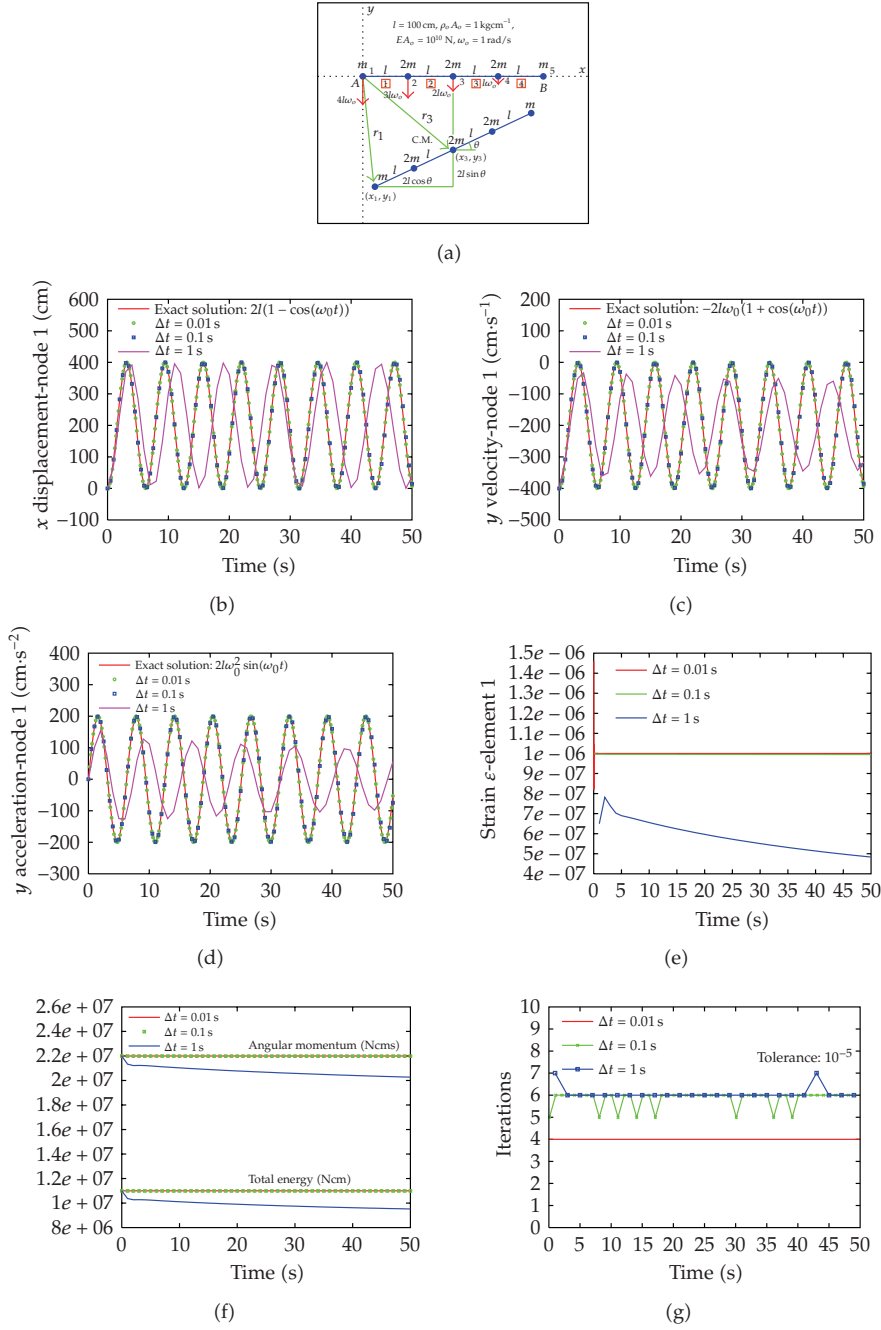


Figure 7: Four-bar-chain. Solution with the implicit-composed algorithm.

with respect to pole B, is $H_o = 44ml^2\omega_o = 0.22 \times 10^8 \text{ kg} \cdot \text{cm}^2/\text{s}$. The components of the displacement, velocity, and acceleration vectors of node 1 (pole A) may be obtained by the

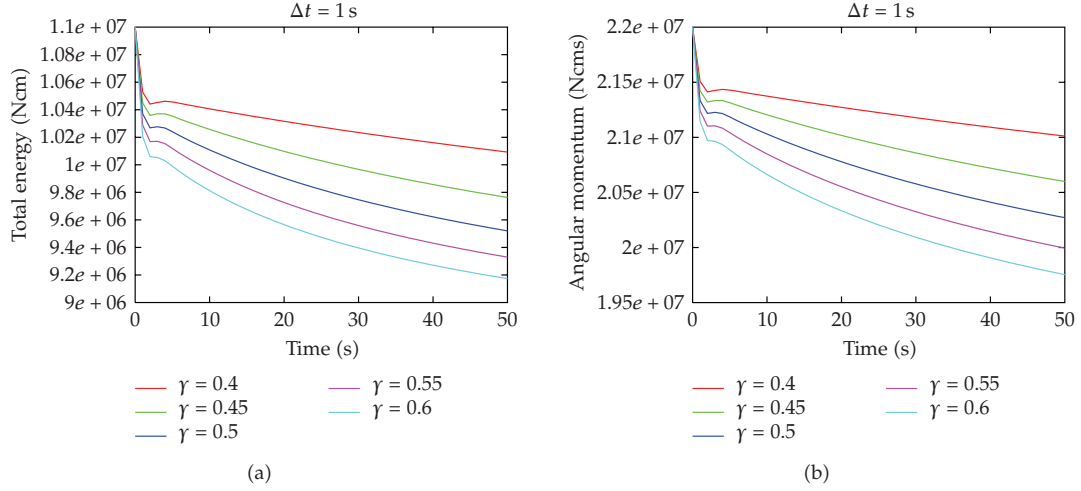


Figure 8: Four-bar-chain. Energy-momentum decaying with different sub-step sizes.

following expression:

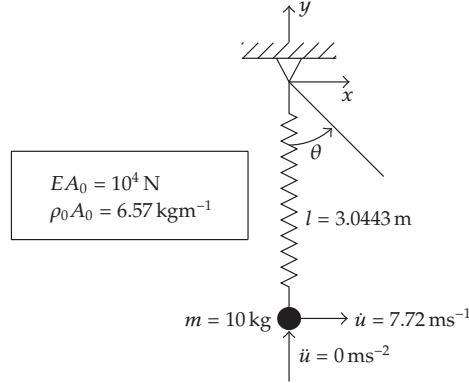
$$\begin{aligned}
 u_{x_1} &= 2l[1 - \cos(\omega_o t)]; & u_{y_1} &= -2l[\omega_o t + \sin(\omega_o t)]; \\
 \dot{u}_{x_1} &= 2l\omega_o[\sin(\omega_o t)]; & \dot{u}_{y_1} &= -2l\omega_o[1 + \cos(\omega_o t)]; \\
 \ddot{u}_{x_1} &= 2l\omega_o^2[\cos(\omega_o t)]; & \ddot{u}_{y_1} &= 2l\omega_o^2[\sin(\omega_o t)].
 \end{aligned} \tag{5.1}$$

The period of this system is given by $T = 2\pi/\omega_o = 6.28$ seconds, which corresponds to a turnaround of 360° . Three time steps are used for this example: $\Delta t = 0.01$ second, $\Delta t = 0.1$ second, and $\Delta t = 1$ second, which correspond to the following ratios to the period, that is, $\Delta t/T = 0.0016, 0.016$, and 0.16 in the same order, to the following angles $0.57^\circ, 5.73^\circ$, and 57.3° . These angles represent small, moderate, and large rotations, respectively.

The transient analysis is carried out for a total time duration of $t = 50$ seconds or, approximately, 8 cycles. Figures 7(b), 7(c), and 7(d) plot as functions of time the x -displacement, the y -velocity, and the y -acceleration of the node-1, respectively. These transient responses are compared to the exact solution in (5.1). For the time steps $\Delta t = 0.01$ second and $\Delta t = 0.1$ second, there is an excellent agreement to the exact solution. Conversely, for time step $\Delta t = 1$ second, significant errors in the period and in the amplitude are observed. Note these errors increase in the subsequent cycles. Consequently, the displacement, velocity, and acceleration obtained for the time step $\Delta t = 1$ second are not suitable to represent the physical problem studied in this example. In Figure 7(e), the magnitude of element-1 axial strains do not exceed $\varepsilon \leq 1.1 \times 10^{-6}$ due to the hypothesis of rigid-body motion. Figure 7(f) shows, for $\Delta t = 0.01$ second and $\Delta t = 0.1$ second, the numerical dissipation of the total potential energy and the angular momentum are insignificant. However, for $\Delta t = 1$ second, an excessive numerical dissipation is observed and grows along the time. Figure 7(g) shows the number of iterations necessary to get convergence in the solution. As a final point, it is remarkable that the algorithm shows numerical stability even for too large time step, for example, $\Delta t = 1$ second. This can be seen in Figure 7(f) noticing that no excessive increase of energy-momentum of the system is observed.

Table 3: Energy-momentum decaying at $t = 50$ seconds with $\Delta t = 1$ second.

γ	Total energy	Angular momentum
0.40	8.24%	4.49%
0.45	11.25%	6.37%
0.50	13.45%	7.86%
0.55	15.19%	9.12%
0.60	16.60%	10.21%

**Figure 9:** Elastic pendulum. Data and initial conditions.

For $\Delta t = 1$ second, the energy-momentum decay, shown in Figures 8(a) and 8(b), increases proportional to γ . Table 3 shows these decays for $t = 50$ seconds. In that table, it can be observed that the values of these decays are less than 17% for the potential energy and less than 11% for the angular momentum.

5.3. Elastic pendulum

This example was analyzed by Kuhl and Crisfield [2] and Bathe [8], among other researchers. The geometrical and physical characteristics of the elastic pendulum, the initial conditions, the boundary conditions, and other data of the problem are in Figure 9. The pendulum was discretized with one biarticulated 2D finite element bar which has two degrees of freedom restrained and two degrees of freedom released. An axial stiffness $EA = 10^4 \text{ N}$ is assumed. A nonzero initial velocity is considered. No gravitational force is assumed to act, and therefore no external force is applied at the free end-node of the pendulum. Therefore, the total potential energy and the angular momentum are kept constants along the time. The potential energy is $\pi_o = m\dot{u}_o^2/2 = 298 \text{ N}\cdot\text{m}$. The angular momentum is $H_o = l m \dot{u}_o = 235 \text{ kg}\cdot\text{cm}^2/\text{s}$. In this example, the period is given by $T = \pi\sqrt{2l/g} = 2.47$ seconds, which corresponds to 1 cycle or a complete turnaround of the pendulum in 2.47 seconds. In addition, Due to the axial elastic behavior of the pendulum bar, other oscillation frequency exists, a high axial frequency corresponding to $T = 0.28$ seconds. To capture this axial frequency, two time steps are adopted: $\Delta t = 0.01$ second and $\Delta t = 0.05$ seconds which correspond to the following ratios to the period; that is, $\Delta t/T = 0.036$ and 0.18 , respectively.

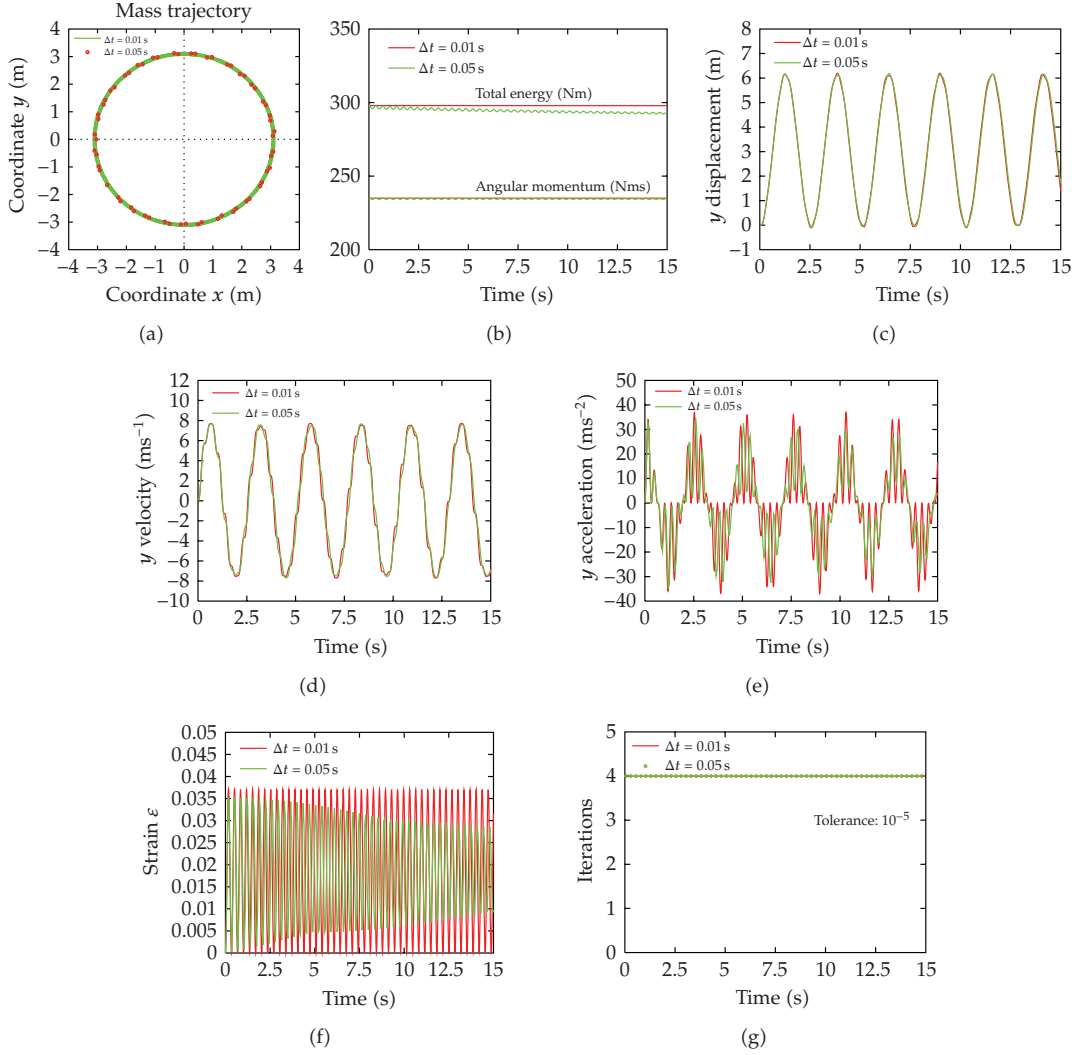


Figure 10: Elastic pendulum. Solution with the implicit-composed algorithm.

Although, in this case, there are oscillations in high frequencies, no sudden growth is observed in the amplitude of the axial oscillations and in the energy-momentum of the pendulum system. These can be demonstrated in Figures 10(b) and 10(f), respectively. Figure 10(a) shows the pendulum trajectories. The complete agreement of the trajectories is clear. Examining Figure 10(b), for $\Delta t = 0.01$ second, the numerical dissipation detected is minimal either for the total potential energy as well as for the angular momentum. However, for $\Delta t = 0.05$ seconds, there are small numerical dissipations increasing along the time. Figures 10(c) and 10(d) show the displacement and velocity of node 2 in the y -direction, respectively. In these figures, for both time steps used, the transient responses are almost coincident. However, in Figure 10(e), significant errors in the amplitude and in the acceleration period are detected.

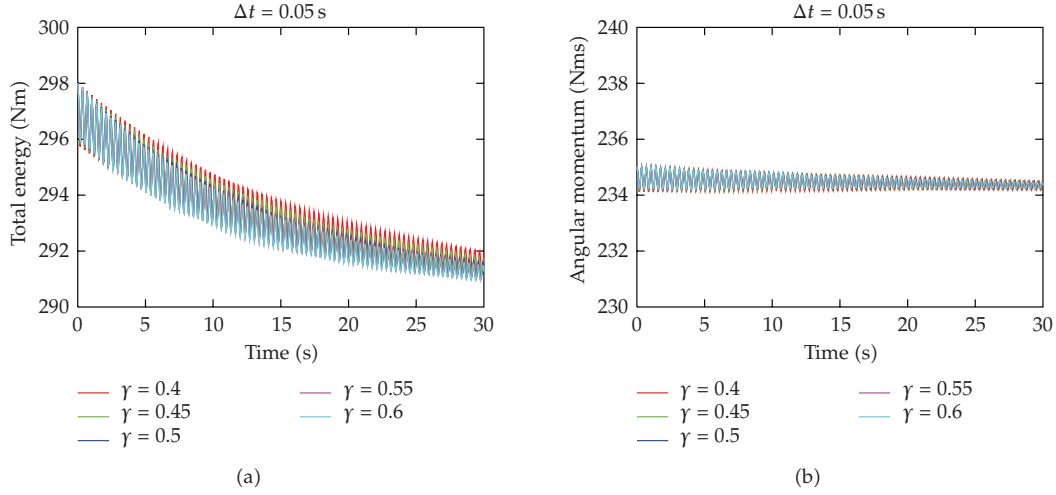


Figure 11: Elastic pendulum. Energy-momentum decaying with different substep sizes.

Table 4: Energy-momentum decaying at $t = 30$ seconds with $\Delta t = 0.05$ seconds.

γ	Total energy	Angular momentum
0.40	2.03%	0.21%
0.45	2.10%	0.22%
0.50	2.19%	0.25%
0.55	2.25%	0.27%
0.60	2.26%	0.27%

Furthermore, for $\Delta t = 0.05$ seconds, Figure 10(f) shows the axial oscillations and depicts the significant errors in the amplitudes due to numerical dissipation. With this large Δt , it is impossible to have a more precise response of the system under high frequency. Finally, Figure 10(g) represents the number of iterations to get convergence in the solutions. For the time step $\Delta t = 0.05$ seconds, the decays of the total potential energy and the angular momentum, shown in Figures 11(a) and 11(b), respectively, are practically the same for different substeps used. In Table 4, these decays are reported for $t = 30$ seconds and it is clear that the decays are very small and almost at the same amount.

6. Concluding remarks

Concerning the performance of the implicit-composed algorithm applied to nonlinear dynamic analysis, the following conclusions may be taken. (a) The algorithm is easy to implement in a computer program. (b) The mathematical formulation of the algorithm is very simple. (c) The algorithm is effective to deal with large translations and rotations due to rigid-body motions. (d) For time steps Δt with ratios to the period $\Delta t/T \leq 0.1$, the algorithm presents an insignificant numerical dissipation, however, for $\Delta t/T > 0.1$, an increasing numerical dissipation is observed. (e) The computational cost of the algorithm is twice greater than the computational cost of the trapezoidal rule due to the two iterative cycles needed in each time step. (f) The algorithm preserves the energy-momentum without the need of

Lagrange multipliers or without any imposition in the algorithm for energy-momentum conservation. (g) The algorithm allows the user to work with symmetric matrices. (h) The method is applicable to elastic and inelastic analyses. (i) No additional variables like Lagrange multipliers are used. (j) For too large time step, even with inaccurate solution, the method is stable.

From the view of the authors, the excessive numerical dissipation when using a too large time-step is the major drawback of the present scheme, for applications in nonlinear analyses in practical problems.

References

- [1] K.-J. Bathe, *Finite Element Procedures*, Prentice-Hall, Englewood Cliffs, NJ, USA, 1996.
- [2] D. Kuhl and M. A. Crisfield, "Energy-conserving and decaying algorithms in non-linear structural dynamics," *International Journal for Numerical Methods in Engineering*, vol. 45, no. 5, pp. 569–599, 1999.
- [3] J. Chung and G. M. Hulbert, "A time integration algorithm for structural dynamics with improved numerical dissipation: the generalized- α method," *Journal of Applied Mechanics*, vol. 60, no. 2, pp. 371–375, 1993.
- [4] D. Kuhl and E. Ramm, "Constraint energy momentum algorithm and its application to non-linear dynamics of shells," *Computer Methods in Applied Mechanics and Engineering*, vol. 136, no. 3–4, pp. 293–315, 1996.
- [5] J. C. Simo and N. Tarnow, "The discrete energy-momentum method. Conserving algorithms for nonlinear elastodynamics," *Zeitschrift für Angewandte Mathematik und Physik*, vol. 43, no. 5, pp. 757–792, 1992.
- [6] L. Collatz, *The Numerical Treatment of Differential Equations*, Springer, New York, NY, USA, 3rd edition, 1966.
- [7] R. E. Bank, W. M. Coughran Jr., W. Fichtner, E. H. Grosse, D. J. Rose, and R. K. Smith, "Transient simulation of silicon devices and circuits," *IEEE Transactions on Computer-Aided Design of Integrated Circuits and Systems*, vol. 4, no. 4, pp. 436–451, 1985.
- [8] K.-J. Bathe, "Conserving energy and momentum in nonlinear dynamics: a simple implicit time integration scheme," *Computers & Structures*, vol. 85, no. 7–8, pp. 437–445, 2007.
- [9] K.-J. Bathe and M. M. I. Baig, "On a composite implicit time integration procedure for nonlinear dynamics," *Computers & Structures*, vol. 83, no. 31–32, pp. 2513–2524, 2005.
- [10] W. T. Matias Silva, "Aplicaciones de algoritmos que conservan la energia-momentum en dinámica no-lineal," in *Congreso de Métodos Numéricos en Ingeniería*, pp. 1–20, Granada, Spain, July 2005.
- [11] M. A. Crisfield and J. Shi, "A co-rotational element/time-integration strategy for nonlinear dynamics," *International Journal for Numerical Methods in Engineering*, vol. 37, no. 11, pp. 1897–1913, 1994.

Research Article

Identification of Stochastic Loads Applied to a Nonlinear Dynamical System Using an Uncertain Computational Model

C. Soize¹ and A. Batou^{1,2}

¹ *Université Paris-Est, Laboratoire Modélisation et Simulation Multi Echelle, MSME FRE3160 CNRS, 5 bd Descartes, 77454 Marne-la-Vallée, France*

² *R&D Department Analyse Mécanique et Acoustique, EDF, 1 avenue du Général de Gaulle, 92140 Clamart Cedex, France*

Correspondence should be addressed to C. Soize, christian.soize@univ-paris-est.fr

Received 6 April 2008; Accepted 4 June 2008

Recommended by Jose Balthazar

This paper deals with the identification of stochastic loads applied to a nonlinear dynamical system for which a few experimental responses are available using an uncertain computational model. Uncertainties are induced by the use of a simplified computational model to predict the responses of the real system. A nonparametric probabilistic approach of both parameter uncertainties and model uncertainties is implemented in the simplified computational model in order to take into account uncertainties. The level of uncertainties is identified using the maximum likelihood method. The identified stochastic simplified computational model which is obtained is then used to perform the identification of the stochastic loads applied to the real nonlinear dynamical system. A numerical validation of the complete methodology is presented.

Copyright © 2008 C. Soize and A. Batou. This is an open access article distributed under the Creative Commons Attribution License, which permits unrestricted use, distribution, and reproduction in any medium, provided the original work is properly cited.

1. Introduction

This paper is devoted to the identification of a stochastic load applied to a nonlinear dynamical system for which a few measurements of its responses are available and for which an uncertain simplified computational model is used. In the dynamical system, the uncertainties are taken into account in the context of the probability theory. Consequently, the uncertain simplified computational model is in fact a stochastic simplified computational model for which the input is a stochastic process (stochastic load) and for which the linear operators of the computational model are random. This identification is then performed using the stochastic simplified computational model which allows the responses of the real system to be predicted and, then, the stochastic loads to be identified in minimizing a certain distance between the experimental

responses and the random responses calculated with the stochastic simplified computational model. In fact, the methodology presented is developed in the context of the nonlinear dynamical analysis of tube bundles in pressurized water reactor. The stochastic loads applied to the tubes which have to be identified are then induced by the turbulent flow. Since such a nonlinear dynamical system is very complex, the computational model developed cannot exactly represent the complexity of the system. Consequently, the identification is not performed using a computational model which has the capability to accurately predict the experimental responses but is performed using a simplified computational model containing model errors. In order to perform a robust identification of the stochastic loads with respect to model uncertainties in the nonlinear dynamical computational model, a probabilistic model of uncertainties allowing both parameter uncertainties and model uncertainties to be taken into account is introduced. The responses of the computational model are then random and the randomness is due to the stochastic loads and is due to the stochasticity of the system. In a first step, the probability model of uncertainties in the computational model is identified using the maximum likelihood method. We then deduce a stochastic computational model which allows a robust identification of stochastic loads to be carried out with respect to uncertainties in the nonlinear computational model. The second step is devoted to the stochastic inverse problem consisting in identifying the stochastic loads. From a theoretical and methodological point of view, we then present a complete probabilistic construction and the associated methodology to solve an inverse problem consisting of the identification of a Gaussian stationary stochastic process which is the input of a continuous nonlinear dynamical system with random operators and for which the stochastic output is measured. It should be noted that, if the parametric probabilistic approach is usual to take into account system parameter uncertainties, in the present paper, both the system parameter uncertainties and the model uncertainties are taken into account using a nonparametric probabilistic approach consisting in directly modeling the linear operators of the dynamical system by random operators using the random matrix theory.

Section 2 deals with the construction of the mean computational model. In Section 3, the probabilistic model of the stochastic loads is introduced. Section 4 is devoted to the identification of the stochastic load. The last section presents a numerical validation of the methodology proposed.

2. Mean computational model

Let Ω be the domain of the dynamical system having a nonlinear behavior due to the presence of elastic stops located to several points of the part of the boundary of Ω . The domain Ω is decomposed in two bounded open subdomains of \mathbb{R}^3 : the subdomain Ω^A and the subdomain Ω^B . The subdomain Ω^A is constituted of a three-dimensional linear viscoelastic medium with instantaneous memory and there are elastic stops located at κ points $\mathbf{x}^1, \dots, \mathbf{x}^\kappa$ in the boundary Γ^A of $\partial\Omega^A$. In addition, the subsystem occupying the subdomain Ω^A is fixed on the part Γ_0^A of its boundary $\partial\Omega^A$. The outward unit normal of $\partial\Omega^A$ is denoted by \mathbf{n}^A . The subdomain Ω^B is constituted of a three-dimensional linear viscoelastic medium with instantaneous memory, fixed on the part Γ_0^B of its boundary $\partial\Omega^B$. The outward unit normal of $\partial\Omega^B$ is denoted by \mathbf{n}^B . Consequently, each uncoupled subsystem Ω^A and Ω^B does not have rigid body displacement. These two subsystems are coupled on the common coupling interface Γ_C . One then has $\partial\Omega^A = \Gamma_0^A \cup \Gamma^A \cup \Gamma^C$ and $\partial\Omega^B = \Gamma_0^B \cup \Gamma^B \cup \Gamma^C$. We are interested in constructing the stationary random responses of the nonlinear stochastic dynamical system excited by stationary stochastic

processes. Consequently, we will not introduce the initial conditions and we will assume that the time parameter t belongs to \mathbb{R} .

2.1. Mean boundary value problems

2.1.1. Mean boundary value problems for the linear subsystem Ω^B

Let $\mathbf{x} = (x_1, x_2, x_3)$ be the cartesian coordinates and $\mathbf{u}^B(\mathbf{x}, t)$ be the displacement field for the linear subsystem Ω^B at time t . The external prescribed volumetric and surface forces fields applied to Ω^B and to its boundary Γ^B are denoted by $\mathbf{f}_{\text{vol}}^B(\mathbf{x}, t)$ and $\mathbf{f}_{\text{surf}}^B(\mathbf{x}, t)$. The stress tensor $\sigma^B(\mathbf{x})$ is written as $\sigma_{ij}^B(\mathbf{x}) = a_{ijkh}^B(\mathbf{x})\varepsilon_{kh}^B(\mathbf{u}^B) + b_{ijkh}^B(\mathbf{x})\varepsilon_{kh}^B(\dot{\mathbf{u}}^B)$ where $\varepsilon_{kh}^B(\mathbf{u}^B) = (\partial u_k^B / \partial x_h + \partial u_h^B / \partial x_k) / 2$ is the linearized strain tensor. The fourth-order tensors $a^B(\mathbf{x})$ and $b^B(\mathbf{x})$ verify the usual properties of symmetry and positiveness [1]. Then, the displacement field $\mathbf{u}^B(t)$ verifies, for all $t \in \mathbb{R}$ and for $i = 1, 2, 3$, the mean boundary value problem

$$\begin{aligned} \rho^B \ddot{u}_i^B - \frac{\partial \sigma_{ij}^B}{\partial x_j} &= f_{\text{vol},i}^B \quad \text{in } \Omega^B, \\ \sigma_{ij}^B n_j^B &= f_{\text{surf},i}^B \quad \text{on } \Gamma^B, \\ \sigma_{ij}^B n_j^B &= f_{\text{coupl},i}^B \quad \text{on } \Gamma^C, \\ u_i^B &= 0 \quad \text{on } \Gamma_0^B, \end{aligned} \tag{2.1}$$

in which a dot means the partial time derivative and a double dot means the double partial time derivative, where $\mathbf{f}_{\text{coupl}}^B = (f_{\text{coupl},1}^B, \dots, f_{\text{coupl},3}^B)$ is the forces induced by the subsystem Ω^A on Ω^B via the coupling interface Γ^C . One has used the classical convention for summations over repeated latin indices. The parameter $\rho^B(\mathbf{x})$ is the mass density for the subsystem Ω^B .

2.1.2. Mean boundary value problems for the nonlinear subsystem Ω^A

Let $\mathbf{u}^A(\mathbf{x}, t)$ be the displacement field for the nonlinear subsystem Ω^A at time t . The external prescribed volumetric and surface forces fields applied to Ω^A and to its boundary Γ^A are denoted by $\mathbf{f}_{\text{vol}}^A(\mathbf{x}, t)$ and $\mathbf{f}_{\text{surf}}^A(\mathbf{x}, t)$. Since Ω^A is occupied by a linear viscoelastic material with instantaneous memory, the stress tensor $\sigma^A(\mathbf{x})$ is written as $\sigma_{ij}^A(\mathbf{x}) = a_{ijkh}^A(\mathbf{x})\varepsilon_{kh}^A(\mathbf{u}^A) + b_{ijkh}^A(\mathbf{x})\varepsilon_{kh}^A(\dot{\mathbf{u}}^A)$ where $\varepsilon_{kh}^A(\mathbf{u}^A) = (\partial u_k^A / \partial x_h + \partial u_h^A / \partial x_k) / 2$ is the linearized strain tensor. The fourth-order tensors $a^A(\mathbf{x})$ and $b^A(\mathbf{x})$ verify, as above, the usual properties of symmetry and positiveness. Then, the displacement field $\mathbf{u}^A(t)$ verifies, for all $t \in \mathbb{R}$ and for $i = 1, 2, 3$, the mean boundary value problem

$$\begin{aligned} \rho^A \ddot{u}_i^A - \frac{\partial \sigma_{ij}^A}{\partial x_j} &= f_{\text{vol},i}^A \quad \text{in } \Omega^A, \\ \sigma_{ij}^A n_j^A &= f_{\text{surf},i}^A - \sum_{k=1}^{\kappa} f_i^{\text{NL},k}(\mathbf{u}(\mathbf{x}^k, t)) \delta_0(\mathbf{x} - \mathbf{x}^k) \quad \text{on } \Gamma^A, \\ \sigma_{ij}^A n_j^A &= f_{\text{coupl},i}^A \quad \text{on } \Gamma^C, \\ u_i^A &= 0 \quad \text{on } \Gamma_0^A, \end{aligned} \tag{2.2}$$

in which $\mathbf{f}_{\text{coupl}}^A = (f_{\text{coupl},1}^A, \dots, f_{\text{coupl},3}^A)$ is the forces induced by the subsystem Ω^B on Ω^A via the coupling interface Γ^C . The forces $\mathbf{f}^{\text{NL},k}(\mathbf{u}(\mathbf{x}^k, t))$ represent the actions exerted by the elastic stop located at point \mathbf{x}^k on the subsystem Ω^A and $\delta_0(\mathbf{x} - \mathbf{x}^k)$ is the surface Dirac measure such that, for all continuous function \mathbf{g} defined on Γ^A , one has $\int_{\Gamma^A} \delta_0(\mathbf{x} - \mathbf{x}^k) \mathbf{g}(\mathbf{x}) ds(\mathbf{x}) = \mathbf{g}(\mathbf{x}^k)$. The parameter $\rho^A(\mathbf{x})$ is the mass density for the subsystem Ω^A .

2.1.3. Interface conditions for the coupling of Ω^A with Ω^B

The coupling conditions on Γ^C are written as

$$\begin{aligned} \mathbf{u}^A &= \mathbf{u}^B \quad \text{on } \Gamma^C, \\ \mathbf{f}_{\text{coupl}}^A + \mathbf{f}_{\text{coupl}}^B &= 0 \quad \text{on } \Gamma^C. \end{aligned} \quad (2.3)$$

2.2. Mean finite element model

The mean finite element method [2] is applied to the variational formulation of the boundary value problems defined in Section 2.1.

2.2.1. Mean finite element model for subsystem Ω^B

The \mathbb{R}^{n^B} vector $\mathbb{U}^B(t)$ of the n^B DOF of the subsystem Ω^B is written as $\mathbb{U}^B(t) = (\mathbb{U}_p^B(t), \mathbb{U}_c^B(t))$, where $\mathbb{U}_p^B(t)$ is the $\mathbb{R}^{n_p^B}$ vector of the n_p^B internal DOF and where $\mathbb{U}_c^B(t)$ is the $\mathbb{R}^{n_c^B}$ vector function of the n_c^B coupling DOF on the interface. From (2.1), it can be deduced that the mean finite element model of subsystem Ω^B is written as

$$[\underline{\mathbb{M}}^B] \ddot{\mathbb{U}}^B(t) + [\underline{\mathbb{D}}^B] \dot{\mathbb{U}}^B(t) + [\underline{\mathbb{K}}^B] \mathbb{U}^B(t) = \mathbb{F}^B(t) + \mathbb{F}_{\text{coupl}}^B(t), \quad (2.4)$$

in which $[\underline{\mathbb{M}}^B]$, $[\underline{\mathbb{D}}^B]$, and $[\underline{\mathbb{K}}^B]$ are, respectively, the positive-definite symmetric real positive $(n^B \times n^B)$ mass, damping, and stiffness matrices. The \mathbb{R}^{n^B} vectors $\mathbb{F}^B(t)$ and $\mathbb{F}_{\text{coupl}}^B(t)$ of the external forces and of the coupling forces are written as $\mathbb{F}^B(t) = (\mathbb{F}_p^B(t), 0)$ and $\mathbb{F}_{\text{coupl}}^B(t) = (0, \mathbb{F}_c^B(t))$.

2.2.2. Mean finite element model for subsystem Ω^A

Similarly to Section 2.2.1, the \mathbb{R}^{n^A} vector $\mathbb{U}^A(t)$ of the n^A DOF of the subsystem Ω^A is written as $\mathbb{U}^A(t) = (\mathbb{U}_p^A(t), \mathbb{U}_c^A(t))$, where $\mathbb{U}_p^A(t)$ is the $\mathbb{R}^{n_p^A}$ vector of the n_p^A internal DOF and where $\mathbb{U}_c^A(t)$ is the $\mathbb{R}^{n_c^A}$ -valued function of the n_c^A coupling DOF. From (2.2), it can be deduced that the mean finite element model of subsystem Ω^A is written as

$$[\underline{\mathbb{M}}^A] \ddot{\mathbb{U}}^A(t) + [\underline{\mathbb{D}}^A] \dot{\mathbb{U}}^A(t) + [\underline{\mathbb{K}}^A] \mathbb{U}^A(t) + \mathbb{F}^{\text{NL}}(\mathbb{U}^A(t)) = \mathbb{F}^A(t) + \mathbb{F}_{\text{coupl}}^A(t), \quad (2.5)$$

in which $[\underline{\mathbb{M}}^A]$, $[\underline{\mathbb{D}}^A]$, and $[\underline{\mathbb{K}}^A]$ are, respectively, the positive-definite symmetric real positive $(n^A \times n^A)$ mass, damping, and stiffness matrices. The \mathbb{R}^{n^A} vectors $\mathbb{F}^A(t)$, $\mathbb{F}_{\text{coupl}}^A(t)$, and $\mathbb{F}^{\text{NL}}(\mathbb{U}^A(t))$ of the external forces, of the coupling forces and of the nonlinear forces, are written as $\mathbb{F}^A(t) = (\mathbb{F}_p^A(t), 0)$, $\mathbb{F}_{\text{coupl}}^A(t) = (0, \mathbb{F}_c^A(t))$, and $\mathbb{F}^{\text{NL}}(\mathbb{U}^A(t)) = (\mathbb{F}_p^{\text{NL}}(\mathbb{U}^A(t)), 0)$.

2.2.3. Interface conditions for the coupling of Ω^A with Ω^B

The finite element discretization of the interface conditions defined by (2.3) yields

$$\begin{aligned} \mathbb{U}_c^A(t) &= \mathbb{U}_c^B(t) \quad \text{on } \Gamma^C, \\ \mathbb{F}_{\text{coupl}}^A(t) + \mathbb{F}_{\text{coupl}}^B(t) &= 0 \quad \text{on } \Gamma^C. \end{aligned} \quad (2.6)$$

2.3. Reduced mean matrix model

The continuous linear subsystem Ω^B (linear dynamical subsystem) contains elastic modes in the frequency band of analysis. In addition, the computational model of the continuous linear subsystem Ω^B is uncertain (presence of both the system parameter uncertainties and the model uncertainties). As we have explained in Section 1, these uncertainties are taken into account using the nonparametric approach of uncertainties which requires a reduced matrix order model (see [3–6]). Since we have to represent the effects of this substructure on the nonlinear substructure Ω^A through the coupling interface, it is natural to use the Craig Bampton method [7] in order to reduce the finite element model of subsystem Ω^B . Finally, to reduce the computational cost of the coupled system, subsystem Ω^A is also reduced with the same technique.

2.3.1. Reduced mean matrix model for subsystem Ω^B

The following change of coordinates is introduced:

$$\begin{bmatrix} \mathbb{U}_p^B(t) \\ \mathbb{U}_c^B(t) \end{bmatrix} = [H^B] \begin{bmatrix} \mathbf{y}^B(t) \\ \mathbb{U}_c^B(t) \end{bmatrix}, \quad [H^B] = \begin{bmatrix} [\Phi^B] & [S^B] \\ [0] & [I] \end{bmatrix}, \quad (2.7)$$

in which $[\Phi^B]$ is the $(n_p^B \times N^B)$ real matrix whose columns are the N^B first elastic modes for the subsystem Ω^B with a fixed coupling interface. Those modes $(\phi_1, \dots, \phi_{N^B})$ are associated with the N^B first eigenvalues $0 < \omega_1^2 \leq \dots \leq \omega_{N^B}^2$ such that

$$[\underline{\mathbb{K}}_{pp}^B] \phi^B = \omega^2 [\underline{\mathbb{M}}_{pp}^B] \phi^B, \quad (2.8)$$

where $[\underline{\mathbb{K}}_{pp}^B]$ and $[\underline{\mathbb{M}}_{pp}^B]$ are the internal DOF blocks of the matrices $[\underline{\mathbb{K}}^B]$ and $[\underline{\mathbb{M}}^B]$, where $[S^B] = [\underline{\mathbb{K}}_{pp}^B]^{-1} [\underline{\mathbb{K}}_{pc}^B]$ is an $(n_p^B \times n_c^B)$ matrix, where $[I]$ is the $(n_c^B \times n_c^B)$ unity matrix and where $\mathbf{y}^B(t)$ is an \mathbb{R}^{N^B} -vector. Let $n_q^B = N^B + n_c^B$. Then, the $\mathbb{R}^{n_q^B}$ vector $\mathbf{q}^B(t) = (\mathbf{y}^B(t), \mathbb{U}_c^B(t))$ is a solution of the reduced mean computational model

$$[\underline{\mathbb{M}}^B] \ddot{\mathbf{q}}^B(t) + [\underline{\mathbb{D}}^B] \dot{\mathbf{q}}^B(t) + [\underline{\mathbb{K}}^B] \mathbf{q}^B(t) = [H^B]^T \mathbb{F}^B(t) + [H^B]^T \mathbb{F}_{\text{coupl}}^B(t), \quad (2.9)$$

in which the matrices $[\underline{\mathbb{M}}^B] = [H^B]^T [\underline{\mathbb{M}}^B] [H^B]$, $[\underline{\mathbb{D}}^B] = [H^B]^T [\underline{\mathbb{D}}^B] [H^B]$, and $[\underline{\mathbb{K}}^B] = [H^B]^T [\underline{\mathbb{K}}^B] [H^B]$ are positive-definite symmetric real $(n_q^B \times n_q^B)$ matrices.

2.3.2. Reduced mean matrix model for subsystem Ω^A

Using the same reduction method and introducing the elastic modes of the linear subsystem Ω^A with fixed interface and without elastic stops, the $\mathbb{R}^{n_q^A}$ -vector $\mathbf{q}^A(t) = (\mathbf{y}^A(t), \mathbb{U}_c^A(t))$ verifies the following matrix equation:

$$\begin{aligned} & [\underline{M}^A] \ddot{\mathbf{q}}^A(t) + [\underline{D}^A] \dot{\mathbf{q}}^A(t) + [\underline{K}^A] \mathbf{q}^A(t) + [H^A]^T \mathbb{F}^{\text{NL}}([H^A] \mathbf{q}^A(t)) \\ &= [H^A]^T \mathbb{F}^A(t) + [H^A]^T \mathbb{F}_{\text{coupl}}^A(t), \end{aligned} \quad (2.10)$$

in which the matrices $[\underline{M}^A] = [H^A]^T [\underline{M}^A] [H^A]$, $[\underline{D}^A] = [H^A]^T [\underline{D}^A] [H^A]$, and $[\underline{K}^A] = [H^A]^T [\underline{K}^A] [H^A]$ are positive-definite symmetric real ($n_q^A \times n_q^A$) matrices.

2.3.3. Transient dynamical response of the reduced nonlinear computational model

Let $n_{\mathbb{U}} = n_p^A + n_p^B + n_c$ be the total number of DOF for the nonlinear computational model. The $\mathbb{R}^{n_{\mathbb{U}}}$ -vector $\mathbb{U}(t) = (\mathbb{U}_p^A(t), \mathbb{U}_p^B(t), \mathbb{U}_c(t))$ of the mean nonlinear computational model is written as

$$[\mathbb{U}(t)] = [H] [\mathbf{q}(t)], \quad (2.11)$$

in which the matrix $[H]$ is constructed by the assemblage of $[H^A]$ and $[H^B]$. Let $n_q = N^A + N^B + n_c$. Then, using the coupling conditions defined by (2.6), the \mathbb{R}^{n_q} -vector $\mathbf{q}(t) = (\mathbf{y}^A(t), \mathbf{y}^B(t), \mathbb{U}_c(t))$ is a solution of the reduced nonlinear dynamical system

$$[\underline{M}] \ddot{\mathbf{q}}(t) + [\underline{D}] \dot{\mathbf{q}}(t) + [\underline{K}] \mathbf{q}(t) + \mathcal{F}^{\text{NL}}(\mathbf{q}(t)) = \mathcal{F}(t), \quad (2.12)$$

with

$$[\underline{M}] = \begin{bmatrix} \underline{M}_{yy}^A & 0 & \underline{M}_{yc}^A \\ 0 & \underline{M}_{yy}^B & \underline{M}_{yc}^B \\ \underline{M}_{cy}^A & \underline{M}_{cy}^B & \underline{M}_{cc}^A + \underline{M}_{cc}^B \end{bmatrix}, \quad [\underline{D}] = \begin{bmatrix} \underline{D}_{yy}^A & 0 & \underline{D}_{yc}^A \\ 0 & \underline{D}_{yy}^B & \underline{D}_{yc}^B \\ \underline{D}_{cy}^A & \underline{D}_{cy}^B & \underline{D}_{cc}^A + \underline{D}_{cc}^B \end{bmatrix}, \quad (2.13)$$

$$[\underline{K}] = \begin{bmatrix} \underline{K}_{yy}^A & 0 & \underline{K}_{yc}^A \\ 0 & \underline{K}_{yy}^B & \underline{K}_{yc}^B \\ \underline{K}_{cy}^A & \underline{K}_{cy}^B & \underline{K}_{cc}^A + \underline{K}_{cc}^B \end{bmatrix}, \quad (2.14)$$

$$\mathcal{F}^{\text{NL}}(\mathbf{q}(t)) = \begin{bmatrix} [\Phi^A]^T \mathbb{F}_p^{\text{NL}}([H^A] \mathbf{q}^A(t)) \\ 0 \\ [S^A]^T \mathbb{F}_p^{\text{NL}}([H^A] \mathbf{q}^A(t)) \end{bmatrix}, \quad (2.15)$$

$$\mathcal{F}(t) = \begin{bmatrix} [\Phi^A]^T \mathbb{F}_p^A(t) \\ [\Phi^B]^T \mathbb{F}_p^B(t) \\ [S^A]^T \mathbb{F}_p^A(t) + [S^B]^T \mathbb{F}_p^B(t) \end{bmatrix}. \quad (2.16)$$

3. Stochastic nonlinear computational model including system uncertainties and identification

In this part, firstly the nonparametric probabilistic approach will be used to take into account both data uncertainties and model uncertainties in the reduced mean computational model of the linear subsystem Ω^B of the computational model. This approach which has recently been introduced consists in replacing the mass, damping, and stiffness matrices of reduced mean computational model by random matrices for which the probability distributions are explicitly given by the theory and for which a generator of independent realizations is known. Such an approach has been validated for many cases. For the details concerning the nonparametric probabilistic approach, one refers the reader, for instance, to [3–6]. In such an approach, the levels of uncertainties for the mass, damping, and stiffness random matrices are defined by the dispersion parameters which are defined below. Secondly, these dispersion parameters will be identified using the maximum likelihood method. Finally, the stochastic nonlinear computational model will be introduced and deduced from Section 2.2.3. It should be noted that (2.1) only the linear subsystem Ω^B is assumed to be uncertain and (2.2) the mean nonlinear subsystem Ω^A is representative and consequently, that both data uncertainties and model uncertainties can be neglected. If such an assumption was not verified, then the nonparametric probabilistic approach of uncertainties could always be implemented without any difficulties in this nonlinear subsystem (see for instance [8, 9]).

3.1. Stochastic linear subsystem Ω^B modeling uncertainties

Therefore, the matrices $[\underline{M}^B]$, $[\underline{D}^B]$, and $[\underline{K}^B]$ of the reduced mean computational model are replaced by the random matrices $[\mathbf{M}^B]$, $[\mathbf{D}^B]$, and $[\mathbf{K}^B]$ defined on a probability space $(\Theta, \mathcal{T}, \mathcal{P})$ and such that

$$\begin{aligned} \forall \theta \in \Theta, \quad & [\mathbf{M}^B(\theta)], [\mathbf{D}^B(\theta)], [\mathbf{K}^B(\theta)] \in \mathbb{M}_{n_q^B}^+(\mathbb{R}), \\ E\{[\mathbf{M}^B]\} &= [\underline{M}^B], \quad E\{[\mathbf{D}^B]\} = [\underline{D}^B], \quad E\{[\mathbf{K}^B]\} = [\underline{K}^B], \\ E\{\|[\mathbf{M}^B]^{-1}\|_F^2\} &< +\infty, \quad E\{\|[\mathbf{D}^B]^{-1}\|_F^2\} < +\infty, \quad E\{\|[\mathbf{K}^B]^{-1}\|_F^2\} < +\infty, \end{aligned} \quad (3.1)$$

in which $\mathbb{M}_n^+(\mathbb{R})$ is the set of all the positive-definite symmetric $(n \times n)$ matrices, where $E\{\cdot\}$ is the mathematical expectation and where $\|\cdot\|_F$ is the Frobenius norm such that $\|A\|_F^2 = \text{tr}\{[A]^*[A]\}$ with $[A]^* = [\bar{A}]^T$, $[\bar{A}]$ is the conjugate of $[A]$ and tr is the trace for matrices. Let $[\mathbf{P}^B]$ be the random matrix denoting $[\mathbf{M}^B]$, $[\mathbf{D}^B]$, or $[\mathbf{K}^B]$. The probability distribution of the random matrix $[\mathbf{P}^B]$ depends on the dispersion parameter δ_P^B related to the coefficient of variation $\tilde{\delta}_P^B$ of the random matrix $[\mathbf{P}^B]$ by the equation

$$(\tilde{\delta}_P^B)^2 = \frac{E\{\|[\mathbf{P}^B] - [\underline{P}^B]\|_F^2\}}{\|[\underline{P}^B]\|_F^2} = \frac{(\delta_P^B)^2}{n+1} \left(1 + \frac{(\text{tr}[\mathbf{P}^B])^2}{\text{tr}([\mathbf{P}^B]^2)} \right). \quad (3.2)$$

The dispersion parameter δ_P^B allows the level of uncertainties of the random matrix $[\mathbf{P}^B]$ to be controlled. It can be found in [3, 5] an algebraic representation of random matrix $[\mathbf{P}^B]$ which allows independent realizations to be explicitly constructed in order to solve the random equations by the Monte Carlo method. For each random matrix, this random generator depends only on the mean value, on the dimension of the matrix, and on the dispersion parameter. Such an approach is used in this paper.

3.2. Identification of the dispersion parameters

As explained in Section 3.1, the probability distributions of the random matrices (and then of the random generators) depend on the vector $\boldsymbol{\delta} = (\delta_M^B, \delta_D^B, \delta_K^B)$ of the dispersion parameters which is identified using the measurements. The observation of the stochastic computational model is defined introducing the $n_q^B \times n_q^B$ random complex dynamic stiffness matrix $[\mathbf{A}^B(\omega)]$ of the linear subsystem Ω^B written as

$$[\mathbf{A}^B(\omega)] = -\omega^2 [\mathbf{M}^B] + i\omega [\mathbf{D}^B] + [\mathbf{K}^B]. \quad (3.3)$$

Then the random condensed dynamical stiffness matrix $[\mathbf{Z}^B(\omega)]$ of the linear subsystem Ω^B on the coupling interface is such that $[\mathbf{Z}^B(\omega)] = [\mathbf{A}_{cc}^B(\omega)] - [\mathbf{A}_{cy}^B(\omega)][\mathbf{A}_{yy}^B(\omega)]^{-1}[\mathbf{A}_{yc}^B(\omega)]$. Taking into account the properties of the probabilistic model, it can be shown that, for all ω fixed in \mathcal{B} , the random matrix $[\mathbf{Z}^B(\omega)]$ is invertible almost surely and the random variable $J(\boldsymbol{\delta})$ defined by

$$J(\boldsymbol{\delta}) = \int_{\mathcal{B}} \|[\mathbf{Z}^B(\omega)]^{-1}\|_F^2 d\omega \quad (3.4)$$

exists and has a finite mean value. This random variable gives a measure over \mathcal{B} of the dynamical effects of subsystem Ω^B on the subsystem Ω^A at the coupling interface. It should be noted that the random variable $J(\boldsymbol{\delta})$ depends on $\boldsymbol{\delta}$ because the probability distributions of the random matrices $[\mathbf{M}^B]$, $[\mathbf{D}^B]$, and $[\mathbf{K}^B]$ depend on $\boldsymbol{\delta}$. Let $x \mapsto p_J(x, \boldsymbol{\delta})$ be the probability density function of the random variable $J(\boldsymbol{\delta})$ with respect to dx . For any x fixed in $[0, +\infty[$ and for any value of the vector $\boldsymbol{\delta}$ belonging to the admissible set \mathcal{C}_{ad} of the dispersion parameters, the value $p_J(x, \boldsymbol{\delta})$ of the probability density function is estimated by using the above probabilistic model and the Monte Carlo simulation. The corresponding deterministic experimental value J^{exp} of $J(\boldsymbol{\delta})$ is calculated using experimental data. The method used to identify vector $\boldsymbol{\delta}$ is the maximum likelihood method (see for instance [10]) for the random variable $J(\boldsymbol{\delta})$ for which J^{exp} is one realization. We then have to solve the following optimization problem:

$$\boldsymbol{\delta}^{\text{opt}} = \arg \max_{\boldsymbol{\delta} \in \mathcal{C}_{ad}} (p_J(J^{\text{exp}}; \boldsymbol{\delta})), \quad (3.5)$$

in which $\boldsymbol{\delta}^{\text{opt}}$ is the identified value of $\boldsymbol{\delta}$.

3.3. Random transient dynamical response of the stochastic nonlinear computational model

Using the probabilistic model defined in Section 3.1, the deterministic (2.11) to (2.15) give the following stochastic nonlinear computational model:

$$[\mathbf{U}(t)] = [\mathbf{H}][\mathbf{Q}(t)], \quad (3.6)$$

in which, for all fixed t , the vector-valued random variable $\mathbf{Q}(t)$ verifies

$$[\mathbf{M}]\ddot{\mathbf{Q}}(t) + [\mathbf{D}]\dot{\mathbf{Q}}(t) + [\mathbf{K}]\mathbf{Q}(t) + \boldsymbol{\mathcal{F}}^{\text{NL}}(\mathbf{Q}(t)) = \boldsymbol{\mathcal{F}}(t), \quad (3.7)$$

and where the random matrices $[\mathbf{M}]$, $[\mathbf{D}]$, and $[\mathbf{K}]$ are written as

$$\begin{aligned}
 [\mathbf{M}] &= \begin{bmatrix} \underline{M}_{yy}^A & 0 & \underline{M}_{yc}^A \\ 0 & \mathbf{M}_{yy}^B & \mathbf{M}_{yc}^B \\ \underline{M}_{cy}^A & \mathbf{M}_{cy}^B & \underline{M}_{cc}^A + \mathbf{M}_{cc}^B \end{bmatrix}, & [\mathbf{D}] &= \begin{bmatrix} \underline{D}_{yy}^A & 0 & \underline{D}_{yc}^A \\ 0 & \mathbf{D}_{yy}^B & \mathbf{D}_{yc}^B \\ \underline{D}_{cy}^A & \mathbf{D}_{cy}^B & \underline{D}_{cc}^A + \mathbf{D}_{cc}^B \end{bmatrix}, \\
 [\mathbf{K}] &= \begin{bmatrix} \underline{K}_{yy}^A & 0 & \underline{K}_{yc}^A \\ 0 & \mathbf{K}_{yy}^B & \mathbf{K}_{yc}^B \\ \underline{K}_{cy}^A & \mathbf{K}_{cy}^B & \underline{K}_{cc}^A + \mathbf{K}_{cc}^B \end{bmatrix}.
 \end{aligned} \tag{3.8}$$

4. Identification of stochastic loads

The transient load $\mathbb{F}(t)$ defined by $\mathbb{F}(t) = (\mathbb{F}_p^A(t), \mathbb{F}_p^B(t), 0)$ corresponding to the displacement vector $\mathbb{U}(t) = (\mathbb{U}_p^A(t), \mathbb{U}_p^B(t), \mathbb{U}_c^B(t))$ is modeled by a stochastic process $\{\mathbf{F}(t), t \in \mathbb{R}\}$. Since all the degrees of freedom of the computational model are not excited by this stochastic load, we then introduce the usual projection operator Proj in order to extract the vector $\tilde{\mathbf{F}}(t) = \text{Proj}(\mathbf{F}(t))$ of the nonzero random components of the random vector $\mathbf{F}(t)$. This equation can easily be inversed and yields $\mathbf{F}(t) = \text{Lift}(\tilde{\mathbf{F}}(t))$.

4.1. Construction of the stochastic load $\tilde{\mathbf{F}}(t)$

The stochastic load is modeled by an \mathbb{R}^m -valued Gaussian stationary centred second-order stochastic process $\{\tilde{\mathbf{F}}(t), t \in \mathbb{R}\}$ defined on a probability space $(\Theta', \mathcal{T}', \mathcal{P}')$ different from the probability space $(\Theta, \mathcal{T}, \mathcal{P})$. In addition, it is assumed that the stochastic process is mean square continuous on \mathbb{R} , physically realizable (causal) and for which its matrix-valued autocorrelation function $\tau \mapsto [R_{\tilde{\mathbf{F}}}(\tau)] = E\{\tilde{\mathbf{F}}(t + \tau)\tilde{\mathbf{F}}(t)^T\}$ is integrable on \mathbb{R} . This stochastic process is then completely defined by its matrix-valued spectral density function $[S_{\tilde{\mathbf{F}}}(\omega)] = (2\pi)^{-1} \int_{\mathbb{R}} e^{-i\omega\tau} [R_{\tilde{\mathbf{F}}}(\tau)] d\tau$ which is a continuous and integrable function on \mathbb{R} and which is in values in the set of all the positive $(m \times m)$ hermitian matrices. In addition, we will assume that for all ω in \mathbb{R} , the matrix $[S_{\tilde{\mathbf{F}}}(\omega)]$ is with values in the set $\mathbb{M}_m^+(\mathbb{C})$ of all the positive definite $(m \times m)$ hermitian matrices. Since the stochastic process is assumed to be physically realizable, the matrix valued spectral density function must satisfy the following usual inequality [11, 12]:

$$\int_{\mathbb{R}} \frac{\log(\det[S_{\tilde{\mathbf{F}}}(\omega)])}{1 + \omega^2} d\omega > -\infty. \tag{4.1}$$

The numerical simulation of independent realizations $\{\tilde{\mathbf{F}}(t, \theta'), t \in \mathbb{R}\}$ for $\theta' \in \Theta'$ (trajectories) can easily be generated by using adapted algorithms (see, e.g., [13, 14]).

4.2. Stochastic equation for simulation of responses

We have to identify the stochastic process $\tilde{\mathbf{F}}$ in presence of uncertainties in the linear subsystem Ω^B . This identification consists in identifying the matrix-valued spectral density function $[S_{\tilde{\mathbf{F}}}(\omega)]$ which completely describes the stochastic process. This stochastic inverse problem is formulated as a stochastic optimization problem. Such an identification is performed using the

stochastic equation deduced from (3.6) to (3.8) with (2.15) in which the deterministic load $\mathbb{F}(t)$ is replaced by the stochastic load $\mathbf{F}(t)$. We then have to construct the \mathbb{R}^{n_v} -valued stationary solution $\mathbf{U}_s(t) = (\mathbf{U}_s^A(t), \mathbf{U}_s^B(t), \mathbf{U}_s^C(t))$ (corresponding to $\mathbf{U}(t)$) which is written as

$$[\mathbf{U}_s(t)] = [H][\mathbf{Q}_s(t)], \quad (4.2)$$

in which subindex s is relative to the stationary solution and where the stationary stochastic process $\{\mathbf{Q}_s(t), t \in \mathbb{R}\}$ satisfies the stochastic equation

$$[\mathbf{M}]\ddot{\mathbf{Q}}_s(t) + [\mathbf{D}]\dot{\mathbf{Q}}_s(t) + [\mathbf{K}]\mathbf{Q}_s(t) + \mathcal{F}^{\text{NL}}(\mathbf{Q}_s(t)) = [H]^T \mathbf{F}(t), \quad (4.3)$$

in which $\dot{\mathbf{Q}}_s(t)$ and $\ddot{\mathbf{Q}}_s(t)$ are the mean-square first and second derivative of $\mathbf{Q}_s(t)$. For the identification of $[S_{\tilde{\mathbf{F}}}]$, for all t fixed, we introduce the \mathbb{R}^μ -valued random variable $\mathbf{Z}_s(t) = (Z_{s,1}(t), \dots, Z_{s,\mu}(t))$ which represents the observations of the stochastic computational model made up of components of the vector-valued random response $\mathbf{U}_s(t)$. Thus there exists a projection Proj' from \mathbb{R}^{n_v} into \mathbb{R}^μ such that $\mathbf{Z}_s(t) = \text{Proj}'(\mathbf{U}_s(t))$. For all θ in Θ , the stationary stochastic process $\{\mathbf{Z}_s(t, \theta), t \in \mathbb{R}\}$ is such that $\mathbf{Z}_s(t, \theta) = \text{Proj}'([H]\mathbf{Q}_s(t, \theta))$, where the stationary stochastic process $\{\mathbf{Q}_s(t, \theta), t \in \mathbb{R}\}$ is such that

$$[\mathbf{M}(\theta)]\ddot{\mathbf{Q}}_s(t, \theta) + [\mathbf{D}(\theta)]\dot{\mathbf{Q}}_s(t, \theta) + [\mathbf{K}(\theta)]\mathbf{Q}_s(t, \theta) + \mathcal{F}^{\text{NL}}(\mathbf{Q}_s(t, \theta)) = [H]^T \text{Lift}(\tilde{\mathbf{F}}(t; [S_{\tilde{\mathbf{F}}}])), \quad (4.4)$$

where $\{\tilde{\mathbf{F}}(t; [S_{\tilde{\mathbf{F}}}]), t \in \mathbb{R}\}$ is a stochastic process defined in Section 4.1. Section 4.3 is devoted to the identification of $[S_{\tilde{\mathbf{F}}}]$. In order to perform this identification, we need to introduce an observation relative to the stochastic equation and which is useful to construct the cost function. For all $\theta \in \Theta$, the matrix-valued spectral density function $\{[S_{\mathbf{Z}_s}(\omega, \theta)], \omega \in \mathbb{R}\}$ can be estimated. Generating ν_θ independent realizations of the random matrices $[\mathbf{M}]$, $[\mathbf{D}]$, and $[\mathbf{K}]$, the matrix-valued spectral density function $[S_{\mathbf{Z}_s}]$ is estimated by the Monte Carlo simulation method. For all $\omega \in \mathbb{R}$, one has

$$[S_{\mathbf{Z}_s}(\omega)] = \frac{1}{\nu_\theta} \sum_{i=1}^{\nu_\theta} [S_{\mathbf{Z}_s}(\omega, \theta_i)]. \quad (4.5)$$

4.3. Identification of the stochastic loads

The identification $[S_{\tilde{\mathbf{F}}}]$ is performed in introducing a parametric representation of this function which is rewritten as

$$[S_{\tilde{\mathbf{F}}}(\omega)] = [S(\omega, \mathbf{r})], \quad \omega \in \mathbb{R}, \mathbf{r} \in \mathcal{C}_r, \quad (4.6)$$

in which $\mathcal{C}_r \subset \mathbb{R}^{\nu_r}$ is the admissible set of the parameter \mathbf{r} with values in \mathbb{R}^{ν_r} where ν_r is the number of unknown scalar parameters which have to be identified and where $(\omega, \mathbf{r}) \mapsto [S(\omega, \mathbf{r})]$ is a given function from $\mathbb{R} \times \mathbb{R}^{\nu_r}$ into $\mathbb{M}_m^+(\mathbb{C})$. Therefore, the identification of the stochastic load $\{\tilde{\mathbf{F}}(t), t \in \mathbb{R}\}$ consists in identifying the \mathbb{R}^{ν_r} -valued vector \mathbf{r} . Let $\{\mathbf{Z}_s^{\text{exp}}(t) = (Z_{s,1}^{\text{exp}}(t), \dots, Z_{s,\mu}^{\text{exp}}(t)), t \in \mathbb{R}\}$ be the \mathbb{R}^μ -valued stationary stochastic process which is measured for the manufactured real system and corresponding to the observation stochastic process

$\{\mathbf{Z}_s(t), t \in \mathbb{R}\}$. The matrix-valued spectral density function $\{[S_{Z_s^{\text{exp}}}(\omega)], \omega \in \mathbb{R}\}$ of this stochastic process is estimated using the periodogram method. Then, the parameter \mathbf{r} is estimated in minimizing the distance $D(\mathbf{r}) = \int_{\mathcal{B}} \| [S_{Z_s}(\omega, \mathbf{r})] - [S_{Z_s^{\text{exp}}}(\omega)] \|_F^2 d\omega$ between the matrix-valued spectral density function calculated with the stochastic computational model and the experimental matrix-valued spectral density function. We then have to solve the following optimization problem

$$\mathbf{r}_{\text{opt}} = \arg \min_{\mathbf{r} \in C_r} D(\mathbf{r}), \quad (4.7)$$

in which \mathbf{r}_{opt} is the identified value of the vector \mathbf{r} .

5. Application

In this section, a numerical simulation of a simple example is presented in order to validate the methodology developed in this paper.

5.1. Data for the experimental model

The measurements are generated by an experimental model which is made up of one linear subsystem and one nonlinear subsystem. The linear subsystem is made up of four parallel beams fixed at their ends. The nonlinear subsystem is made up of a beam also fixed at its ends, parallel to the other beams and with one transversal symmetric elastic stop (two identical stops, see Figure 1). The five beams are linked by three transversal grids, each grid being modeled by four transversal springs (see Figure 1). Therefore, the coupling interface between the two subsystems is composed of three points located in the neutral fiber of the beam of the nonlinear subsystem. Each beam is modeled by eight Euler beam finite elements of equal lengths for which the DOF of the two nodes at the ends of the beam are locked. The twelve springs defining the three transversal grids are modeled by twelve spring elements. The two elastic stops are modeled by two springs. We are only interested in the y -direction displacements of the beam of the nonlinear subsystem (see Figure 1). Consequently, each beam has 14 DOF (y -translation and z -rotation). The total number of the free DOF for the linear subsystem is then 59 and the total number of the free DOF for the nonlinear subsystem is then 14. The beam of the nonlinear subsystem is excited by seven transversal forces applied following the y -direction. The vectors of these seven nonzero components are denoted by \mathbf{f}^{exp} . The stochastic process $\{\mathbf{f}^{\text{exp}}(t), t \in \mathbb{R}\}$ is a second-order centred stationary Gaussian stochastic process for which its matrix-valued spectral density function $[S_{\mathbf{f}^{\text{exp}}}(\omega)]$ is such that (2.1) for all i in $\{1, \dots, 7\}$, $[S_{\mathbf{f}^{\text{exp}}}(\omega)]_{ii}$ is a constant on the frequency band of analysis $\mathcal{B} = 2\pi \times [-100, 100]$ rad/s, and (2.2) for all i and j in $\{1, \dots, 7\}$, $|[S_{\mathbf{f}^{\text{exp}}}(\omega)]_{ij}|^2 = \gamma_{ij}(\omega) [S_{\mathbf{f}^{\text{exp}}}(\omega)]_{ii} [S_{\mathbf{f}^{\text{exp}}}(\omega)]_{jj}$ where $\gamma_{ij}(\omega) = \exp(-|x_i - x_j|/\lambda)$ in which $|x_i - x_j|$ is the distance between the two excited points and the value of λ is equal to the quarter of the beam length. In the frequency band of analysis \mathcal{B} , there are 21 eigenfrequencies for the linearized coupled system made up of the linear subsystem coupled with the linear beam of the nonlinear subsystem (nonlinear subsystem without the stops), for which the first three eigenfrequencies are 5.78 Hz, 15.9 Hz, and 31.1 Hz.

5.2. Data for the mean computational model

This part is devoted to the construction of a simplified mean computational model for the nonlinear dynamical system described in Section 5.1. This simplified mean computational model

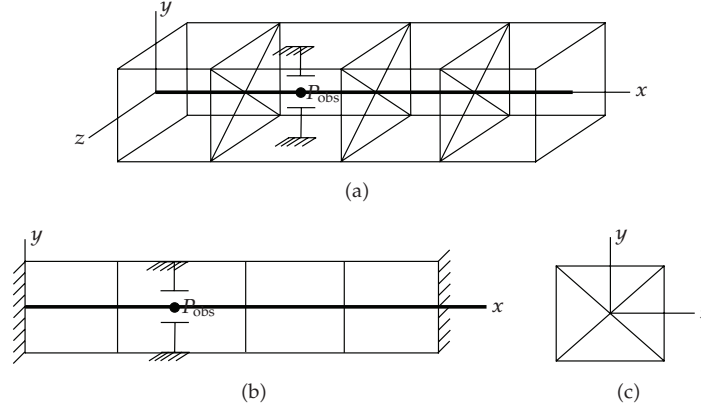


Figure 1: (a) Experimental model: 3D view. (b) Transversal view. (c) Transversal view in the plane of one grid: the 6 diagonal lines represent the 12 springs.

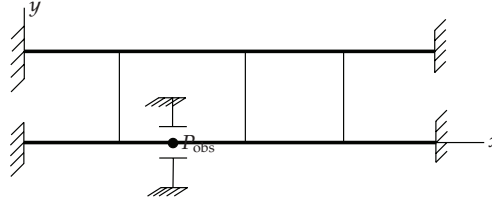


Figure 2: Mean model.

will be used to identify the stochastic loads. It consists in modeling (2.1) the four beams and the three transversal grids of the linear subsystem of the experimental model by a unique equivalent linear Euler beam and by three equivalent springs (see Figure 2) and (2.2) the linear beam with elastic stops of the nonlinear subsystem of the experimental model by a linear beam with two springs for the elastic stops. The section of the equivalent beam for the linear subsystem is arbitrarily chosen and its Young's modulus and its mass density are identified so that the three first eigenfrequencies of this mean computational model are the same that the three first eigenfrequencies of the experimental model. Note that only the three first eigenfrequencies are correctly fitted and consequently, there are model uncertainties in this simplified mean computational model, which are taken into account as explained in Section 3. It should be noted that the objective of this paper is not to construct an accurate mean computational model in order to exactly represent the experimental model, but to test the validity of the use of a simplified mean computational model in order to represent a much more complex system. After identification, the first three eigenfrequencies of the simplified mean computational model are 5.74 Hz, 15.3 Hz, and 30.8 Hz which have to be compared to the first three eigenfrequencies 5.78 Hz, 15.9 Hz, and 31.1 Hz of the experimental model.

5.3. Comparison between the dynamical responses of the experimental model and of the mean computational model for the same given stochastic load

In this section, it is assumed that the stochastic load is given and the same for the experimental model and for the simplified mean computational model. Then, for the two models, the

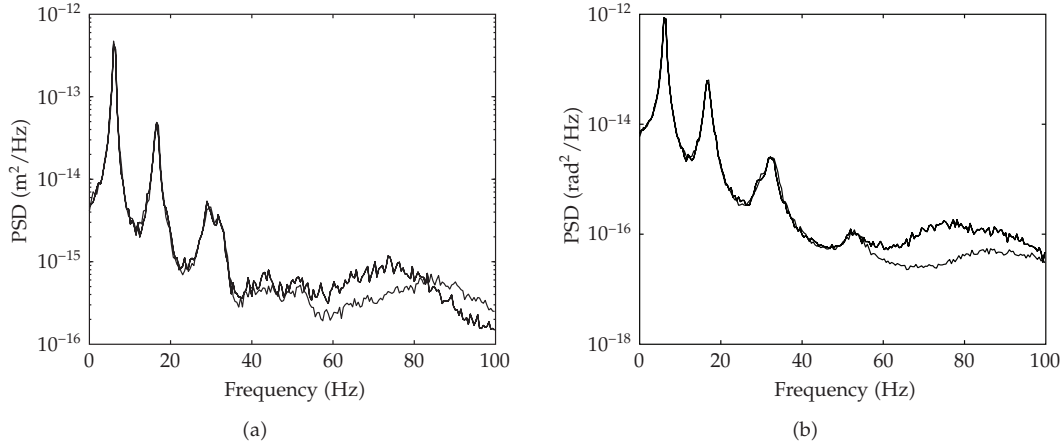


Figure 3: For point P_{obs} , power spectral density function (PSD) for (a) the y -displacement and (b) the z -rotation. Comparison between the experimental model (thin line) and the simplified mean computational model (thick line).

stationary stochastic responses are calculated in the time interval $[0, 220]$ s using an explicit Euler integration scheme. Let P_{obs} be the point of the non-linear subsystem located at the impact point of the elastic stops. The power spectral density functions of the stochastic y -displacement and of the stochastic z -rotation in point P_{obs} (see Figure 3) is estimated using the periodogram method. It can be seen that the prevision given by the mean simplified computational model is good enough in the frequency band $[0, 50]$ Hz. Nevertheless, there are significant differences in the frequency band $[50, 100]$ Hz induced by model uncertainties. This is the reason why the model uncertainties are taken into account in order to extend the domain of validity of the simplified mean computational model in the frequency band $[50, 100]$ Hz in order to perform a robust identification of the stochastic loads.

5.4. System uncertainties modeling and dispersion parameter identification

The nonparametric probabilistic approach of model uncertainties introduced in Section 3.1 is used for stiffness part of the linear subsystem of the simplified mean computational model. We then have to identify the dispersion parameter $\delta = (\delta_K^B)$. Note that the identification procedure which is proposed is independent of the stochastic loads. The estimation of the probability density function in (3.5) is carried out with 200 realizations for the Monte Carlo simulation. Figure 4 shows the likelihood function calculated using (3.5) with $\mathcal{C}_{\text{ad}} = [0, \sqrt{22/34}]$. The maximum is reached for $\delta^{\text{opt}} = 0.45$.

5.5. Case of an unknown stochastic load and its identification

In this section, the responses of the experimental model are given (those constructed in Section 5.3) and the stochastic load $\tilde{F}(t)$ is assumed to be unknown and has to be identified using the uncertain simplified computational model, that is to say the stochastic simplified computational model for which the dispersion parameter has been identified in Section 5.4. We begin defining a model as simple as possible for the stochastic load $\tilde{F}(t)$ introduced in

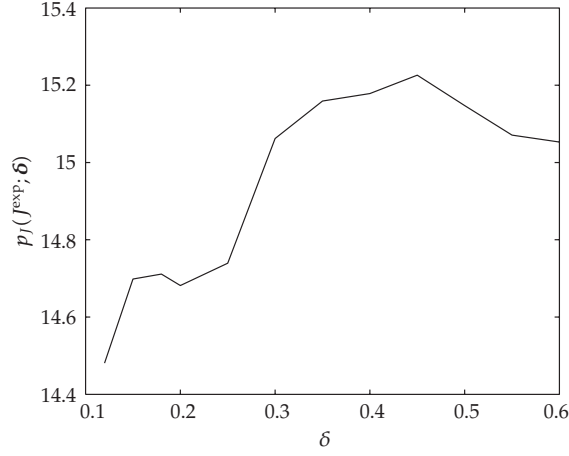


Figure 4: Graph of function $\delta \mapsto p_I(J^{\text{exp}}; \delta)$.

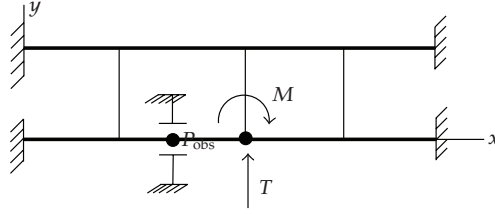


Figure 5: Definition of the stochastic load.

Section 4.1. We have then chosen to model $\tilde{\mathbf{F}}(t)$ as $\{\tilde{\mathbf{F}}(t) = (T(t), M(t)), t \in \mathbb{R}\}$ in which $T(t)$ is a y -force and $M(t)$ is a z -moment applied to the middle of the beam of the nonlinear subsystem (see Figure 5). This force and this moment are independent second-order centred stationary Gaussian stochastic processes. So, they are both completely defined by their power spectral density functions $[S_T(\omega)]$ and $[S_M(\omega)]$. The matrix-valued spectral density function of the stochastic process $\{\tilde{\mathbf{F}}(t), t \in \mathbb{R}\}$ is then defined by

$$[S_{\tilde{\mathbf{F}}}(\omega)] = \begin{bmatrix} S_T(\omega) & 0 \\ 0 & S_M(\omega) \end{bmatrix}, \quad \omega \in \mathbb{R}. \quad (5.1)$$

It is assumed that the function $\omega \mapsto [S_{\tilde{\mathbf{F}}}(\omega)]$ is constant in the frequency band of analysis \mathcal{B} and is such that (4.1) is verified. The experimental stochastic process $\{\mathbf{Z}_s^{\text{exp}}(t), t \in \mathbb{R}\}$ defined in Section 4.3 is composed of $\mu = 7$ stochastic y -displacements. Taking into account (4.6), the function $\omega \mapsto [S_{\tilde{\mathbf{F}}}(\omega)]$, which is a constant diagonal hermitian matrix, can then be rewritten for all ω in \mathcal{B} as

$$[S_{\tilde{\mathbf{F}}}(\omega)] = [S(\omega, \mathbf{r})] = \begin{bmatrix} r_1 & 0 \\ 0 & r_2 \end{bmatrix}, \quad \omega \in \mathcal{B}, \mathbf{r} \in \mathcal{C}_r, \quad (5.2)$$

in which the admissible set $\mathcal{C}_r = \{\mathbf{r} = (r_1, r_2); r_1 > 0, r_2 > 0\}$. This vector \mathbf{r} is identified using the trial method to solve the optimization problem defined by (4.7). Such a method consists in

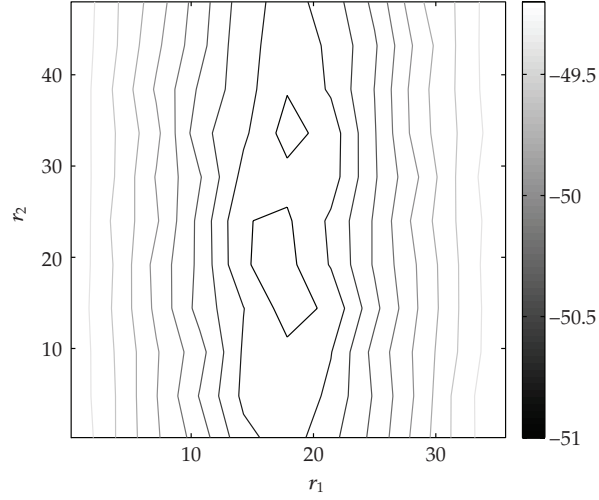


Figure 6: Graph of the cost function $(r_1, r_2) \mapsto \log_{10}(D(r_1, r_2))$.

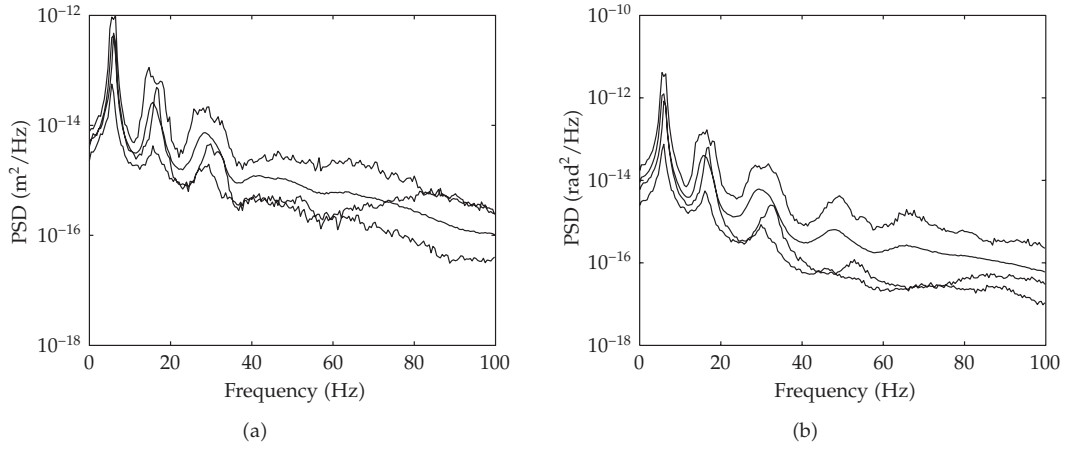


Figure 7: For point P_{obs} , power spectral density function (PSD) for (a) the stochastic y -displacement and (b) the stochastic z -rotation: upper and lower envelopes and mean response (mid thin line); experimental model (thick line).

calculating the cost function $D(\mathbf{r})$ for 100 values of the vector \mathbf{r} . Figure 6 shows the graph of the function $\mathbf{r} \mapsto \log_{10}(D(\mathbf{r}))$ which allows the optimal value \mathbf{r}_{opt} to be determined. The confidence region associated with a probability level $P_c = .95$ of the response of the stochastic simplified computational model on which the identified stochastic load is applied can then be estimated. The comparison between the experimental responses with the responses constructed with the stochastic simplified computational model is given in Figure 7. This figure displays the confidence region of the power spectral density function of the stochastic y -displacement and the stochastic z -rotation for point P_{obs} .

6. Conclusions

We have presented a methodology and its validation to perform the identification of a stochastic loads applied to a complex nonlinear dynamical system for which a few measurements of its responses are available. To carry out this identification, a simplified computational model of the real system is introduced. Since such a simplified computational model induces model uncertainties, a probabilistic model of these uncertainties is introduced in the simplified computational model. The identification of the stochastic loads is then performed using this stochastic computational model which takes into account model uncertainties and consequently, we have validated a method to perform a robust identification with respect to model uncertainties. It should be noted that the nonlinear dynamical system used for this validation is representative of real industrial systems and then validates the methodology proposed.

References

- [1] R. Ohayon and C. Soize, *Structural Acoustics and Vibration*, Academic Press, San Diego, Calif, USA, 1998.
- [2] O. C. Zienkiewicz and R. L. Taylor, *The Finite Element Method*, McGraw-Hill, New York, NY, USA, 4th edition, 1989.
- [3] C. Soize, "A nonparametric model of random uncertainties for reduced matrix models in structural dynamics," *Probabilistic Engineering Mechanics*, vol. 15, no. 3, pp. 277–294, 2000.
- [4] C. Soize, "Maximum entropy approach for modeling random uncertainties in transient elastodynamics," *The Journal of the Acoustical Society of America*, vol. 109, no. 5, pp. 1979–1996, 2001.
- [5] C. Soize, "Random matrix theory for modeling uncertainties in computational mechanics," *Computer Methods in Applied Mechanics and Engineering*, vol. 194, no. 12–16, pp. 1333–1366, 2005.
- [6] C. Soize and H. Chebli, "Random uncertainties model in dynamic substructuring using a nonparametric probabilistic model," *Journal of Engineering Mechanics*, vol. 129, no. 4, pp. 449–457, 2003.
- [7] R. R. Craig Jr. and M. C. C. Bampton, "Coupling of substructures for dynamic analysis," *AIAA Journal*, vol. 6, no. 7, pp. 1313–1319, 1968.
- [8] C. Desceliers, C. Soize, and S. Cambier, "Nonparametric parametric model for random uncertainties in nonlinear structural dynamics: application to earthquake engineering," *Earthquake Engineering and Structural Dynamics*, vol. 33, no. 3, pp. 315–327, 2004.
- [9] R. Sampaio and C. Soize, "On measures of nonlinearity effects for uncertain dynamical systems-application to a vibro-impact system," *Journal of Sound and Vibration*, vol. 303, no. 3–5, pp. 659–674, 2007.
- [10] R. J. Serfling, *Approximation Theorems of Mathematical Statistics*, Wiley Series in Probability and Mathematical Statistics, John Wiley & Sons, New York, NY, USA, 1980.
- [11] Yu. A. Rozanov, *Stationary Random Processes*, Holden-Day, San Francisco, Calif, USA, 1967.
- [12] C. Soize, *The Fokker-Planck Equation for Stochastic Dynamical Systems and Its Explicit Steady State Solutions*, vol. 17 of *Series on Advances in Mathematics for Applied Sciences*, World Scientific, River Edge, NJ, USA, 1994.
- [13] M. Shinozuka, "Simulation of multivariate and multidimensional random processes," *The Journal of the Acoustical Society of America*, vol. 49, no. 1, pp. 357–367, 1971.
- [14] F. Poirion and C. Soize, "Numerical methods and mathematical aspects for simulation of homogeneous and non homogeneous Gaussian vector fields," in *Probabilistic Methods in Applied Physics*, pp. 17–53, Springer, Berlin, Germany, 1995.

Research Article

Homotopy Perturbation Method for Solving Reaction-Diffusion Equations

Yu-Xi Wang, Hua-You Si, and Lu-Feng Mo

School of Information Engineering, Zhejiang Forestry College, Lin'an 311300, Zhejiang, China

Correspondence should be addressed to Lu-Feng Mo, molufeng@126.com

Received 16 November 2007; Revised 11 February 2008; Accepted 27 February 2008

Recommended by Paulo Gonçalves

The homotopy perturbation method is applied to solve reaction-diffusion equations. In this method, the trial function (initial solution) is chosen with some unknown parameters, which are identified using the method of weighted residuals. Some examples are given. The obtained results are compared with the exact solutions, revealing that this method is very efficient and the obtained solutions are of high accuracy.

Copyright © 2008 Yu-Xi Wang et al. This is an open access article distributed under the Creative Commons Attribution License, which permits unrestricted use, distribution, and reproduction in any medium, provided the original work is properly cited.

1. Introduction

In this paper, we consider a reaction-diffusion process governed by the nonlinear ordinary differential equation [1]:

$$y''(x) + y^n(x) = 0, \quad 0 < x < L, \quad (1.1)$$

with boundary conditions

$$y(0) = y(L) = 0, \quad (1.2)$$

where $y(x)$ represents the steady-state temperature for the corresponding reaction-diffusion equation with the reaction term y^n ; n is the power of the reaction term (heat source), generally it follows $n > 0$, L is the length of the sample (heat conductor). The physical interpretation of (1.1) was given in [1].

Recently, various different analytical methods were applied to nonlinear equations arising in engineering applications, such as the homotopy perturbation method [2–10], and exp-function method [11, 12], a complete review is available in [13]. This problem was studied

by Lesnic using Adomian method [1], and by Mo [14] using variational method. In this paper, the homotopy perturbation method [2, 3, 13] is applied to the discussed problem, and the obtained results show that the method is very effective and simple.

2. Homotopy perturbation method

In order to use the homotopy perturbation, we construct a homotopy in the form [2, 3, 13]

$$(1 - p)(y'' - y_0'') + p(y'' + y'') = 0 \quad (2.1)$$

with initial approximation

$$y_0(x) = ax(1 - x) = ax - ax^2, \quad (2.2)$$

where a is an unknown constant to be further determined. It is obvious that (2.2) satisfies the boundary conditions.

We rewrite (2.1) in the form of

$$y'' + 2a - p(2a - y'') = 0. \quad (2.3)$$

We suppose the solution of (2.3) has the form

$$y(x) = y_0(x) + py_1(x) + p^2y_2(x) + \dots. \quad (2.4)$$

Substituting (2.4) into (1.1) and equating the terms with the identical powers of p , we can solve y_0, y_1, y_2, \dots sequentially with ease. Setting $p = 1$, we obtain the approximate solution of (1.1) in the form of

$$y(x) = y_0(x) + y_1(x) + y_2(x) + \dots. \quad (2.5)$$

To illustrate its solution procedure, we consider some special cases.

Case 1 ($n = 2$). Under such case, we can easily obtain sequentially

$$\begin{aligned} y_0'' &= -2a, \\ y_1'' &= 2a - y_0^2, \\ y_2'' &= -2y_0y_1. \end{aligned} \quad (2.6)$$

We, therefore, obtain the approximate solution in the form of

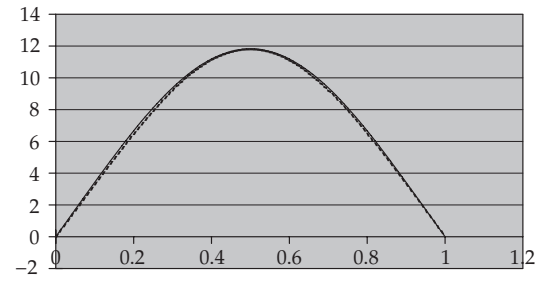
$$y(x) = ax(1 - x) + ax^2 - a^2\left(\frac{1}{30}x^6 - \frac{1}{10}x^5 + \frac{1}{12}x^4\right) - \left(a - \frac{1}{60}a^2\right)x. \quad (2.7)$$

In order to identify the unknown constant a in (2.7), we apply the method of weighted residuals. Substituting (2.7) into (1.1) results in the following residual:

$$R(x, a) = y''(x) + y''(x). \quad (2.8)$$

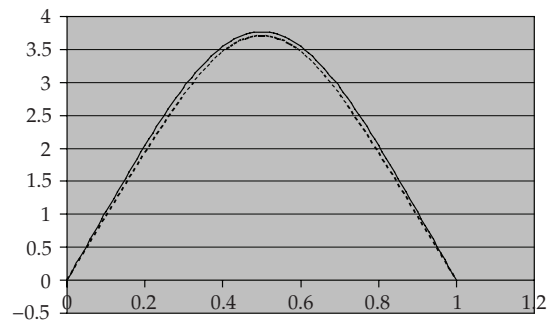
It is obvious that $R(0, a) = 0$ and $R(1, a) = 0$. We locate at $x = 1/3$, and set $R(1/3, a) = 0$, yielding the result

$$a = 45.4205. \quad (2.9)$$



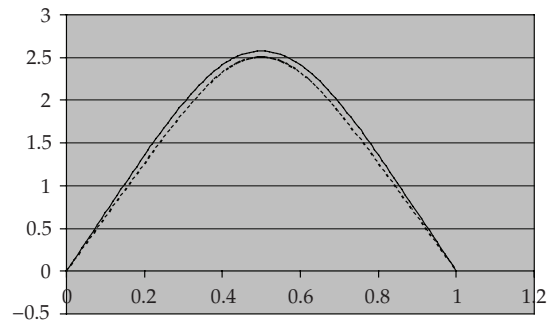
----- Exact solution
 — Approximate solution

(a) $n = 2$



----- Exact solution
 — Approximate solution

(b) $n = 3$



----- Exact solution
 — Approximate solution

(c) $n = 4$

Figure 1: Comparison of approximate solutions with exact ones. Continued line: approximate solution; discontinued line: exact solution.

Case 2 ($n = 3$). The solution procedure is the same as that for Case 1. We can easily obtain the following linear equations:

$$\begin{aligned}a &= 14.2657, \\y_1'' &= 2a - y_0^3, \\y_2'' &= -3y_0^2 y_1.\end{aligned}\tag{2.10}$$

We obtain the following second-order approximate solution:

$$y(x) = ax(1-x) + ax^2 - a^3 \left(-\frac{1}{56}x^8 + \frac{1}{14}x^7 - \frac{1}{10}x^6 + \frac{1}{20}x^5 \right) - \left(a - \frac{1}{280}a^3 \right)x.\tag{2.11}$$

Similarly, we locate at $x = 1/3$, and set $R(1/3, a) = 0$ to identify the unknown constant, which reads $a = 14.2657$.

Case 3 ($n = 4$). By the same manipulation as illustrated in above cases, we obtain

$$\begin{aligned}y_0'' &= -2a, \\y_1'' &= 2a - y_0^4, \\y_2'' &= -4y_0^3 y_1, \\y(x) &= ax(1-x) + ax^2 - a^4 \left(\frac{1}{90}x^{10} - \frac{1}{18}x^9 + \frac{3}{28}x^8 - \frac{2}{21}x^7 + \frac{1}{30}x^6 \right) - (a - 7.9410^{-4}a^4)x.\end{aligned}\tag{2.12}$$

Using the method of weighted residuals, we set $R(1/3a) = 0$, resulting in $a = 9.6320$.

Figure 1 shows the remarkable accuracy of the obtained results.

3. Conclusion

The homotopy perturbation method deforms a complex problem under study to a simple problem routinely. If initial guess is suitably chosen, one iteration is enough, making the method a most attractive one. The method is of remarkable simplicity, while the obtained results are of utter accuracy on the whole solution domain. The method can be applied to various other nonlinear problems without any difficulty.

References

- [1] D. Lesnic, "A nonlinear reaction-diffusion process using the Adomian decomposition method," *International Communications in Heat and Mass Transfer*, vol. 34, no. 2, pp. 129–135, 2007.
- [2] J.-H. He, "New interpretation of homotopy perturbation method," *International Journal of Modern Physics B*, vol. 20, no. 18, pp. 2561–2568, 2006.
- [3] J.-H. He, "A coupling method of a homotopy technique and a perturbation technique for non-linear problems," *International Journal of Non-Linear Mechanics*, vol. 35, no. 1, pp. 37–43, 2000.
- [4] T. Ozis and A. Yildirim, "A comparative study of He's homotopy perturbation method for determining frequency-amplitude relation of a nonlinear oscillator with discontinuities," *International Journal of Nonlinear Sciences and Numerical Simulation*, vol. 8, no. 2, pp. 243–248, 2007.

- [5] A. Belendez, A. Hernandez, T. Belendez, et al., "Application of He's homotopy perturbation method to the Duffing-harmonic oscillator," *International Journal of Nonlinear Sciences and Numerical Simulation*, vol. 8, no. 1, pp. 79–88, 2007.
- [6] X.-C. Cai, W.-Y. Wu, and M.-S. Li, "Approximate period solution for a kind of nonlinear oscillator by He's perturbation method," *International Journal of Nonlinear Sciences and Numerical Simulation*, vol. 7, no. 1, pp. 109–112, 2006.
- [7] M. Dehghan and F. Shakeri, "Solution of an integro-differential equation arising in oscillating magnetic fields using He's homotopy perturbation method," *Progress in Electromagnetics Research*, vol. 78, pp. 361–376, 2008.
- [8] F. Shakeri and M. Dehghan, "Inverse problem of diffusion equation by He's homotopy perturbation method," *Physica Scripta*, vol. 75, no. 4, pp. 551–556, 2007.
- [9] M. Dehghan and F. Shakeri, "Solution of a partial differential equation subject to temperature overspecification by He's homotopy perturbation method," *Physica Scripta*, vol. 75, no. 6, pp. 778–787, 2007.
- [10] D. D. Ganji and A. Sadighi, "Application of He's homotopy-perturbation method to nonlinear coupled systems of reaction-diffusion equations," *International Journal of Nonlinear Sciences and Numerical Simulation*, vol. 7, no. 4, pp. 411–418, 2006.
- [11] S.-D. Zhu, "Exp-function method for the Hybrid-Lattice system," *International Journal of Nonlinear Sciences and Numerical Simulation*, vol. 8, no. 3, pp. 461–464, 2007.
- [12] S.-D. Zhu, "Exp-function method for the discrete mKdV lattice," *International Journal of Nonlinear Sciences and Numerical Simulation*, vol. 8, no. 3, pp. 465–468, 2007.
- [13] J.-H. He, "Some asymptotic methods for strongly nonlinear equations," *International Journal of Modern Physics B*, vol. 20, no. 10, pp. 1141–1199, 2006.
- [14] L.-F. Mo, "Variational approach to reaction-diffusion process," *Physics Letters A*, vol. 368, no. 3–4, pp. 263–265, 2007.

Research Article

Numerical Stability Test of Neutral Delay Differential Equations

Z. H. Wang

*Institute of Vibration Engineering Research, Nanjing University of Aeronautics and Astronautics,
210016 Nanjing, China*

Correspondence should be addressed to Z. H. Wang, zhwang@nuaa.edu.cn

Received 24 October 2007; Revised 1 March 2008; Accepted 16 March 2008

Recommended by Jose Balthazar

The stability of a delay differential equation can be investigated on the basis of the root location of the characteristic function. Though a number of stability criteria are available, they usually do not provide any information about the characteristic root with maximal real part, which is useful in justifying the stability and in understanding the system performances. Because the characteristic function is a transcendental function that has an infinite number of roots with no closed form, the roots can be found out numerically only. While some iterative methods work effectively in finding a root of a nonlinear equation for a properly chosen initial guess, they do not work in finding the rightmost root directly from the characteristic function. On the basis of Lambert W function, this paper presents an effective iterative algorithm for the calculation of the rightmost roots of neutral delay differential equations so that the stability of the delay equations can be determined directly, illustrated with two examples.

Copyright © 2008 Z. H. Wang. This is an open access article distributed under the Creative Commons Attribution License, which permits unrestricted use, distribution, and reproduction in any medium, provided the original work is properly cited.

1. Introduction

Many engineering systems can be modeled as neutral delay differential equations (NDDEs) that involve a time delay in the derivative of the highest order [1–9], which are different from retarded delay differential equations (RDDEs) that do not involve a time delay in the derivative of the highest order [10–14]. For example, a system, which consists of a mass mounted on a linear spring to which a pendulum is attached via a hinged massless rod, is used to predict the dynamic response of structures to external forces using a set of actuators, and it is modeled as an NDDE if the delay in actuators is taken into consideration [7]. While the RDDEs have been studied intensively in the literature (see, e.g., [10–14]), the NDDEs have been investigated relatively few. Analysis shows that, both RDDEs and NDDEs may exhibit very complicated nonlinear dynamics. For example, a first-order autonomous DDE can exhibit chaotic motion,

and a first-order autonomous NDDE with a single delay can even admit homoclinic snaking [5]. Complex behaviors of dynamical systems come out after certain stationary solutions lose their stability, so stability analysis plays a fundamental role in system dynamics. Usually, the stability analysis for equilibriums of DDEs can be investigated on the basis of the method of Lyapunov's function (al) including the LMI (linear matrix inequality) method, or by means of the root location of the characteristic functions for equilibriums [10–14]. In particular, the stability can be studied on the basis of stability switches [7, 8, 10, 14], if the delay effect on the stability is addressed. In this case, the delay interval is divided into a number of subintervals by the critical values of delay for which the system changes its equilibriums from stable status to unstable status, or from unstable status to stable status, as the delay passes through the critical delays, and the system has the same stability in each subinterval. If a DDE admits a number of stability switches, then the system can be stabilized or destabilized by adjusting the delay value only. It is worthy to note that, however, the stability may be very poor in some delay intervals for which the system is asymptotically stable [14]. Thus, in practical applications, it is required not only to know whether the time-delay system is asymptotically stable, but also to know the stability margin. Therefore, a computational algorithm for finding the characteristic root with maximal real part (rightmost root for short) of an NDDE is preferable.

The characteristic quasipolynomial of a DDE has an infinite number of roots that do not have closed form, and the roots can be found numerically only. Though the famous Newton-Raphson method works effectively in finding a root of a nonlinear equation for a properly chosen initial guess, it does not work in finding the rightmost root of an NDDE *directly* from the characteristic quasipolynomial. In [15], an iterative scheme was proposed for the calculation of the rightmost root of an RDDE, where the rightmost root was assigned to be the rightmost root of a simplified polynomial resulted from the quasipolynomial in each step of the iteration. The problem is that the iterative sequence in [15] is frequently not convergent. Recently, the author shows in [16] that the Newton-Raphson method or the Halley method computes effectively the rightmost roots of RDDEs if Lambert W function [17] is applied.

In this paper, we are interested in the stability test of NDDEs,

$$\dot{x}(t) + C\dot{x}(t - \tau) = Ax(t) + Bx(t - \tau), \quad x \in \mathbb{R}^n, \quad (1.1)$$

whose characteristic equations are assumed in the form

$$\Delta(\lambda) := (1 - pe^{-\lambda\tau})\lambda^n + a_1(e^{-\lambda\tau})\lambda^{n-1} + \dots + a_n(e^{-\lambda\tau}) = 0, \quad (1.2)$$

where p is a constant, and the coefficients $a_j(z)$ are polynomials in z . The systems discussed in [1–9] fall into the category of (1.1). If $p = 0$, then the trivial solution $x = 0$ is asymptotically stable if and only if $\Delta(\lambda)$ has roots with negative real parts only [10–14], which is equivalent to $\alpha < 0$, where

$$\alpha = \max\{\operatorname{Re} \lambda : \Delta(\lambda) = 0, \lambda \in \mathbb{C}\}. \quad (1.3)$$

This may not be the case of NDDEs. If $|p| = 1$, the condition “ $\Delta(\lambda)$ has roots with negative real parts only” is *not* equivalent to $\alpha < 0$, because the infinite characteristic roots with negative real parts may accumulate *on* the imaginary axis as shown in Section 2.1. If $|p| > 1$, $\Delta(\lambda)$ has always roots with positive real part, so $x = 0$ is unstable for all given $\tau > 0$. Thus, only

$|p| < 1$ is assumed true in this paper, for which “ $\Delta(\lambda)$ has roots with negative real parts only” is equivalent to $\alpha < 0$.

The aim of this paper is to generalize the iterative method developed in [16] for calculating the rightmost root of RDDEs to the stability test of NDDEs. The method will be briefly introduced in Section 2, and two examples will be given in Section 3 to demonstrate the efficiency of the proposed method. A few concluding remarks will be given in Section 4.

2. An algorithm for calculating the rightmost characteristic root of time-delay systems

A real α corresponds to a real characteristic root or a pair of complex conjugate characteristic roots. For simplicity, such characteristic root(s) is called the rightmost root in this paper. In this section, the Newton-Raphson method will be combined with a special function-Lambert W function to find out the rightmost root of $\Delta(\lambda)$.

2.1. An explicit stability criterion for a first-order RDDE

Let us consider a first-order retarded delay differential equation described by

$$\dot{x}(t) + ax(t) + bx(t - \tau) = 0. \quad (2.1)$$

The characteristic equation corresponding to the trivial solution $x = 0$ is

$$\Delta(\lambda) := \lambda + a + be^{-\lambda\tau} = 0. \quad (2.2)$$

On the basis of Lambert W function, the stability condition can be presented explicitly. In fact, Lambert W function $w = W(z)$ is defined as the solution of a transcendental equation

$$we^w = z, \quad (z \in \mathbb{C}). \quad (2.3)$$

It has infinite branches, denoted by $W_k(z)$, $k = 0, \pm 1, \pm 2, \dots$, respectively. $W_0(z)$ is the unique branch that is analytic at the origin $z = 0$, and is called the principal branch. For more details about Lambert W function, it is referred to [17–19].

Now, if $\Delta(\lambda) = 0$, then $(\lambda + a)e^{\lambda\tau} = -b$, and $\tau(\lambda + a)e^{(\lambda + a)\tau} = -b\tau e^{a\tau}$. Thus, the characteristic roots can be expressed explicitly in terms of Lambert W function [17]

$$\lambda_k = -a + \frac{W_k(-b\tau e^{a\tau})}{\tau}, \quad k = 0, \pm 1, \pm 2, \dots \quad (2.4)$$

Moreover, it has been proved in [19]: for arbitrary $z \in \mathbb{C}$, one has

$$\max_{k=0, \pm 1, \pm 2, \dots} \operatorname{Re} W_k(z) = \operatorname{Re} W_0(z), \quad (2.5)$$

where $\operatorname{Re} z$ stands for the real part of $z \in \mathbb{C}$. Thus, the rightmost root of (2.1) is λ_0 , and the trivial solution, $x = 0$, of (2.1) is asymptotically stable if and only if $\operatorname{Re} \lambda_0 < 0$, namely,

$$\operatorname{Re} W_0(-b\tau e^{a\tau}) < \tau \operatorname{Re} a. \quad (2.6)$$

Such a stability condition can be checked easily, because Maple, Matlab, and Mathematica, the three popular mathematical softwares, provide a calculator of Lambert W function.

2.2. A numerical scheme for neutral delay differential equations

It is not possible to gain an explicit form of the rightmost root, as done above, for other delay differential equations. Thus, an iterative algorithm was proposed in [16] for calculating the rightmost root of RDDEs whose characteristic equation reads

$$\Delta(\lambda) := \lambda^n + a_1(e^{-\lambda\tau_1}, e^{-\lambda\tau_2}, \dots, e^{-\lambda\tau_m})\lambda^{n-1} + \dots + a_n(e^{-\lambda\tau_1}, e^{-\lambda\tau_2}, \dots, e^{-\lambda\tau_m}) = 0, \quad (2.7)$$

where the coefficients $a_j(z_1, z_2, \dots, z_m)$ are polynomials. The main points of this iterative method are summarized as follows.

2.2.1. Choice of the initial guess

A properly chosen initial value is important in the applications of iterative methods. For our problem, one can firstly chose freely a complex number λ_0 and then refine it to be the rightmost root of the following polynomial equation

$$\lambda^n + a_1(e^{-\lambda_0\tau_1}, e^{-\lambda_0\tau_2}, \dots, e^{-\lambda_0\tau_m})\lambda^{n-1} + \dots + a_n(e^{-\lambda_0\tau_1}, e^{-\lambda_0\tau_2}, \dots, e^{-\lambda_0\tau_m}) = 0, \quad (2.8)$$

where the coefficients a_j are assigned to fixed values. Note that the notation λ_0 here denotes the initial guess, rather than the rightmost root given in Section 2.1.

2.2.2. Construction of the algorithm

For certain fixed constants $a > 0$ and b , define

$$F(\lambda) = a\lambda + b - W_0((a\lambda + b - \Delta(\lambda))e^{a\lambda+b}), \quad (2.9)$$

where $W_0(z)$ is the principal branch of Lambert W function, and the constants a, b are *not large* to avoid numerical problems due to large factor. Then the Newton-Raphson method is employed to find the rightmost root of $\Delta(\lambda) = 0$;

$$\lambda_{i+1} = \lambda_i - \frac{F(\lambda_i)}{F'(\lambda_i)}, \quad (i = 0, 1, 2, \dots); \quad (2.10)$$

which has quadratic convergence for unrepeated roots. Alternatively, Halley's method

$$\lambda_{i+1} = \lambda_i - \left(1 - \frac{1}{2} \frac{F(\lambda_i)F''(\lambda_i)}{(F'(\lambda_i))^2}\right)^{-1} \frac{F(\lambda_i)}{F'(\lambda_i)}, \quad (i = 0, 1, 2, \dots) \quad (2.11)$$

can be used. This algorithm has order 3 of convergence for unrepeated roots. The iteration is stopped at step N if

$$|\lambda_N - \lambda_{N-1}| < \varepsilon, \quad (2.12)$$

for a given tolerance ε .

2.2.3. Verification of the computational result

Due to (2.5), it is expected that λ_N resulted from (2.10) or (2.11) is the rightmost root of the delay differential equation, namely, for any root λ of $\Delta(\lambda) = 0$, one has

$$\operatorname{Re} \lambda \leq \operatorname{Re} \lambda_N. \quad (2.13)$$

Equation (2.13) is guaranteed if the Nyquist plot of $\Delta(i\omega + \operatorname{Re} \lambda_N)/(1 + i\omega)^n$ passes through the origin of the complex plane and the Nyquist plot of $\Delta(i\omega + \operatorname{Re} \lambda_N + \mu)/(1 + i\omega)^n$ does not encounter the origin for very small $\mu > 0$. The method of Nyquist plot was originally proposed in [20] for RDDEs, and extended to NDDEs in [21].

Such a scheme works also for the quasipolynomial defined in (1.1) for NDDEs with $|p| < 1$.

2.3. Accumulation of the characteristic roots

The different branches of Lambert W function can be used to find different roots of $\Delta(\lambda) = 0$. For simplicity, let us calculate the roots of a first-order autonomous NDDE $\dot{x}(t) = -\dot{x}(t - \tau) - ax(t)$ with

$$\Delta(\lambda) = \lambda + \lambda e^{-\lambda\tau} + a. \quad (2.14)$$

Let $W_k(z)$ be the k th branch of Lambert W function defined in Section 2.1, and define

$$F_k(\lambda) = \lambda + a - W_k(-\tau \lambda e^{a\tau})/\tau, \quad (k = 0, \pm 1, \pm 2, \dots), \quad (2.15)$$

then all the characteristic roots, computed by using the Newton-Raphson method or Halley's method for $F_k(\lambda)$, have negative real parts, and they accumulate on the imaginary axis as shown in Table 1. As a result, the solution $x = 0$ is not stable, though all the roots of $\Delta(\lambda)$ have negative real parts.

The condition $|p| < 1$, required in the proposed algorithm for finding the rightmost root, is not satisfied in this example. The branch $W_0(z)$ yields the leftmost root, rather than the rightmost root.

3. Two illustrative examples

In this section, the iterative method proposed in Section 2 will be applied to calculate the rightmost roots of two NDDEs discussed in the literature.

3.1. A neutral delayed oscillator

Let us firstly consider the stability of a second-order NDDE [7] arising from structure dynamics

$$\ddot{x}(t) + 2\xi\dot{x}(t) + x(t) + p\ddot{x}(t - \tau) = 0, \quad (3.1)$$

where $0 < p < 1$. The characteristic equation is

$$\Delta(\lambda) := \lambda^2 + 2\xi\lambda + 1 + p\lambda^2 e^{-\lambda\tau} = 0. \quad (3.2)$$

Table 1: Numerical calculation of the roots of $\Delta(\lambda)$ in (2.14) with $\tau = 0.3$, $a = 0.5$.

Branch	Characteristic root	Branch	Characteristic root
-200	$-0.2572 \times 10^{-9} - 0.4178 \times 10^4 i$	1	$-0.3631 \times 10^{-2} + 0.1063 \times 10^2 i$
-100	$-0.9644 \times 10^{-9} - 0.2084 \times 10^4 i$	2	$-0.4200 \times 10^{-3} + 0.3147 \times 10^2 i$
-20	$-0.2498 \times 10^{-5} - 0.4084 \times 10^3 i$	3	$-0.1517 \times 10^{-3} + 0.5239 \times 10^2 i$
-10	$-0.1052 \times 10^{-4} - 0.1990 \times 10^3 i$	4	$-0.7747 \times 10^{-4} + 0.7333 \times 10^2 i$
-5	$-0.4688 \times 10^{-4} - 0.9427 \times 10^2 i$	5	$-0.4688 \times 10^{-4} + 0.9427 \times 10^2 i$
-4	$-0.7747 \times 10^{-4} - 0.7333 \times 10^2 i$	10	$-0.1052 \times 10^{-4} + 0.1990 \times 10^3 i$
-3	$-0.1517 \times 10^{-3} - 0.5239 \times 10^2 i$	20	$-0.2498 \times 10^{-5} + 0.4084 \times 10^3 i$
-2	$-0.4200 \times 10^{-3} - 0.3147 \times 10^2 i$	100	$-0.9644 \times 10^{-9} + 0.2084 \times 10^4 i$
-1	$-0.3631 \times 10^{-2} - 0.1063 \times 10^2 i$	200	$-0.2572 \times 10^{-9} + 0.4178 \times 10^4 i$
0	-0.2410	500	$-0.1386 \times 10^{-10} + 0.1046 \times 10^5 i$

Each root must be a root of a certain branch of the following equation:

$$F_k(\lambda) := 2\xi\lambda + 1 - W_k(-\lambda^2(1 + pe^{-\lambda\tau})e^{2\xi\lambda+1}) = 0, \quad (k = 0, \pm 1, \pm 2, \dots). \quad (3.3)$$

Then the rightmost root can be found out from $F_0(\lambda) = 0$ via the Newton-Raphson method or Halley's method. For example, let $p = 0.2$, $\xi = 0.05$, and calculate the rightmost root for four special cases: $\tau = 1, 5, 7.5, 11$.

To this end, one chose freely an initial guess, say $\lambda_0 = 1.0 + 3.0i$. Because the simplified polynomial equation $\lambda^2 + 2\xi\lambda + 1 + p\lambda^2e^{-\lambda_0} = 0$, corresponding to (2.8), has two complex roots

$$-0.5971 \times 10^{-1} + 0.1036 \times 10i, \quad -0.4813 \times 10^{-1} + 0.1038 \times 10i, \quad (3.4)$$

the initial guess can be refined as $\lambda_0 = -0.4813 \times 10^{-1} + 0.1038 \times 10i$ for $\tau = 1$. The choice of an initial guess with negative real part is also understandable from the Nyquist plot. Due to Figures 1(a), 1(b), where the Nyquist plot does not encounter the origin of the complex plane, so the trivial solution $x = 0$ is asymptotically stable, and consequently, the rightmost root must have negative real part.

With this λ_0 , the 4th iteration of the Newton-Raphson method gives $\lambda_4 = -0.1155 - 0.9220i$. As shown in Figure 1(c), the Nyquist plot of $\Delta(i\omega - 0.1155)/(1 + i\omega)^2$ passes through the origin, it follows that $\lambda_4 = -0.1155 - 0.9220i$ is the rightmost root for $\tau = 1$.

Similarly, starting from $\lambda_0 = -0.4813 \times 10^{-1} + 0.1038 \times 10i$, the 4th iteration, 6th iteration, and 4th iteration of the Newton-Raphson method give the rightmost roots $0.3125 \times 10^{-1} + 0.9810i$, $-0.6278 \times 10^{-1} - 0.8692i$, and $0.2546 \times 10^{-1} - 0.9986i$ for $\tau = 5, 7.5, 11$, respectively. The numerical results are in agreement with that obtained in [7].

Moreover, as shown in Figure 2, the curve of the real parts of the rightmost roots with respect to the delay can be produced numerically by means of the proposed algorithm, if the delay effect on the asymptotical stability is addressed. From Figure 2, where the initial guess is taken as $\lambda_0 = -0.4813 \times 10^{-1} + 0.1038 \times 10i$, we see that the trivial solution $x = 0$ of (3.1) exhibits two stability switches in $\tau \in [0, 7]$, occurs at $\tau_{10} = 3.2742$, and $\tau_{20} = 6.1742$, respectively, and the corresponding rightmost roots can be found to be $\pm 1.1032i$, $\pm 0.9252i$, respectively. This is the same result as that obtained on the basis of stability switches [7]. In fact, $\Delta(i\omega) = 0$ gives $(1 - p^2)\omega^4 + (4\xi^2 - 2)\omega^2 + 1 = 0$. When $p = 0.2$, $\xi = 0.05$, one has two positive roots $\omega_1 = 1.1032$ and $\omega_2 = 0.9252$, and the corresponding minimal critical delays, determined from $\Delta(i\omega) = 0$, are found easily to be $\tau_{10} = 3.2742$ and $\tau_{20} = 6.1742$, respectively.

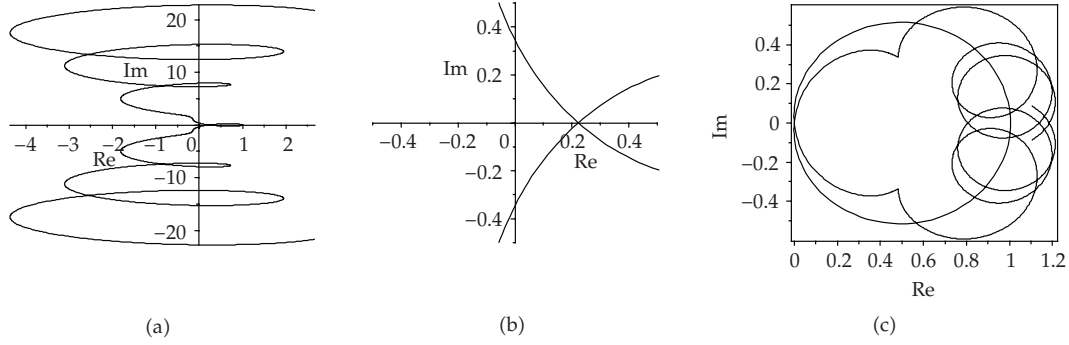


Figure 1: Graphical test for the rightmost root of (3.1): (a) the Nyquist plot of $\Delta(i\omega)/(1+i\omega)^2$; (b) zoomed around the origin in plot (a); (c) the Nyquist plot of $\Delta(i\omega - 0.1155)/(1+i\omega)^2$.

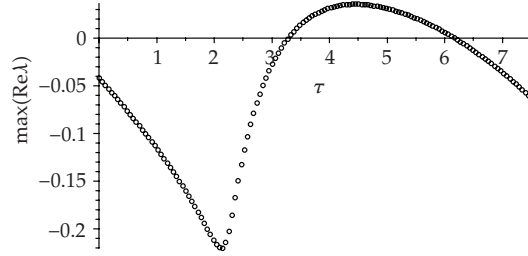


Figure 2: The solution $x = 0$ of (3.1) is asymptotically stable if $\tau \in [0, 3.2742) \cup (6.1742, 7]$, or it is unstable if $\tau \in (3.2742, 6.1742)$.

From Figure 2, we see also that at $\tau = 2.12$, the rightmost root $-0.2201 - 0.1061 \times 10i$ has the smallest negative real part. This fact indicates that a proper chosen delay value can improve the stability of an NDDE.

3.2. An NDDE with two delays

Now, let us consider an NDDE with two delays [22]

$$\frac{d}{dt} \left(x(t) - \frac{3}{4}x(t-1) + \frac{1}{2}x(t-2) \right) = \frac{1}{4}x(t) + \frac{3}{4}x(t-1) \quad (3.5)$$

to show that the method work also for NDDEs with multiple delays. The characteristic equation is

$$\Delta(\lambda) := \lambda \left(1 - \frac{3}{4}e^{-\lambda} + \frac{1}{2}e^{-2\lambda} \right) - \frac{1}{4} - \frac{3}{4}e^{-\lambda} = 0. \quad (3.6)$$

As shown in Figure 3(a), the Nyquist plot of $\Delta(i\omega)/(1+i\omega)$ encounters the origin of the complex plane, so the trivial solution $x = 0$ of (3.5) is unstable, and the rightmost root must have positive real part. To find out the rightmost root, let

$$F(\lambda) = \lambda - \frac{1}{4} - W_0 \left(\left(\lambda - \frac{1}{4} - \Delta(\lambda) \right) e^{\lambda-1/4} \right), \quad (3.7)$$

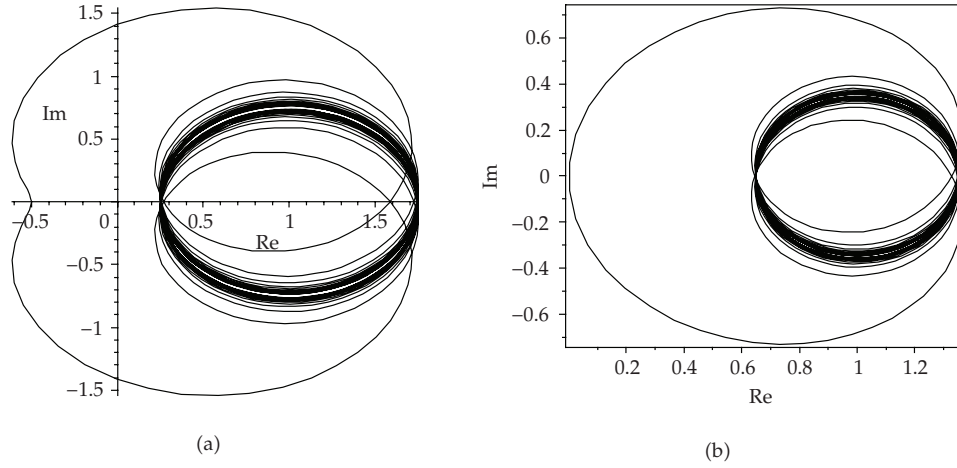


Figure 3: Graphical test for the rightmost root of (3.5): (a) the Nyquist plot of $\Delta(i\omega)/(1+i\omega)$; (b) the Nyquist plot of $\Delta(i\omega + 0.7581 + 0.001)/(1+i\omega)$.

where $W_0(z)$ is the principal branch of Lambert W function. Then, choose freely an initial guess, say $\lambda_0 = 1.0 + 2.0i$, and refine it as the root of $\lambda(1 - 3e^{-\lambda_0}/4 + e^{-2\lambda_0}/2) - 1/4 - 3e^{-\lambda_0}/4 = 0$, namely, replace it with $\lambda_0 = -0.9513 \times 10^{-1} - 0.2924i$. Then the third iteration of the Newton-Raphson method gives $\lambda_3 = 0.7581$. Moreover, the Nyquist plot in Figure 3(b) shows that $\lambda_3 = 0.7581$ is the rightmost root, because the Nyquist plot of $\Delta(i\omega + 0.7581 + 0.001)/(1+i\omega)$ does not encounter the origin. This result is the same as the one obtained by using DDE-BIFTOOL [22, 23].

Moreover, when a negative feedback control $-u x(t)$ is performed on to (3.5),

$$\frac{d}{dt} \left(x(t) - \frac{3}{4}x(t-1) + \frac{1}{2}x(t-2) \right) - \frac{1}{4}x(t) - \frac{3}{4}x(t-1) = -u x(t), \quad (3.8)$$

the unstable equilibrium is stabilized if one chooses, for example, $0.5 < u < 1.5$, as shown in Figure 4.

4. Conclusions

In this paper, the iterative method based on Lambert W function for calculating the rightmost roots of RDDEs is extended to the stability test of a kind of NDDEs for which the asymptotical stability is guaranteed if all the characteristic roots have negative real parts. Two illustrative examples show that the method works effectively. The numerical scheme enables one not only to know whether the time-delay system is asymptotically stable, but also to know the stability margin. A rigorous mathematical treatment of the iterative method such as the convergence of the iterative sequence, however, is not available in this paper and is left for future consideration.

Though the investigation is made mainly for NDDEs with fixed parameters, the proposed scheme does work for some NDDEs with a parameter falling in a given interval. As shown in the first illustrative example from structure dynamics, for example, the iterative method can produce a plot of the real part of the rightmost root with respect to the delay, from

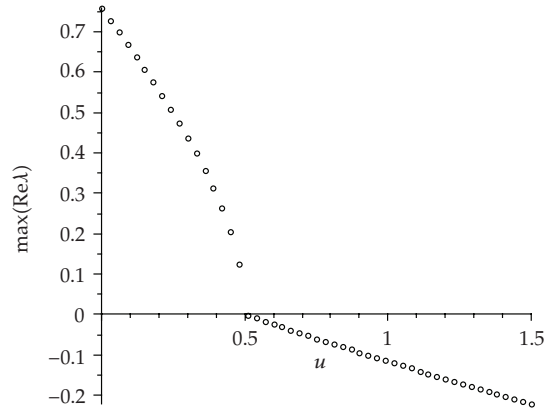


Figure 4: The plot of the real part of the rightmost root with respect to the feedback gain u for (3.8).

which one can easily determine for what value of delay the system is asymptotically stable, and for what value of delay, the system is unstable. It reveals also that a proper chosen delay value can improve the stability of an NDDE. In the second illustrative example, an interval of the feedback gain is determined for stabilizing the unstable equilibrium of the NDDE by using the iterative method.

Acknowledgment

This work was supported by FANEDD of China under Grant no. 200430, and by NSF of China under Grant no. 10532050.

References

- [1] G. Stépán and Z. Szabó, "Impact induced internal fatigue cracks," in *Proceedings of the ASME Design Engineering Technical Conferences (DETC '99)*, Las Vegas, Nev, USA, September 1999.
- [2] A. Bellen, N. Guglielmi, and A. E. Ruehli, "Methods for linear systems of circuit delay differential equations of neutral type," *IEEE Transactions on Circuits and Systems*, vol. 46, no. 1, pp. 212–216, 1999.
- [3] A. G. Balanov, N. B. Janson, P. V. E. McClintock, R. W. Tucker, and C. H. T. Wang, "Bifurcation analysis of a neutral delay differential equation modelling the torsional motion of a driven drill-string," *Chaos, Solitons and Fractals*, vol. 15, no. 2, pp. 381–394, 2003.
- [4] Z. N. Masoud, M. F. Daqaq, and N. A. Nayfeh, "Pendulation reduction on small ship-mounted telescopic cranes," *Journal of Vibration and Control*, vol. 10, no. 8, pp. 1167–1179, 2004.
- [5] D. A. W. Barton, "Dynamics and bifurcations of non-smooth delay equations," Ph.D. dissertation, University of Bristol, Bristol, UK, 2006.
- [6] Z. N. Masoud and A. H. Nayfeh, "Sway reduction on container cranes using delayed feedback controller," *Nonlinear Dynamics*, vol. 34, no. 3-4, pp. 347–358, 2003.
- [7] Y. N. Kyrychko, K. B. Blyuss, A. Gonzalez-Buelga, S. J. Hogan, and D. J. Wagg, "Real-time dynamic substructuring in a coupled oscillator-pendulum system," *Proceedings of the Royal Society of London A*, vol. 462, no. 2068, pp. 1271–1294, 2006.
- [8] Y. N. Kyrychko, S. J. Hogan, A. Gonzalez-Buelga, and D. J. Wagg, "Modelling real-time dynamic substructuring using partial delay differential equations," *Proceedings of the Royal Society of London A*, vol. 463, no. 2082, pp. 1509–1523, 2007.
- [9] Z. N. Masoud, A. H. Nayfeh, and D. T. Mook, "Cargo pendulation reduction of ship-mounted cranes," *Nonlinear Dynamics*, vol. 35, no. 3, pp. 299–311, 2004.

- [10] Y. Kuang, *Delay Differential Equation with Applications in Population Dynamics*, vol. 191 of *Mathematics in Science and Engineering*, Academic Press, Boston, Mass, USA, 1993.
- [11] Y. X. Qin, Y. Q. Liu, L. Wang, and Z. X. Zhen, *Stability of Motion of Dynamical Systems with Time Lag*, Science Press, Beijing, China, 2nd edition, 1989.
- [12] G. Stépán, *Retarded Dynamical Systems: Stability and Characteristic Functions*, vol. 210 of *Pitman Research Notes in Mathematics Series*, Longman Scientific & Technical, Harlow, UK, 1989.
- [13] S.-I. Niculescu, *Delay Effects on Stability. A Robust Control Approach*, vol. 269 of *Lecture Notes in Control and Information Sciences*, Springer, London, UK, 2001.
- [14] H. Y. Hu and Z. H. Wang, *Dynamics of Controlled Mechanical Systems with Delayed Feedback*, Springer, Berlin, Germany, 2002.
- [15] J. M. Krodkiewski and T. Jintanawan, "Stability improvement of periodic vibration of multi-degree-of-freedom systems by means of time-delay control," in *Proceedings of the International Conference on Vibration, Noise and Structural Dynamics*, vol. 1, pp. 340–351, Venice, Italy, April 1999.
- [16] Z. H. Wang and H. Y. Hu, "Calculation of the rightmost characteristic root of retarded time-delay systems via Lambert W function," submitted to *Journal of Sound and Vibration*.
- [17] R. M. Corless, G. H. Gonnet, D. E. G. Hare, D. J. Jeffrey, and D. E. Knuth, "On the Lambert W function," *Advances in Computational Mathematics*, vol. 5, no. 4, pp. 329–359, 1996.
- [18] C. Hwang and Y.-C. Cheng, "A note on the use of the Lambert W function in the stability analysis of time-delay systems," *Automatica*, vol. 41, no. 11, pp. 1979–1985, 2005.
- [19] H. Shinozaki and T. Mori, "Robust stability analysis of linear time-delay systems by Lambert W function: some extreme point results," *Automatica*, vol. 42, no. 10, pp. 1791–1799, 2006.
- [20] M. Y. Fu, A. W. Olbrot, and M. P. Polis, "Robust stability for time-delay systems: the edge theorem and graphical tests," *IEEE Transactions on Automatic Control*, vol. 34, no. 8, pp. 813–820, 1989.
- [21] M. Y. Fu, A. W. Olbrot, and M. P. Polis, "The edge theorem and graphical tests for robust stability of neutral time-delay systems," *Automatica*, vol. 27, no. 4, pp. 739–741, 1991.
- [22] W. Michiels and T. Vyhldal, "An eigenvalue based approach for the stabilization of linear time-delay systems of neutral type," *Automatica*, vol. 41, no. 6, pp. 991–998, 2005.
- [23] K. Engelborghs, T. Luzyanina, and G. Samaey, "DDE-BIFTOOL v2.0: a Matlab package for the computation analysis of delay differential equations," Tech. Rep. TW220, Department of Computer Science, Katholieke Universiteit Leuven, Leuven, Belgium, 2001.

Research Article

Dynamical Models for Computer Viruses Propagation

José R. C. Piqueira and Felipe Barbosa Cesar

*Escola Politécnica da Universidade de São Paulo, Avenida Prof. Luciano Gualberto, travessa 3 - 158,
05508-900 São Paulo, SP, Brazil*

Correspondence should be addressed to José R. C. Piqueira, piqueira@lac.usp.br

Received 28 March 2008; Revised 9 May 2008; Accepted 30 May 2008

Recommended by Jose Balthazar

Nowadays, digital computer systems and networks are the main engineering tools, being used in planning, design, operation, and control of all sizes of building, transportation, machinery, business, and life maintaining devices. Consequently, computer viruses became one of the most important sources of uncertainty, contributing to decrease the reliability of vital activities. A lot of antivirus programs have been developed, but they are limited to detecting and removing infections, based on previous knowledge of the virus code. In spite of having good adaptation capability, these programs work just as vaccines against diseases and are not able to prevent new infections based on the network state. Here, a trial on modeling computer viruses propagation dynamics relates it to other notable events occurring in the network permitting to establish preventive policies in the network management. Data from three different viruses are collected in the Internet and two different identification techniques, autoregressive and Fourier analyses, are applied showing that it is possible to forecast the dynamics of a new virus propagation by using the data collected from other viruses that formerly infected the network.

Copyright © 2008 J. R. C. Piqueira and F. B. Cesar. This is an open access article distributed under the Creative Commons Attribution License, which permits unrestricted use, distribution, and reproduction in any medium, provided the original work is properly cited.

1. Introduction

A few decades ago, computer viruses arose in the form of programs with simple code and able to undermine the smooth operation of a machine. Initially, in spite of the large number of viruses, they caused minor damages to machinery and their spread was very slow. Over the years, due to the rapid development of technology, such as software and hardware, the development and popularization of the Internet and the great variety of equipment using software and networks, viruses have become a major threat [1].

Currently, these virus programs have more complex codes, being able to produce mutations of themselves, and their detection and removal by antivirus programs became more

difficult [2]. Their goals go much further than simply damaging a machine. They are capable of acquiring personal data of users of networks, such as a bank account, and cause severe damages to large corporations [3].

In view of these concerns, a better understanding of the computer viruses spreading dynamics is mandatory. To improve the safety and reliability in computer systems and networks, it is important to have the capacity of recognizing and combating the several types of infections faster and more effectively [4, 5].

Research actions started at the end of the 80s with the classical paper of Kephart et al. [6] proposing an ecosystem approach for computational systems. Then, the efforts were concentrated on the development of antivirus programs, responsible for the detection and removal of viruses, based on the previous recognition of the infection code based on the models shown in [2, 7, 8]. These programs have a great upgrading power, but act just as simple vaccines against diseases [2, 4]. They are not able to predict the behavior of networks when an infection is established in a machine and, consequently, cannot support preventive attitude against virus actions based on events of the network.

The first effort to produce models for the spreading of computer viruses based on their epidemiological counterparts is reported in [7] with the initial ideas for deriving long-term behaviors considering the graph representing the network connections. Then, with Markov chains representing the local behavior of infection action in a single node, susceptible-infected-removed (SIR) models were presented trying to fit the long-term behavior of the viruses propagation [9].

This kind of approach had some attention in the last five years and the relations between spreading viruses and topological parameters of the network were studied, being successful mainly when modeling the propagation by email networks [10]. Besides, SIR models were modified [5] and applied to guide infection prevention [11, 12], deriving expressions for epidemiological thresholds [11–13].

This work focuses on the achievement of models for the dynamics of the spread of certain viruses, mainly taking into account the correlation functions between the several viruses spreading data, during a certain period of time. Thus, the number of infections from a type of virus could be foreseen in the short term by comparison with other viruses or with notable events in the network, which would support preventive policies.

In order to provide simple algorithms to allow operational facility, simple autoregressive models are chosen [14, 15]. Considering the periodicity of the data collected, Fourier models are also tried, producing the same results of the autoregressive ones.

2. Methodology

The data to be collected for modeling computer infections propagation are the number of daily, weekly, and monthly infections for several computer viruses. These numbers are found in the Internet, for instance, in <http://www.avira.com/>, and support the development of linear identification models.

The next step is the choice of a specific virus to be analyzed, in the enormous range of possibilities. In this work, a premise was taken into consideration: in order to have an efficient identification, the several chosen viruses need to present similar propagation dynamics. Here, the high incidence of cases reported and the email spreading compose the chosen criterion.

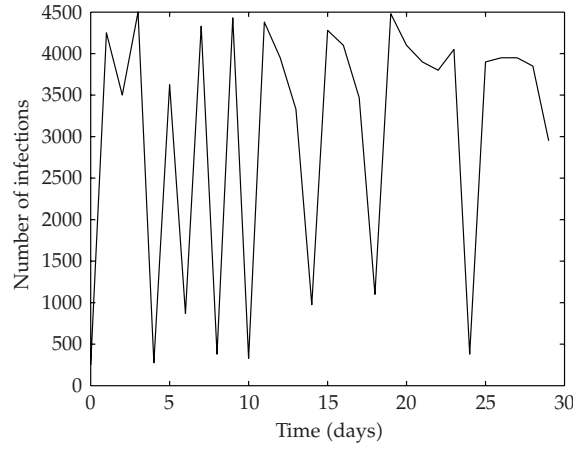


Figure 1: *Wormnetsky.p* temporal evolution.

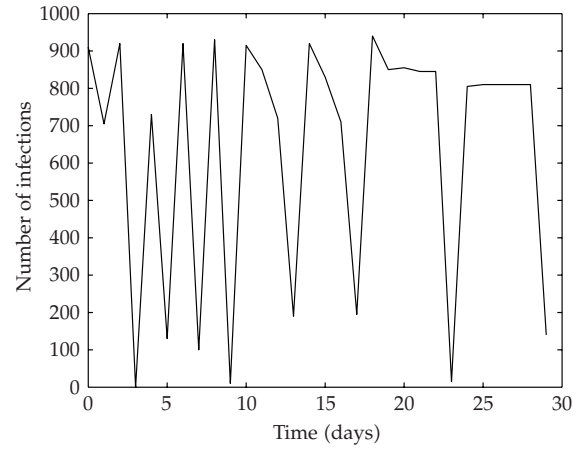


Figure 2: *Wormmytob.mr* temporal evolution.

Wormnetsky.p, *wormmytob.mr*, and *trdir.stration.ge* were chosen, that is, two worms and a trojan. Figures 1, 2, and 3 show the dynamical evolution of the number of infections with *wormnetsky.p*, *wormmytob.mr*, and *trdir.stration.ge*, respectively.

First, in order to verify the relations among the viruses, cross-correlation coefficients are calculated. Considering two signals $x(t)$ and $y(t)$ simultaneously sampled in regular T intervals, and calling $x(nT)$ and $y(nT)$ their n samples, for a certain time interval containing N sample periods, the cross-correlation coefficient, ρ , between $x(t)$ and $y(t)$ measures how they are related with each other in this interval (see [16, page 206]). Table 1 summarizes the cross-correlation coefficients, calculated for the three pairs of infection signals, for the time interval of Figures 1, 2, and 3, sampling the data daily.

The results from Table 1 indicate acceptable correlation between the spread of the viruses chosen, corroborating the visual similarity between the temporal evolution of the three infections. Due to this, only *wormnetsky.p* is considered to identify the system parameters to be

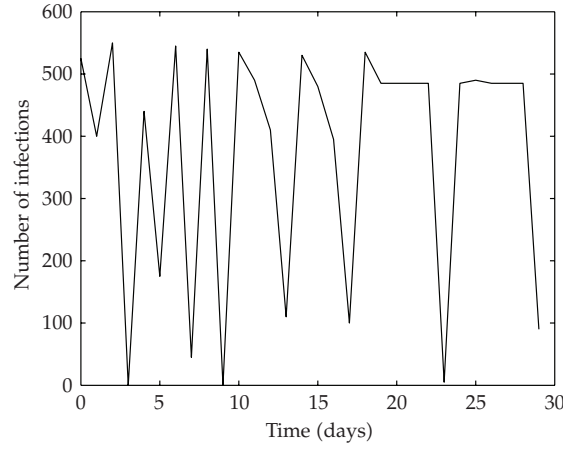


Figure 3: *Trdir.stration.gen* temporal evolution.

Table 1: Viruses cross-correlation coefficients.

Viruses	Cross-correlation coefficient
<i>Wormnetsky.p, wormmytob.mr</i>	0.39312
<i>Wormnetsky.p, trdir.stration.ge</i>	0.40541
<i>Wormmytob.mr, trdir.stration.ge</i>	0.99435

used to provide short-term forecasts for the three viruses. Following this identification strategy, model accuracy is checked.

3. System identification algorithms

In order to identify the parameters to model the temporal evolution of the infections by the three types of viruses selected here, two approaches were followed:

- (i) using a linear autoregressive model, that is, consider that the current value of a variable depends only on the former values, up to a certain delay [14, 15];
- (ii) identifying the main frequencies of the time series and treating them as Fourier series [14, 15].

3.1. Autoregressive model

Considering a regularly sampled signal $y(k)$, its estimated value at instant k is given by

$$y(k) = \sum_{i=1}^d p_i y(k-i), \quad (3.1)$$

where p_i are the model parameters to be estimated by using the minimum square method, and d is the maximum delay to be considered [14, 15], measured by the number of sampling intervals.

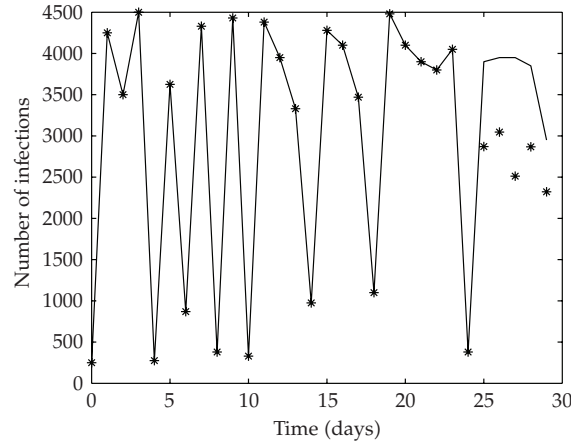


Figure 4: *Wormnetsky.p* temporal evolution simulation ($d = 10$).

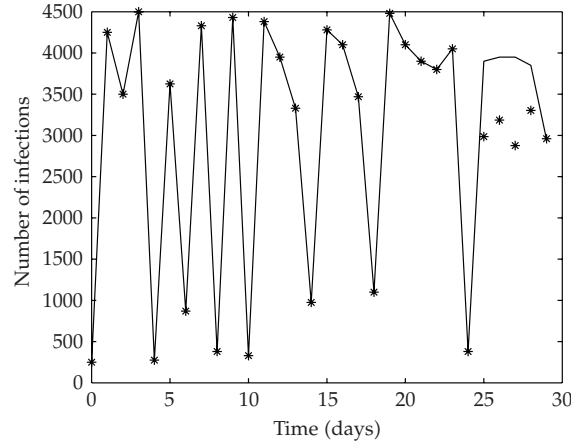


Figure 5: *Wormnetsky.p* temporal evolution simulation ($d = 15$).

By using a “free-prediction” strategy, the vector data are divided into two parts: one is used for the identification of the system parameters and the other for the simulation and validation of the model. In the case of the data described in Section 2, the 25 first samples are used for identification and the last 5 for simulation. Different values of d are considered and Figures 4, 5, and 6 show the results for d equal to 10, 15, and 24, respectively, with the continuous line representing the real data and the asterisks representing the simulation results.

In order to compare the several chosen delays, Table 2 shows the mean-square estimation error in each case. Considering these results, from now on, all models will use $d = 15$.

To have an idea of the efficiency of the adopted identification strategy, the estimated parameters for *wormnetsky.p* are used to model the dynamics of *wormmytob.mr* and *trdir.stration.gen*. The results are shown in Figures 7 and 8, respectively, with the continuous line representing the real data and the asterisks representing the simulation results. Table 3 summarizes the mean-square errors of these simulations.

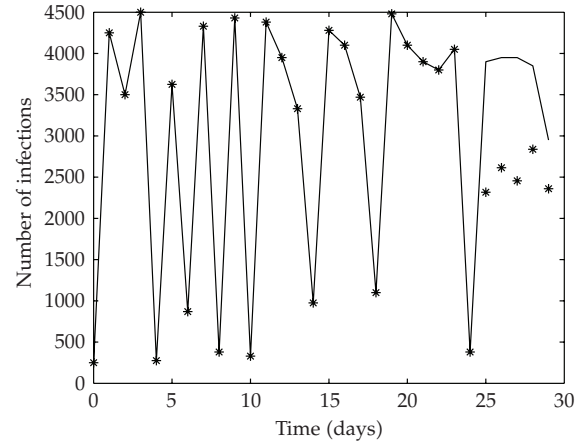


Figure 6: *Wormnetsky.p* temporal evolution simulation ($d = 24$).

Table 2: Estimation errors in autoregressive models for *wormnetsky.p*.

d	Mean-square estimation error(%)
10	5.5773
15	4.1751
24	6.8542

Table 3: Estimation errors in autoregressive models for *wormmytob.mr* and *trdir.stration.ge*.

Virus	Mean-square estimation error(%)
<i>Wormmytob.mr</i>	17.142
<i>Trdir.stration.ge</i>	18.32

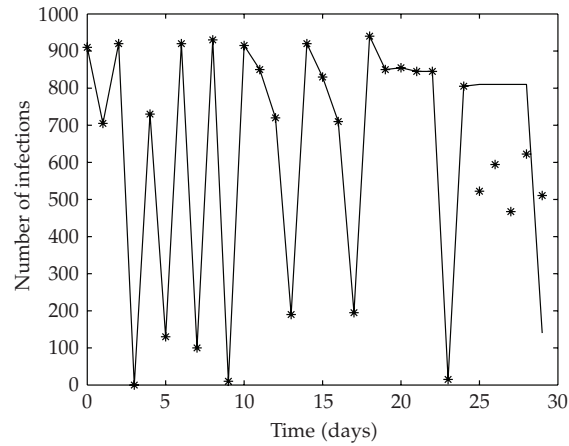


Figure 7: *Wormmytob.mr* temporal evolution simulation.

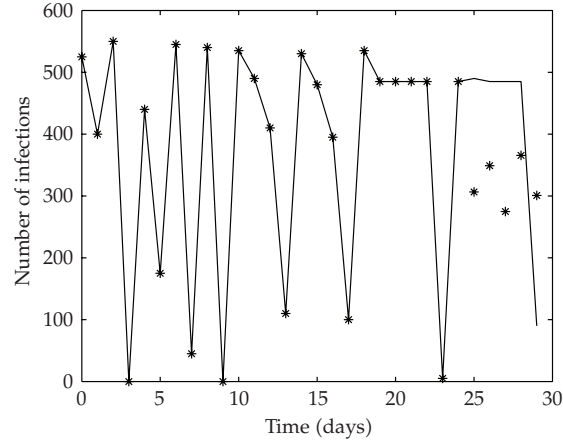


Figure 8: *Trdir.stration.gen* temporal evolution simulation.

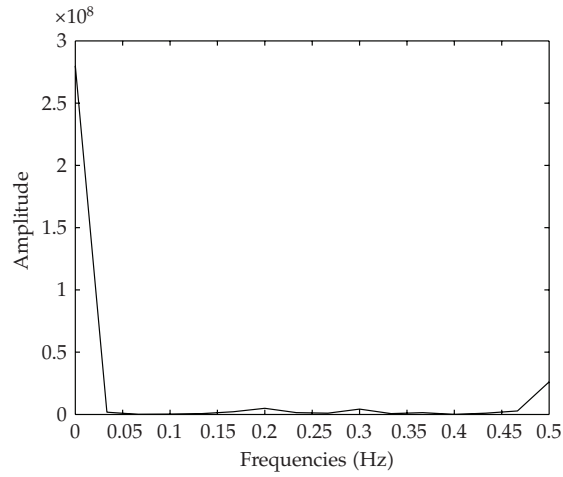


Figure 9: *Wormnetsky.p* frequency spectrum.

The simulations performed taking into account only the parameters calculated for the *wormnetsky.p* show that the short-term estimations of new infections are not precise for *wormmytob.mr* and *trdir.stration.ge*, as expected, because the same model is used for different viruses. Nevertheless, the model is able to predict with some accuracy the increasing and decreasing tendencies in their dynamics. This knowledge permits the implementation of preventive policies, considering only the *wormnetsky.p* propagation profile.

3.2. Fourier series model

Observing the strong oscillatory character of the three different viruses studied, a model considering the signals as a sum of cosines was developed. Figures 9, 10, and 11 present the frequency spectrum for the temporal evolution of the *wormnetsky.p*, *wormmytob.mr*, and

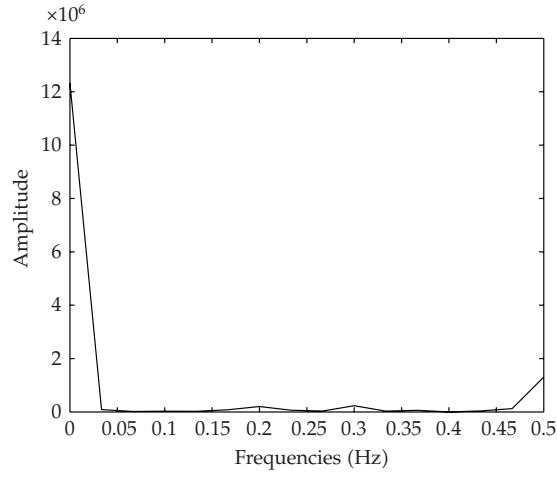


Figure 10: *Wormmytob.mr* frequency spectrum.

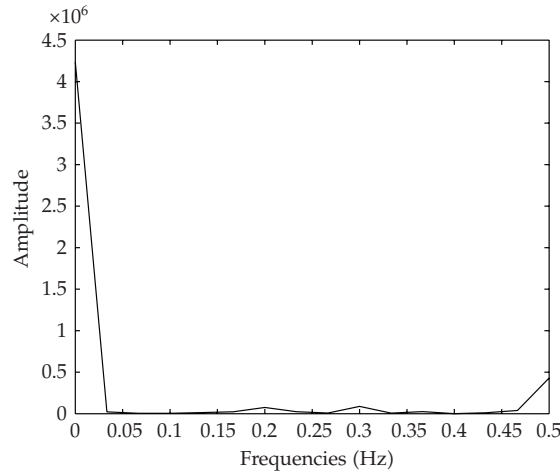
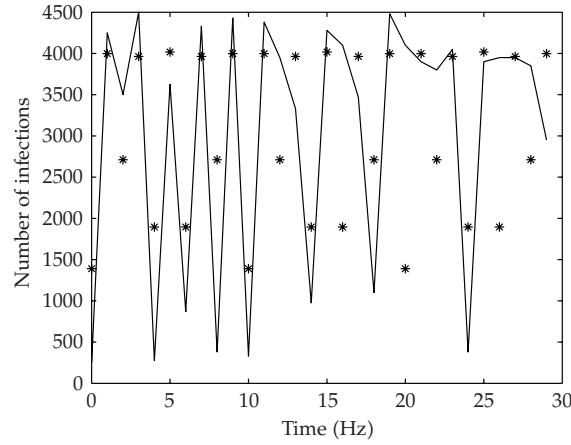
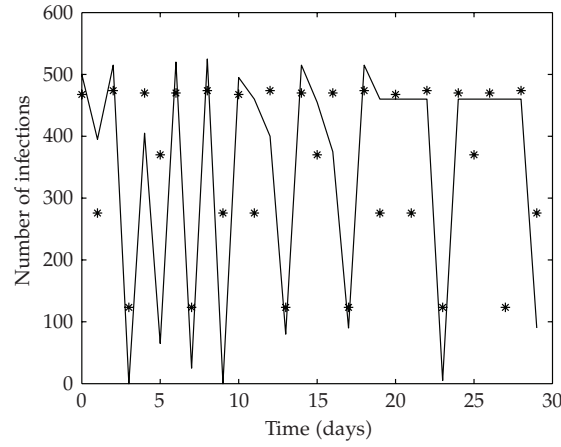


Figure 11: *Trdir.stration.gen* frequency spectrum.

trdir.stration.ge propagation. As one can see, the main frequencies of the three dynamic behaviors are the same.

Figures 9, 10, and 11 indicate that a good set of frequencies for developing the model is $F = [0 \ 0.2 \ 0.3 \ 0.5]$. Following the same reasoning used in Section 3.1 for identification, the model parameters are calculated by using only the data from *wormnetsky.p* and the predictions of new infections for *wormmytob.mr* and *trdir.stration.ge* are obtained by using the same parameters.

To have an idea about the efficiency of the adopted identification strategy by using Fourier methods, Figures 12, 13, and 14 show the predicted dynamics of *wormnetsky.p*, *wormmytob.mr*, and *trdir.stration.gen*, respectively, with the continuous line representing the real data and the asterisks representing the simulation results. Table 4 summarizes the mean-square errors of these simulations.

Figure 12: *Wormnetsky.p* Fourier model.Figure 13: *Wormmytob.mr* Fourier model.

As in autoregressive models, simulations performed taking into account only the parameters calculated for the *wormnetsky.p* show that the short-term estimations of new infections are not precise for *wormmytob.mr* and *trdir.stration.ge*, as expected, because the same model is used for different viruses. But, again, the model is able to predict with some accuracy the increasing and decreasing tendencies in their dynamics, allowing to establish preventive policies by using only the data from *wormnetsky.p* propagation.

4. Conclusions

Two different models for the dynamics of computer viruses propagation were compared: autoregressive and Fourier analysis presenting similar results. They provide good predictions for three different types of infections by using the data collected for just one of them.

In spite of not being totally satisfactory, these models present the possibility of predicting increasing and decreasing tendencies in the propagation of a certain type of virus by using the

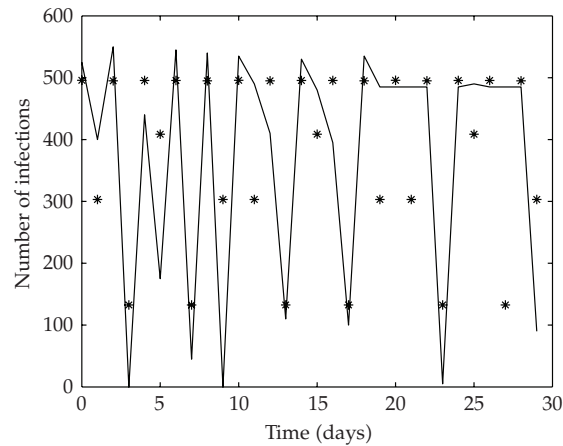


Figure 14: *Trdir.stration.gen* Fourier model.

Table 4: Estimation errors in Fourier models for *wormnetsky.p*, *wormmytob.mr*, and *trdir.stration.ge*.

Virus	Mean-square estimation error(%)
<i>Wormnetsky.p</i>	7.0354
<i>Wormmytob.mr</i>	16.778
<i>Trdir.stration.ge</i>	18.096

accumulated experience with another one. It seems that this point could be used to predict and control the infection levels in advance, providing preventive actions in order to increase safety and reliability.

Acknowledgments

The first author is supported by FAPESP and CNPq and the second author is supported by the Brazilian Oil Agency.

References

- [1] P. J. Denning, *Computers under Attack*, Addison-Wesley, Reading, Mass, USA, 1990.
- [2] P. S. Tippet, "The kinetics of computer virus replication: a theory and preliminary survey," in *Safe Computing: Proceedings of the 4th Annual Computer Virus and Security Conference*, pp. 66–87, New York, NY, USA, March 1991.
- [3] F. Cohen, "Models of practical defenses against computer viruses," *Computers & Security*, vol. 8, no. 2, pp. 149–160, 1990.
- [4] S. Forrest, S. A. Hofmayer, and A. Somayaji, "Computer immunology," *Communications of the ACM*, vol. 40, no. 10, pp. 88–96, 1997.
- [5] J. R. C. Piqueira, B. F. Navarro, and L. H. A. Monteiro, "Epidemiological models applied to viruses in computer networks," *Journal of Computer Science*, vol. 1, no. 1, pp. 31–34, 2005.
- [6] J. O. Kephart, T. Hogg, and B. A. Huberman, "Dynamics of computational ecosystems," *Physical Review A*, vol. 40, no. 1, pp. 404–421, 1989.
- [7] J. O. Kephart, S. R. White, and D. M. Chess, "Computers and epidemiology," *IEEE Spectrum*, vol. 30, no. 5, pp. 20–26, 1993.

- [8] J. O. Kephart, G. B. Sorkin, and M. Swimmer, "An immune system for cyberspace," in *Proceedings of the IEEE International Conference on Systems, Men, and Cybernetics (SMC '97)*, vol. 1, pp. 879–884, Orlando, Fla, USA, October 1997.
- [9] L. Billings, W. M. Spears, and I. B. Schwartz, "A unified prediction of computer virus spread in connected networks," *Physics Letters A*, vol. 297, no. 3-4, pp. 261–266, 2002.
- [10] M. E. J. Newman, S. Forrest, and J. Balthrop, "Email networks and the spread of computer viruses," *Physical Review E*, vol. 66, no. 3, Article ID 035101, 4 pages, 2002.
- [11] B. K. Mishra and D. Saini, "Mathematical models on computer viruses," *Applied Mathematics and Computation*, vol. 187, no. 2, pp. 929–936, 2007.
- [12] B. K. Mishra and N. Jha, "Fixed period of temporary immunity after run of anti-malicious software on computer nodes," *Applied Mathematics and Computation*, vol. 190, no. 2, pp. 1207–1212, 2007.
- [13] M. Draief, A. Ganesh, and L. Massoulié, "Thresholds for virus spread on networks," *Annals of Applied Probability*, vol. 18, no. 2, pp. 359–378, 2008.
- [14] L. Ljung, *System Identification*, Prentice-Hall, Upper Saddle River, NJ, USA, 1999.
- [15] L. A. Aguirre, *Introdução à Identificação de Sistemas*, Editora UFMG, Belo Horizonte, MG, Brazil, 2004.
- [16] P. Olofsson, *Probability, Statistics, and Stochastic Processes*, John Wiley & Sons, Hoboken, NJ, USA, 2005.